NORTHWESTERN UNIVERSITY

Probing the Interface of Particles and Waves Using Fourier Transform Spectroscopy

A DISSERTATION

SUBMITTED TO THE GRADUATE SCHOOL IN

PARTIAL FULFILLMENT OF THE REQUIREMENTS

for the degree

DOCTOR OF PHILOSOPHY

Field of Chemistry

by:
Shawn (Zhao) Irgen-Gioro

EVANSTON, ILLINOIS

September 2021

Abstract

When a collection of individual units behave synchronously, it is often useful to describe the actions of the group. Broadly speaking in Physics, individuals are described as particles and collective actions are described using waves. However, the dynamic symphony of life ordains that orchestral sections play in harmony for a finite amount of time. To generalize an ancient Chinese proverb: "All objects, long divided, must unite. Long united, must divide."

Coherence is the the measure of the spatial and temporal scales that the wave description of reality breaks down. All functions can be Fourier decomposed into a sum of sines and cosine waves, but there exists an intricate relationship between the frequency of a wave and the timescale it can exist on. Heuristically, bigger things move slower. In Quantum Mechanics, this frequency-time relationship has a limit that is quantitatively defined in the Uncertainty Principle. States that have well defined energies (and thus frequencies) must exist for many cycles of oscillation and persist for a long time. Objects that exist for a short amount of time must be composed of many different energies (that oscillate in phase).

Collective behavior at a molecular scale can be studied using Fourier transforms. Chapter 1 introduces how light-matter interactions and interferometers are implemented in so called Fourier Transform Spectroscopies to uncover the timescales at which energetic

wavepackets disperse. Chapter 2 applies the techniques introduced in Chapter 1 to polymers, repeating chains of individual units that have delocalized electronic states. Chapters 3, 4, and 5 dive deep into coherence observed in photosynthetic proteins, which are evolutionarily optimized formations of chromophores designed to transfer energy. In Chapters 6 and 7, the ability for quantum objects to have coherence with themselves is investigated. Lastly, Chapter 8 generalizes our molecular understanding of coherence to processes occurring at a cellular and whole brain level.

Acknowledgements

My parents, Xin Su 苏欣 and Xing Zhao 赵兴, came to America in 1993 to give my brother, Allan, and me the best life they could envision. They arrived in a foreign land with little besides a few suitcases of clothes and an ardent belief that their duty was to provide the next generation the best chance possible to succeed. They exceeded that calling. If they thought there would be personal sacrifice for the benefit of their children, they never hesitated. I'll never repay my debt to them, but they know that I'll live my life carrying on their values. I am eternally grateful, and to them this thesis is dedicated.

My support system went beyond my parents to an amazing network of family and friends. First and foremost, to my significant other, Minji - you inspire me day in and day out. You are not only my rock, but are the base in which all dreams are built. Will H. once told me that you are the average of the 5 people you spend the most time with, and I can only hope that is true to gain some of your compassion, tenacity, and clarity for what truly matter in life. To Zack K., Thomas H., Jade W., Katie B., Justin R., Tom M., and Alex M., I admire how each of you navigate through life, and I thank you for giving me the perspective that I sometimes lack.

I was extremely lucky to bond deeply with my colleagues here at Northwestern. My cohort was filled with individuals passionate about science, sturdy in their knowledge base, and dedicated to helping each other. Among others, Jake R., Karthik G., Suyog P.,

Christian C., Xinyi J., Nate F., Jack O., Wooje C., Albert V., Adam P., Elamar H., Naomi D., Justin H., David X., Aaron S., Paul B., Eunice B., Jon S., Jovan N., Yue W., Austin E., Matt N., Joaquin A., Ryan H., Nolan W., Mark K. and Daylan S. enriched my life in and out of lab and for them I am grateful.

My technical and personal growth in the past 5 years is attributable to a few mentors. Boris S. was a successful 5th year student when I started, but always found time to indulge my nascent scientific ideas. He never hesitated to put down his more important tasks to show me how something worked, and I have tried to pass that on. Austin S. is one of the most talented scientists I know and one of the best scientific communicators around. His ability to implement complicated experiments and explain them simply is renown from all people who knew him. I had the privilege of working closely with him, and he has made me a better scientist and person. To other mentors: Rafa L., Bram C., Will H., Sunhong J., I wouldn't be here without your contributions, and I thank you all.

Finally, the two PIs I've worked for have shaped me from a meandering thinker to a purposeful experimentalist. Prof. Elad Harel believed in me, entrusted me with difficult experiments, and showed me my first steps. His propensity to come up with state-of-the-art technologies astounded me. Our problems turned into results typically from a sudden idea he had or code that he had written, and for his contributions to my career I am eternally grateful. If Prof. Elad Harel showed me how to walk, Prof. Emily A. Weiss taught me how to fly. Under her guidance, I was able to flourish as an independent thinker, a useful collaborator, and a hub of spectroscopy. She showed me new realms of what spectroscopy can do, how science is meant to be applied, and how to develop a culture of vibrant ideas and synergistic cooperation. Her logical, detail oriented, and highly versatile thinking is something I aim to emulate. I hope to continue to learn from

her for years to come.

Contents

List of Figures

Time and Frequency: An Introduction to Fourier Spectroscopy

1.1 Time Keeping

1.1.1 Computational Clocks

Early Christianity had a big problem on their hands. On the surface, calculating the date of Easter to celebrate the resurrection of Jesus is a seemingly easy proposition. The Bible states that the resurrection occurred on the 3rd day of Passover, which occurs on the first full Moon following the spring equinox. However, tracking the lunar phases against the solar based Julian calendar was a challenge. The period of a lunar month is 29.5306 days, while the solar year is 365.2422 days (numbers not yet known at the time). This means that not only is the equinox constantly changing, but pinpointing *which* full moon qualifies as the first full moon after the equinox is difficult since neither events fell on the same calendar day every year. To further complicate matters, the Christian Church declared that Easter must be celebrated on a Sunday. This adds a 3rd criteria. The day of week that the correct full moon occurs is needed to figure out which Sunday date is worthy of a proper Easter Celebration.

An experimentalist might wish to dispense with this predictive burden. Muslims celebrate the beginning of Ramadan by waiting to *observe* the crescent moon in their ninth month to appear to begin fasting, regardless of when in the solar year that month occurs. However, Christians start their celebrations with Lent, 40 days before Easter, and they would like to finish on the correct date. Ideally, the date of Easter could be calculated for years to come. "There are many indications that the sole important application of arithmetic in Europe in the Middle Ages was the calculation of the date of Easter."[1]

The calculation of the date of Easter is called the computus, and some of the earliest computational devices were designed to perform it. Multi-step algorithms were handled mechanically, with "profile wheel" rims that traced out mathematical functions, ratchets that acted as modulos, and gear ratios that approximated sidereal days to within a second a century.[2] All of this possible with pendulums synchronizing and driving movement. One particular clock that has been operational with no electricity since 1842, survived Y2K, and will calculate the date of Easter for centuries to come is the Strasbourg Astronomical Clock, Figure 1.1

Naming this masterpiece a "clock" is diminutive. It tracks the position of over 5,000 stars in the sky, along with the positions of all the planets. Numerous ornate automata imbue the clock with deep religious and philosophical symbolism. At noon, Jesus and the 12 apostles appear to be blessed in turn. The days of the week are counted off by seven Greco-Roman Gods. Paintings of figures such as Urania and Copernicus grace the panels. All this, encased in a 3 tower, Renaissance, brass, glass, and stone structure. Only with the marriage of fundamental astronomical research, cutting edge mathematics, precise engineering, artistry, and philosophy, was the construction of this clock possible.

(A) Wide Angle View of Clock

(B) Close up of computus that calculates the date of Easter

FIGURE 1.1: The Strasbourg Astronomical Clock In the Cathédrale Notre-Dame of Strasbourg, Alsace, France. Photo by David Iliff. License: CC BY-SA 3.0

In my own scientific career, I have desired to work on modern "clock problems." Problems in which only through centuries of human achievement in the mathematics, physics, chemistry, and engineering, can we probe questions that, in turn, make us reflect on our own place in the universe.

1.1.2 Coupling of Clocks

The pendulum was the driving force that synchronized all gears, pulleys, and ratchets that powered the Strasbourg Astronomical Clock on the timescale of seconds. Consequently, the clock synchronized the movements of millions of Christians on time timescale of months. In modern digital electronic devices, synchronization of parallel processes is achieved in a similar manner. Modern processors have clock speeds on the order of GHz, or a billions of times a second. A clock signal is generated using an oscillator, which may be a RC circuit, but more commonly a quartz piezo-electric is used. Like a metronome keeping an orchestra in time, a modern digital computer's clock coordinates the action of different circuits.

With abundant synchronization in the world around us and a mechanical understanding of how coordination can be artificially created, it is tempting to attribute biological collective action to individuals following either a leader or a clock. Instead, what we find in nature is that collective behavior does not need to arise from a centralized source. Flocks of birds can turn in unison, where the shape of the collective is better described using fluids than individual particles.[3] Brain regions will begin to synchronously fire together for a period of time when communicating.[4] In Mitosis or cell division, assemblies of microtubules form spindles, line up chromosomes, and push the two halves of the cells apart, Figure 1.2.[5] As opposed to a mechanism of top down control, nature is full of small interactions between individual units that create emergent behavior. Place two (mechanical) metronomes on a table next to each other, and they will beat in sync even if their set frequencies are not exactly the same.

The synchronization of pendulum systems was a phenomena not lost on early clock makers. It used to be difficult to make two perfectly identical clocks, so that one clock was

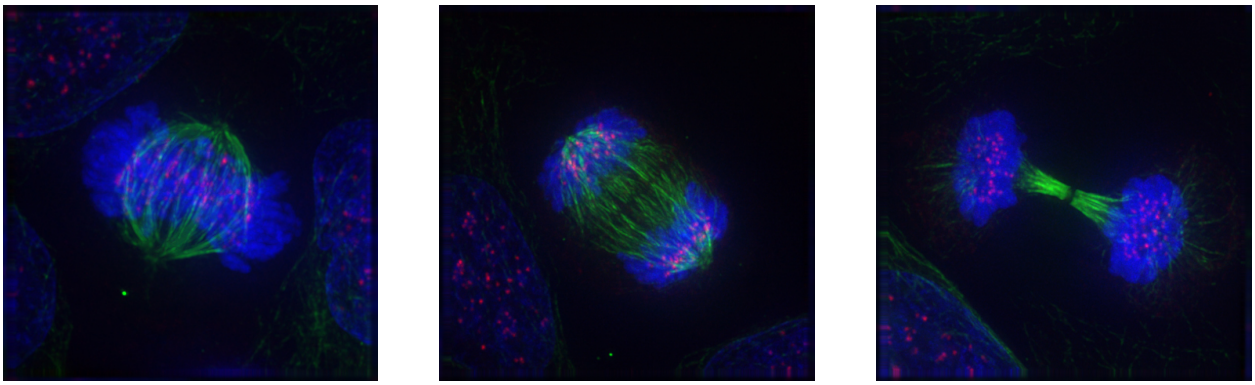

(A) Metaphase: chromosomes are centered and spindles are formed

(B) Anaphase: Microtuble spindles begin to pull chromosomes apart

(C) Telophase: Mitosis is complete as new nuclear envelopes begin to form

FIGURE 1.2: Synchronization of microtubules in Mitosis. Microtubules are stained green while chromosomes are stained in blue. Photo by Roy van Heesbeen. License: CC BY-SA 3.0

always faster or slower than the other. Christiaan Huygens, a 17th century Dutch mathematician and clock maker, first noticed that if you placed two pendulum clocks on a common support, over the course of half an hour, eventually the two clocks would become locked at the same frequency. At the time, Huyges did not have Newton's mathematical tools to describe his system, something we might now call "coupled oscillators."

A pendulum oscillates with continuous period under a few assumptions. Having a large, dense mass bob reduces the effect of friction and air drag. More importantly for our purposes, the small angle approximation $sin(x) \approx x$ allows the system to be described using a *linear* restoring force. Consider an ideal 2D pendulum with mass, m, fixed to a point with a mass-less string with length, l, swinging with angular displacement, θ. Newton's second law gives us the force applied on the mass as:

$$F = ma = -mgsin(\theta) \approx -mg\theta$$

so that

$$a \approx -g\theta.$$

The role of the small angle approximation in this scenario is to create a *linear* applied force on the mass bob with respect to θ, where g is the local acceleration due to gravity. Knowing that

$$a = \frac{dv}{dt} = \frac{d^2s}{dt^2} = \frac{d^2(l\theta)}{dt^2} = l\frac{d^2\theta}{dt^2}$$

and using the position of the bob, $s(\theta) = l\theta$, the overall equation of motion is can be written as a second order differential equation describing simple harmonic motion.

$$\frac{d^2\theta}{dt^2} + \frac{g}{l}\theta = 0.$$

With the initial conditions $\theta(0) = \theta_0$ and $\frac{d\theta}{dt}(0) = 0$, the pendulum moves as a function of time as a continuous oscillation.

$$\theta(t) = \theta_0 cos(\sqrt{\frac{g}{l}}t).$$

Utilizing the small angle approximation is a neat mathematical tool, but its utility also expresses a truth about the world around us. Many of the systems we deal with are near or at equilibrium, sitting at local minima of potential energy surfaces. A potential energy surface is a way to represent energetic states, and it is convenient since gravity gives us intuition of objects tending towards lower potential energy states. A potential energy surface can be drawn as the result of many different forces such as gravitational, electrostatic, and magnetic forces, but its generality is what gives it power. In the same way balls stop at the bottom of hills, the energetic physical world around us is filled with phenomena occurring around stable energetic states.

Given an arbitrary potential energy surface near equilibrium, we can Taylor expand our potential energy surfaces to reveal why oscillatory systems are so ubiquitous. For an arbitrary smooth 1D potential energy surface, a Taylor expansion gives:

$$U(x) = U_0 + U_1(x - x_0) + U_2(x - x_0)^2 + ...$$

The first term of our Taylor expansion, U_0, is a constant. Relative energies can be shifted by a constant with no change of dynamics of the system. A pendulum behaves the same (neglecting the change of local gravitational constant) if it is resting on a table or on the floor. Thus, the first term can be set as $U_0 = 0$ with no loss in generality. The second term is related to the derivative of the potential energy surface $U_1 = U'(x_0)$. If x_0 is the equilibrium position, by definition the derivative of our potential energy surface at that point is 0 so that the second term can be neglected as well. The third term is related to the second derivative of the potential energy surface $U_2 = \frac{1}{2}U''(x_0)$. Since we are at a potential energy *minima* and not a *maxima*, the value of $U''(x_0)$ is generally positive (and typically non-zero) so that we can define $U''(x_0) \equiv k$. If we truncate the higher order expansion terms, which is valid if we do not move far from the equilibrium position x_0, this gives an approximation of the *all* potential energy surfaces near equilibrium as:

$$U(x) \approx \frac{1}{2}k(x - x_0)^2$$

Remembering that $F = -U'(x)$, we find that near equilibrium, our approximation results in a *linear* restoring force. The same as for the pendulum:

$$F = -k(x - x_0)$$

This type of energetic system is known as the **simple harmonic oscillator** and is important because **all objects moving in the vicinity of potential energy minimums can be described using potential energies of this form**. Whether it is an ice cube sitting in still water, leaves swaying in the wind, or the pendulums of clocks, all motions can be described using harmonic oscillators to a certain degree.

While the generality of the simple harmonic oscillator demonstrates that all behavior can be "wave-like," its utility is in how we can use it to understand collections of individuals. Isolated oscillators can have individual behavior with unique trajectories. However, once oscillators come into contact, they can become *coupled*, which was the effect that Huygens observed when his clocks were on a common support. The motion of the pendulum was transmitted through the wooden beam, so that his normally isolated oscillators became one collective unit.

We showed above that an isolated oscillator has a motion that can be described using a cosine wave with a fixed natural frequency. Oscillators that are coupled will oscillate together in collective "normal" modes that are combinations of the individual natural frequencies.

The motion of N coupled oscillators is best described using matrix form. Using Newton's second law again:

$$\mathbf{M}\mathbf{x}'' = -\mathbf{K}\mathbf{x}$$

where $\mathbf{M}$ is an $N \times N$ "mass matrix," $\mathbf{K}$ is a $N \times N$ "spring constant matrix," and $\mathbf{x}$ is a $N \times 1$ column vector. $\mathbf{M}$ is generally a diagonal matrix simply representing the mass of each oscillator. If the $\mathbf{K}$ matrix is also a diagonal matrix, then the matrix equation simplifies to an set of independent simple harmonic oscillators. Coupling between oscillators is

represented by off diagonal elements in $\mathbf{K}$. Since we know the resulting motion is going to be a cosine, we can rewrite $\mathbf{x}(t) = Re(\mathbf{a}e^{i\omega t})$, which when substituted into the above matrix equation gives:

$$-\omega^2\mathbf{M}\mathbf{a}e^{i\omega t} = -\mathbf{K}\mathbf{a}e^{i\omega t}$$

When rearranged, we find ourselves dealing with an eigenvalue problem of the form:

$$(\mathbf{K} - \omega^2\mathbf{M})\mathbf{a} = 0$$

apart from the trivial solution of $\mathbf{a} = 0$, which corresponds to no motion, the frequency of *any* linearly coupled oscillator system can be solved with

$$\det(\mathbf{K} - \omega^2\mathbf{M}) = 0$$

For example, a simple 2 oscillator system, where the two masses are equal and the individual spring constants are the same, but are coupled with coupling strength, j the $\mathbf{M}$ and $\mathbf{K}$ can be expressed as

$$\mathbf{M} = \begin{bmatrix} m & 0 \\ 0 & m \end{bmatrix} \quad \text{and} \quad \mathbf{K} = \begin{bmatrix} k & -j \\ -j & k \end{bmatrix}$$

resulting in

$$(\mathbf{K} - \omega^2\mathbf{M}) = \begin{bmatrix} k - m\omega^2 & -j \\ -j & k - m\omega^2 \end{bmatrix}.$$

The determinant of $(\mathbf{K} - \omega^2\mathbf{M})$ is $(k - m\omega^2)^2 - j^2$, so that the frequencies of the coupled system are

$$\omega_1 = \sqrt{\frac{k-j}{m}} \quad \text{and} \quad \omega_2 = \sqrt{\frac{k+j}{m}}$$

The takeaway from this mathematics should be that coupled oscillators exhibit collective oscillations that depend on the coupling strength j. The individual blocks no longer move with an individual frequency, but are parts of a collective. Furthermore, the matrix formulation of normal modes makes it so that large systems of oscillators can be similarly understood. In these larger systems, the collective motion of the blocks can result in slow temporal frequencies and consequently large spatial wavelengths. Describing the movement of an individual block necessitates an understanding of the whole system.

1.1.3 A Loss of Collective Behavior

Normal modes are an illustrative example in physics of collective behavior because of the simplicity of the mathematics. However, the underlying principle is that if the coupling strength between individual units can overcome the dissimilarities between individuals, collective units can be formed. These collective units can do more than dictate the movement of individual blocks. The collective motions can be carriers of information as well.

Consider the situation illustrated in figure 1.3. We know that this 4×4 nearest-neighbor-coupled mass-spring array will exhibit collective motions. If all of a sudden, the mass of one of the blocks changed, then the collective frequency would change as well. If we imagine the mass-spring array to be the surface of a drum, a change in the collective frequency might indicate an object falling on the batter head. Or if we imagine the masses to be protein units, we can imagine the changing of the mass to be a protein-protein

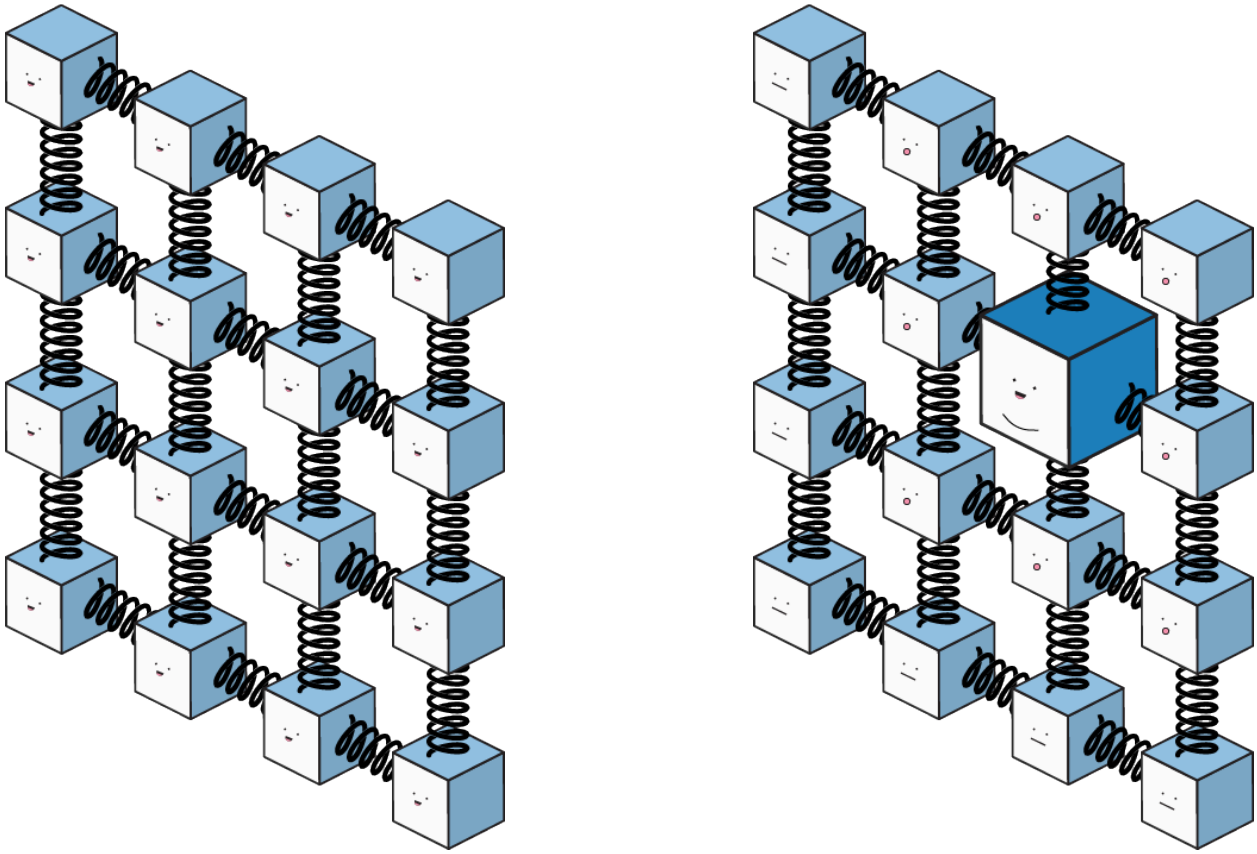

(A) A set of masses and springs will exhibit collective movement

(B) Change at an individual site is reflected in the collective frequency

FIGURE 1.3: A comparison of mass-spring arrays. A local change of mass is observed by the collective as a change of normal mode frequency. However, depending on the relative mass and coupling strength of the springs, the effect of change of mass at one site may closer sites differently than further ones

interaction occurring. From the point of view an individual block, a change of collective frequency can carry *information* about what is happening at other sites.

If all of the natural world is connected, then why is this description of reality not predominant? This is something Christiaan Huygens investigated as well with his pendulum clocks. He noticed that when the clocks were hanging on different walls, no synchronization was observed. When the clocks were across the room from one another, they still had some non-zero coupling. There were air currents generated by the movement of the weights, and the walls were still connected through the structure of the building, but no synchronization materialized. The reason why the far-away clocks do not synchronize may seem obvious - there are other competing effects. The minuscule amount of coupling force generated by transmitted air currents was drowned out by a draft in the house, and the tiny bit of vibration transmitted through the beams of the house were small in comparison to the tap dancing of their upstairs neighbor.

The distinction between forces bringing individuals together and forces that are disrupting collective motion is made by distinguishing the **system** and the **environment**. Generally, if the coupling strength between individual units in a system is greater than the coupling of the system to the environment, then collective behavior can be observed. Returning to figure 1.3, we see that not all blocks react similarly to the change of mass. Closer blocks might feel a larger change in motion, while further blocks can remain neutral. If we imagine an even larger, wall sized mass-spring array, we have a physical intuition that the entire wall would not oscillate with a collective frequency unless the springs were very tightly wound. Pushing on a wall of highly coupled springs would result in a large area of deformation. The same amount of force applied to a mass-spring wall tied together with string would have a much smaller deformation area.

Fourier transforms are useful in studying wave behavior because they decompose complicated wave-forms into linear combinations of simpler sine and cosine waves. The Fourier transform of an infinitely propagating sine wave is a delta function, since it is perfectly described using one frequency. However, as discussed, real-world wave-like properties do not propagate forever and therefore the Fourier transform have a distribution of frequencies. The larger the width of frequencies after a Fourier transform, the more localized wave is. Conversely, a narrow frequency distribution in the Fourier transform means the original function was wave-like for a long period of time, or over a large spatial area. Taken to the extreme, the Fourier transform of an infinitely localized delta function is 1. There is no frequency information contained in a 0D point. Figure 1.4 shows an image of a brick house and its Fourier transform. If the image was only of the bricks, we would find a very well defined spatial frequency in the Fourier transform. Instead, because the picture is of a brick building with finite boundaries to the brick, the 2D Fourier transform is quite complicated. Different portions of the Fourier transform are windowed and inverse Fourier transformed to look like the original image. The pink portion of the Fourier Transform contains no high frequency information, such that all the walls are all smooth, and even the complicated ripples in the curtain in the window are neatly periodic. The blue portion of the Fourier transform contains high frequency information such that slow changes like the hue of the sky are neglected. Instead, the high spatial frequency bricks are the main feature captured. Information about the spatial extent of the bricks end is captured in the shape of the peak in the Fourier domain.

The Fourier transform not only captures the amplitude of certain oscillation frequencies, but also captures the phase. **Coherence** describes a set of individual waves that evolve in time with a fixed phase relationship. Within the framework of coupled mass-springs,

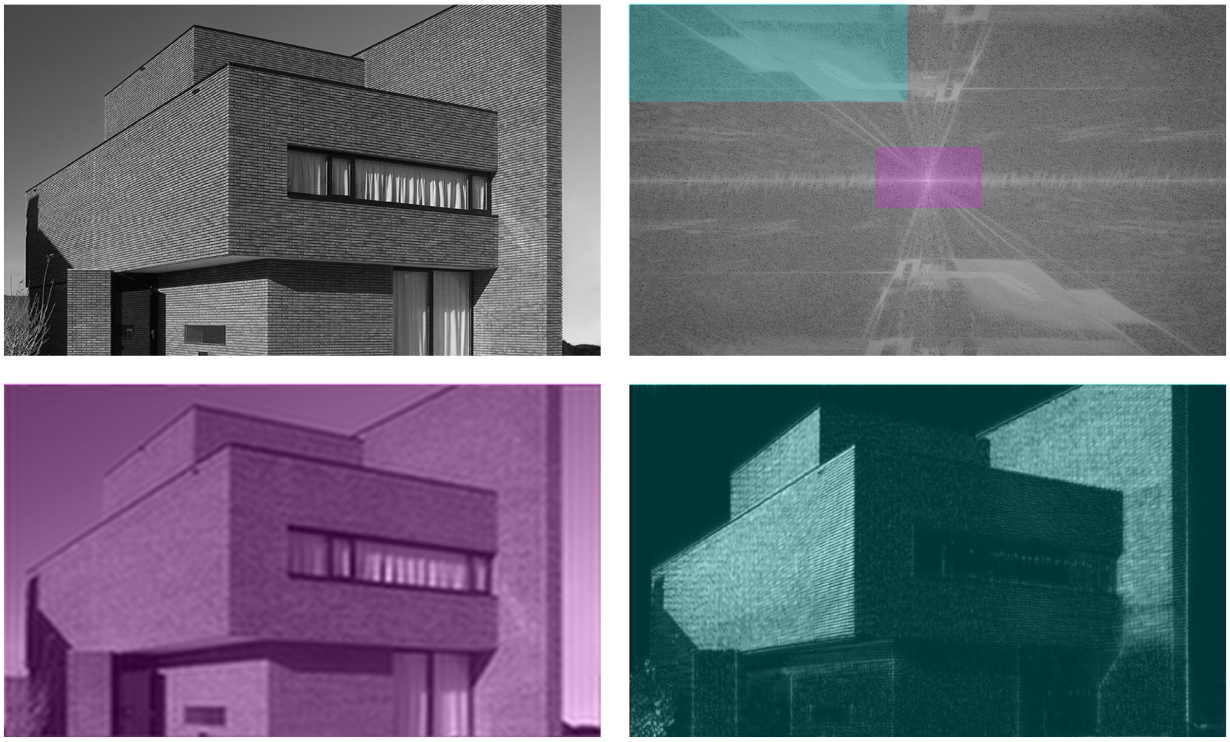

FIGURE 1.4: A brick house and its Fourier transform. The two images on the bottom are the inverse Fourier transforms of the colored regions in the Fourier Transform. The low frequency information is contained in the pink trace while higher frequencies are seen in the blue trace

coherence is manifest as individual block "sites" moving together with a collective frequency. Oscillators with different frequencies can also be coherent if over many cycles of oscillation, there is a periodic return to a certain configuration. **Decoherence** is the dynamic process in which coherence is lost due to interactions with the environment. If over many cycles, the relative positions of the oscillators is randomized, a loss of coherence has occurred. This thesis describes the study of coherence in quantum mechanical systems using Fourier transform spectroscopies. Up until this point, all descriptions of physical systems have been classical. However, we will see that many of the same physical intuition can be applied to the quantum world, and the central premise of our questioning is the same. For our quantum mechanical systems, how well does the wave-like description of reality work, and what are the implications of information and energy transfer across coherent delocalized states?

1.2 Quantum Clocks

1.2.1 Coupled Quantum Oscillators

Quantum coupled oscillators energetically behave quite similarly to their classical analogues. If we concern ourselves first with the time-independent Schrödinger equation first, and add how the system propagates with time later, the comparison is clearer. The time-independent Schrödinger equation is an eigenvalue equation, where the resulting wave functions are eigenfunctions of the Hamiltonian operator with corresponding eigenvalues E.

$$\hat{H}|\Psi\rangle = E|\Psi\rangle$$

The quantum Hamiltonian corresponds to the total energy of the system. One particularly useful model Hamiltonian we will examine more closely the Holstein Hamiltonian which describes coupled quantum harmonic potentials. In this case, each harmonic potential may represent a molecular electronic transition, along with vibrations of the molecule that accompany the change in electronic state. The total Hamiltonian H_{tot} is given as: [6]

$$H_{tot} = H_e + H_v + H_{ev}$$

$$H_e = \sum_{k,k'}^{N_e} e_{k,k'} B_k^\dagger B_{k'}$$

$$H_v = \sum_{k=1}^{N_e} \sum_{\alpha=1}^{N_v} \frac{\Omega_{k\alpha}}{2} (P_{k\alpha}^2 + X_{k\alpha}^2)$$

$$H_{ev} = \sum_{k=1}^{N_e} \sum_{\alpha=1}^{N_v} \Omega_{k\alpha} \kappa_{k\alpha} B_k^\dagger B_k X_{k\alpha}$$

This Hamiltonian describes the energies of coupled quantum oscillators. The total Hamiltonian is a sum of three different Hamiltonians, representing the electronic states, the vibrational states, and the coupling between electronic and vibrational degrees of freedom.

The electronic Hamiltonian, H_e, describes the energies of electrons at different sites. $B_k^\dagger$ and B_k are creation and annihilation operators that are mathematical tools to create create excitation at a specific site k. With them, we can define the energy of each individual site $e_{k=k'}$. For situations in which $k \neq k'$, $e_{k \neq k'}$ represents the amount of coupling between sites k and k' . The result of this Hamiltonian looks quite similar to the **K** matrix we defined for the mass-spring array, where the diagonal elements were related to the oscillation frequency of an individual unit, and the coupling strengths are off diagonal elements of the matrix. The vibrational Hamiltonian builds set of "ladder" states on top of each

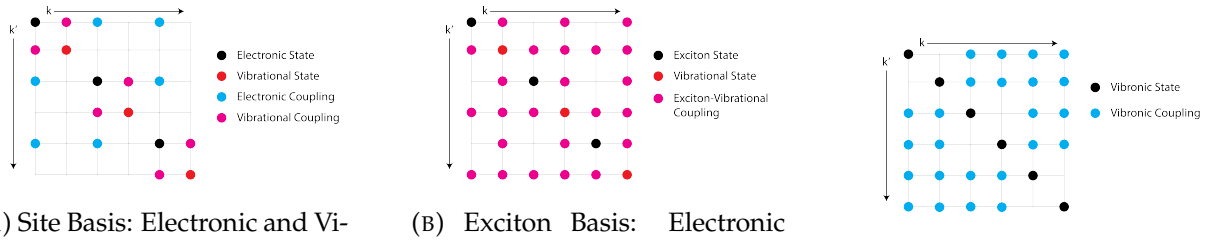

(A) Site Basis: Electronic and Vibrational energies are localized on individual sites

(B) Exciton Basis: Electronic states are delocalized across multiple chromophores

(C) Vibronic Basis: Electronic and Vibrational states are mixed

FIGURE 1.5: Schematic representation of total Hamiltonian H_{tot}, $\mathcal{H}_{ex}$, and $\mathcal{H}_{vib}$

electronic state with dimensionless position $X_{k\alpha}$, momentum $P_{k\alpha}$, and frequencies $\Omega_{k\alpha}$ of harmonic mode α. Finally, the vibrational states are coupled to the electronic states via H_{ev} and $\kappa_{k\alpha}$, which is simply controls the strength of interaction between mode α on site k. Diagonalizing the total Hamiltonian gives eigenvalue energies E. If there are no off-diagonal elements to the total Hamiltonian, the eigenvalues E are simply the energies of the uncoupled individual sites. However, with electronic coupling $e_{k\neq k}$, and electronic vibrational coupling H_{ev}, the resulting eigenstates are combinations of the energies of individual sites electronic and vibrational energies.

Instead of looking at the eigenvalues of the total Hamiltonian, other forms of the same Hamiltonian rotated into different basis may be more informative to understand how the collective states are built. A rotation matrix can be defined that only diagonalizes certain portions of the Hamiltonian. For example, if we wish to consider only the effects of electronic coupling, we can define a rotation matrix

$$e_{kk'} = \sum_{n=1}^{N_e} O_{nk} E_n O_{nk'}$$

which can be in turn applied to the total Hamiltonian to see its effect on all states

$$\mathcal{H}_{ex} = OH_{tot}O^{\dagger}$$

Shown in figure 1.5, the "site basis" is the original formulation of the Hamiltonian, with local site energies depicted in black, electronic coupling between sites depicted in blue, localized vibrations depicted in red, and the coupling of vibrations to pigment electronic states depicted in magenta. The rotation that removes the electronic coupling creates delocalized electronic states, called "excitons" that are linear combinations of individual site electronic states. The effect of creating delocalized electronic states can also have a cascading affect on the coupling of vibrational states. Originally, each set of vibrations were coupled to only one site. However, since the excitons are combinations of local site electronic states, the vibrations are now coupled to all the delocalized excitons (as long as that exciton is partially constituted from the site that the vibration is coupled to). A similar rotation matrix can also be created to "vibronic" states, or states created from a combination of electronic and vibrational degrees of freedom. While this rotation conceptually still has individual sites, the effect of creating vibronic states is that all vibronic rungs are coupled to each other since each vibronic state contains a bit of the electronic states that are Coulombicly coupled.

The net effect of electronic and vibrational coupling for the model quantum Hamiltonian that we have considered is that the final set of states are combinations of individual site electronic and vibrational degrees of freedom. Similar to the case of the mass-spring array, the energies of individual sites are depend intricately on the coupling strength between units. The final states of the coupled system may be shifted drastically from the original site electronic and vibrational energies, an effect I will later show experimentally in

Chapter 5. Furthermore, ability for excitation (whether it be electronic or vibrational) to be delocalized across multiple sites recontextualizes our earlier questions about the extent of wave-like behavior. To what extent do molecular systems, coupled electronically and vibrationally, act as a collective unit, and on what temporal and spatial scale does the wave-like behavior persist for?

1.3 Time Evolution of Energies

To understand how oscillators evolve in time, we have to introduce the *time-frequency domain*. Up until this point, the oscillators we have dealt with have had their frequency (related to the energy of the state) defined by the spring constants and masses for our classical system, and the Holstein Hamiltonian for our quantum system. To understand how these oscillators might interact, how they might dynamically generate collective systems, and how a collective might decohere into the constituent parts requires more than the static oscillator description we have developed so far.

The time-frequency domain is actually quite common; music is perceived this way. The audible spectrum for a healthy human ear ranges from 20 - 20,000 Hz (oscillations per second) for individual notes. However, we do not consider isolated notes, or even combination of notes music. Instead, their evolution in time over the course of seconds to minutes to hours is what is sometimes called the "universal language".

A canon is a form of music in which a theme is played against itself, where various voices can join in to harmonize with the the other participating voices. Each progression of notes acts both as melody and harmony, progressing in a repeating manner on the timescale of .1 -.01 Hz. As humans, our perception of this slow oscillation is much different than the

fast oscillations. The high frequency notes are directly perceived as sound. For the lower frequency oscillations that define the structure of the canon, our ear picks out melody and harmony dynamically from a the same line of notes to generate meaning through context.

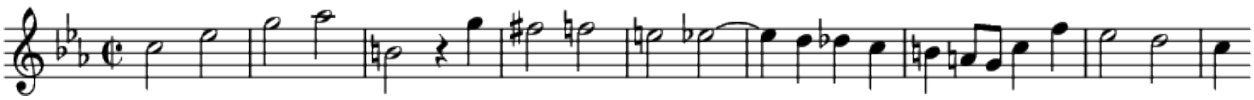

FIGURE 1.6: The Royal Theme from Musikalisches Opfer or Das Musikalische Opfer (The Musical Offering) BWV 1079 by J.S. Bach

Figure 1.6 is the Royal Theme from J.S. Bach's "Musical Offering" to Frederick the Great of Prussia. The musical score breaks the sound wave into discrete chunks of time, and plots each note's instantaneous frequency vertically as a function of time horizontally. This Royal Theme is manipulated in numerous ways by Bach. Not only does he delay the voices, but the different voices play the theme with different pitches (frequency). The voices can also sing the theme with different speeds, where the second voice might be twice as fast or slow as the first. The notes might be inverted, or the theme may be played backwards. All of these transformations are performed in the "Musical Offering" to dynamically bring notes in and out of resonance with each other within the structure of the canon.

Quantum Mechanics is not so different, except the relevant timescales are much faster. An electronic transition that sits in the visible region of the electromagnetic spectrum oscillates at 500-1000 THz (10^{12} times a second), while a vibration oscillates at 1-100 THz. The dynamic processes we are interested in, charge and energy transfer (Chapter 6), vibrations bringing electronic states into resonance (Chapter 2), decoherence of electronic (Chapters 4 and 7) and vibrational (Chapters 3 and 5) collectives similarly occur at the 10 fs (10^{-15} s) - 1 ns (10^{-9} s) timescale.

For our quantum mechanical system, it is advantageous to use a *density matrix*,

$$\rho(t) \equiv |\Psi(t)\rangle\langle\Psi(t)|,$$

in defining the time evolution of our system, since it represents the probability of finding a particle in a particular state. Since

$$\rho(t) = \sum_{n,m} c_n(t)c_m^*(t)|n\rangle\langle m|$$

$$\equiv \sum_{n=m} \rho_{nm}(t)|n\rangle\langle m|,$$

the density matrix elements are

$$\rho_{nm} \equiv c_n c_m^*.$$

When $n = m$, the density matrix element gives the probability of occupying a quantum state $\rho_{nn} = c_n c_n^* = p_n \geq 0$. Thus, the diagonal elements of the density matrix are referred to as **populations**.

We can introduce the concept of *time evolution* of our density matrix by expanding our definition of ρ and substituting the Schrödinger equation $\frac{d}{dt}|\Psi\rangle = -\frac{i}{\hbar}H|\Psi\rangle$.

$$\frac{d}{dt}\rho = \frac{d}{dt}(|\Psi\rangle\langle\Psi|) = \left(\frac{d}{dt}|\Psi\rangle\right)\cdot\langle\Psi| + |\Psi\rangle\cdot\left(\frac{d}{dt}\langle\Psi|\right)$$

$$\frac{d}{dt}\rho = -\frac{i}{\hbar}H|\Psi\rangle\langle\Psi| + \frac{i}{\hbar}|\Psi\rangle\langle\Psi|H$$

$$\frac{d}{dt}\rho = -\frac{i}{\hbar}H\rho + \frac{i}{\hbar}\rho H = -\frac{i}{\hbar}[H,\rho]$$

The last equation is called the *Liouville-Von Neumann Equation*, which describes the time evolution of the density matrix. For an example 2-level eigenstate basis of H:

$$\frac{d}{dt}\begin{pmatrix}\rho_{11} & \rho_{12}\\ \rho_{21} & \rho_{22}\end{pmatrix} = -\frac{i}{\hbar}\left[\begin{pmatrix}\epsilon_1 & 0\\ 0 & \epsilon_2\end{pmatrix}\begin{pmatrix}\rho_{11} & \rho_{12}\\ \rho_{21} & \rho_{22}\end{pmatrix} - \begin{pmatrix}\rho_{11} & \rho_{12}\\ \rho_{21} & \rho_{22}\end{pmatrix}\begin{pmatrix}\epsilon_1 & 0\\ 0 & \epsilon_2\end{pmatrix}\right]$$

$$= -\frac{i}{\hbar}\begin{pmatrix}0 & (\epsilon_1-\epsilon_2)\rho_{12}\\ (\epsilon_2-\epsilon_1)\rho_{21} & 0\end{pmatrix},$$

we find that

$$\dot{\rho}_{12} = \frac{i}{\hbar}(\epsilon_1 - \epsilon 2)\rho_{12} \longrightarrow \rho_{12}(t) = e^{-i\frac{(\epsilon_1-\epsilon_2)}{\hbar}t}\rho_{12}(0)$$

$$\dot{\rho}_{21} = \frac{i}{\hbar}(\epsilon_2 - \epsilon 1)\rho_{21} \longrightarrow \rho_{21}(t) = e^{+i\frac{(\epsilon_1-\epsilon_2)}{\hbar}t}\rho_{21}(0)$$

The off-diagonal elements of our density matrix oscillate in time, with a frequency defined by the energy difference between eigenstates. These off-diagonal elements of the denisty matrix are called **coherences** and represent the oscillatory behavior of quantum coherent superpositions in the system. The timescale that the coherence decays is the *dephasing* rate, and it represents the timescale that the system loses its ability to collectively oscillate, whether that be through different members of the ensemble experiencing different energetic fluctuations or coherence is lost due to intrinsic quantum interactions with the environment. Appendix C introduces a formalism known as "Coherent Modified Redfield Theory" that mathematically describes how interactions with the environment affect coherence dephasing rates.

Through the study of coherences and the timescales they decay on, we can learn about the processes that cause individual quantum states to lose synchronization. We shall see in the next section

that through the use of ultra-short laser pulses, we can establish initial states, and watch as those states evolve with time. We will be able to track the frequency of the oscillation, as well as their loss of coherence over time. Like a horse race, all of the different eigenstates of our system are neatly arranged in a starting gate by our laser pulses. When the states are allowed to evolve, some states naturally evolve with faster or slower coherence times, but we may sometimes find that the coherence *between* states is different than we would expect if the states of our system are completely uncorrelated. Thus, the coherence lifetime gives us information both about our *system* and the *environment*. Much like our classical example of Huygens coupled clocks, if correlations within the system can overcome disorder introduced by the environment, extended periods of coherence will be observed.

1.4 Time Domain Spectroscopy

Another oscillatory system most of us are familiar with is a swing. When the swing has no motion, we have the trivial result of 0 Hz frequency and over the course of time, our swing is perfectly localized. A reasonable child would like to be pushed periodically with a driving force, and a reasonable parent would realize that pushing the swing periodically in resonance with the oscillation frequency of the swing results in the optimal swing experience. We might say that the periodic pushes of the parent are *in phase* with the oscillation of the swing. If there is substantial *phase noise*, the timing of each push is random and the result is a strange trajectory of the oscillator.

Probing molecular quantum states with pulses of light is similar. Light radiated by a light bulb or the sun has randomized phase, while pulses from lasers have a well-defined *spectral* phase. We can use these laser pulses to manipulate our system and learn about

the internal workings of molecules. We use lasers to transition between different states, allow the system to evolve naturally without perturbation, and probe the evolution of the system.

Light-matter interactions can be understood mathematically by expanding the induced polarization P of our system. The polarization can be thought of as how much a system gets moved from equilibrium by a driving force. At low intensity or field strengths, the induced polarization is *linearly* related to how strong the electric field (from our input light) is:

$$P = \epsilon_0 \chi^{(1)} \mathcal{E}$$

where ϵ_0 is the electric permittivity of free space, $\mathcal{E} \propto E_0 cos(\omega t - kz)$ is the real electric field, and $\chi^{(1)}$ is called the linear susceptibility. The resulting polarization will have the same oscillatory frequency as the input light, and will oscillate in time phase shifted by π. The final total electric field will be a combination of the input field and the resulting field generated by the oscillating polarization, also called the *signal*. If the input field and the signal field destructively interfere due to out-of-phase oscillations, the resulting total field will have a reduced intensity. This is the *time domain* description of light absorption by a molecule. Typically, absorption is thought of in the frequency domain, where a molecule will only absorb light if the energy of the input light matches the energy difference between energetic states (along with other selection rules). However, this is where our classical conception of a swing may help us. When driven from equilibrium, the molecule's induced polarization will evolve in time with a particular trajectory related to the energies of its states. That oscillation's interference with the input light can cause certain frequencies of light to be diminished. The total field resulting from the light-matter interaction can then be Fourier transformed back into energy, informing us about what

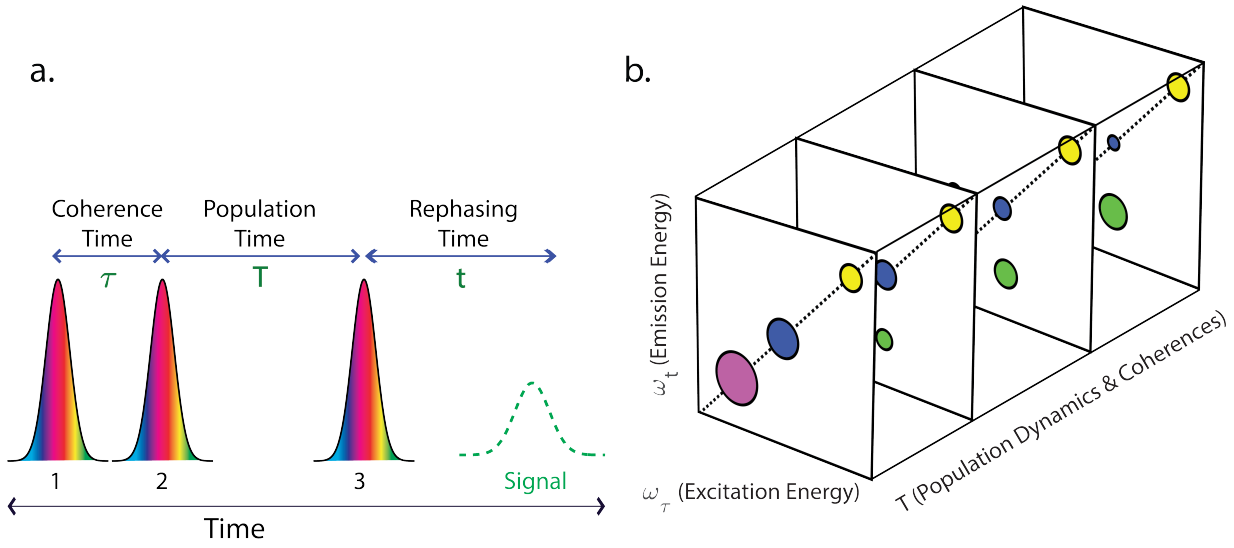

FIGURE 1.7: Multidimensional Coherent Spectroscopy. (a) A series of pulses interact with a quantum system as a function of delay between pulses (b) The oscillations observed in time as a function of pulse delay can be Fourier transformed to reveal the energies of the coherences observed. For 2D electronic spectroscopy, two dimension correspond to energy of the state being excited (ω_τ) and emitted (ω_t), and the third dimension (T) corresponds to population dynamics and low frequency coherences.

energies are "absorbed" by the molecule.

Higher order corrections to the induced polarization correspond to how a quantum system might react *nonlinearly* and falls in the domain of *non-linear optics*.[7, 8] One particular technique that will appear numerous times in this thesis is known as *multidimensional coherent spectroscopy* to reliabily interact with the higher order terms of the polarizability, $\chi^{(N)}$. This technique uses a series of pulses to periodically transition the quantum system of interest between different states, and observes the coherences created by each pulse as a function of delay between the pulses. Figure 1.7 shows a version of multidimensional coherent spectroscopy known as 2D electronic spectroscopy (2DES). In this technique, a series of three pulses are used. The reason why it is called a *2D electronic* spectroscopy is

because two of the dimensions typically correspond to high frequency oscillations of electronic coherences, or coherences between the ground and an excited state. The first time delay, τ encodes information about the coherence after excitation, while the final time delay, t encodes information about the final states. The time delay between the 2nd and 3rd pulse is called the *population* or *coherence* time, T, because slower processes typically occur during this time period. The second pulse generates either excited state populations or coherences with a small energy difference, so that the coherences oscillate with a relatively slow frequency. The different time dimensions can be Fourier transformed to reveal the energies of the coherences. The first time delay τ becomes ω_τ, and reveals the energies of the electronic states that were excited by the first pulse. The second time delay T becomes ω_T and reveals closely spaced eigenstates of the excited and ground state, and the third time delay t becomes ω_t and represents the energies of the electronic transitions spanned by the third pulse. This type of experiment is considered a *time domain spectroscopy* since information about the molecules is collected in the time domain and *Fourier transformed* into energies. These are also sometimes called *Fourier transform spectroscopies*.

1.5 Quantum Coherence

Multi-dimensional spectroscopies are typically understood in a *semi-classical* framework, meaning the molecular or material systems they interact with are treated quantum mechanically, but the light used in the experiments is treated classically. Chapter 7 will deal with a type of time-domain spectroscopy in which the light will need to be treated quantum mechanically since we will only be observing one photon at a time.

The strangeness of "photon counting" can be pondered by considering what happens to light when entering an interferometer. Interferometers used widely in all time-domain

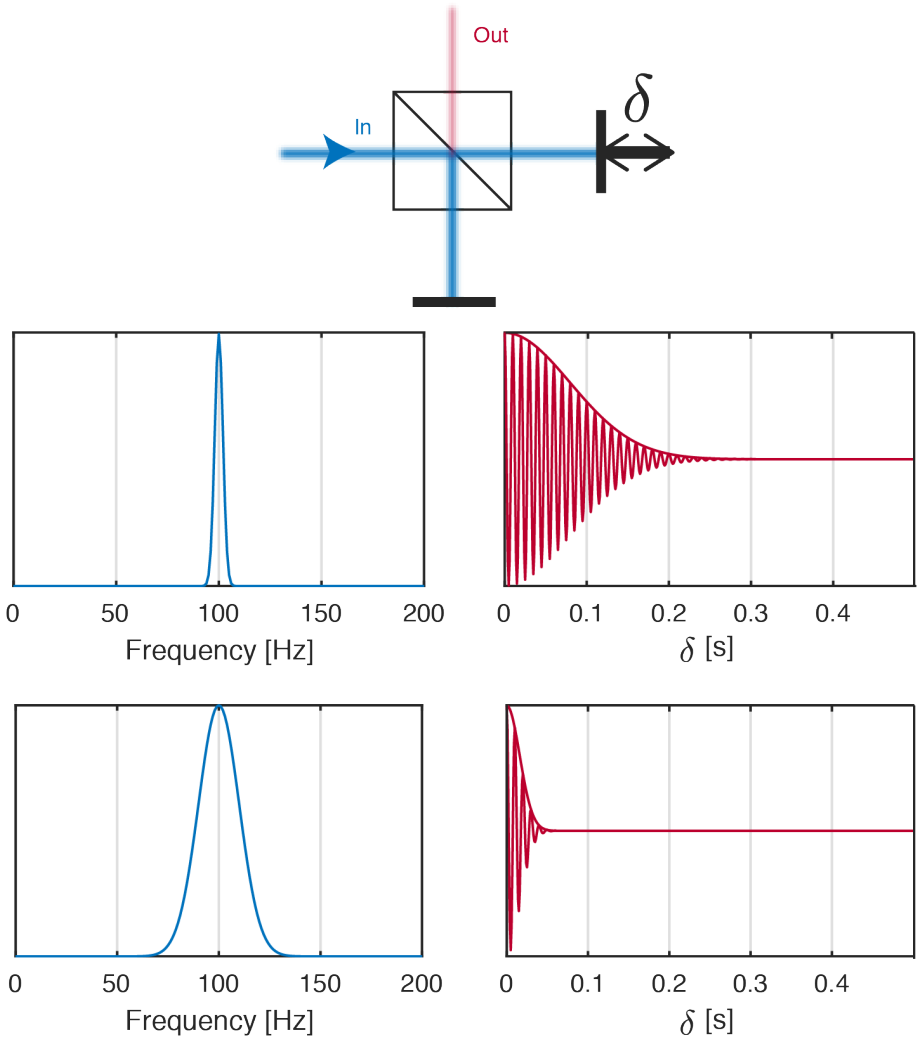

FIGURE 1.8: Fourier transforms as performed by an interferometer. Interferometers act as Fourier transforms for input waves as a function of path length difference between interferometer arms, δ

spectroscopies since it is one way to convert frequencies into time. Figure 1.8 shows a Michaelson interferometer and the resulting interferogram measured at the output as a function of pathlength difference, δ, between the two arms. When a wave enters an interferometer, it encounters a beam splitter, which creates two possible paths in which the light can proceed. The two paths are then recombined at the same beam splitter. If the two path lengths are equal, constructive interference occurs and the output is maximized. However, if the path length difference between the two arms creates a π phase difference between the two waves, destructive interference occurs and the output intensity is minimized. In this way, the output of an interfermeter as a function of path length difference δ is a Fourier transform of the input wave. We learned earlier that only a Fourier transform of a delta function will oscillate as $\delta \to \infty$. Thus, for any energy state with finite distribution of energies (or spectrum), the Fourier transform's decay is indicative of the time (and consequently length) scale the input wave is *coherent* with itself.

So what happens when only a single photon enters an interferometer? A single photon cannot go down both paths at the same time, but it can still display interference.[9] The mere possibility of the alternative pathway is enough to cause interference. This feature of quantum systems can be exploited to extract information about a system without directly interacting with it in so-called *interaction-free measurements*. Figure 1.9 depicts how this might occur in an experiment known as the Elitzur–Vaidman Dud Bomb Problem.[10] Figure 1.9(a) is a Mach-Zehnder interferometer, which is almost identical to the Michaelson interferometer except that instead of using the same beam splitter to create the two possible paths and recombine the two possible paths, two beam splitters are used so that there are now two output paths, **A** and **B**. Many of the properties of the Mach-Zehnder interferometer are the same as the Michaelson. When $\delta = 0$, the two paths constructively

interfere, so that all the input light is output on one of the beam splitters. In the configuration drawn in Figure 1.9(a), the output light always goes to detector **A** when $\delta = 0$. Let's put a measuring device on one of the arms of the interferometer to determine which path the photon goes down. For dramatic effect, let's say that on the lower arm, a light sensitive bomb is placed. If a photon goes down the lower arm of the interferometer, the entire apparatus is destroyed. However, if the photon proceeds down the upper arm of the interferometer, the photon apparatus survives, but the interference does not. This is because *any* measurement giving information about which path the photon proceeds along destroys the interference at the second beam splitter. Imagine that we had a random assortment of bombs and dud bombs, bombs that explode and bombs that do not explode after hit with light, and light can reflect off them just like a normal mirror. We can use this apparatus to test whether or not the bombs are real or not by measuring the interference at the output. If we have interference, we know that we have a dud bomb. If the bomb is real, then half the time the apparatus is destroyed (since half the time, the photon takes the lower interferometer path). However, even when the photon takes the upper route of the interferometer, we still know that the bomb is real because the interference is destroyed. Thus, we have obtained information about the realness of the bomb, without having to probe it directly. Instead, we used the quantum possibility of a photon going down the measurement path to obtain information. What we undertake in Chapter 7 is the detection of interference of single photons to understand how material properties affect the quality of interference and the extent to which interference persists (coherence).

The Elitzur–Vaidman Dud Bomb Problem highlights why quantum interference and the measurement of coherence is so broadly applicable. The ability for quantum states to maintain superpositions and spatially extended collective states opens the door for new

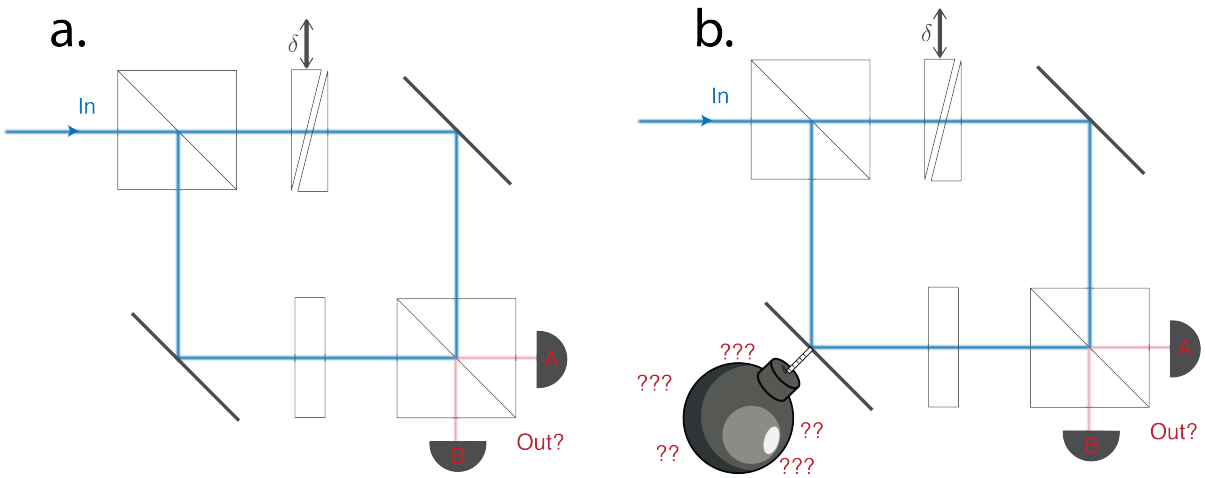

FIGURE 1.9: Elitzur–Vaidman Dud Bomb Problem. (a) Due to interference, a single photon entering the Mach-Zehnder interferometer will deterministically go to detector A when $\delta = 0$. (b) If an object has the possibility of destroying (any sort of measurement) a photon arriving at the lower arm of the interferometer, the interference at the output beam splitter will be destroyed even if the photon doesn't go down the path with the measurement.

modalities of *information transfer*. In this thesis, I will describe numerous experiments I have performed to understand how far this quantum information can be shared, in both space and in time. Whether or not this modality of information transfer is utilized meaningfully in biological systems is an open question, but the *extent* to which quantum information *can* be shared via electronic and vibrational degrees of freedom is examined.

1.6 Why Coherences?

What makes the most cosmological events more meaningful than simple daily coincidences? Why is it more meaningful that the conditions for an eclipse (that the ratio between the apparent diameters of moon and the sun is the same as the ratio between the distances between the earth and the moon and the earth and the sun) exist for only the

period of time humans are alive to observe it more meaningful than an ant dying on a day it rains? Taken to the cosmological and relativistic extreme, no coincident events exist in absolute terms, only in a particular reference frame. If that is the case, what defines the inherent meaning behind individual unit maintaining coherence for a certain period of time to form a collective unit?

Any road trip leaving Chicago's suburb of Evanston, where Northwestern University is located, is bound to pass through many corn fields. When looking into the fields, it may appear that the corn is randomly distributed. However, if you turn your head to the exact angle aligned with the rows of corn, you will see that there is an implicit order governing the field. In Physics, we often attribute beauty and truth in terms of economy and symmetry. We look for broad explanatory power with few initial assumptions. Coherence is a bottom-up way to understand the complexity of our world, as opposed to a top-down organizational framework. I do not claim to have found truth or beauty in the observation of coherences and their lifetimes, but I do hope that this thesis helps you turn your head, just a little bit.

Coherences of Conjugated Polymers

Adapted from: **Irgen-Gioro, S.**; Roy, P.; Padgaonkar, S.; Harel, E. Low Energy Excited State Vibrations Revealed in Conjugated Co-Polymer PCDTBT through Variable Bandwidth Noise Minimization *J. Chem. Phys.*, **2020** 152 (4) 044201

2.1 Collective Low Frequency Vibrations From Conjugated Polymers

Low energy vibrations in the excited state have been hypothesized to play an important role in quickly and efficiently generating free charges in bulk heterojunctions of some conjugated polymer systems. While time-resolved vibrational spectroscopies seemingly are well poised to address the relationship between kinetics and vibrational motions after initial photoexcitation, uncertainty in the measurement arises due to overlapping signals and difficulties in assigning observed oscillatory signals to the molecular response. Here, we demonstrate a high sensitivity strategy to distinguish between signal oscillations originating from lab noise and those molecular in origin in order to isolate the low energy excited-state vibrations in the model conjugated copolymer PCDTBT. Furthermore, to distinguish modes that may be implicated in different kinetic pathways, coherent signal

oscillations extracted from 2-dimensional electronic spectroscopy (2DES) are compared for the polymer in two solvents with different polarities resulting in different kinetics. We observe that the change in solvent affects dynamics on the >2 ps scale but not on the time scale required for free charge generation in heterojunctions ($\sim$200 fs time scale). By the same token, the excited state vibrational modes that appear and disappear based on solvent polarity may also be associated with the slower kinetic process. The observation of low energy vibrational motions coupled to the excited state manifold that persists through the solvent change and thus can be associated with the fast kinetic process supports the hypothesis that direct polaron formation, rather than exciton formation and diffusion followed by interfacial charge separation, is a more likely route toward free charges in organic heterostructures.

2.2 Background

Owing to their high internal efficiency, strong visible absorption, and economic viability, conjugated donor-acceptor copolymers are being considered as possible low-cost alternatives to silicon photovoltaic devices acting as light absorbers and electron donors.[11] When blended with electron acceptors such as fullerene into an organic bulk heterojunction, mobile free charges appear faster than is predicted by traditional models in which excitons diffuse to the interface and form interfacial charge separated states.[12–14] While this speed helps explain the efficiency and, in turn, the performance of these materials in a photovoltaic context, the mechanism utilized in route to generating free charges is under debate.[15, 16] The disparity in the time scales initially prompted researchers to suggest that the transport is at least partially coherent, which could increase exciton

diffusion lengths and the transport rate. In highly structured and perfectly ordered π-conjugated chains, strong intrachain electronic coupling leads to extended delocalization where transport occurs stochastically by means of population relaxation.[17] However, many polymers demonstrating fast long-range transport are amorphous and have a significant degree of disorder. While disorder may limit the extent of delocalization, this is only the case for isolated electron-hole pairs or excitons. Polarons, quasiparticles that result from coupling of the charges with the geometric motion of the polymer chain, may help facilitate free charge generation by utilizing this disorder to their advantage.[16, 18–21] These amorphous polymer systems exist in an intermediate coupling regime in which the geometric relaxation energies are on the same order of magnitude as the electronic coupling.[15] This leads to an interplay of delocalization and localization where collective jumps in excitation that are delocalized over many chromophores reduce the number of diffusive steps required, sometimes referred to as "supertransfer." [22]

Coupling of electronic motion to vibrational modes is intrinsic to conjugated polymers since the lowest energy transition involves the same π orbitals that delocalize electron density along the polymer chain. Any modification to these bonds (C–C stretching or ring breathing modes) will modify the π-π* electronic transitions. These vibrational energies are typically in the thousands of wavenumbers regime and are relevant to intrasegment dynamics.[23] Electron-phonon coupling in this higher energy regime is typically more experimentally accessible using methods such as Femtosecond Stimulated Raman Spectroscopy (FSRS) and Infrared-Active Vibrational (IRAV) spectroscopy, and previous studies have successfully correlated structural changes to polaron formation.[24–27] In the case of amorphous polymers, charge carriers need to jump between chain segments. This intersegment interaction has weaker wavefunction overlap, leading to coupling strengths

in the 50–500 cm^{-1} regime, where a different set of vibrational modes are relevant.[15] Recent work has proposed that polarons and excitons are vibronically coupled, resulting in the direct generation of polarons rather than mobile charges that follow from the dissociation of excitons.[28] Other studies have proposed that vibrations that are strongly coupled to excitons create a high density of states that entropically favor electron and hole hopping between subunits rather than electron-hole attraction.[29–33] This high density of states is also thought to explain the weak correlation between energy-level alignment of exciton states and power conversion efficiency of organic photovoltaic devices.[15, 34] Natural multichromophoric photosynthetic complexes have demonstrated similar strategies to increase transport lengths in the presence of structural disorder that may be applied to electronic-vibrational coupling in conjugated polymers. In particular, studies show that a high density of vibronic states along with vibrations equal to the energy gap between electronic states result in a resonant condition conducive to fast transfer.[35, 36]

While it is clear that the characterization of transient low energy vibrations on the electronic excited state is important, access to this energy regime is difficult experimentally. Raman based techniques have an inherent trade-off between time resolution and the ability to observe low frequency modes, and direct detection of IR-active modes requires generation of far-IR light, which is extremely challenging below $\sim$500 cm^{-1}. Instead of using narrow-band pulses to generate population in the excited state, techniques such as impulsive vibrational spectroscopy or 2-dimensional spectroscopy (2DES) use compressed broadband light to simultaneously track populations and coherences, which report on both the kinetics and vibrations in the time domain. However, since vibrations are detected as fluctuations of the signal in time, periodic lab noise can be mapped onto the

signal and may cast doubt onto whether the detected oscillations are physically meaningful. Furthermore, even when a signal is confirmed to arise from a molecular vibration, assignment of how that vibration couples to any particular electronic state is ambiguous. Here, we develop a method which we call Variable Bandwidth Noise Minimization (VBNM) to separate out signals from the system of interest from parasitic signals that arise from laboratory noise lab frame. To further isolate the mechanism of carrier generation, kinetic pathways are distinguished through the variation of solvent polarity, which in turn allows for assignment of vibrations to a particular dynamic process.[37] For solvents without a strong hydrogen bonding network, the change of dielectric constants can be understood within the framework of the Stark effect, meaning that changes in transition energies are related to the difference of a particular state's permanent dipole moment and polarizability in the two solvents.[38, 39] Leveraging the fact that copolymer's charge transfer states have separated charges leading to large electric dipole moments ($\mu = qd$) amenable to change, vibrations associated and not associated with that kinetic pathway can be separated out by comparing the coherences observed in different solvents.

Our study focuses on one of the well-celebrated conjugated "push-pull" polymers, which alternates between electron rich and deficient units, PCDTBT within the poly-(2,7-carbazole) family synthesized by Leclerc et al. as shown in Fig. 2.1(a).[40] Exhibiting high stability in air, photovoltaic cells fabricated with a PCDTBT blend active layer may achieve photoconversion efficiencies beyond 6%, and internal quantum efficiencies near 10% have been reported.[13, 41, 42] Both the absorption and fluorescence of PCDTBT in chlorobenzene and toluene are shown in Fig. 2.1(a). The lowest energy absorption peak has been assigned to a localized charge transfer transition, in which the electron density is concentrated at several electron-accepting units, which are themselves distributed over

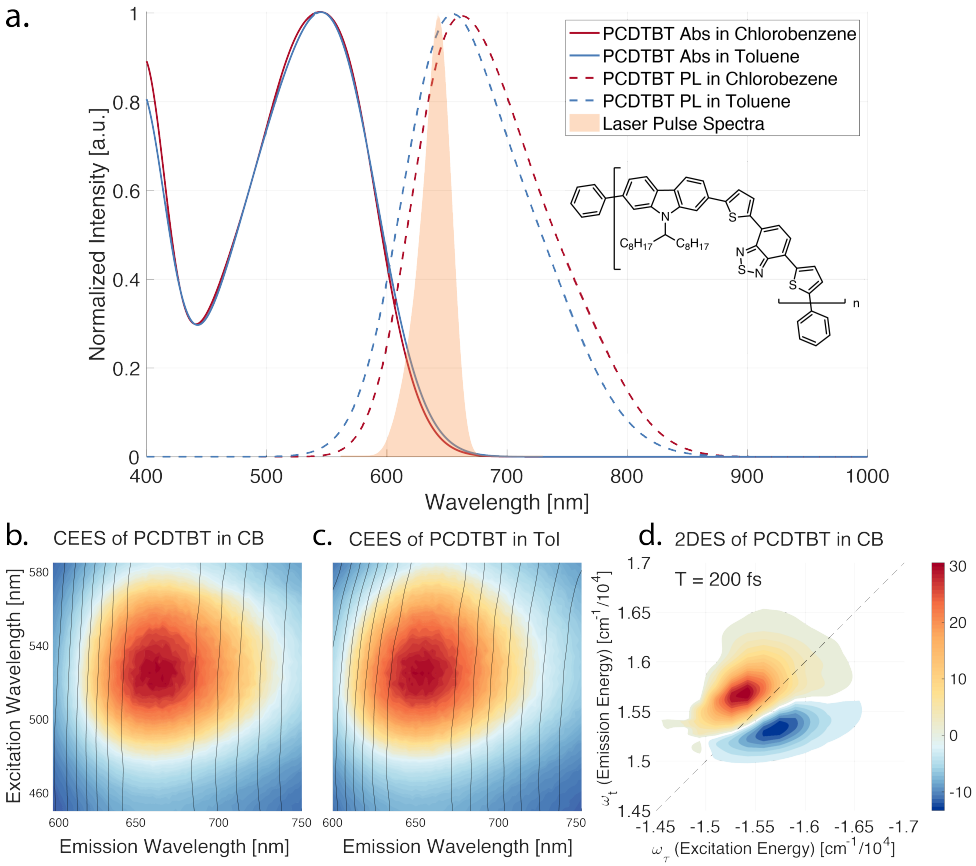

FIGURE 2.1: (a) Absorption and photoluminescence (excited at absorption maximum) of PCDTBT in both chlorobenzene and toluene. Combined Excitation Emission Spectra (CEES) of PCDTBT in chlorobenzene (b) and toluene (c). Contour lines drawn from emission spectra normalized at each emission peak. This helps show that in chlorobenzene (CB), PCDTBT's emission spectra's peak position is independent of excitation energy, while in toluene (TL), excitation of the inhomogeneous broadened absorption spectra yields emission from distinct subpopulations. (d) Slice of 2DES spectra at a fixed T = 200 fs along dimensions popularly interpreted as excitation and emission dimensions. Positive features represent either ground state bleach or stimulated emission features while negative features represent excited state absorption (ESA). Our spectra are in good agreement with previous work by the Scholes group who detailed the dynamics in Ref. [19] and assigned the ESA to the polaron state formed in ∼200 fs. Our study instead focuses on coherences observed as oscillations of the signal as a function of T.

the chain.[43] The transition is inhomogeneous broadened, arising from the different torsion, coiling, and folding configurations of the backbone. Previous work has documented excited state dynamics following excitation of this transition tracked through ENDOR, 2DES, fluorescence upconversion, and Transient Absorption (TA) spectroscopies, but distinguishing between different kinetic processes after photoexcitation has been challenging.[12, 16, 44, 45] Provencher et al. doped a PCDTBT film and found that the polarons exhibit a broad absorption stretching from ∼1.2 to 2.0 eV (620–1030 nm) peaking at 1.7 eV (∼730 nm) assigned to be from interband transitions.[26] However, since other excited species also have absorption in the same region, other handles such as kinetic rates or vibrational peak amplitudes have been used to track polaron population.[12] While the exact dynamics after photoexcitation is unknown, the fact that free charges are generated within ∼200 fs in the polymer heterostructures has led some to suggest that local structural lattice distortions of the copolymer directly self-localize charges as polarons without needing to diffuse to the interface's charge transfer state.[12, 16, 43] 2DES performed on this system by the Scholes group tracked peak energies of ground state bleach (GSB) and excited state absorption (ESA) features to observe internal relaxation on a ∼200 fs time scale that they assigned geometric changes but did not directly observe any excited state vibrations in the form of coherences.[19]

2.3 Results

PCDTBT is studied in two aromatic solvents, toluene and chlorobenzene, to examine the effect of solvent polarity on the generation of polarons and charge transfer states. A combined excitation and emission (CEES) plot is displayed in Fig. 2.1(b), which shows the fluorescence spectra of PCDTBT in chlorobenzene as a function of excitation wavelength.

The emission spectra are consistent, independent of the excitation wavelength. However, when the same measurement is performed for PCDTBT in toluene [Fig. 2.1(c)], the fluorescence peak shifts as a function of the excitation energy. Since the absorption is primarily inhomogeneously broadened, changing excitation wavelengths photoselects for differently twisted subpopulations resulting in a shifting fluorescence peak. In chlorobenzene, this effect is not seen due to the fact that all the excited species relax to a common untwisted planar configuration, a key result from the Scholes group report.[19] Another key result from the previous 2DES study was that an excited state absorption (ESA) was observed to appear within ∼200 fs. A slice of the 2DES measured in our experiment at a fixed population time of 200 fs is shown in Fig. 2.1(d) and shows a negative ESA feature to the Stokes side of the diagonal, the same energy as the polaron absorption and in agreement with the previous 2DES study.[26] The same time slice in both solvent does not show differences in peak energies, suggesting that the ESA feature is insensitive to solvent change at early times.

Transient absorption (TA) spectroscopy is performed to examine the changes to the kinetic pathways of the polymer in the two solvent environments. Using a narrow-band pump wavelength of 500 nm, a broadband probe is used to examine the energy region where the absorption, fluorescence, and polaron state transitions exist. The TA spectra for the polymer in chlorobenzene are shown in Fig. 2.2(a) and show that immediately after excitation, two peaks around 550 nm and 670 nm appear. These can be assigned to be the ground state bleach (GSB) and stimulated emission (SE), respectively, from the steady state absorption and fluorescence spectra. The stimulated emission peak grows in and shifts toward lower energies as probe delay increases. In order to better characterize the transfer processes and the state energies involved, global analysis was performed. Figure

2.2(b) displays the result of this fitting, which deconstructs the original dataset into a set of spectra each containing only either a positive or a negative amplitude exponential with the same time constant that can be summed to reconstruct the original data. Each of these Decay Associated Spectra (DAS) readily shows the probe energy at which the signal either rises or decays at the same rate, with a positive amplitude corresponding to a decay of signal while a negative amplitude exponential represents a growth of signal. While only two components are displayed for the scans in both solvents, the full set of dynamic components can be found in Appendix A along with the reconstructed dataset to be compared with the original data. Comparing the fastest two dynamic components of the DAS of PCDTBT in the two solvents show that the component with a time constant of $\sim$200 fs is similar for both scans. However, a comparison of the $\sim$2 ps components shows that the growth of signal is centered at a lower energy for chlorobenzene. This may be more readily seen in the inset to the right of the 2D DAS plots, which show that the zero-crossing point for the DAS is the same for the $\sim$200 fs component but shifts to the red for the $\sim$2 ps component. Since chlorobenzene is the more polar solvent, the intramolecular charge transfer state should be more stabilized in this environment. We thus assign the slower 2 ps component to the exciton mediated intramolecular charge transfer process, but no processes faster, namely, the polaron formation, were affected by the solvent change.

As opposed to the narrow-band pump in TA, 2DES's use of a broadband pump is capable of creating vibrational coherences and thus detecting excited state vibrations as oscillations of the signal as a function of population time. In this methodology, broadband compressed laser pulses initiate vibrations on the ground and excited states that are observed as oscillations as a function of delay between laser pulses and Fourier transformed into the frequency domain. However, time-domain measurements are susceptible to different

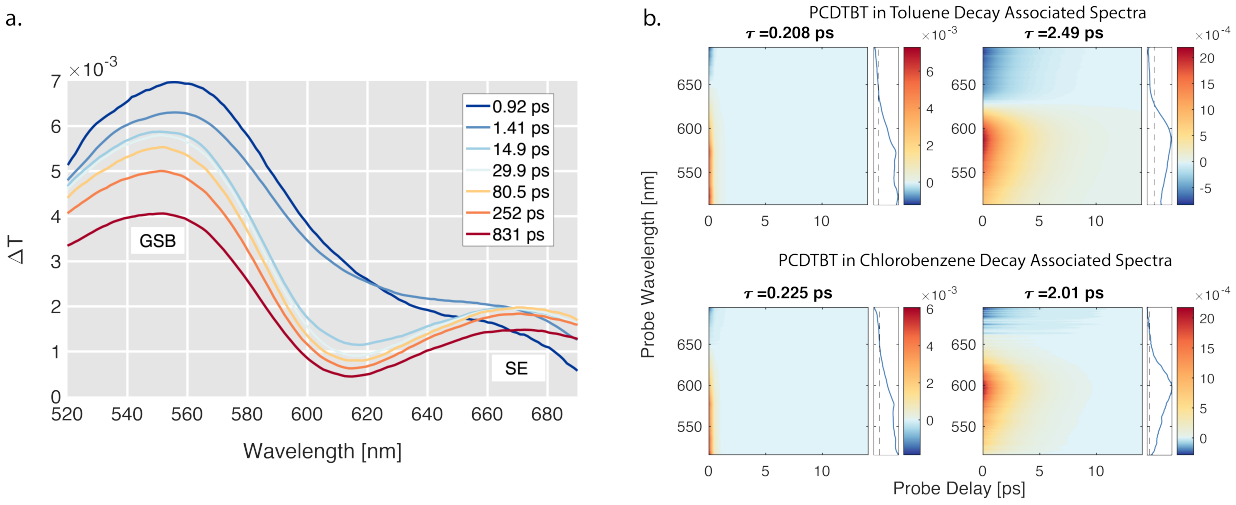

FIGURE 2.2: Transient absorption of PCDTBT shown as a function of probe wavelength and probe delay. (a) Immediately after excitation, two peaks, assigned to be ground state bleach and stimulated emission, are observed. (b) Global analysis is used to recover the decay associated spectra (DAS). Only the two fastest components are shown here, but they can be used to illustrate the fact that the fastest ∼200 fs component is agnostic to the choice of solvent. However, the change in solvent polarity changes the energy in which the signal rises on a ∼2 ps time scale. This is more clearly seen in the inserts to the right of the DAS, where the zero crossing point for the ∼200 fs component does not change between solvents, but the zero crossing in the ∼2 ps component shifts to the red in chlorobenzene. This establishes that processes happening faster than 2 ps are insensitive to solvent change.

sources of noise than frequency-domain techniques, which in turn casts doubt on the reliability of low energy peaks. Previous work in our group has demonstrated how to reduce phase and amplitude pink ($1/f$) noise through a combination of techniques to increase acquisition speed and stability, but narrow-band noise (ex. 60 Hz electrical noise, periodic flow of sample, mechanical vibrations, etc.) persists.[46, 47] While pink noise may hinder observation of coherences, narrow-band noise is potentially more troublesome as it casts doubt on whether observed peaks are real. This ambiguity has hampered the broad application of time domain vibrational spectroscopy in the case of weak signals at low-frequency. Here, we introduce a procedure to vary the bandwidth of measurement to isolate the molecular response.

The difference between oscillations arising from molecular vs instrument response hinges on the fact that the molecular response depends on the time delay between laser pulses and instrument response depends on events happening in lab time. Therefore, if the time step between laser pulses is varied, the molecular vibrational frequencies should not change (given they are not being aliased). However, the oscillations introduced by lab noise show up at different frequencies. This VBNM procedure is demonstrated experimentally on a nonresonant scan of chlorobenzene in Fig. 2.3. As the step size of the scan is varied, certain peaks stay constant, while others change along with the bandwidth based on the Nyquist criteria. To isolate the peaks that are constant, taking the minimum value of a frequency between scans ensures that any peak that is not constant between all the scans is removed. Comparing the minimization of the scans of 11, 13, and 15 fs steps to the individual scans, it can be seen that many peaks have been removed that may have previously been incorrectly assigned to ground state modes of chlorobenzene. Of course, this procedure relies on the fact the noise peaks can be shifted significantly

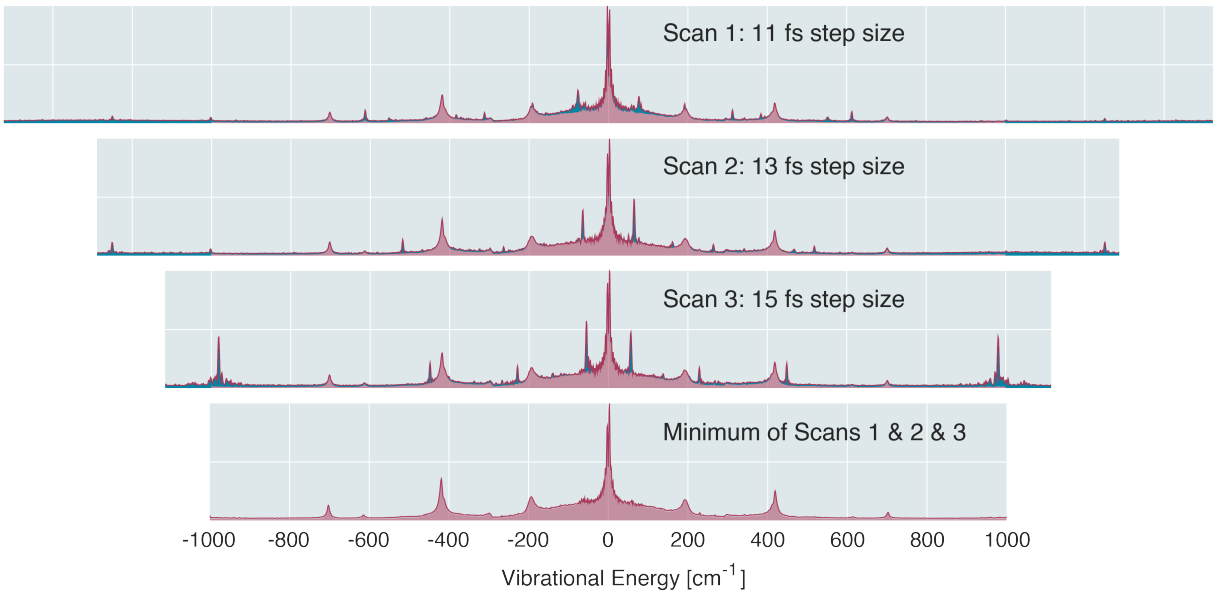

FIGURE 2.3: Experimental demonstration of the Variable Bandwidth Noise Minimization (VBNM) scheme for time resolved vibrational measurements. Due to the fact that molecular response is insensitive to the bandwidth of measurement (given the signal is not being aliased) while narrow-band noise scales along with bandwidth, the two types of oscillation can be separated out by taking scans with different step sizes. Comparing the scan at a set step size vs the minimization of three scans with different step sizes, peaks that may have been misinterpreted as molecular response are removed. The minimized scan is overlaid on the differing step size scans, highlighting which peaks persist (in red) and which get removed through this minimization procedure (blue).

(more than the noise peak width). Thus, although the noise peaks can be shifted through other means (such as changing the acquisition speed of the camera), we find that changing the step size allows for the greatest noise peak shifts without negatively affecting the signal-to-noise ratio (SNR). This technique works well by simply minimizing two scans, but additional scans allow for averaging between scans. Although not implemented in this study, previous work has shown additional SNR benefits of averaging combinations of different scans before taking the lowest value.[48]

With confidence in the reliability of the low energy coherences, the VBNM procedure is applied in 2DES of toluene only, chlorobenzene only, PCDTBT in toluene, and PCDTBT in chlorobenzene, which are displayed in Figs. 2.4(a)–(d). The assignment of these modes to the excited state is confirmed comparing the coherences to nonresonant Raman as well as identifying the Liouville pathways examined in the experiment, discussions of which may be found in the supplementary material. Taking the scan in two different solvents allows for modes of the polymer to be separated from solvent modes as well as distinguish vibrations associated with a specific kinetic process. Any peak that appears and disappears is associated with the slower kinetic processes that were sensitive to the solvent change. The color coding helps guide the interpretation as peaks colored in blue are assigned to be from the solvent, while the peaks in red are the ones that persist between the solvent change.

2.4 Discussion

The VBNM and change of solvent both are general strategies to filter out congested spectra applied in our case to associate excited state vibrations to particular kinetic processes. The TA and fluorescence measurements demonstrate that the more polar chlorobenzene

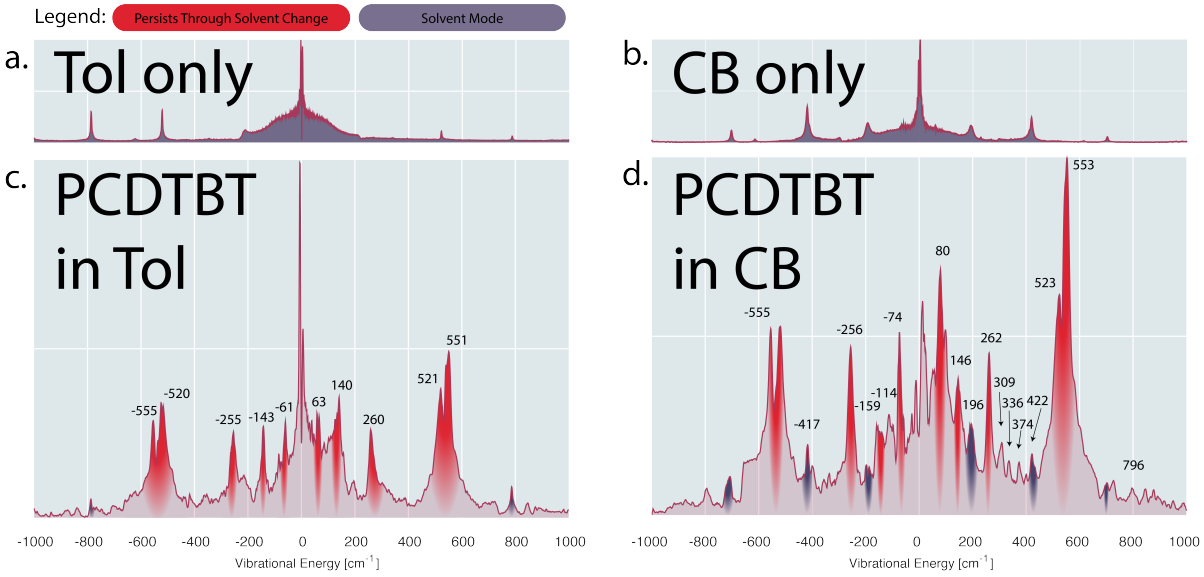

FIGURE 2.4: Coherences measured in (a) toluene only, (b) chlorobenzene only,(c) PCDTBT in toluene, and (d) PCDTBT in chlorobenzene, and Modes associated with the solvent are colored in blue, while peaks that are persist through the solvent change are marked in red. Since the solvent change affected only slower kinetic pathways, the modes unaffected by the solvent change are hypothesized to be involved in the generation of polarons.

solvent stabilizes the charge transfer state of PCDTBT and affects kinetics on a time scale longer than ∼2 ps. On the other hand, the time scale that free charges are generated in heterojunctions is not affected by the solvent change. This observation along with the fact that the fast time scale is associated with excited state vibrational modes leads us to assign this early kinetic process to direct polaron formation, a mechanism described in P3HT 2DES studies.[28] This paints the picture that the generation of polarons and the population of intramolecular charge transfer states are two competitive kinetic pathways. Observation of both electronic and vibrational spectral signatures of polarons directly after photoexcitation makes it seem likely that polarons are the likely source of ultrafast free carriers in heterojunctions.[16, 28, 49]

Our study identifies a set of vibrations that are coupled to the lowest excited state transition that may be involved in polaron formation. In particular, the modes with energy <100 cm^{-1}, ∼140 cm^{-1}, ∼260 cm^{-1}, ∼520 cm^{-1}, and ∼550 cm^{-1} all can be assigned to motions of the polymer and persisted through the solvent change. The <100 cm^{-1} mode that shows up in toluene at ∼60 cm^{-1} and in chlorobenzene at ∼80 cm^{-1} are of particular interest as half a period of their vibration is in the 200 fs–300 fs range. This half period is important because this is the time scale in which the vibration reaches its maximum displacement representing the time scale at which the phonon or molecular structure lags behind. Once the phonon catches up and localizes the charge, electron-hole attraction is greatly reduced thus suppressing recombination.[15] Thus, the time scale of polaron formation and the period of these <100 cm^{-1} modes suggest this mode as a good candidate for the reaction coordinate for polaron formation. However, without more interpretation of what physical motions each of the identified modes correspond to, it is difficult to unequivocally isolate which modes are important. What is clearly shown is that the excited

state of this highly efficient conjugated polymer studied is coupled to many low energy vibrational motions. Understanding the differing role each of these modes play will be an area of future research.

Previous reports of coherences from 2DES have utilized the pattern in which coherences show up in their spectrum, known as beat maps, to assign the origin of the coherences to either the exciton, charge transfer state, or the polaron.[28, 50] Beat maps for coherences found in our study can be found in the supplementary material. However, broad overlapping features arising from the high density of states of the polymer system along with our room temperature measurement complicate the assignment of coherences originating from particular excited states.

2.5 Conclusion

Utilizing new experimental techniques to suppress laser and laboratory noise, our study reports on low energy vibrations coupled to the excited state of the conjugated polymer PCDTBT. A comparison of PCDTBT in two solvents reveals that kinetic processes occurring on a >2 ps time scale are affected by the solvent polarity, while the ∼200 fs time scale of polaron formation is not. This information is applied to the study of the excited state vibrations of the polymer, where certain coherences disappear and appear in the different solvent environments, while modes associated with the polaron should remain. Identification of modes likely associated with polaron formation helps to untangle the complicated excited state landscape. This methodology to assign vibrational function by changing chemical parameters will be explored further in future research.

2.6 Methods

2.6.1 Spectroscopic Data Collection

CEES data were taken on the photon-counting fluorescence spectrometer (PC1 by ISSTM). Absorption spectra are taken on a Shimadzu UV-1800 spectrometer. PL data displayed in Fig. 2.1(a) are simply a single row of the CEES chosen with a 545 nm excitation wavelength. Raman data were collected using a Horiba LabRAM HR Evolution with 785 nm excitation and 600 gr/mm. Samples were in taken in a 2 mm quartz cuvette with an integration time of 400 s with 2 accumulations to account for stray cosmic rays.

Transient absorption was collected using a commercial Helios system described in detail in the supplementary material of Ref. [51]. The pump energy used was 1 mW of 1 kHz light at 500 nm generated by an optical parametric amplifier (TOPAS-C from Light Conversion). Probe delays were taken out to 3 ns.

The spectroscopic setup used to collect the 2DES has been described in detail previously in Ref. [46]. Briefly, broadband pulses are generated from a 3rd harmonic non-collinear optical parametric amplifier (3H-NOPA) (ORPHEUS-N) seeded by a 200 kHz 1028 nm laser (Pharos) compressed with a prism compressor and measured using transient grating frequency-resolved optical gating (TG-FROG) at the sample position with solvent (pulse characterization found in Appendix A). The spectrometer is built in a passively phase stable configuration, and the signal is detected using Gradient Assisted Photon Echo Spectroscopy (GRAPES). Since GRAPES encodes τ delays spatially and ω_t is resolved using a spectrometer, the only delay to be scanned is T. This delay is scanned continuously without stopping the stage allowing for a full 3D dataset to be collected in <2 s lab time. This rapid acquisition beats out much of the $1/f$ noise. In order for the scans with different

step sizes to be correlated, no parameters are changed between different scans other than the step size. The phase of the complex signal is retrieved through spectral interferometry. Interference with a local oscillator allows for retrieval of a relative phase. The phase of the nonresonant signal is known to be purely dispersive, so the relative phase of the nonresonant signal to the local oscillator is used to roughly phase the PCDTBT signal. The phase is fine tuned by making sure that the 2DES signal summed along matches the pump probe signal according to the projection-slice theorem. Verification of the pump probe signal relative to the sum of the 2DES signal can be found in Appendix A.

2.6.2 Variable Bandwidth Procedure

The signal obtained with different step sizes yields different bandwidths along ω_T but the same range of ω_τ and ω_t. ω_T is first obtained for each ω_τ and ω_t by removing the population dynamics through a global analysis procedure described in Ref. [46] and then Fourier transforming the residual. The largest step size determines the bandwidth relevant for the minimization procedure. All three scans are interpolated onto a new ω_T axis (or simply the ω_T axis of the largest step size scan). For each point in ω_τ and ω_t, the different scans now with the same number of points along ω_T are minimized with respect to each other. To get the figures shown in Figs. 2.3 and 2.4(a)–(d), the minimized 3D data cube is summed along ω_τ and ω_t. This procedure relies on a high degree of correlation between scans of different step sizes. Thus, it is critical that no parameters of the scan are changed other than the step size.

2.6.3 Sample Preparation

PCDTBT was bought from Sigma-Aldrich (Mw 20,000–100,000) and used without further purification. Previous 2DES measurements of PCDTBT were limited by scatter due to formation of large aggregates at higher concentration. We found that starting with low concentrations and slowly adding in solute to reach relatively high concentrations of PCDTBT removes scattering. For the 2DES measurement of PCDTBT in chlorobenzene had an optical density of 0.19 in a 200 m quartz flow cell and 0.18 in toluene.

2.6.4 Acknowledgements

The authors thank the Keck facility, especially Dr. Ronald Soriano, at Northwestern University for his help with the CEES measurement. This work made use of the Keck-II facility of Northwestern University NUANCE Center, which has received support from the Soft and Hybrid Nanotechnology Experimental (SHyNE) Resource (No. NSF ECCS-1542205); the MRSEC program (No. NSF DMR-1720139) at the Materials Research Center; the International Institute for Nanotechnology (IIN); the Keck Foundation; and the State of Illinois, through the IIN. This work was supported by the Air Force Office of Scientific Research (Grant No. FA9550-14-1-0005) and the Packard Foundation (Grant No. 2013–39272) in part.

Vibronic Coherences of Bacteriochlorophyll

Adapted from: **Irgen-Gioro, S.**; Spencer, A.P.; Hutson, W.O.; Harel, E. Coherences of Bacteriochlorophyll a Uncovered Using 3D-Electronic Spectroscopy. *J. Phys. Chem. Lett*, **2018** 9 (20) 6077-6081.

3.1 Vibronic Coherence Observed in Bacteriochlorophyll *a*

Mapping the multidimensional energy landscape of photosynthetic systems is crucial for understanding their high efficiencies. Multidimensional coherent spectroscopy is well suited to this task but has difficulty distinguishing between vibrational and electronic degrees of freedom. In pigment–protein complexes, energy differences between vibrations within a single electronic manifold are similar to differences between electronic states, leading to ambiguous assignments of spectral features and diverging physical interpretations. An important control experiment is that of the pigment monomer, but previous attempts using multidimensional coherent spectroscopy lacked the sensitivity to capture the relevant spectroscopic signatures. Here we apply a variety of methods to rapidly

acquire 3D electronic–vibrational spectra in seconds, leading to a mapping of the vibrational states of Bacteriochlorophyll a (BChl*a*) in solution. Using this information, we can distinguish features of proteins containing BChl*a* from the monomer subunit and show that many of the previously reported contentious spectral signatures are vibrations of individual pigments.

3.2 Background

The evolution of photosynthetic bacteria paralleled the development of the early Earth and forms the energetic basis of life. Whereas the earliest photosystems were composed mainly of reaction centers, pigment–protein complexes (PPCs) that both absorbed light and executed reactions, millions of years of evolutionary optimization led to the development of entire PPC arrays capable of producing chemical energy at near-unit quantum efficiency.[52–54] Anaerobic photosynthetic bacteria, whose primary chromophore is Bacteriochlorophyll (BChl), has become a well-studied model system due to a relatively simple structure while retaining desirable photophysical properties. Located on the intracytoplasmic membrane of these bacteria, PPCs consist of pigments (BChl) noncovalently bound to structural units (apoproteins). The relative orientation of the BChl within the protein scaffolding modulates the energy states and coupling, in turn, dictating function.

Whereas the crystal structure of many of these PPCs has been resolved, the question of how structure affects energy-transfer dynamics remains open. Steady-state resonance Raman spectroscopies suggest that certain residues are coordinated to parts of the BChl macrocycle, but they fail to probe the femto/picosecond time-scale transfer process and

time-dependent coupling between excitonic states.[55] Femtosecond time-resolved spectroscopy gives information on dynamics and also has the capability of detecting oscillatory features, or coherences, which arise from two energy states maintaining a quantum-mechanical phase relationship with each other. Using compressed laser pulses broad enough to span multiple states, the energy difference of the states that compose the superposition can be observed. Early experiments performed using pump–probe methods with short pulses on PPCs found coherences at the energy difference between excited electronic states.[56] The development of 2D electronic spectroscopy (2DES) allowed researchers to decongest complicated spectra over excitation and emission axes, resulting in an increased sensitivity for detecting coherences. This led to a flurry of studies on a variety of PPCs that reported coherences at the energy level difference between donor and acceptor states, suggesting the importance of these coherences in the energy-transfer process.[57–63] 2DES allows for simultaneously high spectral and temporal resolution, but it does not provide unambiguous assignment to the origin of the observed coherences to vibrational or electronic states. Typically, such discrimination is possible because electronic and vibrational motions exist on very different time scales and energies. However, in these PPCs, the energy level difference between excited electronic states is in the same energy regime as vibrations within a single electronic manifold. While this characteristic may lead to coupled vibrational-electronic (vibronic) states that mediate efficient transfer, it also leads to difficulties in understanding the nature of these states. Uncovering whether the coherences exist between vibrations on the same excitonic manifold or two different manifolds drastically changes the physical interpretation, but definitive assignment of the states involved has remained elusive.[64]

3.3 Results

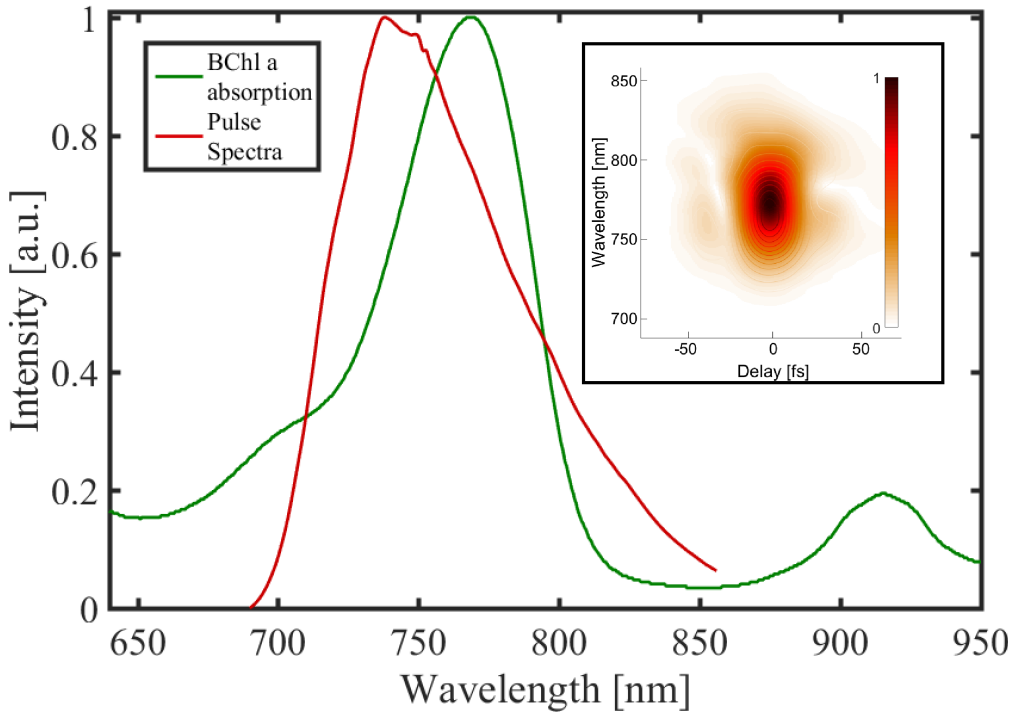

FIGURE 3.1: Near-IR absorption spectrum of BChl*a* compared with pulse spectrum, tuned for coverage of the Qy (S1) band. (Insert) TG-FROG trace of pulse used.

A key control experiment to understanding 2DES of coupled BChl systems is that of the BChl monomer, in which the vibrational and electronic coherences can be distinguished. This is achieved in our experiment because only one electronic state is within the bandwidth of the laser pulse, leading all coherences to be vibrational in nature. Figure 3.1 shows the absorption spectrum of BChl*a* as well as the pulse spectrum used in our experiment. Some variants of nonlinear spectroscopy have reported Raman active modes of BChl*a*, but previous attempts at this control experiment have yielded no positive results; that is, no coherences were observed that coincided with those in the multichromophoric

system.[65, 66] Because resonance Raman experiments show a litany of low-frequency vibrations in BChl*a* and 2DES of PPCs shows strong coherences, the null results from BChl*a* have been used to justify nonvibrational origins of PPC coherences.[65, 67] We find that the main reason for the discrepancies between 2DES experiments on BChl and on PPCs composed of them is the combination of multiple field–matter interactions that nonlinearly scale the transition moments, combined with poor dynamic range in the acquisition of weak signals. To address this issue, we overcome the typical $1/f$ noise (i.e., pink noise) distribution of most laboratory setting by acquiring the entire $128 \times 916 \times 2560$, 32-bit data set in <2 s.[68] This setup is sensitive enough to capture the nonresonant response of the solvent, which is used to characterize the instrument. Using the solvent scan, the phase of our resonant scan can be recovered, and any frequencies of the solvent/instrument can be removed using a global analysis procedure, similar to one previously described by Collini et al.[69] Shown diagrammatically in Figure 3.2 (top), the goal is to transform the original data, $\mathbf{Y}$, into a matrix multiplication of two matrices, $\mathbf{G}$ and $\mathbf{T}$. Briefly, a m by N_2 basis set, $\mathbf{T}$, is created, where m represents the number of bases and N_2 is the number of time points in the population time (the second time delay). The amplitudes of each of the basis sets, $\mathbf{G}$, can be retrieved by taking the inverse of $\mathbf{T}$ and multiplying it by $\mathbf{Y}$, or $\mathbf{G} = \mathbf{Y}\mathbf{T}^{-1}$. Using nonlinear regression to minimize $f(\mathbf{T}) = (\mathbf{Y} - \mathbf{G}\mathbf{T})$ returns the basis set that best describes the data. This procedure decomposes the spectrum, as a particular basis (a $1 \times N_2$ vector) multiplied by its corresponding amplitude will create a 3D spectrum with only that component. Figure 3.2b shows a few examples of bases and their respective amplitudes. The beating frequencies that were found in the nonresonant scan were added to the basis set and fixed (not regressed). An example of a noise peak can be seen at the bottom of Figure 3.2b, with characteristic features such

as a negative decay time constant as well as having an amplitude that matches the intensity of the integrated 2DES along T. All of the bases that were found in the nonresonant scan are multiplied by their corresponding amplitude to create a noise-only spectrum. This is then subtracted from our data to remove the contributions to the signal from those components. A detailed description of our experimental methods can be found in 3.5.

The real rephasing portion of the spectra is displayed in Figure 3.3 at T = 43 fs. The positive signal that lies on diagonal is a combination of excited-state emission (ESE) and ground-state bleach (GSB). An example point is chosen to view the time transient with the exponential decay terms removed and a Fourier transform performed to view the coherence frequencies. The coherences from every point in the 2D spectrum are then summed and are displayed in Figure 3.4 with previously reported transient grating (TG) frequencies by Scherer et al. shown as white lines.[70] It is worthwhile to note that projecting the 3D spectrum into 1D averages over weaker features, as seen in a comparison of the beating spectrum in Figures 3.3 and 3.4. Our phased spectrum has the added benefit of distinguishing positive and negative frequencies, which informs us whether the coherences are on the ground or excited state. Because of the choice of phase-matching conditions ($k_s = -k_1 + k_2 + k_3$), the two rephasing pathways, ESE and GSB, differ in what happens in the second light–matter interaction.[71] The two pathways have been diagrammatically represented in 3.5. ESE allows for both positive and negative frequencies, whereas GSB only allows for negative frequencies unless the system is initially in an excited vibrational state, which has significant population only for energies under kT = $\sim$207 cm^{-1} in our room-temperature experiment. Whereas the GSB and ESE features are probably overlapping, meaning coherences probably also exist on the ground state, we can assign coherences to the excited state because of the roughly equal intensity positive

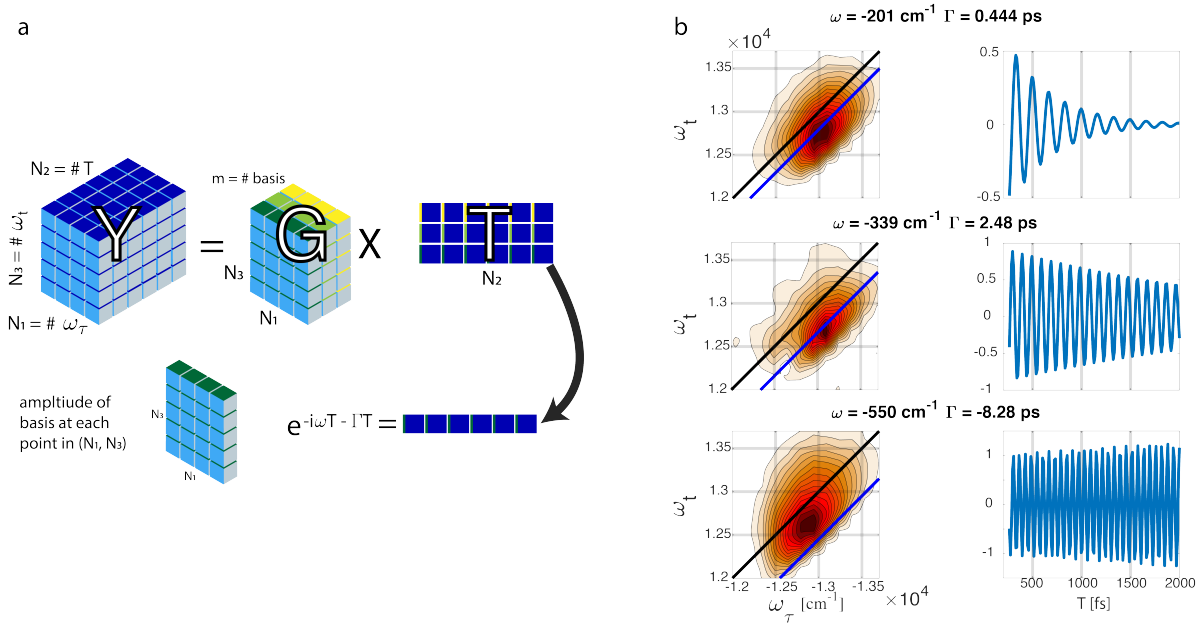

FIGURE 3.2: Using global analysis to identify noise peaks. (a) The 3D data set can be thought of as a result of matrix multiplication between an $N_1 \times N_3 \times m$ matrix and an $m \times N_2$ matrix, where m is the number of bases. Each basis is a complex exponential, and the corresponding $N_1 \times N_3$ matrix represents the amplitude of that basis for every point in the 2D pump–probe spectrum. (b) A few examples of the amplitudes and bases extracted from our BChl*a* spectra. Noise peaks are identified by the solvent-only scan and also do not decay within the T range (0–10 ps). The mode at 550 cm^{-1} is an example of a noise peak. Another trait that confirms this is a noise peak is that the max amplitude of the beat does not lie on the blue line, which is separated from the main diagonal by the oscillation energy. All frequencies that were found in the solvent-only scan are removed by multiplying their respective basis by their amplitude to create a noise-only spectrum, which is then subtracted from the original data.

and negative coherences.

Comparing BChl*a* coherences to coherences observed in PPCs that contain BChl*a*, we find many similarities. A few examples are in Table 3.1. It can be seen that many previously reported coherences in PPCs are Franck–Condon active modes of the pigment monomer, making the long lifetimes of coherences less remarkable than if spatially separated electronic states could maintain correlation. Indeed, a recent study showed that Fenna–Matthews–Olson (FMO) coherence frequencies and lifetimes are insensitive to the electronic energies.[72] With definitive assignment of the origin of coherences, the identified vibrational states provide a basis for more in-depth interpretation of PPC 2DES. It can be seen that transitions in PPCs are not coupled to all of the BChl*a* vibrations available. Arranging the pigments in different geometric orientations, the PPC can select for useful vibrations given the purpose of the specific transition. For example, it has been shown experimentally that vibrational–exciton resonance enhances energy-transfer rates.[73] Even within this framework, it has been unclear up until now whether useful vibrations in PPCs originate from collective motions or from individual pigments. In LH2, the mode that is implicated in mode-assisted transport is at 735 cm^{-1}. Using this study to assign

Pigment Protein Complex	Reported Coherence (cm^{-1})	BChl*a* Coherence (cm^{-1})
Fenna-Matthews-Olson Complex [58, 72]	160, 200	201
Light-Harvesting Complex 2 [63]	750	737
B820 subunit of Light-Harvesting Complex 1 [62]	345, 416, 546, and 735	349, 413, 539, and 737

TABLE 3.1: Comparing PPC and BChl*a* Coherence Frequencies

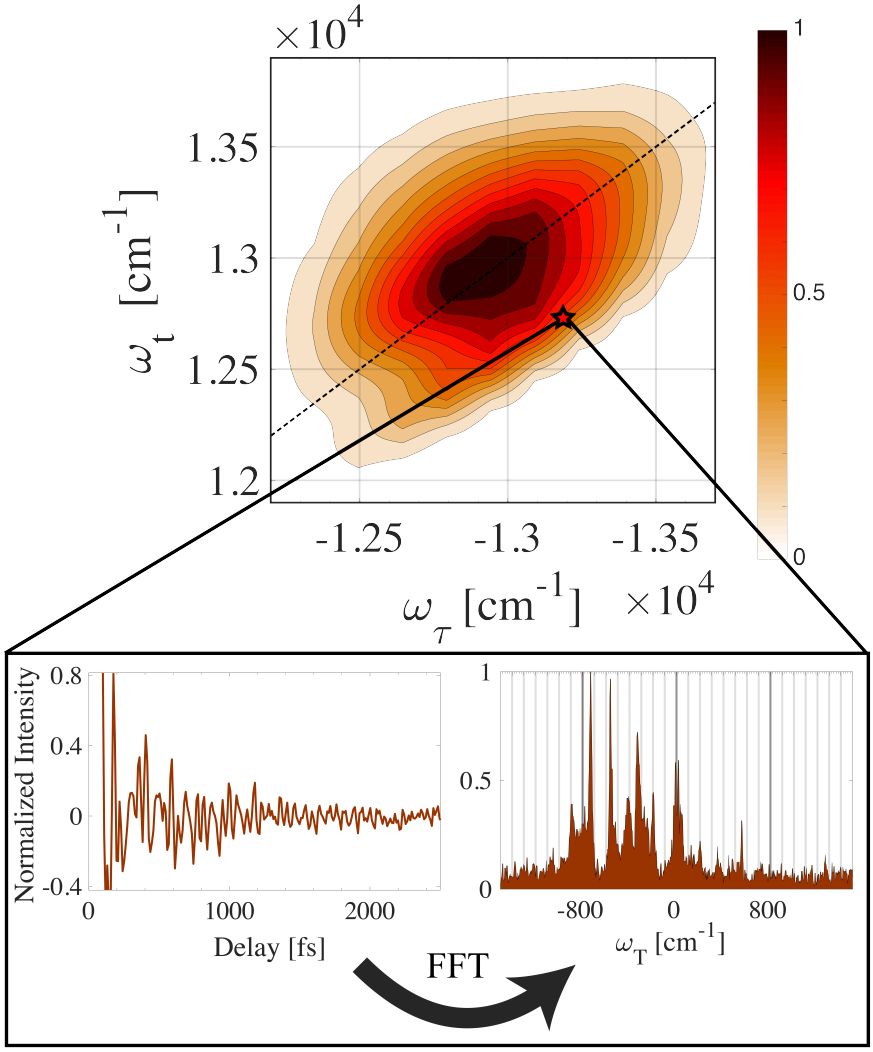

FIGURE 3.3: (Top) Real rephasing spectrum at T = 43 fs. An example point is picked from the structureless ground-state bleach feature at ω_τ = -13,389 cm^{-1} and ω_t = 12,776 cm^{-1}, for which we display the time domain coherences along with the Fourier transform to extract the coherence frequency.

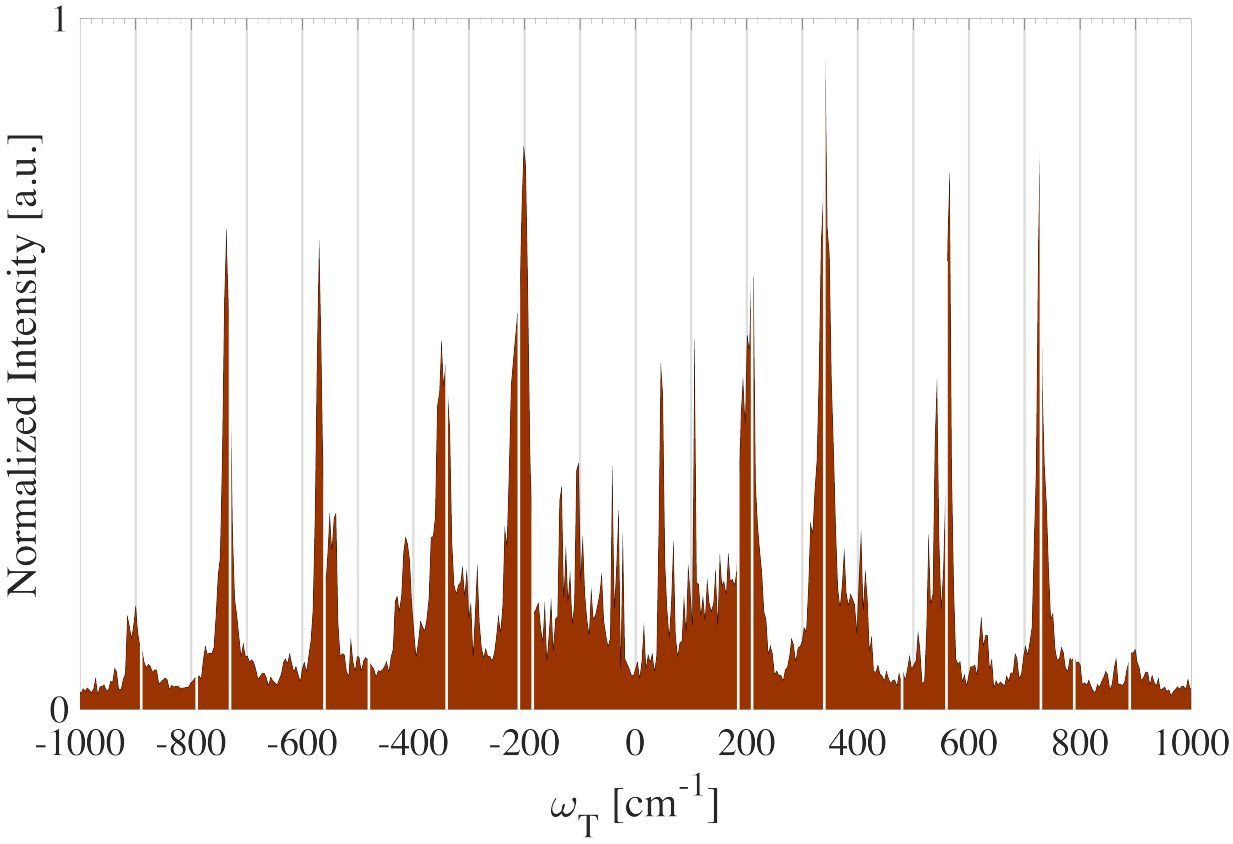

FIGURE 3.4: Summed coherence energies from all points in 2DES spectra. White lines represent reported frequencies from transient grating experiments.[70]

the origin of the coherence and previous work in normal-mode analysis of Raman studies, we can assign the mode that participates in the B800–B850 transfer step to symmetric in-plane bend of $NC_aC_m(\alpha)$.[74] Whereas most of the coherences can be attributed to pigment vibrations, some are still uncertain. In particular, FMO has two low-frequency modes around 160 and 200 cm^{-1}, only one of which definitively corresponds to coherences found in BChl*a*.[72] The 200 cm^{-1} mode has been reported as Mg-sensitive and has been assigned to be an out-of-plane MgN deformation.[74, 75] The 160 cm^{-1} mode, which is also a strong coherence in LH2 and B820, is not observed with high intensity in our experiment or in previous TG experiments.[66, 70] However, previous shifted excitation Raman difference spectra show a 177 cm^{-1} mode with larger intensity than both the 212 cm^{-1} mode and the 730 cm^{-1} mode.[67] The mode has also been characterized in the excited state using nonphotochemical hole burning and is observed at 166 cm^{-1}.[76] The low relative intensity in this particular experiment is puzzling, especially knowing the mode's strength in PPC 2DES and monomer Raman experiments.

Although not all coherences can be attributed to pigment vibrations, most of the previously reported coherences at the electronic energy level differences can be. Much attention has been placed on the electronic states of PPCs, but the vibrational landscape is equally important. Strongly coupled vibrations can broaden electronic transitions, allowing for better spectral overlap, as well as funnel energy to the vibrational ground state through internal relaxation. While the exact role of vibrations in PPCs is still up for debate, the ability to assign spectral signatures of coherences in PPCs to vibrations of the monomer subunit is an important step.

Whereas this study can assign many of the long-lived coherences to vibrations, coherences that decay with a lifetime of $\sim$100 fs are not found in the BChl spectra. In fact,

if coherence frequencies and lifetimes are fit for $T > 250$ fs and projected back to $T = 0$, then only population dynamics remain. Contrastingly, in LH2, mutant studies with the B800 band removed found a fast dephasing coherence assigned to the B850 and B850*, and simulations back up the idea of a rapidly dephasing B800 and B850 excitonic coherence on that time scale.[77, 78] In FMO, similar <100 fs dephasing is seen, also assigned to excitonic coherences.[79] Thus, with definitive assignment of long-lived coherences as vibrations and lack of fast dephasing coherences in the monomer, these previously reported $\sim$100 fs dephasing coherences are most likely excitonic in nature, matching expected dephasing rates. Using the same global analysis technique used to remove the solvent response from our data, long-lived coherences can be removed to better reveal the excitonic lifetimes and frequencies. Knowing the long-lived coherences are vibrations and rapidly dephasing coherences are excitonic helps align the interpretation of 2DES with physical models.

3.4 Conclusion

Improvements in 2DES experimental data collection and analysis have enabled us to extract the vibrational coherence energies of BChl*a*. This has demonstrated that many of the previously reported coherences that were attributed to long-lived coherences between excited electronic states are most likely vibrations in individual pigments. However, 2DES of BChl does not display fast dephasing lifetimes, demonstrating that previously reported coherences that dephase at $\sim$100 fs lifetime are most likely excitonic in nature. It is still unknown why the vibrational coherence energies match up with many of the excitonic energy gaps reported in ultrafast energy transfer in PPCs. With the ability to provide

vibrations at a variety of energies and easily tune the electronic structure through spatial manipulation, it can be seen why BChl*a* is used as a pigment in a variety of PPCs. Whether PPCs developed their electronic states to have energy gaps the same as the vibrations available from the BChl, the PPCs and BChl structures coevolved with each other, or the energies matching up is coincidental remains an open question.

3.5 Methods

3.5.1 Spectroscopic Setup

Traditional 3DES requires that two time delays be scanned with sufficient resolution to meet the Nyquist–Shannon criterion, slowing down the acquisition relative to a pump-probe experiment, where only one time dimension is scanned. We exploit the spatial properties of light, focusing the three excitation beams to a line rather than a point and tilting the two pump pulses (1 and 2) relative to one another to form a temporal gradient moving along the focal line that spatially encodes the excitation frequency dimension (ω_τ). By directly detecting the radiated signal spectrum (ω_t) using a spectrograph, only the remaining waiting or population time delay (T) between pulse 2 and 3 must be scanned in the so called GRAPES configuration.[80] The challenges in GRAPES relative to traditional "point-by-point" methods include the need for higher average excitation beam power, increased total scatter, and the need for a 2D sensor rather than a line camera, which are generally faster. However, since the signal is sparse in frequency along the excitation dimension and the excitation energies are known, the spatially multiplexed dimension can be undersampled. While undersampling aliases the signal, it enables higher acquisition speeds without sacrificing resolution. The remaining waiting time dimension

is "rapid-scanned," meaning the stage moves continuously, outputting triggers to the camera at the desired time delays.[81] Combined with a high-speed sCMOS camera (Andor Zyla 5.5) running at a frame rate of 650 Hz, this methodology allows us to complete a $128 \times 916 \times 2560$ pixel scan in under two seconds. The excitation dimension, ω_τ, was detected over a range of 222 fs with a step size of 1.75 fs. The waiting time dimension, ω_T, was scanned from 0 to 10 ps with a 11 fs steps. The detection dimension, ω_t, is dispersed by a grating in a spectrometer. The signal is isolated from excitation beam scatter through Fourier filtering. We would like to note that the reported negative result by Fransted et al. also used the GRAPES configuration.[65] Our additional sensitivity is gained from the rapid scan and the under-sampling of the tau dimension, which increase the acquisition speed. Furthermore, rastered step scanning two time dimensions introduces noise disproportionately along the two dimensions, leading to good 2D plots with one noisy dimension. Our methodology does not have this issue and allows for slicing/projecting along any plane and good success with data analysis techniques.

Phasing GRAPES data has been accomplished by the Engel group, but is highly sensitive to many factors.[82] One of the challenges of phasing GRAPES is that the relative phase between the signal and the local oscillator may have a spatial dependence. Furthermore, aberrations that may arise between the sample and camera and chirp may cause the phase difference between signal and LO to have significant nonlinear terms. We overcome these challenges by using the non-resonant scan to create a phase mask that is then applied to our resonant scan. While this signal is weak, a variety of methods can be used to separate the signal from scatter. Apart from boosting the signal strength with the LO, the spectral interference gives us an opportunity to distinguish our signal from scatter through

Fourier filtering. We first un-tilt our spectra (due to beam 3 and the LO being tilted relative to each other), which allows for a tight window to be applied. If the spectrometer's resolution is high enough, scatter from all the beams other than beam 3 can be removed. Secondly, we step the population time finely enough so that the electric field of the excitation pulses can be sampled, akin to the Engel groups work on highly scattering live cells.[83] We expect our signal to rise and fall on a $\sim$15 fs time scale while scatter oscillates with a 2.66 fs period for 800 nm light allowing us to Fourier filter along the population time. The solvent non-linear response is purely dispersive (i.e., phase-shifted by $\pi/2$ relative to pulse 3), so the phase of the solvent signal relative to a local oscillator is used to determine the phase of the resonant BChl signal. The phase of the 2D spectrum is then fine-tuned to match the pump-probe signal, which according to the Fourier projection-slice theorem is a projection of the 2DES signal along the excitation axis. The TG-FROG signal displayed in Figure 1 is one row taken from the non-resonant scan, corresponding to a fixed tau delay. The second harmonic non-collinear optical parametric amplifier (2H-NOPA) was homebuilt built to allow for broadband coverage of the desired spectral range and compressed with chirped mirrors (Layertech 109347) and fused silica wedges.[84]

3.5.2 Sample Preparation

We studied the most common BChl variant, BChl*a*, found in purple and green bacteria. Rhodobacter *sphaeroides* 2.4.1 (ATCC 17023) is grown semi-anaerobically under lamps at 30 C in a shaker in ATCC Medium 550: R 8 A H medium. Cells were pelleted with an ultracentrifuge and resuspended in methanol (plus .005 M sodium ascorbate), kept in the dark and cold for about half an hour, and sedimented by centrifugation. This extraction is repeated until sedimented cells become colorless.[85] The resulting supernatant contains

both BChl and carotenoids, which is run through an AKTAxpress FPLC to ensure purity. The resulting solution is placed into a rotovap to achieve a suitable optical density for spectroscopic measurements.

3.5.3 Global Analysis

The global analysis follows previous reports for both transient absorption and multi-dimensional spectroscopies.[69, 86] The general assumption is that the data can be separated into a multiplication of two matrixes **Y** = **GT** where **Y** is the original data, **G** is the amplitudes of each basis, and **T** contain the basis sets. Since the time evolution of the density matrix $\rho \equiv \langle\psi|\psi\rangle$ containing populations and coherences is well known from the Liouville-Von Neumann representation of the Schrödinger's equation:

$$\frac{d}{dt}\rho = -\frac{i}{\hbar}[H,\rho]$$

$$\frac{d}{dt}\begin{pmatrix}\rho_{11} & \rho_{12}\\ \rho_{21} & \rho_{22}\end{pmatrix} = -\frac{i}{\hbar}\left[\begin{pmatrix}\epsilon_1 & 0\\ 0 & \epsilon_2\end{pmatrix}\begin{pmatrix}\rho_{11} & \rho_{12}\\ \rho_{21} & \rho_{22}\end{pmatrix} - \begin{pmatrix}\rho_{11} & \rho_{12}\\ \rho_{21} & \rho_{22}\end{pmatrix}\begin{pmatrix}\epsilon_1 & 0\\ 0 & \epsilon_2\end{pmatrix}\right]$$

so that:

$$\dot{\rho_{11}} = 0 \qquad \dot{\rho_{22}} = 0$$

$$\dot{\rho_{12}} = -\frac{i}{\hbar}(\epsilon_1 - \epsilon_2)\rho_{12} \qquad \dot{\rho_{21}} = -\frac{i}{\hbar}(\epsilon_1 - \epsilon_2)\rho_{21}$$

the second time (population time) dimension is chosen due to the ease of representing the signal as a sum of complex exponentials. Thus, **T** is written as an m by N_2 matrix where

each row, m, is a complex exponential with only two parameters. Single value decomposition is first used to estimate m, which is the inner dimension in the matrix multiplication. In practice, we find it useful to run the global analysis three times. Once with only real exponentials to remove the population dynamics. Taking the Fourier transform of the remaining signal gives us good initial values to do the global analysis again with complex exponentials as our basis. Finally, the parameters from the two global analysis runs are used initial values for the final run of the global analysis which fits both populations and coherences. Since the problem is linear in **G** and nonlinear in **T**, we can find the amplitudes of the basis by taking the inverse of **T** and multiplying it by our original data **G** = $\mathbf{YT}^{-1}$. This means that our minimization is a function of only the basis set since we are looking for the $\mathbf{GT} = \mathbf{YT}^{-1}\mathbf{T} = \mathbf{Y}$. We find through simulations that this methodology reliably returns coherence frequencies, but not lifetimes. If two peaks are overlapped, it may return one broadened peak. Because of this limitation, we use the global technique not to analyze our data but to remove components we do not want meaning no erroneous features will be added. Figures 3.4 is still the result of normal Fourier analysis after the noise components have been removed.

3.5.4 Excited State Emission vs Ground State Bleach Pathway

Each pulse interacts with the density matrix element's bra or ket quantum states, either promoting or demoting the states within the pulse bandwidth. While this conserves energy, the total momentum of the numerous interaction is also conserved. Thus, we can select a certain subset of interaction pathways spatially. In our experiment, we choose the "re-phasing" 4WM pathway, corresponding to $-k_1 + k_2 + k_3$. Knowing our system starts in the ground state, the first interaction then must be a promotion into the excited state

of the bra. The second interaction however can be a promotion of the ket to the excited state, or it could be a demotion of the bra back down to the ground state, both interactions contributing a positive momentum interaction. This differentiation can be seen diagrammatically in figure 3.5. The bra interactions are denoted with a dotted arrow while the solid arrow represents interaction with the ket. The differentiation of what happens with the second pulse is what distinguishes the two pathways. As shown in the previous section, coherences oscillate in the second time period, T, with a frequency related to the energy level difference $\epsilon_1 - \epsilon_2$. The sign of the frequency depends on which value of energy is larger. For excited state emission, because the coherences are happening on the excited state, both the positive and negative frequencies are allowed. For the coherences to have a positive frequency in the ground state bleach pathway, the initial state needs to be an excited vibrational state. This can occur due to thermal population, but above kT = $\sim$207 cm^{-1}, there will not be sufficient population for coherences to be detected. Our experiments detect both the ground state bleach and excited state emission pathways and can see equal intensity positive and negative frequencies. Thus, we are able to state that many of the coherences we observe are on the exited state manifold.

3.5.5 Acknowledgments

We thank the recombinant protein production core, specifically Dr. Sergii Pshenychnyi, at Northwestern University for their help, advice, and equipment lending. Also, we thank Prof. Pamela Parkes-Loach and Prof. Paul Loach in their guidance in growing bacteria. This work was supported by the Air Force Office of Scientific Research (FA9550-14-1-0005), and the Packard Foundation (2013-39272) in part.

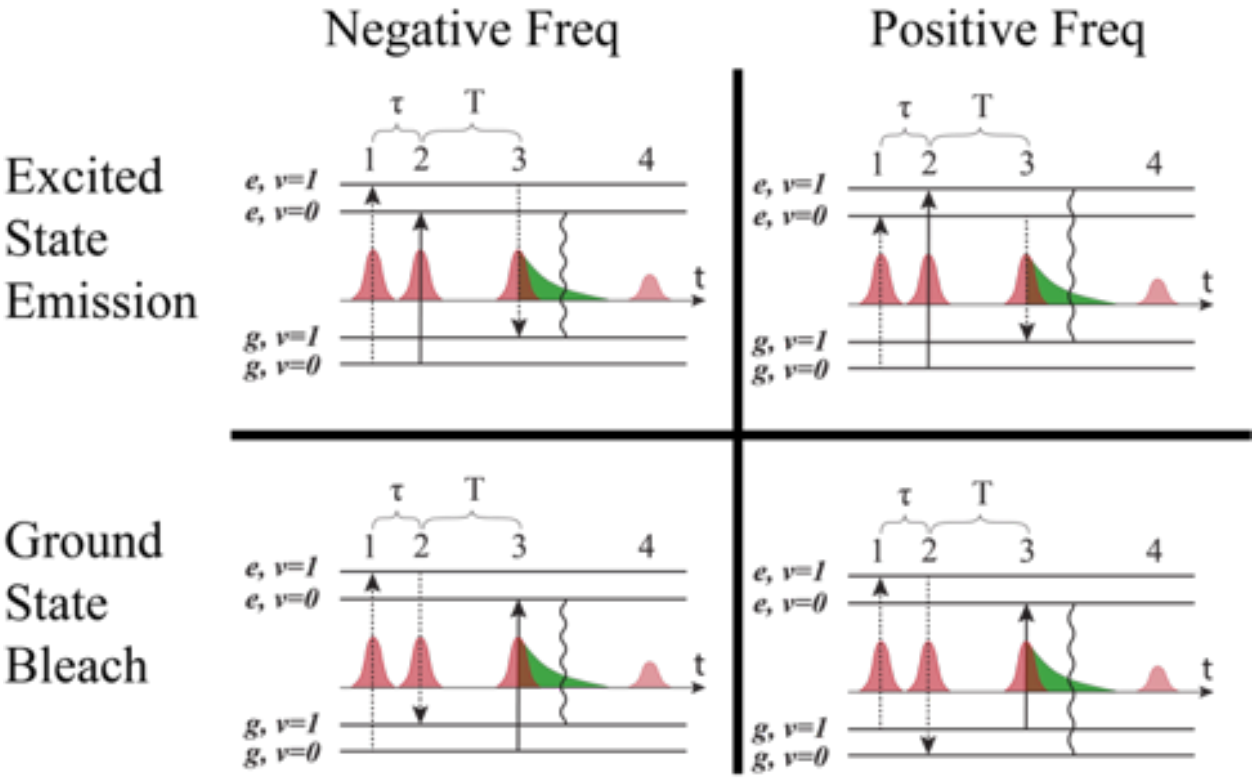

FIGURE 3.5: Distinguishing pathways based on positive and negative coherence frequencies. Excited state emission pathways can have either positive or negative coherence frequencies within the laser bandwidth while ground state bleach features can only have negative frequencies unless the system is initially in an excited vibrational state.

Electronic Coherence of Photosynthetic Proteins

Adapted from: **Irgen-Gioro, S.**; Gururangan, K.; Saer, R.; Blankenship, R.; Harel, E. Electronic Coherence Lifetimes of the Fenna-Matthews-Olson Complex and Light Harvesting Complex II. *Chem. Sci.*, **2019** 10 (45) 10503 - 10509.

4.1 Coherence Between BChl*a* Electronic States in Photosynthetic Proteins

The study of coherence between excitonic states in naturally occurring photosynthetic systems offers tantalizing prospects of uncovering mechanisms of efficient energy transport. However, experimental evidence of functionally relevant coherences in wild-type proteins has been tentative, leading to uncertainty in their importance at physiological conditions. Here, we extract the electronic coherence lifetime and frequency using a signal subtraction procedure in two model pigment-protein-complexes (PPCs), light harvesting complex II (LH2) and the Fenna–Matthews–Olson complex (FMO), and find that the coherence lifetimes occur at the same timescale (<100 fs) as energy transport between

states at the energy level difference equal to the coherence energy. The pigment monomer bacteriochlorophyll *a* (BChl*a*) shows no electronic coherences, supporting our methodology of removing long-lived vibrational coherences that have obfuscated previous assignments. This correlation of timescales and energy between coherences and energy transport reestablishes the time and energy scales that quantum processes may play a role in energy transport.

4.2 Background

The timescale in which a system maintains phase correlation, or coherence lifetime, dictates the observation of quantum interference at a macroscopic level.[87] For electronic states, stochastic energy fluctuations cause coherences between the ground and the excited states to decay on the order of 10^{-14} seconds. In the late 2000's, the assumption that coherences between two excited electronic states should be on a comparable timescale was challenged when a series of experiments observed coherences for hundreds of femtoseconds, with possible functional implications for energy transport in photosynthetic systems.[88–94] These initial experiments disputed the notions that the excited states' independent interaction with the thermal bath would rapidly destroy coherences between excitonic states (electronic coherences) and the conventional description of energy transfer using standard and modified Förster theory.[95, 96] However, more recent work has suggested that the spectroscopic signatures that began this debate, namely long-lived (hundreds of femtoseconds to picoseconds dephasing rate) coherences, can been attributed to originate from vibrations of the chromophores (vibrational coherences).[97–101] In order to re-establish the timescale in which quantum effects may play a role in

photosynthetic proteins, our study details a systematic method to extract electronic coherence lifetimes applied to two photosynthetic proteins, light harvesting complex 2 (LH2) and Fenna–Matthews–Olson (FMO) complex, using Multi-Dimensional Electronic Spectroscopy (nDES).

The nDES signal is generated with a series of three compressed broadband laser pulses, measured as a function of delay between the pulses, generating a 3D dataset. Two of these dimensions measure coherences between the ground and the excited state, which are popularly interpreted as the absorption frequency, ω_τ, and the emission frequency, ω_t. The "population time", T, contains both population dynamics and the coherences between states within the excited or ground state manifold, which are the focus of this study and are detected as oscillations of the signal as a function of T. A recent theoretical study by Gelin et al. clearly partitions how electronic and vibrational degrees-of-freedom contribute to coherences at different timescales.[102] At a <100 fs timescale, the time evolution is independent of nuclear degrees-of-freedom and is exclusively determined by electronic coupling. On a longer timescale, delocalized vibrations coupled electronic states form "vibronic" coherences, which eventually turn into purely vibrational coherences after a critical time $\tau_D \cong 2\pi/\sigma$, where σ is the dispersion of the static disorder. Understanding experimentally exactly when the signal transitions between different regimes of coherences gives microscopic details on the system-bath coupling. With a theoretical basis for what we expect to observe, our study aims to re-establish the timescale of electronic coherence in model photosynthetic proteins.

Previous studies have assigned large amplitude coherences that dephase at a $\sim$100 fs timescale to be electronic coherences.[101, 103–108] However, the multitude of overlapping signals at early timepoints makes it difficult to extract values of the frequency and

dephasing rate of the electronic coherence. The most common method currently to extract these parameters is to try to extrapolate the frequency based off estimating the period of oscillation, but trying to approximate the frequency of a damped oscillator this way is fraught with errors, especially in the case spectral congestion. The experimental measurement of electronic coherence lifetime and frequency is further complicated because the time domain signals are convolved with the instrument response correlation time. It is known that laser power and phase fluctuations follow a $1/f$ distribution, leading to pulses at long time intervals to become increasingly uncorrelated.[106] Thus, if a scan takes too long to acquire, coherence lifetimes will be artificially shortened. Previous measurements done by the corresponding author on LH2 showed coherences decaying with a $\sim$100 fs lifetime,[89] but our current measurements see the same coherences out to many picoseconds as a result of the fast measurement, in which the entire scan is completed before significant loss of pulse correlation (typically, less than 2 s). Our study combines the rapid acquisition experimental methodology, which provides high SNR data, with a systematic procedure to extract electronic coherence to overcome these challenges.

4.3 Results

nDES spectra are taken for BChl*a*, LH2, and FMO, and in the case of LH2 and FMO a bimodal distribution of coherence lifetimes is observed. The long-lived coherences show agreement with a recent control experiment measured in our lab of vibrational coherences in BChl*a* and gives us confident assignment of long-lived coherences as primarily vibrational in origin.[99] The contributions from population dynamics and vibrational coherences are removed with global analysis.[107] Briefly, the 3D spectrum is written as a matrix multiplication of a basis set of real or complex exponentials and its amplitude

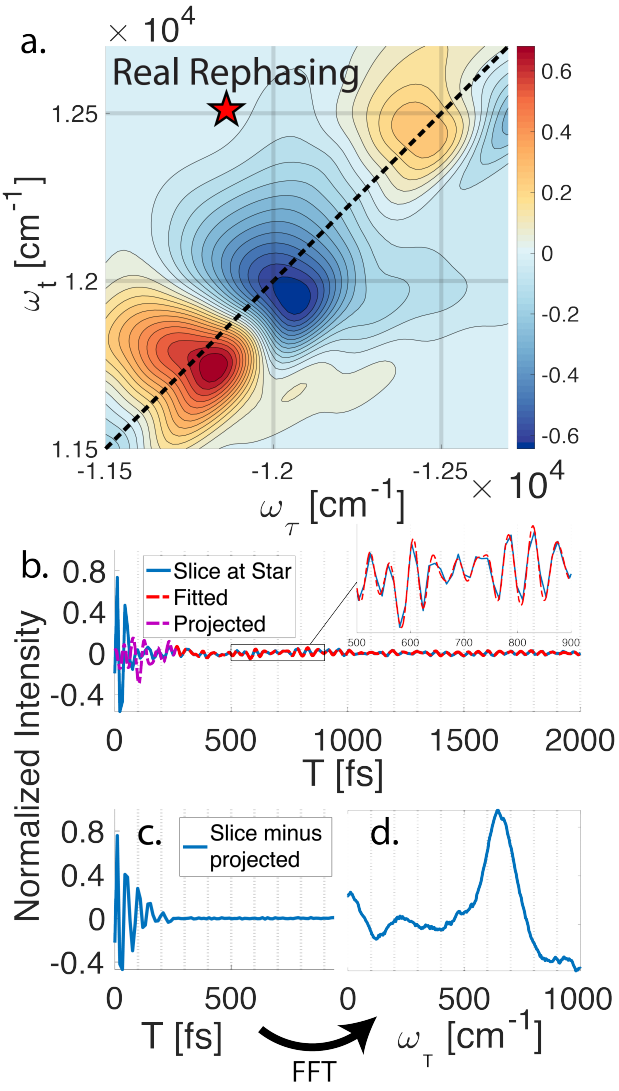

FIGURE 4.1: Methodology of extracting electronic coherence from the light harvesting complex II. (a) A slice of the real rephasing LH2 3DES spectrum is shown at T = 43 fs. (b) An example point from (a) is chosen at the star with population dynamics subtracted using global analysis. The residual (blue) is fit for later time points (red) and projected back to the early time points (purple). (c) The short lifetime coherences are revealed once the projected coherences are subtracted. (d) A Fourier transform is performed on (c) to reveal the line width and coherence frequency.

for each point in the 2D spectra. Variable projection is used to find the basis set that best describes the full spectra, which essentially decomposes the spectrum into the contributions from each of the basis functions, allowing for reconstruction of spectra from a subset of components. This procedure is first run with a basis set of real exponentials, and the reconstructed spectra is subtracted to remove the contribution from population dynamics. The residual is run through global analysis again using a basis set of complex exponentials. In the second global analysis run, the early time points are excluded, and only later time points are considered. Thus, the reconstructed spectrum contains contributions only from the long-lifetime coherences. The resulting spectra is then subtracted from the population subtracted spectra to reveal the rapidly dephasing coherences in the typically congested first few hundred femtoseconds. This systematic method of subtracting vibrations is insensitive to the choice of cut-off time as long as one chooses a time longer than the electronic coherence lifetime because they have negligible contribution to the signal at long time points. We recently used a similar method to remove contributions to the signal from solute-only third order response and is described in more detail in this context in the methods section.[99] Fig. 4.1 diagrammatically shows how the vibration subtraction procedure is performed in LH2. The real rephasing spectra is shown in (a) at T = 43 fs. Once the population dynamics are removed, each point in the 2D spectrum contains oscillations as a function of T, which are the electronic and vibrational coherences (b). The long-lifetime coherences are fit at later time points and projected back to T = 0 with their respective amplitudes found through global analysis. Subtracting these contributions from long-lived coherences reports on the electronic coherences (c). These short-lived coherences can then be Fourier transformed to reveal the line width and coherence frequency (d).

The vibrational subtraction analysis is first performed on BChl*a*, which is the monomer pigment found in both LH2 and FMO. Coherences of BChl*a* must be vibrational in origin since there is only one accessible excited electronic state within our pulse bandwidth. The sum of the Fourier transformed residual, like the one seen in Fig. 4.1(d), for the entire 2D spectrum can be seen in Fig. 4.2. This analysis on BChl*a* shows no remaining electronic coherence peaks, only a background that comes primarily from imperfect subtraction of real exponentials, non-exponential signals, and remaining $1/f$ noise.

Unlike BChl*a* where no electronic coherences are possible, LH2 and FMO may show both electronic and vibrational coherences owing to the high-density of excitonic states within the pulse bandwidth. The same subtraction procedure applied on LH2 and FMO, as seen in Fig. 4.2(b and c), show broad peaks. For FMO, the main peak is centred around $\sim$350 cm^{-1}. FMO is a system of 8 BChl, with one weakly surface bound BChl likely to become disassociated during the process of isolation and purification. The seven remaining excitonic states have energies ranging from 12,120 to 12,670 cm^{-1} and the energy level difference of some of the excitons are displayed as sticks in Fig. 4.2(b).[108] The closest excitonic energy level difference to the observed peak is between excitons 7 and 2 using the numbering of BChls chosen by Fenna and Matthews.[109] It is thought that excitons are delocalized across 1/2, 3/4, and 5/6/7, and even though excitons 7 and 2 are neighbouring chromophores, they are predicted to have relatively weak excitonic coupling.[110] Previous reports of rapidly dephasing coherences in FMO found that the lowest oscillation frequency was well above the distribution of excitonic energy level differences ($\sim$600 cm^{-1}), not matching any exciton energy differences.[101] In LH2, the electronic coherence extracted is centred at $\sim$630 cm^{-1}. However, since the excitonic energies are ambiguous, no proposed energy level differences are drawn. The main complicating factor is the

high density of excitonic states with similar energies that can be modulated by specific instances of disorder.[111] From the absorption spectrum, the energy level difference of the two BChl*a* rings, B800 and B850, is 735 cm^{-1}. Previous work on a mutant of LH2 with the B800 band removed observed an electronic coherence at 687 cm^{-1}, which was assigned to be between B850 and a higher lying excitonic state B850*.[103] Although there is uncertainty to which states the observed coherences are between, it is clear that both FMO and LH2 contain rapidly dephasing coherences that do not exist in BChl*a*.

Global analysis with a complex exponential basis retrieves the lifetime and energy of the electronic coherence peaks. For LH2 the main peak is centred at 680 cm^{-1} with a lifetime of 81 fs, and for FMO it is at 390 cm^{-1} with a lifetime of 57 fs. However, we find that global analysis sometimes has difficulty in retrieving lifetimes of broadened peaks and is sensitive to the number of exponentials used to fit a given peak. Thus, the lifetimes extracted with global analysis are supplemented with the $1/e$ decay rates from the time domain of individual points in the 2D spectra. Estimating the electronic decoherence rates from the time traces, like the one seen in Fig. 4.1(c), gives ~80 and ~60 fs dephasing rates for the largest peaks of LH2 and FMO, respectively. These dephasing rates can be compared to the expected dephasing rates, which are revealed using the antidiagonal slice of the 2D spectrum. The antidiagonal slice reveals the homogenous broadening of a state, which is related to the dephasing time between the ground and excited state by $\tau = [\pi c \Delta]^{-1}$ where Δ is the FWHM of a fitted Lorentzian. This holds true even in the presence of strong vibronic coupling.[112] While FMO's expected dephasing rate matches the coherence lifetime, the estimated lifetimes of the B800 and B850 states in LH2 gives 56 and 42 fs respectively (slices and fits shown in Appendix B). The measured electronic coherence lifetime of ~80 fs is unexpectedly longer than the dephasing rate of

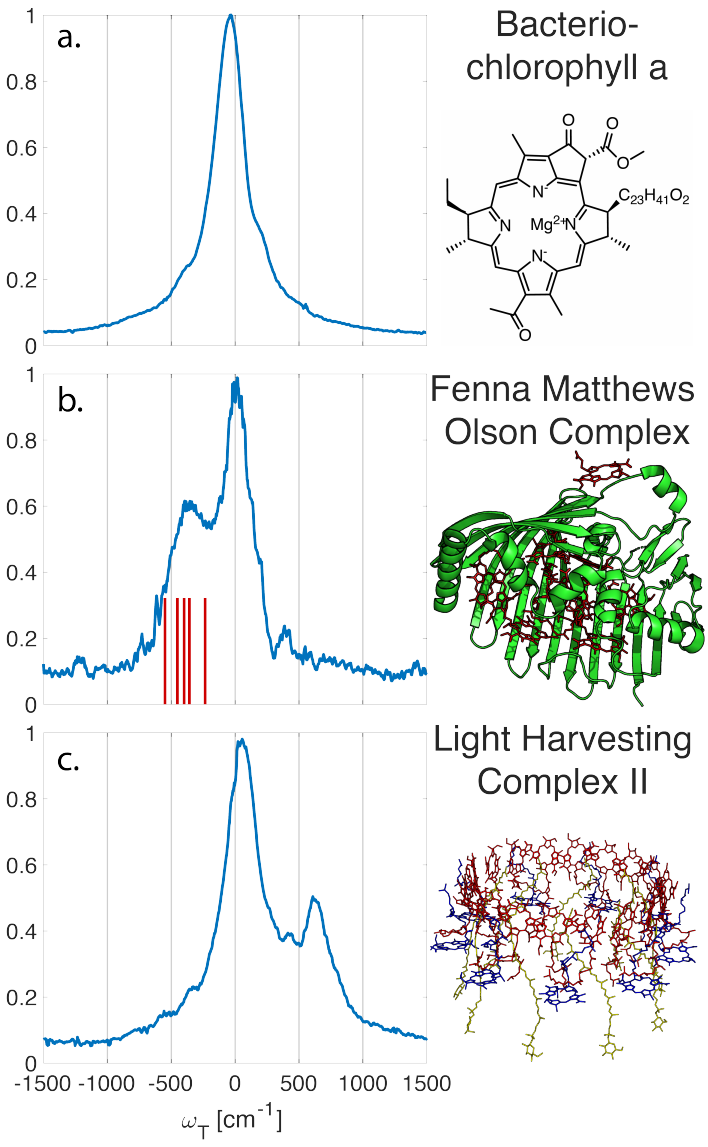

FIGURE 4.2: Sum of the electronic coherences over the entire 2D spectrum. (a) The BChl*a* spectra contains only vibrational coherences. With the long-lived coherences subtracted, no additional peaks are observed. Both (b) FMO and (c) LH2 have multiple electronic states within the bandwidth of the pulse and display fast decaying coherences. For FMO, excitonic energy level differences are drawn as a stick spectrum for differences between 330–550 cm^{-1}. The closest excitonic energy level difference to the main peak is between excitons 7 and 2 at 400 cm^{-1}, with the energy levels taken from ref. [108]

the individual states. Gelin et al. offers another method to predict the coherence lifetime using the expression $\tau^{-2} = \sum_{k=1}^{N} J_{1k}^2$, where N is the number of chromophores and J is the inter-site electronic coupling strength.[102] Comparison to their predicted value of 53 fs of the electronic coherence lifetime of FMO, we find good agreement. However for LH2, which has more chromophores and higher coupling strength (at least in the B850 band), we should expect the coherence lifetime to be even shorter.[113] This trend holds true for the rates extracted from the anti-diagonal slices, but not for the electronic coherence measured in the time domain. Using both metrics, we find that the measured electronic coherence lifetime is longer than predicted. The electronic coherence frequency and lifetimes obtained from our methodology are summarized in Table 4.1.

Protein	Global Lifetime	Global Frequency	Fourier Lifetime	Fourier Frequency	Expected Dephasing
FMO	57 fs	390 cm^{-1}	60 fs	350 cm^{-1}	60 fs
LH2	81 fs	680 cm^{-1}	80 fs	630 cm^{-1}	42-56 fs

TABLE 4.1: Comparing PPC and BChl*a* Coherence Frequencies

Since our experiment establishes that the electronic coherences are happening at a <100 fs timescale, for coherences to be functional and not simply a phenomenon universal to all molecules there has to be biologically relevant processes happening on the same timescale. For FMO, the kinetic rates between all sites has been well characterized and shows that this timescale is irrelevant for exciton transport.[108] However, in LH2, <100 fs timescale processes have been implicated in both energy transfer between the rings through intermediate states and population transfer to states with mixed excitonic and charge transfer character process.[114–116] Thus, we will take a closer look at the population dynamics extracted during the first iteration of global analysis. This viewed the signal as a sum of contributions from real exponentials, $e^{-t/\tau}$, described with a single

parameter, which is the decay lifetime τ. The associated amplitude for a given exponential decay at each point on the 2D spectra is called the Decay Associated Spectra (DAS) beatmap and shows all species that have dynamic components over T with a given rate. The difficulties of interpreting DAS in general are explored in Appendix B, but interpretation of the BChl*a* spectra is simplified because it only contains one electronic excited state with simpler dynamical processes compared to FMO or LH2. Furthermore, the BChl*a* 2D spectrum contains no contributions from ESA, so positive signal on the DAS beatmap indicates a decay of signal while negative areas indicate signal growth. In Fig. 4.3, it can be seen that the DAS for BChl*a* and LH2 both possess similar fast (<100 fs) components. In the BChl*a* 15 fs component, the signal grows in on the Stokes shifted side of the diagonal while decaying on the anti-Stokes side, indicating a global shift of energies. However, since this component is on the timescale of our pulse duration, we assign this to instrument response. The other components of the BChl*a* indicate growth of signal pumping at higher energies and probing at lower energies, $[\omega_\tau, \omega_t]$ = [-12,800, 12,500] cm^{-1}, indicated on Fig. 4.3 with circles. This growth of signal at the lowest energy state suggests these components are internal relaxation processes. Utilizing the BChl*a* assignments to inform the DAS beatmaps in LH2, the 15 fs component is similarly assigned to be instrument response. However, for the LH2 74 fs component, non-internal relaxation processes distinct from the BChl*a* 76 fs DAS beatmap appear. Amplitude at the downhill cross-peak at $[\omega_\tau, \omega_t]$ = [-12,400, 11,700] cm^{-1}, highlighted on Fig. 4.3 in the hexagon, indicating a pump and probe energy level difference of $\sim$700 cm^{-1}, shows energy transfer at the same timescale and energy as the electronic coherence. Dynamic processes that may be occurring at a <$\sim$100 fs timescale are discussed later, but it is possible that the same state in coherence are experiencing energy transfer at this ultrafast timescale. The slower rates of LH2 are attributed to decay of the ground state bleach of the B800 and B850 rings and

population transfer between the two rings. Specifically, the ∼3.6 ps decay shows up only on the B850 band of LH2 and the broad bi-excitonic ESA feature. The similar lifetimes, also seen in pump-probe experiments, have been used to justify that the ESA originates from the excited B850 ring.[117] The other two slower 472 and 949 fs components are difficult to assign due to the similarity of features. It is possible that they are the same component, which would agree with previous reports have indicated that the B800 and B850 transfer rate occurs with τ = 700 fs.[118]

4.4 Discussion

Identifying the lifetime and energy of electronic coherences limits the role of electronic coherences to the <100 fs timescale and in turn what biological functions may be implicated. Although it is possible that electronic coherence coincidentally occurs at the same timescale as dynamic processes between states of the same energy level difference, the large body of work on LH2 provides clues to which states may be involved in the electronic coherence. One likely possibility is that the coherence observed here is between the B850 and B850* state, which would be the same coherence previously observed in the mutated species by the Engel group.[103] B850* refers to the higher lying excited states of the B850 ring's excitonic progression. Although the typically named $k = \pm 1$ transition contains most of the total oscillator strength, symmetry breaking allows for other transitions that overlap the B800 band. This model predicts that energy transport within the B850 band occurs on a <100 fs timescale.[116] Atomistic modelling of LH2 has shown that in the unmutated species, the B850* state mixes with the B800 state and that excitation becomes delocalized across both rings. This mixed state is thought to be an intermediate

between the B800 and B850 ring, mediating stepwise downhill transport.[115] Thus, coherences within the excitonic manifold of B850 offer explanations to both the <100 fs electronic coherence and energy transfer. However, another mutant study where the B850 band is shifted to 810 nm revealed a dark state with charge transfer character around 850 nm,[114] but with no electronic coherences reported. This study revealed that excitations in the B800 band are transferred to the CT state in a <100 timescale. In the unmutated species, this CT state is theorized to mix with the B850 ring further adding energy levels to an already congested energy landscape. Due to the multitude of possible states involved, we cannot confidently assign the states in coherence purely based off the energy of the electronic coherence observed.

4.5 Conclusion

Observation of excitonic coherences in photosynthetic complexes on the timescale of biologically relevant dynamics constrains the time and energy scales that electronic coherences may play a role. Electronic decoherence lifetimes were extracted from FMO and LH2, while similar analysis on their pigment monomer, BChl*a* revealed no early time coherences. While the majority of exciton transport in these systems happens on a picosecond timescale and is dominated by spatially directed dipole coupling, our study suggests that there may still be a niche function for electronic coherence at a <100 fs timescale.

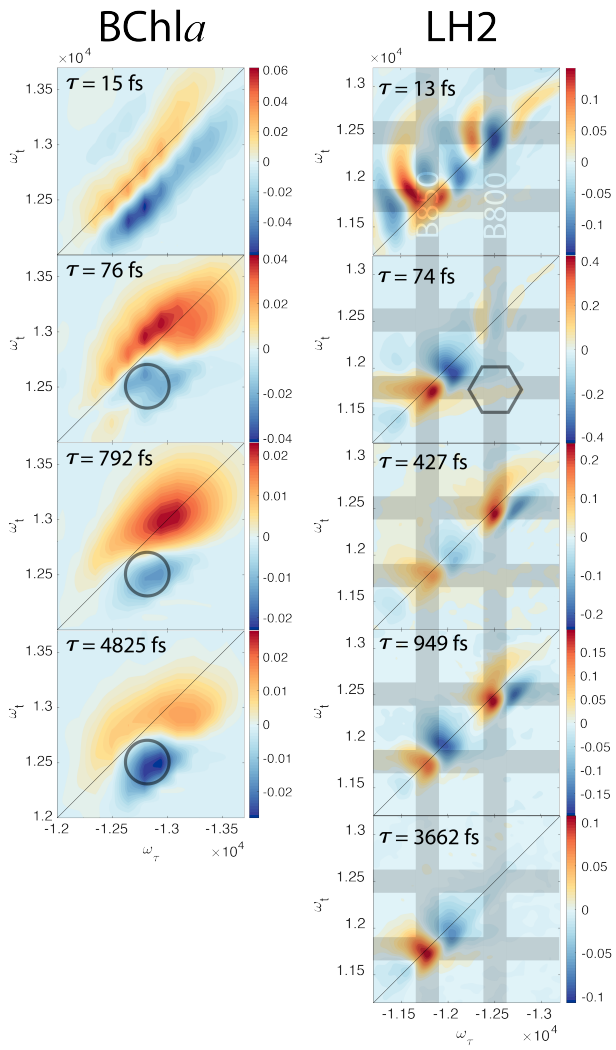

FIGURE 4.3: DAS beatmaps of BChl*a* (left) and LH2 (right). The BChl*a* assignments are aided by only having one electronic state within the bandwidth of the laser and simpler dynamic processes. The BChl*a* 13 fs component indicates a global shift energy and is attributed to a Stokes shift convolved with instrument response. The 76 fs component appears to be an internal relaxation process with signal growth at the low energy side of the spectra (highlighted in the circle). The 74 fs LH2 component most likely has similar internal relaxation processes, but also appears to have amplitude at the downhill cross-peak $[\omega_\tau, \omega_t]$ = [-12,400, 11,700] cm^{-1}, located in the hexagon, at roughly the electronic coherence energy. Grey bands are located on the energies of the B800 and B850 states.

4.6 Methods

4.6.1 Global Analysis

The 3D spectrum, **Y**, is a $N_\tau \times N_T \times N_t$ matrix. This can be rewritten as a matrix multiplication problem, **Y** = **GT**, where **G** is a $N_\tau \times N_t \times m$ matrix and T is a $m \times N_T$ matrix, and m is the number of basis sets. **T** is what is referred to as the basis set, as each $1 \times N_T$ row of the matrix is either a real or complex exponential depending on if populations or coherences are fit. **G** is the associated amplitude of each basis. In the case of real exponentials, the $N_\tau \times N_t \times 1$ matrix associated with a given exponential is the DAS beatmap. Since **G** can be solved for by multiplying the original data by a basis set, $\mathbf{G} = \mathbf{YT}^{-1}$, the entire optimization can be boiled down to finding the basis set that best describes the data. Using variable projection, this minimizes the number of parameters needed to be solved. To fit later times, only data past a certain time point is considered so that the basis set now is described by a $m \times (N_T - N_{exclude})$ matrix, where $N_{exclude}$ is the number of early time points no longer considered. To extrapolate, the **G** from the late times is multiplied by a new basis set that now includes the early time points, keeping the same coefficients for each complex exponential basis. Our methodology of fitting later time points and projecting the fit back to the early time points is tested out on simulated spectra in Appendix B.

4.6.2 Sample Preparation

LH2 and BChl*a* are isolated from Rhodobacter *sphaeroides* 2.4.1. FMO is extracted from Chlorobaculum *tepidum*. Details can be found in Appendix B.

4.6.3 Acknowledgements

We thank the recombinant protein production core, specifically Dr Sergii Pshenychnyi, at Northwestern University for their help, advice, and equipment lending. Also, we thank Prof. Pamela Parkes-Loach and Prof. Paul Loach in their guidance in growing bacteria. This work was supported by the Air Force Office of Scientific Research (FA9550-14-1-0005), and the Packard Foundation (2013-39272) in part.

Coupled Vibronic Pigments

Adapted from: **Irgen-Gioro, S.**; Gururangan, K.; Spencer, A.P.; Harel, E. Non-Uniform Excited State Electronic-Vibrational Coupling of Pigment-Protein Complexes *J. Phys. Chem. Lett*, **2020** 11 (24), 10388-10395

5.1 Electronically Coupled Vibronic Pigments in Pigment Protein Complexes

Photosynthetic organisms exploit interacting quantum degrees of freedom, namely intrapigment electron-vibrational (vibronic) and interpigment dipolar couplings (*J*-coupling), to rapidly and efficiently convert light into chemical energy. These interactions result in wave function configurations that delocalize excitation between pigments and pigment vibrations. Our study uses multidimensional spectroscopy to compare two model photosynthetic proteins, the Fenna-Matthews Olson (FMO) complex and light harvesting 2 (LH2), and confirm that long-lived excited state coherences originate from the vibrational modes of the pigment. Within this framework, the *J*-coupling of vibronic pigments should have a cascading effect in modifying the structured spectral density of excitonic states. We show that FMO effectively couples all of its excitations to a uniform set of

vibrations while in LH2, its two chromophore rings each couple to a unique vibrational environment. We simulate energy transfer in a simple model system with non-uniform vibrational coupling to demonstrate how modification of the vibronic coupling strength can modulate energy transfer. Because increasing vibronic coupling increases internal relaxation, strongly coupled vibronic states can act as an energy funnel, which can potentially benefit energy transport.

5.2 Background

Among the many light-harvesting complexes found in nature, LH2 from purple bacteria and FMO from green-sulfur bacteria are among the most extensively studied model pigment-protein complexes, both of which have evolved to rapidly and efficiently transport excitations in route to the reaction center.[119] Although both proteins contain the same pigment (bacteriochlorophyll a or simply BChl*a*), they employ distinctive geometrical arrangements that alter the Coulombic interaction of the pigment's transition dipole moment, so-called *J*-coupling. Here, we focus on the pigment interactions that give rise to the near-infrared (near-IR) absorption features that serve to absorb and transfer excitation (Figure 5.1(a)). FMO's near-IR peak contains a series of energetic steps to allow excitation from the chlorosome antenna to proceed energetically downhill toward the reaction center with an efficiency of $\sim$48%.[120] Structurally, FMO is a trimer with each subunit containing seven BChl*a* molecules wrapped in a "string bag" of mainly β-sheets kept far enough apart to prevent concentration quenching.[121] An eighth surface-bound BChl*a* is postulated to serve as an entry point for excitation from the chlorosome antenna to FMO.[122] Simulations[123, 124] of exciton migration as a function of the number and

density of chromophores in a random arrangement find FMO-like structures to have relatively high efficiency and robustness to structural variation. Though this design serves the purpose of FMOs well, it limits the spatial extent of exciton energy transport (EET). LH2 has two near-IR bands that arise from the two-ring-like arrangement of BChl*a*, called B800 and B850 for their respective absorption wavelengths. The B850 ring consists of nine strongly coupled BChl*a* dimers, while the B800 ring consists of nine weakly coupled monomers.[125] These near-IR bands both directly absorb light and act as intermediate states, routing excitation from photoexcited carotenoids and higher-lying states of LH2 to the LH1-reaction center complex with near-unity transport efficiency.[126–129] It has been suggested theoretically[130] that the high spatial symmetry of LH2's rings allows transfer in any direction, increases robustness against disorder, and minimizes the biochemical resources needed by introducing void spaces that do not participate in efficient transfer across space.

In addition to structural differences that modify *J*-coupling, the coupling of pigment vibrations to the electronic states represents another opportunity to tune the excited state potential energy manifold.[131] Shown diagrammatically in Figure 5.1(b) and explained mathematically in the Appendix C, a pigment's vibronic states result from a linear combination of the underlying electronic and vibrational states, with the ratio of mixing depending on the coupling strength. For multichromophoric systems with *J*-coupling, the mixing of excited electronic states also has the potential to affect the coupling strength of vibrations because the resulting excitonic states are formed from combinations of pigment vibronic states. The change in a particular vibration's coupling strength to the excitonic manifold due *J*-coupling can be described with a generalized Huang-Rhys factor.[6] However, experimentally untangling the precise contributions from the pigment

electronic and vibrational degrees of freedom remains difficult and has been a source of much discussion and debate about the role of coherence in energy transfer.[132–135] Our approach is to comparatively study the excitonic landscape of FMO and LH2 and their chromophore, BChl*a*, to uncover the underlying design principles of the two proteins using multidimensional electronic spectroscopy (nDES).

Timing a series of compressed broadband laser pulses, nDES measures a correlation map in which each dimension represents a particular quantum-mechanical degree of freedom, such as those associated with an electronic or vibrational transition. Each pulse interaction generates either a population or coherence, which can be conceptualized as the electronic system existing in a single state or being in a superposition between states. Traditionally, coherences are distinguished on the basis of whether the two states in superposition are different vibrations within the same excited state or belong to different excited states entirely. Although a careful choice of pulse spectra and phase-matching geometry restricts the type of interaction possible for each pulse, in complicated systems with broad and overlapping energy levels, ambiguity often hampers assignment of whether coherences are primarily vibrational or electronic in origin.[136] In photosynthetic bacteria, observations[88, 133, 137] of coherences seemingly originating between electronic states with lifetimes longer than the expected dephasing times prompted questions about the role of coherences in facilitating energy transfer. Recently, a FMO mutagenesis study by the Scholes group[100] demonstrated that coherence frequencies and lifetimes do not change with electronic state shifts, suggesting long-lived coherences were not between electronic states. Our group performed its own control experiment on BChl*a*,[99, 138, 139] observing vibronic coherences at the same frequency as previous reports of long-lived coherences, evidence that coherences observed in proteins were primarily vibronic in origin.

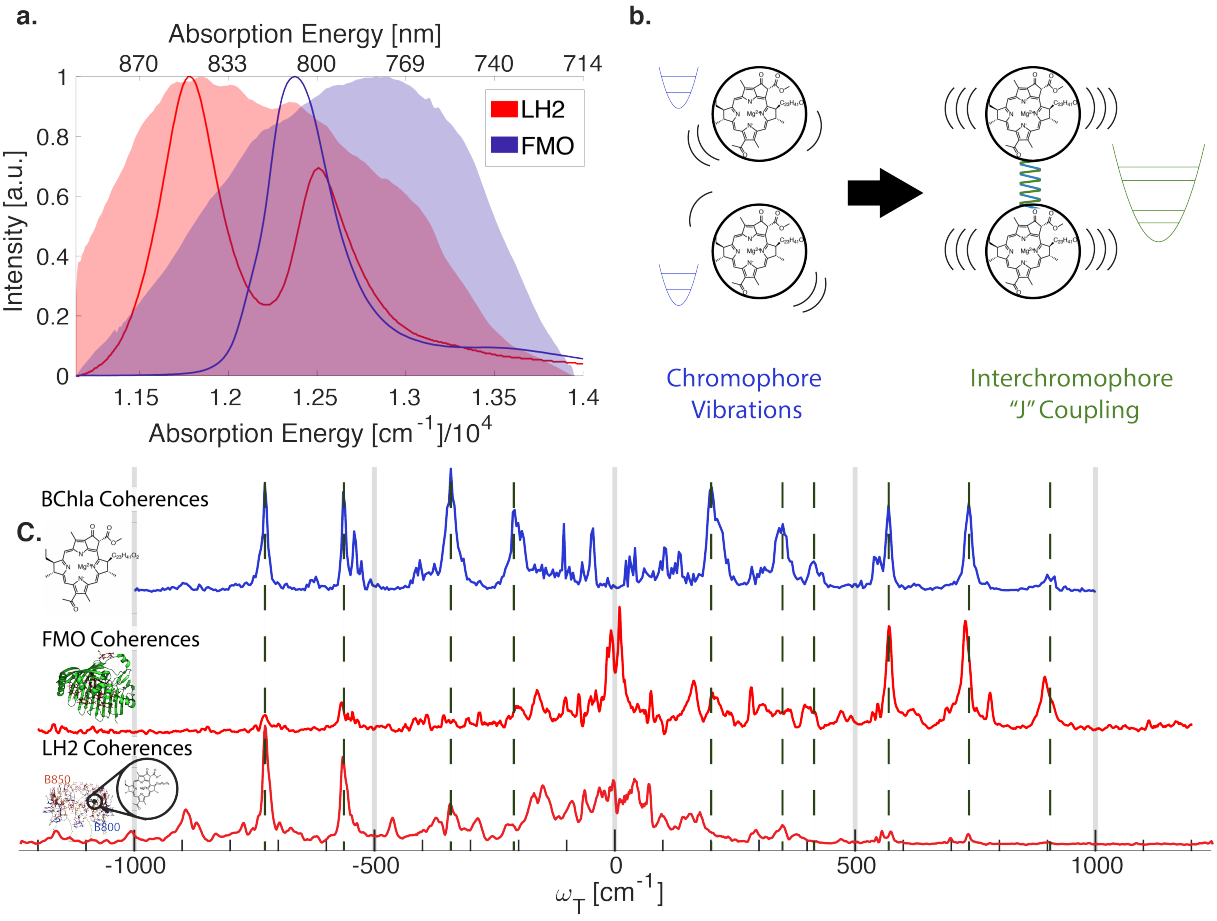

FIGURE 5.1: (a) Absorption spectra (line plot) of LH2 and FMO and pulse spectra (area plot) used in their respective nDES experiments. (b) In individual pigments, the interaction of electronic and vibrational states creates "vibronic" energy manifolds. When pigments are electronically coupled together, their resulting energy states are combinations of vibronic states. (c) Coherences of BChl*a*,(23) FMO, and LH2 demonstrating that coherences observed from proteins are primarily vibronic states of the pigment and not protein scaffolding, solvent modes, etc.

Subtracting out the long-lived coherences allowed us to reveal the coherence lifetime and frequency between states primarily electronic in origin at a <100 fs time scale.[140] With a better understanding of the origins of the signals being observed, the study presented here is poised to examine the excitonic landscape of the two model photosynthetic proteins.

5.3 Results

To compare the coherence frequencies of BChl*a*, FMO, and LH2, we measure the nDES spectra at room temperature in which two dimensions correspond to single-quantum coherences (SQCs) and the third corresponds to zero-quantum coherences (ZQCs). SQCs represent coherences between the ground and the single-exciton (excited) manifold, while ZQCs are those between states on the same manifold. The two SQC dimensions may be loosely interpreted as excitation and detection frequency axes. One-dimensional ZQC spectra for BChl*a*, LH2, and FMO are displayed in Figure 5.1(c) and are constructed by integrating over the two SQC dimensions. Previous work from our group and the groups of both Collini and Ogilvie[99, 138, 139] has assigned these coherences to originate from the excited state. Dotted lines are drawn from select peaks of the BChl*a* ZQCs and overlaid on the FMO and LH2 plots, highlighting that most of the protein coherences originate from the vibronic states of the pigment. It has previously been suggested[141] that the observed coherences arise from modulation of the interchromophore distance, mediated by the protein motions. However, even coherence frequencies that do not match exactly with isolated BChl*a* coherences are common between the proteins, namely, the 163 and 466 cm^{-1} modes, suggesting these coherences do not arise from structural differences between proteins. Coherences in FMO at the energy level difference between

exciton states are observed, similar to previous work.[88, 105] For LH2, the energy gap between the B800 and B850 rings can be crudely estimated from the absorption maximum to be $\sim$735 cm^{-1}, while a coherence is observed at 733 cm^{-1}. This vibrational mode has been implicated in mode-mediated coherent population exchange,[141, 142] in which a vibrational mode that is equal to the energy gap between two electronic states enhances EET. It should be noted that for both FMO and LH2, a high density of electronic states, equal to the number of chromophores in each protein, exists. This makes the high density of BChl*a* vibrational modes ideal, as it allows for the electronic-vibrational resonance between many pairs of states.[143]

Assigning coherences of FMO and LH2 to originate from pigment vibronic states rather than protein phonon modes prompts a comparison between an understanding of the system as interacting vibronic pigments vs electronic states in a fixed continuous or structured thermal bath. To investigate this difference, the ZQC plots from Figure 5.1(c) are resolved as a function of excitation energy. Panel a of Figure 5.2 serves as a reference to the nomenclature and interpretation of the three dimensions, while panels b and c show the correlation between excitation and emission energy at a short delay time (T = 43 fs) for LH2 and FMO, respectively. The negative features result from ESA, while positive features represent either ground state bleach (GSB), excited state emission (ESE), or a combination of both. For LH2 (Figure 5.1(b)), the two positive features correspond to the GSB/ESE feature of the B800 and B850 rings. The spectral separation of signals from the two rings allows for better confidence in assigning coherences to originate from a particular set of pigments. FMO's (Figure 5.1(c)) broad overlapping features at room temperature make distinguishing contributions of the signal from the different pigments challenging. Panels d and e of Figure 5.1 show ZQCs as a function of excitation energy

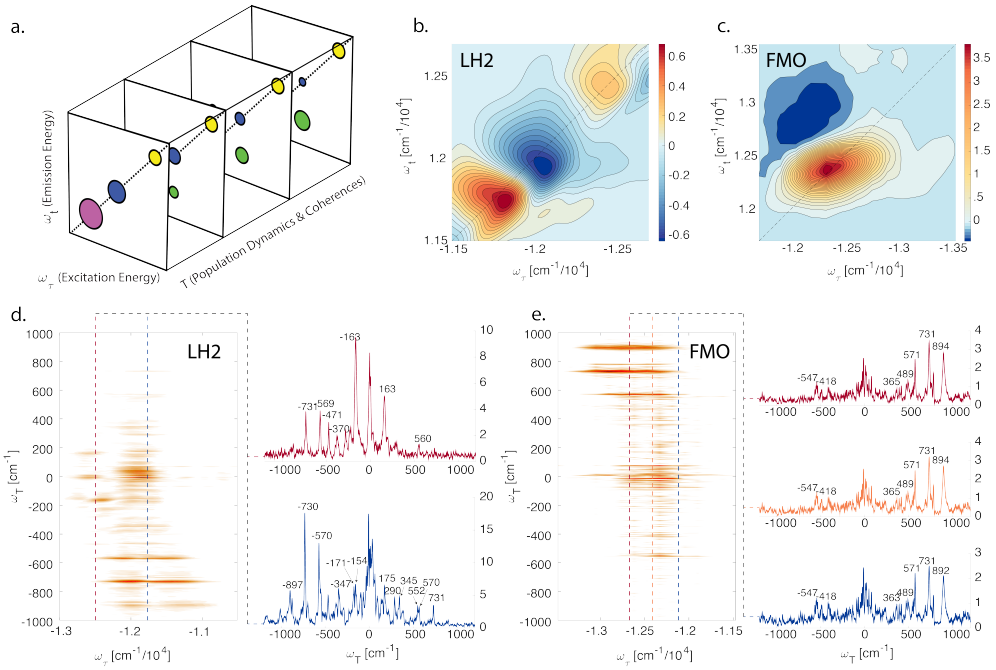

FIGURE 5.2: (a) Three-dimensional spectra have two dimensions corresponding to SQC and one to ZQC. The two SQC coherence axes are commonly interpreted as excitation and emission axes, while the ZQC reports on the energy of states within the single exciton manifold. Oscillations of the signal as a function of T can be Fourier transformed to obtain the ω_T axis. Excitation-emission plots at a fixed T are shown for (b) LH2 and (c) FMO. LH2's two positive peaks corresponding to B800 and B850 are spectrally separated, while FMO's positive feature is spectrally congested. Because the first pulse interacts with the system at equilibrium, resolving the vibrational frequencies over ω_τ allows for rough assignment of vibrations to a particular state. (d) For LH2, the two rings of pigments are considered distinct excitonic manifolds (with next neighbor coupling of 24 cm^{-1} for B800 and $\sim$300 cm^{-1} for B850) and have distinct coherence frequencies and intensities.[144] For FMO, where the chromophores form one excitonic manifold, there is no variation in coherence frequency or intensity along ω_τ. The two-dimensional plot is sliced along two ω_τ energies that correspond to B800 (red) and B850 (blue), and differences in coherence frequencies can be seen. (e) In FMO, the excitons interact with a uniform set of vibrations. The slices correspond to the energies of excitons 7 (red), 4 (orange), and 1 (blue) according to exciton energies extracted in ref [108]

integrated over the emission energy. The excitation axis indicates the electronic band to which the associated vibration is coupled. For LH2 (Figure 5.1(d)), a clear difference between the coherences after initial excitation of either B800 and B850 can be seen. While the pulse spectra may play a role in the relative intensities of the peaks, we observe that in our experiment, the intensity of the B850 band's ZQC peaks is higher than in B800, demonstrating a stronger transition moment to the vibrational states. Slices of the data at B800 (red) and B850 (blue) are shown to the right of the two-dimensional plot. Shifts in coherence energies demonstrate the non-uniform contribution of vibrations to the excitonic states for the two rings. In addition to peak shifts between B800 and B850, we observe that certain coherences split into two peaks. For example, the peak at -163 cm^{-1} splits into peaks at -171 and -154 cm^{-1}, and the peak at 560 cm^{-1} splits into peaks at 552 and 570 cm^{-1}. In stark contrast to LH2, FMO shows no such dependence of coherence amplitudes and frequencies on electronic excitation energy. The reference lines on which the slices are drawn along the energies for excitons 1, 4, and 7 in Figure 5.1(e) are according to ref [108]. Alternative explanations for the different coherences observed for different excitation energies are explored in Appendix C, but the conclusion is that these features likely arise from differences in the excited state excitonic landscape resulting from the interaction of the vibronic pigments and varied electronic J-coupling.

Our experiment establishes that the excited state coherences observed in the pigment-protein complexes originate from vibronic transitions. Furthermore, we find that the excited state coherences of the proteins may be slightly shifted relative those of the pigment. One of the largest differences between an isolated pigment and the protein is the presence of J-coupling, and so we focus our investigation on the interplay of J-coupling

and electron-vibrational coupling in electronic structure and kinetics. Gelin et al. recently tackled a similar problem by performing perturbative calculations for the effect of vibronic coupling on the basis that diagonalizes the J-coupling. This change of basis challenges the notion of localized pigment modes in J-coupled systems since delocalized electronic excitation may modify the effective coupling to pigment vibrational modes. This aggregate effect is described using a "generalized" Huang-Rhys factor.[6] We emphasize that the strength of coupling of an individual pigment's electronic state to its vibrations is not being modified, only that excited state vibrations can be modified by J-coupling so that the excitonic states have vibronic coupling strengths different from those of the individual pigment. Additionally, if the vibrations are treated nonperturbatively so that the eigenvalues of the entire J-coupled vibronic pigment Hamiltonian (details in Appendix C) are found, the energies of the vibrations may also be shifted relative to the vibrational energies in the individual pigment.

Because the effect of J-coupling is to modify the effective coupling strength of a set of electronic states to pigment vibrations, we aim to understand how this effect might influence rates of energy transport. Using a J-coupled vibronic dimer as an exemplary system whose vibronic states are treated nonperturbatively, we apply coherent modified Redfield theory (CMRT) to explore the broader implications of including specific pigment vibrations in the system Hamiltonian.[145] Specifically, we wish to know whether allowing each electronic state to have different effective coupling strengths to vibrational modes can have an effect on excitonic energy transport (EET). Figure 5.3(a) pictorially describes our model with two J-coupled vibronic pigments. The two excited electronic states, separated by an energy gap of 600 cm^{-1}, share a common ground state, and each linearly couples to a vibrational mode with a frequency ω_0 of 215 cm^{-1}. Each state contains two

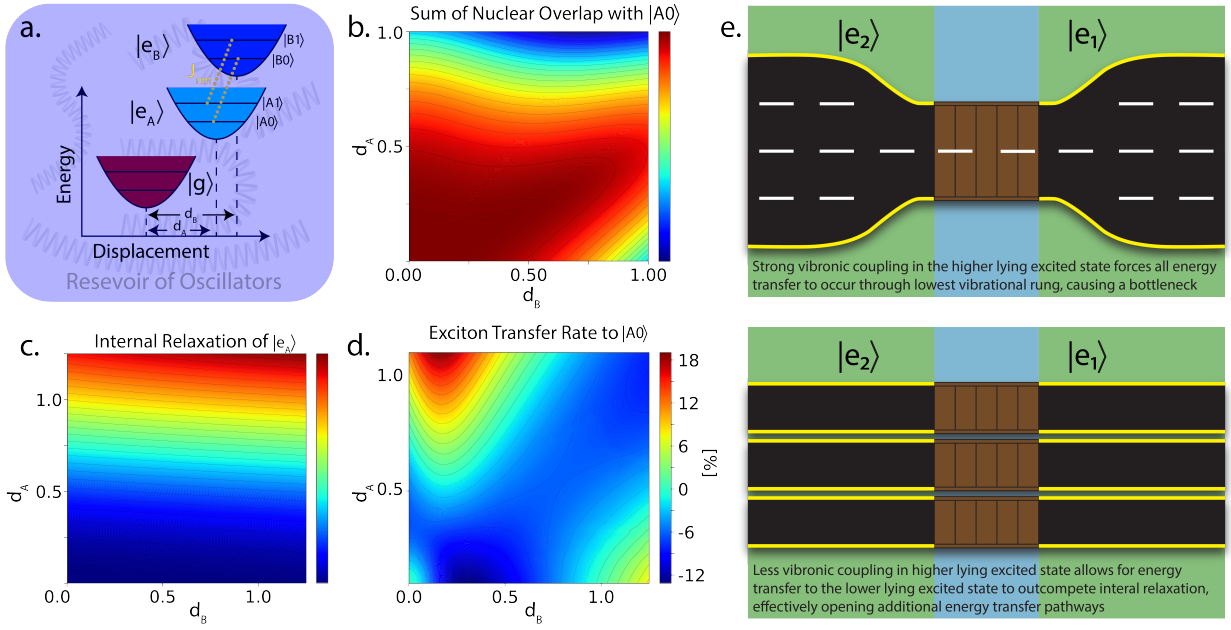

FIGURE 5.3: (a) Diagrammatic representation of the model used to investigate the role of a non-uniform vibronic landscape. The two electronic manifolds contain one vibration each, with the states enumerated as shown. The transfer rates are calculated using coherent modified Redfield theory for a distribution of displacements on the lower (d_A) and upper (d_B) manifolds. (b) Sum of the nuclear overlap of all excited states with $|10\rangle$ for different displacements. (c) Dependence of the internal relaxation of e_A on displacements. The rate is heavily dependent on the displacement of its own manifold but also weakly dependent on the displacement of the other manifold. (d) For an initial population evenly distrusted on the upper manifold, the exciton transfer rate to state A_0 is calculated. The relative rate enhancement is calculated relative to the $(0,0)$ point where there is no vibrational coupling on either manifold. While an enhancement region exists in the weak coupling regime (dA = dB = 0), similar to FMO's scheme, a rate enhancement for dA > dB exists, similar to LH2's strong vibronic coupling of the lower-energy B850 ring relative to the higher-energy B800 ring. (e) Having a large dB increases the internal relaxation within a manifold but as a result causes a bottleneck from the lowest vibrational rung. Instead, having low displacement in the donating manifold opens up additional energy transfer channels because internal relaxation does not out-compete energy transfer.

vibrational levels, one associated with the vibrational ground state and one associated with a single vibrational excitation. In the site basis, we enumerate the states in the single-exciton manifold as $|n\nu\rangle = |A0\rangle, |A1\rangle, |B0\rangle, |B1\rangle$ where the first index labels the electronic state and the second labels the vibration. We collectively refer to the states in the lower excited state $|A0\rangle, |A1\rangle$ as $|e_A\rangle$ and those in the upper state $|B0\rangle, |B1\rangle$ as $|e_B\rangle$. The coupling of mode ω_0 to excited state $A(B)$ is modeled using a displaced harmonic oscillator Hamiltonian controlled by the dimensionless linear coupling constant $d_{A(B)}$, which we will refer to as the displacement of excited manifold $A(B)$. Increasing displacement increases the coupling strength of the states within the vibronic manifold. Electronic states $|e_A\rangle$ and $|e_B\rangle$ interact with a linear coupling strength J of 60 cm^{-1}. Other work has used similar Hamiltonians and methods to explore the importance of the vibronic density of states, the relative energies of vibrational states, J-coupling, and the electronic energy gap between harmonic oscillators.[6, 133, 141, 146]

When considering a system with both intrapigment vibronic and interpigment J-coupling, it becomes necessary to isolate the effects of each before understanding their interaction. Previous work[147] has shown that vibronic coupling produces EET enhancement through increasing the number of transfer pathways with appreciable Franck-Condon nuclear overlap. Figure 5.3(b) shows this effect via a sum of the nuclear overlap for all states relative to the terminal state $|A0\rangle$. Maximum overlap occurs at low displacements because the two harmonic potentials are on top of each other. As displacements are increased, asymmetry arises because the contribution of overlap from states within the harmonic oscillator is much greater than overlap between oscillators. The overlap

drops for very high values of d_A because, although states $|A0\rangle$ and $|A1\rangle$ have considerable overlap, they fail to efficiently connect to $|e_B\rangle$. To maximize EET from this perspective, the ideal system would have uniform weak coupling to vibrational states so that excitation is directed downhill between electronic states.

Introducing J-coupling has a strong effect on excitation transfer as excitations are delocalized across pigments. To understand the dynamic evolution of our multilevel system, CMRT is used to calculate the rates of transfer among all excitonic states. CMRT has gained popularity in describing EET dynamics and has been shown to predict transfer rates in FMO and LH2.[147] A detailed description of the simulation can be found in Appendix C with the rates of transfer among all states shown. In Figure 5.3(c), we show the rate of aggregate transfer from state $|A1\rangle$ to $|A0\rangle$ interpreted as the internal relaxation between the states on $|e_A\rangle$. This rate is strongly dependent on d_A as expected when varying the coupling between the vibrational states, peaking at high values of d_A. It also shows a weak dependence on dB owing to the mixing between vibronic states in $|e_A\rangle$ with $|e_B\rangle$ due to J-coupling. Figure 5.3(d) shows the rate of excitation transfer to $|A0\rangle$ for an initial excitation delocalized equally between $|B0\rangle$ and $|B1\rangle$. Crucially, we notice that it exhibits a balance of the effects depicted in panels b and c of Figure 5.3. Because J-coupling can efficiently connect $|e_B\rangle$ to $|e_A\rangle$, the system maximizes d_A to take advantage of fast internal relaxation to move excitation from $|A1\rangle$ to $|A0\rangle$ Additionally, d_B should be kept low because internal relaxation in $|e_B\rangle$ is maximized for high d_B. High internal relaxation in $|e_B\rangle$ would bottleneck excitation in $|B0\rangle$ with fewer available vibronic pathways to reach $|A0\rangle$ as compared to using both $|B0\rangle$ and $|B1\rangle$ to reach $|A0\rangle$. The governing design principle in this model is for low d_B to suppress internal relaxation within $|e_B\rangle$ and to maximize the number of vibronic pathways to $|e_A\rangle$, while using high d_A to encourage fast internal

relaxation to bring excitation anywhere in $|e_A\rangle$ to $|A0\rangle$. In effect, $|e_A\rangle$ acts as a "vibronic sink" to funnel excitation from $|e_B\rangle$ to $|A0\rangle$.

Our experiment confirms that the LH2 and FMO long-lived excited state coherences originate from pigment vibrations, which are affected by J-coupling. We further demonstrate using modeling that in addition to simply modifying the electronic states, J-coupling can affect the coupling strength of phonons, which in turn may also affect EET. We hypothesize that the interchromophore J-coupling is the origin of the non-uniform vibrational modes of the different excitonic manifolds and that it has an effect on energy transfer. FMO's vibrational coupling to the excitons is uniform and weak, so that the conceptual understanding of mixed electronic states in a fixed spectral density holds. On the contrary, LH2's non-uniform vibrational coupling requires explicit consideration of the mixing of vibronic pigments. In our modeling, we find that having asymmetric vibronic coupling of different excitonic manifolds is beneficial, because internal relaxation can collect excitation from all transfer pathways and rapidly shuttle energy to the lowest-energy state. Our simplified model is a starting point for contextualizing our experiment, but we realize that EET dynamics of the fully modeled vibrationally dressed electronic states of FMO and LH2 may have additional complications.

How vibrational modes are treated, whether explicitly in the system Hamiltonian or lumped into a structured spectral density, while mathematically similar can lead to different conceptual understandings of transport efficiency. The strength of the system-bath interaction can be considered in two limiting cases. When system-bath coupling is much stronger than interstate coupling, energy transfer proceeds with thermalization at each step, resulting in the dissipation of energy from the system to the bath. In the opposite limit, if the interaction with the environment is weak compared to interstate coupling,

there is an absence of thermalization on the time scale of the transfer.[148] By moving the vibrational states from the bath to the system, we can explicitly track how energy moves through the vibronic states, rather than being lost to thermalization. Thus, strong vibronic coupling may enhance transfer efficiency because energy transferred to vibronic states is not permanently lost and still can reach the terminal state. Vibronic coupling can thus play a key role in quickly transferring energy before equilibration with the environment is realized.

5.4 Conclusions

Our study comparing the differences in design principles of two photosynthetic proteins built from the same pigment reveals two strategies for designing the vibrational landscape to complement the exciton states. We contended that LH2's excitonic states would best be described through *J*-coupling between vibronic pigments, and FMO is more amenable to be described as a system of electronic states uniformly interacting with a thermal bath of oscillators. In simulating a model system with non-uniform vibrational coupling, we find that strong vibronic coupling can act like an energetic funnel, collecting a broad distribution of energies and internally transferring it to the lowest-energy state with high efficiency.

5.5 Methods

Many of the data collection techniques can be found in previous work[99] but will be briefly covered here. The broadband coverage of the near-IR peaks of LH2 and FMO is achieved using a home-built second harmonic noncollinear optical parametric amplifier

(2H-NOPA)[149] pumped with a PHAROS fundamental pulse running at 200 kHz and compressed with chirped mirrors (Layertech 109347). The nDES photon echo signal is generated in the "BOXCAR" geometry by a series of three pulses and interfered with a local oscillator (LO) to create an interferogram that contains the amplitude and phase of the signal. The high-quality ZQC plots central to the paper are generated by collecting the entire data set in under 2 s, beating out much of the amplitude and phase noise. This is achieved by collecting the signal in the "GRAPES" configuration[150] in which the beams are focused to a line instead of a point, which allows the spatial tilt between beams to encode a time delay between pulses 1 and 2. Pulse 3 is parallel to 2, so the delay between the pulses can be scanned with a stage. We use the Newport XPS stage system to output that triggers the camera at preset locations without stopping. Running an Andor Xyla 5.5 high-speed CMOS camera at 650 Hz allows us to complete a $128 \times 916 \times 2560$ pixel scan in <2 s. The signals are collected in the time domain but are Fourier transformed to the frequency domain. For this work, the early time points (<200 fs) along τ are apodized by a hanning window to ensure contribution from only the rephasing pathway and early time points along T are not considered to focus on the vibrational coherences.

Throughout this work, and especially in the modeling, we try to adhere to specific terminology. When referring to an electronic state and its associated vibrational modes, we are denoting the site basis. This means that the diagonal terms of the Hamiltonian are the energies of the pure states while the off-diagonal terms (which are related to the Huang-Rhys factor and displacement) inform us about the strength of coupling between the electronic and vibrational states. If we were to diagonalize this Hamiltonian, the eigenvalues would be the energies in the vibronic basis. Each vibronic state is some linear combination of the electronic and vibrational states. Because these vibronic states are

the observables in our measurement, it makes the most sense to call the ZQCs observed in BChl*a* "vibronic". Because we know there is only one electronic state observed in BChl*a*, the observed ZQCs can readily be assigned to vibrations of the pigment.

Coulombic *J*-couplings between electronic states similarly are off-diagonal elements of the Hamiltonian in the site basis, but this time between electronic states and not between electronic and vibrational states. If this Hamiltonian were to be written in the vibronic basis, it would appear that the vibronic states would be coupled to each other, due to the fact the vibronic states have some contribution from the pure electronic state. We refer to the observable eigenvalues of this *J*-coupled vibronic system as the exciton basis. Coherences of FMO and LH2 both are between excitonic states, which are delocalized excitations between the electronic and vibrational states of multiple pigments. Thus, our observation of coherences in FMO and LH2 having energies similar to those of the vibronic coherences in BChl*a* inform us only that the protein coherences are primarily vibronic in origin but still are excitonic coherences. *J*-coupling can change the intensity of the excitonic coherences without the vibronic coupling strength of an individual pigment needing to be modified.

Semiconductor Nanocrystals

Adapted from: **Irgen-Gioro, S.**; Yang, M.; Padgaonkar, S.; Chang, W.J.; Zhang, Z; Nagasing, B.; Jiang, Y.; Weiss, E.A. Charge and Energy Transfer in the Context of Colloidal Nanocrystals *Chem. Phys. Rev.*, **2020** 1 (1), 011305

6.1 Energy and Charge Transfer in Semiconductor Nanocrystals

We switch our attention from photosynthetic complexes where our conception of collective quantum states are combinations from pigment electronic states and move onto semi-conductor nanocrystals, which have delocalized electronic states that are confined the spatial boundaries of the nano-scale crystal. As the number of hybrid systems comprising quantum-confined semiconductor nanocrystals and molecules continues to grow, so does the need to accurately describe interfacial energy and charge transfer in these systems. The earliest work often successfully captured at least qualitative trends in the rates of these processes using well-known results from Förster, Dexter, and Marcus theories, but recent studies have showcased how unique properties of nanocrystals drive interfacial energy transfer (EnT) and charge transfer (CT) to diverge from familiar trends. This

chapter first describes how the nanocrystal-ligand system fits, at least superficially, into conventional models for EnT and CT, and then gradually introduces individual properties of nanocrystals that complicate our understanding of EnT and CT mechanisms. The chapter then explores instances in which features of nanocrystals that seem detrimental, such as trap states that introduce non-radiative recombination pathways and strong spin–orbit coupling, can be controlled or used synergistically to produce a wider range of functionality than available in all-molecular donor-acceptor systems.

6.2 Background

In this chapter, we examine the progress in developing a meaningful framework and formalism for describing the dynamics of interfacial energy transfer (EnT) and charge transfer (CT) between colloidal semiconductor nanocrystals—including zero-dimensional quantum dots (QDs) and quasi-2D nanoplatelets (NPLs)—and molecules adsorbed to their surfaces. In recent years, research in the nanocrystal field has extended beyond probes of intrinsic electronic and optical properties into engineering of hybrid inorganic-organic colloidal systems, and use of these hybrid systems in energy harvesting, sensing, quantum information, and photocatalysis. The language typically used to describe the static and dynamic interactions across the inorganic-organic interface of QD-molecule systems is adopted from well-established theory in molecular systems. Swapping molecular donor or acceptor wavefunctions with effective wavefunctions for QDs, these traditional models have had success in predicting EnT/CT rates in many cases. Features that differentiate quantum-confined semiconductors from most molecules—such as the ability to accommodate multi-excitons and charged excitons (trions), and the large spin–orbit coupling—conspire to produce mechanisms absent in the all-molecular picture and

requires us to consider EnT and CT pathways that involve more than the orbitals on the initial donor site and the final acceptor site. Instead of trying to minimize this complexity and forcing QD behavior to conform to established molecular models, one can leverage it to enable function not possible with all-molecular architectures.

This chapter aims to highlight ways that QDs serve as donors and acceptors in EnT and CT processes, often through processes that bypass the pathway mediated by "direct coupling" between the orbitals of the band edge exciton of the QD and the frontier molecular orbitals. We build upon previous reviews and comprehensive textbooks written on EnT and CT in semiconductor and molecular systems[151–154] as well as research on QD electronic structure,[155–158] surface ligands,[159–163] and exciton dynamics[164–167] to focus on cases in which EnT and CT proceed in spite of relatively weak direct electronic coupling between donor and acceptor wavefunctions. We also consider phenomena such as Auger mediated electron transfer, trap mediated energy transfer, and surface mediated photocatalysis as examples of how experiment can push theory to evolve.

The chapter is written in three parts, Scheme 6.1. Section 6.3 sets the foundation for the formalism used throughout the chapter and establishes how coupling between donor and acceptor states is typically described. Section 6.4 introduces features of QDs that distinguish them from molecules and explains how these features can mediate and influence EnT and CT. Section 6.5 describes how the features described in Sec. 6.4 interact with each other and can be utilized synergistically. Overall, rather than wrangling the QD-ligand system into trends predicted by the direct coupling scheme introduced in Sec. 6.3, a more holistic theoretical understanding of their electron dynamics combined with recent advances in synthetic control will, we believe, allow for the creation of QD-molecule complexes with greater function than that of the sum of its parts.

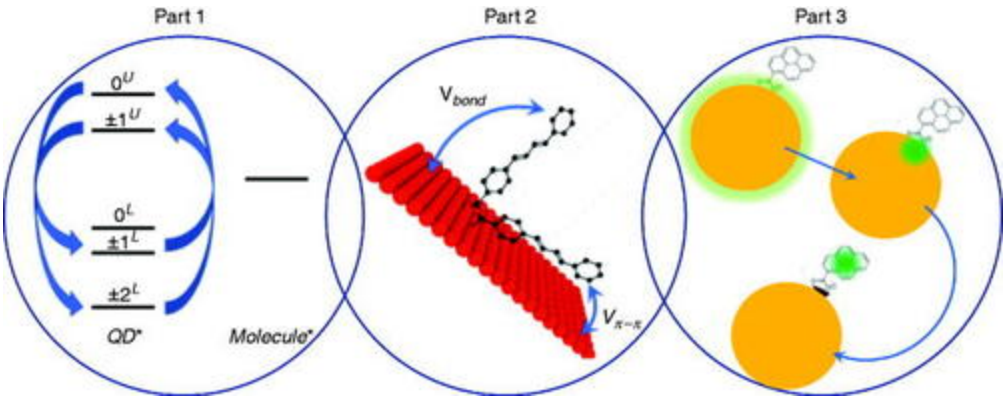

FIGURE 6.1: Images representing the three sections of this chapter. Section 6.3 introduces the electronic structure of excitonic states of QDs. Section 6.4 describes how the contributions of semiconductor character to QDs influence their electron dynamics and interactions with molecules. Section 6.5 illustrates how certain electronic, chemical, and structural features of QDs combine to produce unique photophysical phenomena.

6.3 Formalism of Energy and Charge Transfer and Relevant QD Electronic Structure

In modeling any dynamic process, one of the principal strategies is to treat only a fragment of the system in detail. This strategy underlies, for example, the separation of the electronic and nuclear Hamiltonians in the Born-Oppenheimer approximation, reduction of the number of electronic states considered in describing energy transfer, or description of electron transfer from the perspective of one electron subject to an effective potential. When decomposing a system into fragments, a careful dissection of the system may yield a mostly orthonormal basis set such that the electronic wavefunction describing each fragment does not overlap $\langle \phi_m | \phi_n \rangle = \delta_{mn}$. The single electron energies E_m corresponding to these wavefunctions ϕ_m are sometimes called "site" energies and wavefunctions, respectively. In descriptions of electron and energy transfer, this partitioning results in "donor" and "acceptor" sites, which, in the QD-ligand hybrid system, typically are assigned to the

nanocrystal core and organic ligand, respectively. We shall see later that ligands have the potential to strongly mix with QD surface states, complicating this description, but for the photoinduced charge/energy transfer described directly below, we assume a weak electronic coupling between QD excitons as the "donor" sites and ligand molecular orbitals as "acceptor" sites. If we further limit our discussion to cases in which Fermi's golden rule, $w_{nm} = \frac{2\pi}{\hbar}\rho(E_m)|V_{nm}|^2$, applies (in addition to weak electronic coupling, long time of interest $\tau >> [(2\pi\hbar)/(E_n - E_m)]$, second-order perturbation theory), in principal any energy or charge transfer rate can be calculated with knowledge of the density of states ρ and the matrix element $|V_{nm}| = |\int \Psi_n H \Psi_m d\tau$. Marcus,[168, 169] Dexter,[170] and Förster[171] theory are versions of Fermi's golden rule[151] adapted for calculating electron and energy transfer rates, respectively. Here we use EnT to demonstrate how the V matrix is applied. Other examples of how this formalism can be applied to other forms of exciton dynamics can be found in these useful works.[172, 173] To calculate $|V_{nm}|$ between two equivalent two-level systems, the wavefunctions for representing possible electron configurations can be expressed as:[174]

$$^{1,3}\Psi_1 = \left(|da\bar{d'}\bar{a}| \pm |d'a\bar{d}\bar{a}|\right)/\sqrt{2}, \quad ^{1,3}\Psi_4 = \left(|da\bar{d}\bar{a'}| \pm |da'\bar{d}\bar{a}|\right)/\sqrt{2}$$

$$^{1,3}\Psi_2 = \left(|da\bar{a'}\bar{a}| \pm |a'a\bar{d}\bar{a}|\right)/\sqrt{2}, \quad ^{1,3}\Psi_3 = \left(|ad\bar{d'}\bar{d}| \pm |d'd\bar{a}\bar{d}|\right)/\sqrt{2}$$

and shown schematically in Fig. 6.2. |...| denote Slater determinants, superscripts denote the spin multiplicity, d/a represent the orbitals of the donor/acceptor, d/a are corresponding excited orbitals, and the short bar over an orbital indicates an opposite spin. For the case of EnT, when the donor and acceptor are different species, the initial (R = reagent state) and final (P = product state) wavefunctions can be expressed as a linear

combination of $\Psi_1 \sim \Psi_4$.

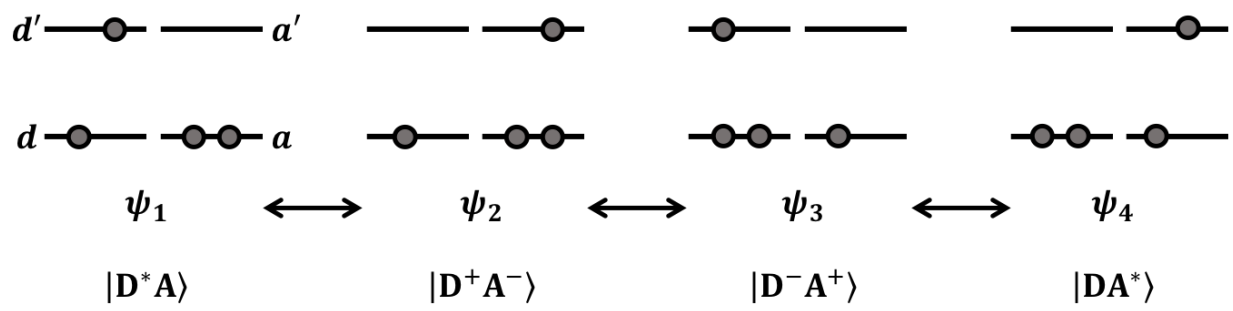

FIGURE 6.2: Wavefunctions of electron configurations of 2-level system. D = donor, A = acceptor.

The electronic coupling term in the Hamiltonian can be written as[175]

$$H_{RP} = \langle |dd'aa||H||ddaa'| \rangle = \underbrace{2(dd'|aa')}_{1} - \underbrace{2(d'a'|ad)}_{2} + ...$$

where term 1 is the Coulombic interaction between the charge transition densities of the donor (dd) and the acceptor (aa), as in Förster theory. Within the dipole-dipole approximation, the electrodynamic interaction can be calculated using the transition dipole moments of the donor and the acceptor. The second term is the "Dexter" term that originates from exchange interactions between donor and acceptor sites and accounts for the indistinguishability of the electrons in many-electron wave functions. The first term decays as R^3, and the second term scales with orbital overlap between the donor and acceptor sites as $e^{-\alpha R}$, where R is the distance between the centroids of the donor and acceptor localized wavefunctions. The Dexter term therefore is more steeply attenuated with respect to the donor-acceptor separation than is Term 1. Dipole-forbidden or spin-forbidden energy transfer processes, including triplet-triplet energy transfer (TTEnT), can be formulated as

a special case of the general energy transfer presented in the equation above, with the key distinction that the exchange integral dominates[170] because the low charge transition density (*aa*) of the molecular acceptor's triplet state minimizes coupling of transition moments to any of the exciton fine states of the QD.[176]

The direct exchange coupling mechanism, which is proposed to mediate TTEnT from CdSe QDs to adsorbed acene ligands, does not straightforwardly account for indirect mechanisms involving intermediate states, such as a charge-transfer pathway observed for QD-to-molecule TTEnT in other systems.[177, 178] Even for systems where no spectroscopic signatures from radical ion intermediates are observed, charge transfer states may still play a role in TTEnT. Lessons from electron transfer and singlet fission in all-organic systems teach us that even if "real" charge separated intermediates are never populated, "virtual" charge transfer states need to be considered as an additional superexchange coupling pathway.[179–181]

In principle, the electronic coupling matrix can be calculated, but in practice, the results depend drastically on the choice of donor and acceptor wavefunctions. Applied to calculating EnT and CT rates of QD-ligand systems, states localized on the ligand are typically described using molecular orbitals, but descriptions of the QD exciton wavefunctions range from effective mass models[155, 158] to more accurate but computationally expensive tight-binding models[182–185] and atomistic approaches.[186–190]

The popularity of the effective mass model stems both from its intuitive explanation of the effect of QD size on its optical spectra and its ease of modification to include interactions such as spin–orbit coupling, crystal field splitting, electron-hole exchange, and electron–phonon coupling.[155, 191–193] The effective mass model describes a carrier's motion under a periodic lattice potential and quantum confinement. The wavefunction is written as

a product of the Bloch wavefunction, representing the contribution from crystal structure, and an envelope wave function, accounting for the confinement. The envelope function is expressed as a product of the spherical Bessel j_L (the n-th root $\psi_{n,L}$) and spherical harmonic $Y_{L,M}$ functions, which introduce a series of discrete energy bands represented by the three quantum numbers n, L and M. We can further simply the problem using the "single band approximation," which assumes weak interactions among QD bands. The result is energies of individual electron/hole levels of $E_{n,L} = \frac{\hbar^2 \psi_{n,L}^2}{2mR^2}$, where R is the radius of the spherical QD and $m = m_e$ or m_h. The single band effective mass model yields a bandgap energy (E_g) that is modified from the bandgap of the bulk semiconductor ($E_{g,0}$) as

$$E_g = E_{g,0} + \frac{\hbar^2 \pi^2}{2m_{e,h}R^2}$$

where $m_{e,h} = \frac{m_e m_h}{m_e + m_h}$ is the reduced electron-hole mass. For QDs with small size, the confinement energy is much larger than the electron-hole binding energy. Consequently, the Coulomb electron-hole interaction can be treated as a perturbation to the single band effective model, adding a correction term to the bandgap energy $\Delta_{e,h} = \frac{-1.765e^2}{\epsilon_{\text{inf}} R}$.

The single band effective mass model serves as an excellent starting point, but it fails to explain certain experimental observations that require a more exact treatment of interband coupling, such as temperature-dependent absorption and emission of QDs. Furthermore, as energy levels become more closely packed, for example in the valence band of CdSe QDs (where $m_h = 2.3m_e$), interband coupling becomes too strong to neglect, and the multiband effective mass model is a better description. In the multiband model, the total momentum quantum number (F) is used to describe QD energy levels: $F = J + L$,

where J is the angular momentum of the envelope function, and L is the angular momentum of the Bloch function. The hole states are represented by a notation such as $1S_{3/2}$, where the lower of J and L is the S, P, D... state, and F is written in the subscript. For CdSe, the lowest energy valence band is a P-type orbital ($L = 1$), which is split by spin–orbit coupling ($\Delta_{SO} \sim 400$ meV) into a twofold degenerate $J = 1/2$ band and a fourfold degenerate $J = 3/2$ band.

A band edge exciton of a CdSe QD comprises an electron in the $1S$ conduction band and a hole in the $1S_{3/2}$ valence band, leading to a 2×4 = eightfold degenerate set of states. As shown in Fig. 6.3, this degeneracy is lifted by a hierarchical series of terms (in decreasing order of interaction strength): crystal field splitting, electron-hole exchange, and electron-phonon coupling. Specifically, the anisotropic crystal field splits the $1S_{3/2}$ hole states into light ($|J_m| = 1/2$) and heavy ($|J_m| = 3/2$) holes. The magnitude of the crystal field splitting depends on the composition, crystal structure, and shape anisotropy of the nanocrystal. Electron-hole exchange further lifts the degeneracy for the J_m states.

Excitons formed by combining the $S = \pm 1/2$ electrons and $J_m = \pm 3/2$ hole states have total angular momentum projections $|N_m| = 1$ and 2. Since the orbital angular momentum of a single photon is 1, optical transitions of the $|N_m| = 2$ exciton are dipole forbidden; this exciton is therefore generally known as a dark exciton (DE), and the $|N_m| = 1$ exciton is known as a bright exciton (BE). Since the electron and hole quantum numbers need to be of the same sign (thus having parallel spins) in order to combine to $|N_m| = 2$, the DE has triplet-like character, while the anti-parallel spins of the BE give it singlet-like character. Due to strong spin–orbit coupling in QD, spin is however not a "good" quantum number and transitions between exciton states amount to an exciton fine structure relaxation

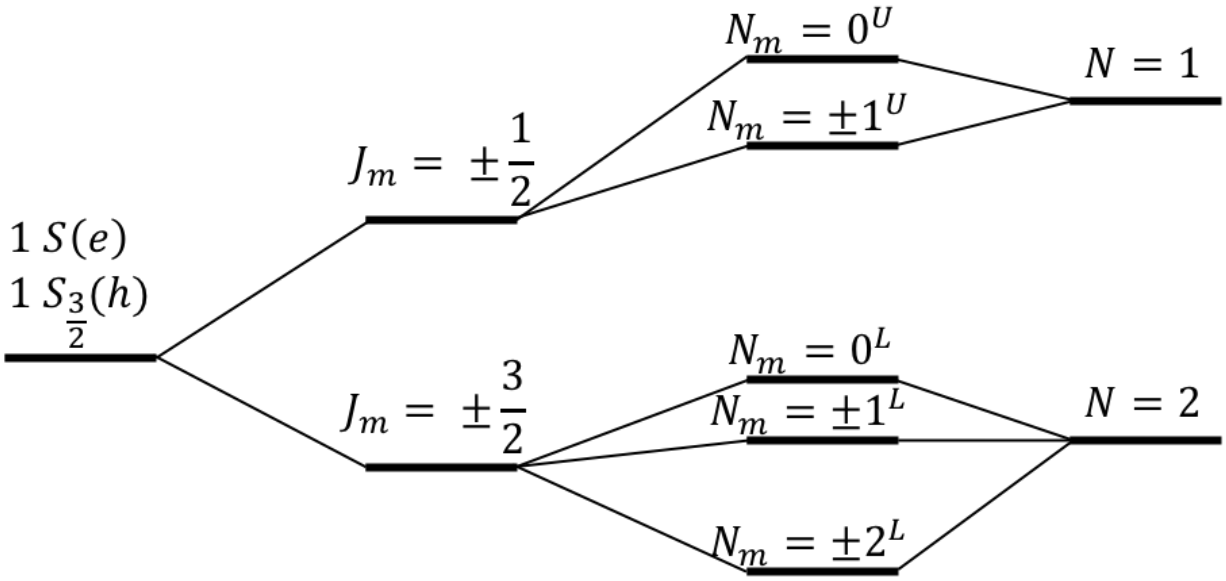

FIGURE 6.3: Lifting of degeneracy of exciton states through crystal field splitting, electron-hole exchange to form excitons with different total angular momentum $N = 1, 2$ (bright and dark excitons, respectively)

(EFSR) problem in which the total angular momentum quantum number N is considered. In calculating EFSR rates, the coupling matrix is composed of two terms.[194] The first is the exciton–phonon coupling term, which describes the nonadiabatic coupling of the electronic states when the geometry is displaced from the equilibrium. This term is responsible for the nonradiative relaxation with no change in spin multiplicity. The second is the spin–orbit coupling term that leads to intersystem crossing.

Even the multiband effective mass model has its limitations, mostly because it fails to capture the atomistic features of the QD. For example, dangling bonds can introduce mid-gap trap states, and surface ligands modify the electronic structure of the core.[195] Atomistic approaches, such as the pseudopotential method,[188] tight-binding model,[196] or ab initio approaches, have been successful in incorporating some of this complexity into the QD's electronic structure.[197] Of course, if these effects do not greatly modify EnT/CT

rates, then the effective mass model is sufficient to describe the QD portion of the donor-acceptor system. As described in Secs. 6.4 and 6.5 of this chapter, recent experimental observations have required theorists to move beyond this simplistic picture.

6.4 How QD Features Affect Energy/Charge Transfer in QD-Molecule Systems

In Sec. 6.3, we sketched out some formalism for the simplest cases of EnT and CT, which occur through direct coupling of QD exciton states and ligand molecular orbitals. There are numerous examples where this description is sufficient to capture the dynamics of EnT/CT. For example, Kodaimati et al. demonstrated that at distances greater than ∼4 nm, EnT rates between QDs can be accurately predicted by Förster theory.[198] Complications arise when multiple coupling pathways are active, which is often the case for EnT/CT to ligands on the QD surface. Although the potential for a variety of EnT/CT processes expands the capabilities of QDs, competing kinetic pathways and involvement of virtual or real intermediate states muddles predictions of net EnT/CT rates. Additional considerations specific to nanomaterials such as dimensionality and the intermolecular structure of self-assembled ligands may require explicit treatment. In this section, we explore examples of how unique properties of QDs affect EnT/CT with a special emphasis on how an understanding of numerous interacting pathways is necessary to understand EnT/CT in QD-ligand systems.

6.4.1 Exciton fine structure dynamics

Many studies that leverage QDs as energy/charge donors occur at room temperature and as a result do not consider the influence of intra-band transitions among thermalized exciton states, especially among states of different spin multiplicity, on EnT/CT dynamics. This simplification is valid for most all-molecular cases since the rate of intersystem crossing is so slow that it does not compete with EnT/CT between donor and acceptor. In contrast, a QD's fast spin-flip rates along with the non-uniform coupling of excitonic sublevels to acceptor states may influence ultrafast CT/EnT dynamics since transitions within the exciton manifold may become a rate limiting step. If we start by only considering the $|N_m|$ = 1 and 2 exciton states (BE/DE) and a molecular acceptor state, it is clear that the electronic coupling of the BE/DE with the molecule will differ due to the differing transition dipole moments of the BE/DE and differences in exchange integrals, so that direct EnT/CT will preferentially proceed through one of these states.

In order to understand which cases of EnT/CT require explicit consideration of the QD's spin-flip dynamics, the timescales of these dynamics must be established. In the most studied QD systems, spherical CdSe QDs, temperature- and magnetic field-dependent measurements of the radiative lifetime constitute some of the earliest evidence of multiple emitting states of QDs and provide a straightforward method to extract BE/DE transition rates.[199] For small (<2 nm) QDs with a single zero phonon line emission at 2 K, the measured radiative lifetime is ∼70, and 20 ns at 140 K. This observation is rationalized in a three-state kinetic model, shown in Fig. 6.4. At low temperatures, the BE does not emit before the state is depopulated by transition to the DE, so all emission is from the DE with a long radiative lifetime.[200] For larger QDs, spin-flip rates have

been reported to be an order of magnitude slower, allowing for low temperature emission from the BE before the spin-flip can occur.[201] The temperature dependence of the spin-flip rate has been modeled by Lounis et al. using the same three-state model as a product of the zero temperature spin-flip rate, γ_0, and the Bose-Einstein phonon number, $N_B = 1/[exp(\Delta E/k_B T)1]$, at temperature T where ΔE is the energy splitting between the BE and DE, which can range from 1 to 20 meV depending on QD size.[202] Since γ_0 is reported to be between 1 and 10 ns^1, and $k_B(T = 300K) \sim 25meV$, room temperature spin-flip lifetimes range from $\sim$1 to 500 ps, well within the range to affect EnT/CT dynamics. At room temperature, cross-polarized transient grating experiments have demonstrated that this ps-timescale spin-flip is attributed to hole flips, while electron spin-flips occur on a nanosecond timescale.[203] These disparate timescales have enabled control of the spin polarization of radical pairs produced upon photoinduced charge transfer in QD-molecule systems. For instance, Wu et al. generated the same charge separated species by excitation of the QD followed by a hole transfer to an alizarin surface ligand, or excitation of the ligand followed by an electron transfer to the QD.[204] The electron/hole transfer was slower than the hole spin-flip but faster than the electron spin-flip, so the radical pair generated by electron transfer was an overall singlet and the radical pair generated by hole transfer was an overall triplet.[205]

6.4.2 Triplet Triplet Energy Transfer (TTEnT)

The electron-hole exchange interaction creates well-separated singlet and triplet states in molecules and correspondingly lifts the degeneracy of bright and dark exciton states in QD. Although spin–orbit coupling and exciton–phonon coupling result in all exciton states having finite singlet and triplet character, the net result is that dark excitons

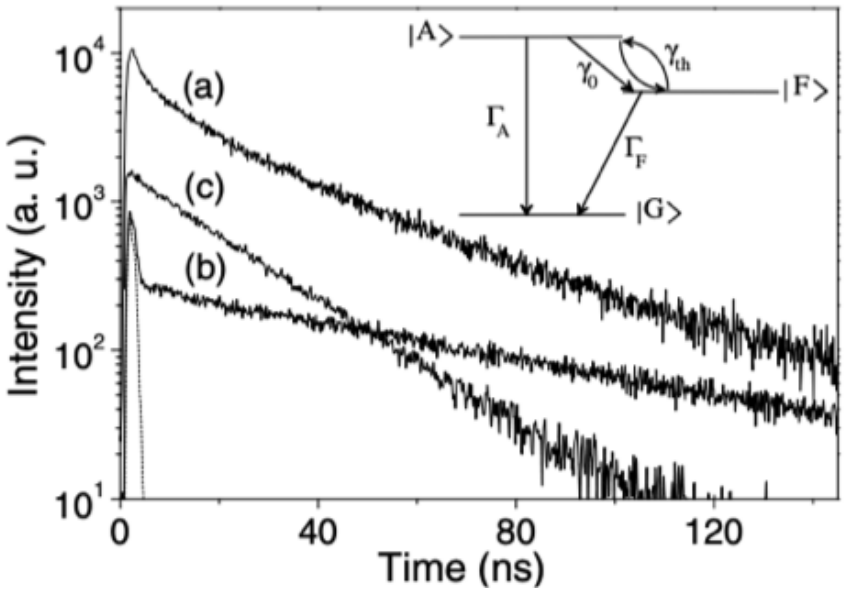

FIGURE 6.4: Emission decay dynamics from CdSe/ZnS QDs with various temperatures. The dark exciton-like decay was observed from a single QD with 16 *K* (b), compared to a single QD emission decay with 140 *K* (c). (a) is the ensemble emission decay spectra at 16 *K*. Reproduced with permission from Labeau et al., Phys. Rev. Lett. 90, 257404 (2003). Copyright 2003 American Physical Society

nonetheless still have mainly triplet character.[182] Direct TTEnT occurs through the Dexter exchange mechanism, and the spin angular momentum is conserved in the transfer process, so it is not surprising that QDs, with rapidly populated dark excitons, are effective triplet donors/acceptors for a variety of applications, including harvesting of triplets generated from singlet fission and photochemical upconversion.[178, 206–208] QDs also offer a significant advantage as photosensitizers/photocatalysts for triplet excited state organic transformations due to tunable exciton energies, relatively narrow linewidths allowing for high selectivity, and negligible singlet-triplet splitting, which yields the highest possible triplet sensitization energy among visible-light-driven sensitizers (up to 3.26 eV).[177, 209]

The presence of both singlet-like and triplet-like sublevels of QD excitons (all within k_BT) limits the yield of TTEnT and complicates mechanistic interpretation, especially in cases where the excitons may also serve as precursors for redox reactions and Förster-type singlet-singlet EnT, and/or serve as acceptors for back EnT/CT (from molecule to QD).[210] Sometimes these pathways work cooperatively. For instance, in QD-BODIPY (4,4-difluoro-4-bora-3a,4a-diaza-s-indacene)-pairs, FRET (Förster Resonance Energy Transfer) and CT pathways outcompete TTEnT, but the FRET pathway results in some yield of the 3[BODIPY]* state as shown in Fig. 6.5. The FRET sensitized 1[BODIPY]* transfers an electron back to the QD, forms a charge separated state in which a spin-flip event occurs, and spin-conserving charge recombination results in 3*[BODIPY]*.[211] The myriad of pathways for generation of molecular triplets from QD donor states complicates predictive theory, but also presents opportunities for creative design of systems for triplet-triggered photocatalysis, photon upconversion, and even quantum information.

6.4.3 Dimensionality and Anisotropy

Advances in colloidal synthesis have expanded the scope of colloidal nanocrystals to include 1D nanorods/wires and 2D nanoplatelets (NPLs) in addition to 0D QDs. The changes in nanocrystal shape introduce new knobs to tune EnT/CT between nanocrystals and molecules via modification of both the density of states and coupling strength in Fermi's golden rule.

Since the density of electron/hole states changes from discrete states in 0D quantum dots to the sawtooth-like quasi-continuum in 1D nanorods, to the step-like quasi-continuum in 2D NPLs, modifications to both the overall rate and the distance dependence of EnT/CT can be observed. As mentioned in Sec. 6.3, EnT between two transition dipoles results in a

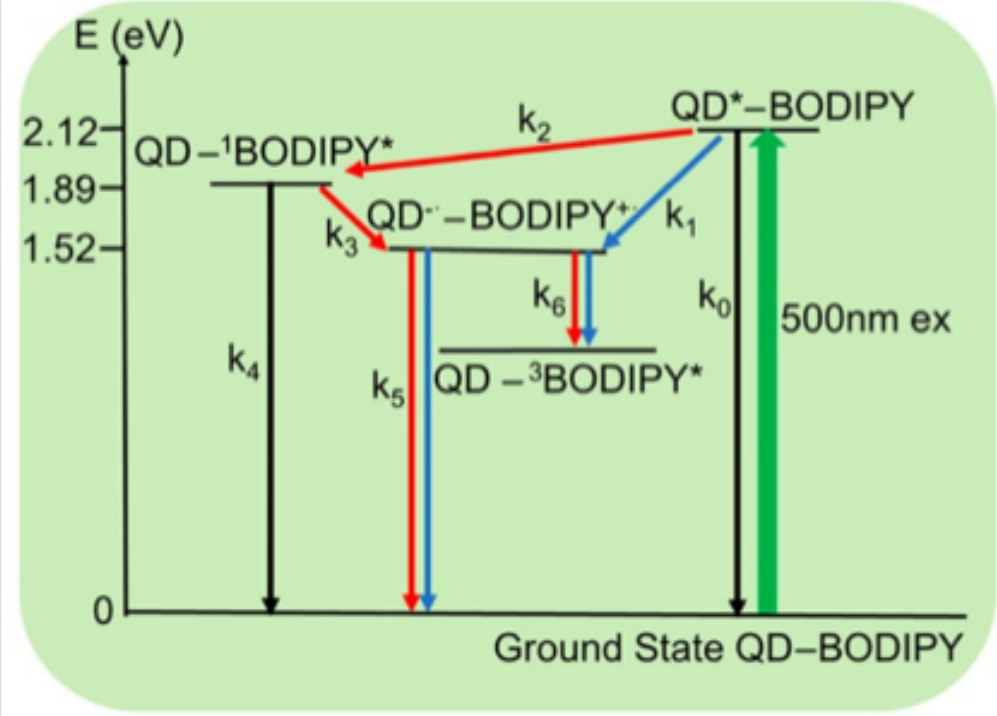

FIGURE 6.5: The efficient molecular triplet states generated through FRET, back electron transfer, and charge recombination, circumventing direct TTEnT between QD and ligand. Reproduced with permission from Jin et al., J. Chem. Phys. 152, 214702 (2020). Copyright 2020 AIP Publishing.

matrix coupling element that is proportional to R^3, so that the overall rate of transfer goes as R^6, but systems with a quasi-continuous density of states modify that dependence. Treating 2D materials as an assembly of incoherent point-like dipoles, these extensions of FRET unlock the possibility to control EnT distance by tuning nanocrystal shape.[212] For example, the interaction between a 0D donor such as pyrene or a CdSe QD and a 2D acceptor like graphene (or 1D carbon nanotubes) yields a distance dependence of Förster-type EnT rate of R^4 (or R^5).[213–215] When 2D materials are utilized as both the donor and the acceptor, the EnT rate scales as R^{-2}. Such shallow distance dependencies have led to intriguingly long Förster radii: 33 nm in the case of EnT from CdSe/CdS NPLs to

a monolayer of MoS_2.[216] The control over density of states similarly allow for modification of the overall EnT/CT rates at a fixed distance.[217] Brumberg et al. measured electron transfer rates across the interfaces of nanocrystal films (0D QDs and 2D NPLs) and found that the fastest electron transfer rate observed was at the NPL-NPL junction, due to its large orbital overlap and large density of acceptor states.[218] Conversely, the CT rate from an NPL donor and a molecular acceptor was smaller than that for a QD donor and molecular acceptor, because the increased delocalization of the exciton within the large lateral area of the NPL decreased the percentage of the wavefunction that overlapped with the acceptor [Fig. 6.6(a)].[219]

Anisotropic confinement in nanocrystals further affects EnT and CT dynamics through the spatial orientation of the transition dipole, tuning the matrix coupling element in Fermi's golden rule. For instance, films of CdSe NPLs have vastly different photoluminescence (PL) lifetimes when aligned face-to-face vs edge-to-edge, due to the additional orbital overlap and the coupling of in-plane transition moments induced by face-to-face stacking [Fig. 6.6(b)].[220] In studies where NPLs are energy acceptors from 0D QDs, NPLs that are stacked face-to-face have a 50% enhancement in FRET yield compared to edge-to-edge stacked NPLs.[221] The spatial orientation of the excitonic wavefunction within a nanocrystal also influences its electronic coupling to ligands. In photocatalytic Pt-CdSe nanorods, the rate of electron transfer to Pt (the catalyst) on the nanorod tip is a factor of 20 slower than to Pt randomly adsorbed along the length of the nanorod.[222] Given the number of properties in 1D and 2D materials that supersede or deviate from those observed in 0D QDs, it is likely that closer examination and modeling of these low-dimensional materials and their mixed-dimensional systems will unlock even more

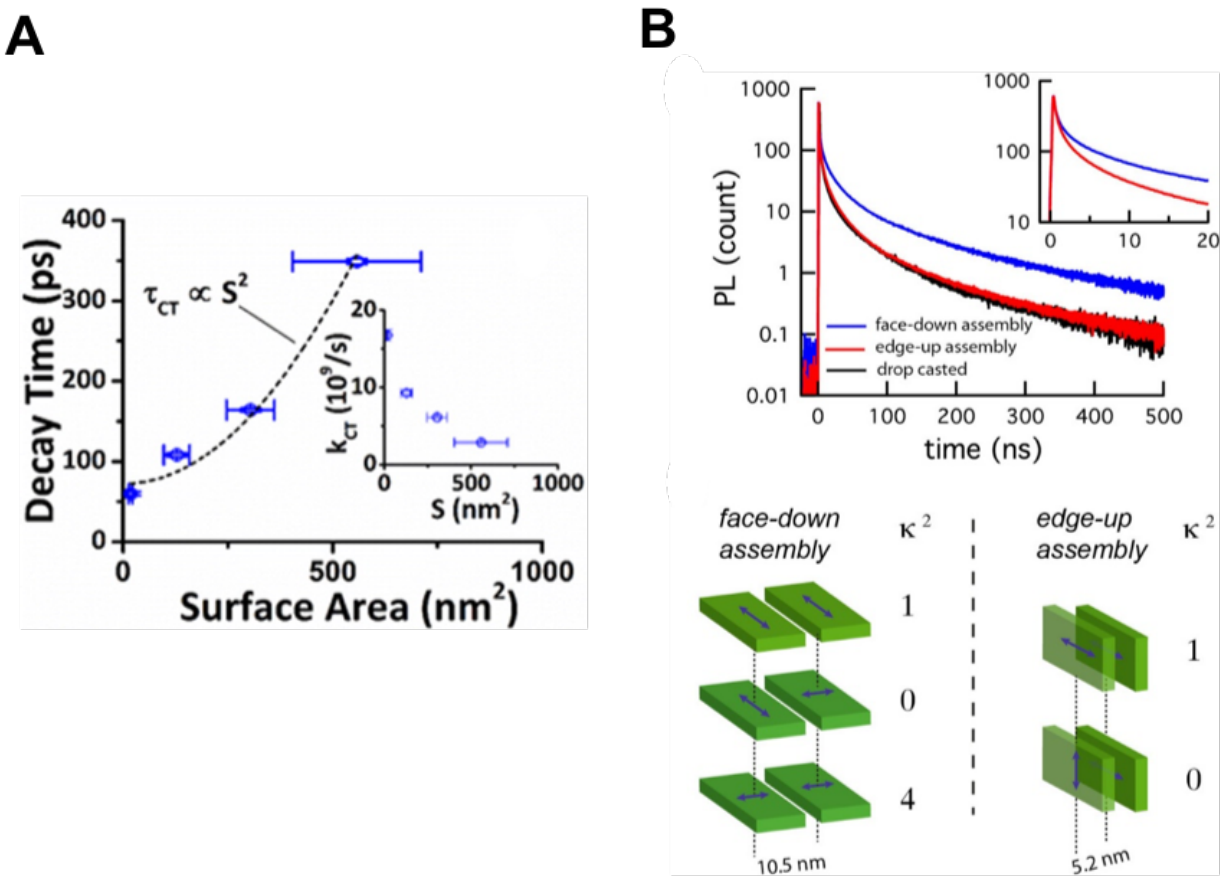

FIGURE 6.6: (a) Inverse dependence of electron transfer rate to NPL surface area. Reproduced with permission from Diroll et al., J. Am. Chem. Soc. 138, 11109 (2016). Copyright 2016 American Chemical Society. (b) PL lifetime of NPL is dependent on its orientation. Reproduced with permission from Goa et al., Nano Lett. 17, 3837 (2017). Copyright 2017 American Chemical Society.

emergent behavior for energy harvesting, photocatalytic, and other light-driven applications.[223]

6.4.4 "Hot" Exciton Relaxation

When attempting to truncate the series of states to consider in modeling an EnT/CT process, it is often assumed that internal relaxation within a donor manifold occurs before EnT/CT occurs. In molecular systems, "hot" carriers quickly thermalize through vibrational relaxation and/or internal conversion to the lowest energy transition so that only the lowest energy transition is considered. In quantum-confined systems such as QDs, carrier cooling via this mechanism is thought to be restricted due to the quantization of exciton energy levels with separations greater than the available phonon modes, so that phonon-mediated relaxation requires multiphonon processes, a low probability event. This phenomenon, which is in many cases negated or obscured by surface state-mediated relaxation, is referred to as the "phonon bottleneck."[224] This slowdown in phonon-mediated relaxation opens the door for other kinetic processes, namely Auger recombination and multiple exciton generation, which similarly relax the hot excitons on an ultrafast timescale but introduce additional considerations. In Auger recombination, the excess energy of electrons is transferred to the hole, which cools more quickly due to a larger effective mass and smaller energy spacing. This process is generally treated with Fermi's golden rule utilizing the Kane model, due to the sensitivity of the Auger relaxation rate to the overlap of electron and hole wavefunctions.[225] In multiple exciton generation (MEG), predicted by Nozik in 2001 and subsequently observed by Schaller and Klimov in 2004 in PbSe QDs,[226, 227] the excess energy of a hot carrier generates a second exciton. This phenomenon has since been observed by others in a variety of quantum-confined structures. However, the theoretical treatment of multiple exciton generation is still under debate, with both coherent and incoherent models being proposed.[228, 229]

Regardless of mechanism, it is known that multi-excitons can be generated on an ultrafast timescale from hot excitons ($\sim$100 fs) in QDs, and their lifetimes are tens to hundreds of ps depending on the material. In certain cases, EnT/CT is competitive with Auger mediated bi-exciton relaxation so that multi-excitonic states can act as energy and charge donors.[230] In the context of QD solar cells, designing fast EnT processes to extract multiple carriers from a single high energy excitation could significantly reduce thermal losses and increase power conversion efficiency. Several recent chapters have covered progress made in understanding these processes fundamentally and in the context of solar cells, so we will not discuss them further here.[231–233]

Auger recombination also has a fundamental role to play in CT dynamics in QD-molecular adsorbate systems. In 2014, Lian, Prezhdo, and coworkers measured interfacial electron transfer rates from CdX (X = S, Se, Te) QDs to three different adsorbed molecular electron acceptors.[234] Variation of QD size and choice of acceptor molecule enabled tuning of the driving force for electron transfer between $\sim$0–1.3 eV. The CT rate increased and then plateaued with increased driving force, even in the Marcus inverted regime, where the CT rate should decrease with increased driving force. Ab initio calculations using a $Cd_{33}Se_{33}$ QD cluster[235] helped explain the phenomenon using the Auger-assisted electron transfer model, which assumes that electron transfer is coupled to the generation of a "hot" hole through the large electron-hole Coulomb interaction in QDs. The "hot" acceptor states reduce the effective driving force in the highly exergonic CT process to eliminate the inverted region, and the remaining energy can be dissipated within the QD. A summary of the model is shown in Fig. 6.7(a). Olshansky et al. attempted to validate the Auger-assisted CT model by measuring the temperature dependence of hole transfer

for a series of ligands to observe the predicted Arrhenius behavior and the activationless regime at low temperatures. What they found however was that the temperature dependence observed in their Arrhenius plots, shown in Fig. 6.7(b), was consistent regardless of driving force, implying a process independent of the ligand was involved. They proposed that a surface trap state may act as an intermediate, further complicating the picture.[236, 237] While the exact mechanism is not clear, what is shown from these studies is that higher lying excited states play a larger role in EnT/CT in QD systems than in all-molecular systems.

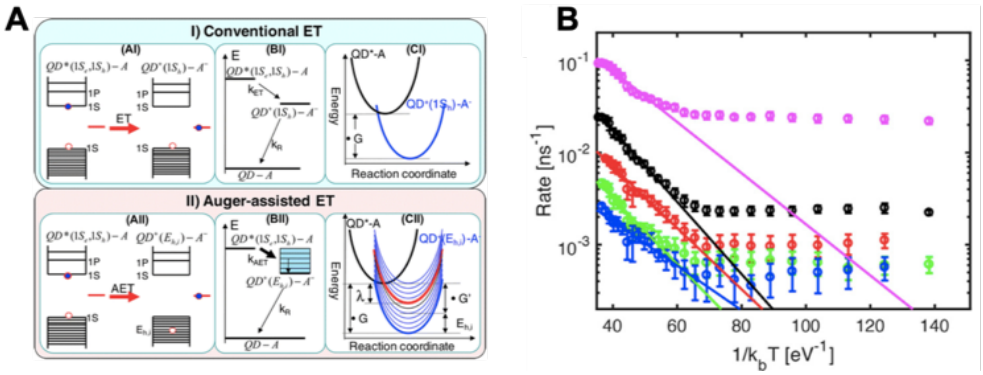

FIGURE 6.7: (a) Inverse dependence of electron transfer rate to NPL surface area. Reproduced with permission from Diroll et al., J. Am. Chem. Soc. 138, 11109 (2016). Copyright 2016 American Chemical Society. (b) PL lifetime of NPL is dependent on its orientation. Reproduced with permission from Goa et al., Nano Lett. 17, 3837 (2017). Copyright 2017 American Chemical Society.

6.4.5 Carrier Localization

Surface or lattice-localized[238] trap states, which are often treated only as non-radiative pathways from the band edge exciton states, resulting in decreased PL quantum yield and emission intermittency ("blinking"), can be leveraged as EnT/CT intermediate states. Traps are generated from local structural defects, such as dangling bonds, vacancies, or anti-site defects in a bulk material, so that they are hard to capture in an effective mass model apart from introducing them after the fact phenomenologically.[239] Trap states are most impactful when their energies are within the bandgap, since electrons or holes trapped within the conduction or valence band have the potential to quickly escape.

Trap states localize charges spatially, which has an effect both on the dynamics of the charge being trapped, and on the conjugate charge through modification of electron-hole overlap. This spatial localization can allow for traps to act as intermediate states that effectively increase the wavefunction overlap between the QD and the molecular acceptor. Wu et al. designed a CdSe nanorod that trapped 99% of all holes with a time constant

of <1 ps (Fig. 6.8).[240] The trapping process out-competed all other recombination pathways, and the trap state had a long lifetime of 360 ns, so it served as a stable intermediate for eventual transfer of the hole out of the QD to a phenothiazine acceptor with near unity yield. Dopant sensitization is another useful process that has been proposed to benefit from localization of excitonic carriers in close proximity to the dopant atom.[241, 242] A weakened exciton electron-hole interaction can also lead to easier charge separation. Ye et al. showed that both electron and hole transfer kinetics may improve with increasing concentration of surface hole trap sites.[243] A higher surface trap concentration was correlated with better adsorption of cocatalysts leading to faster hole transfer, while favorable charge separation increased electron transfer rates by a factor of 6.5.

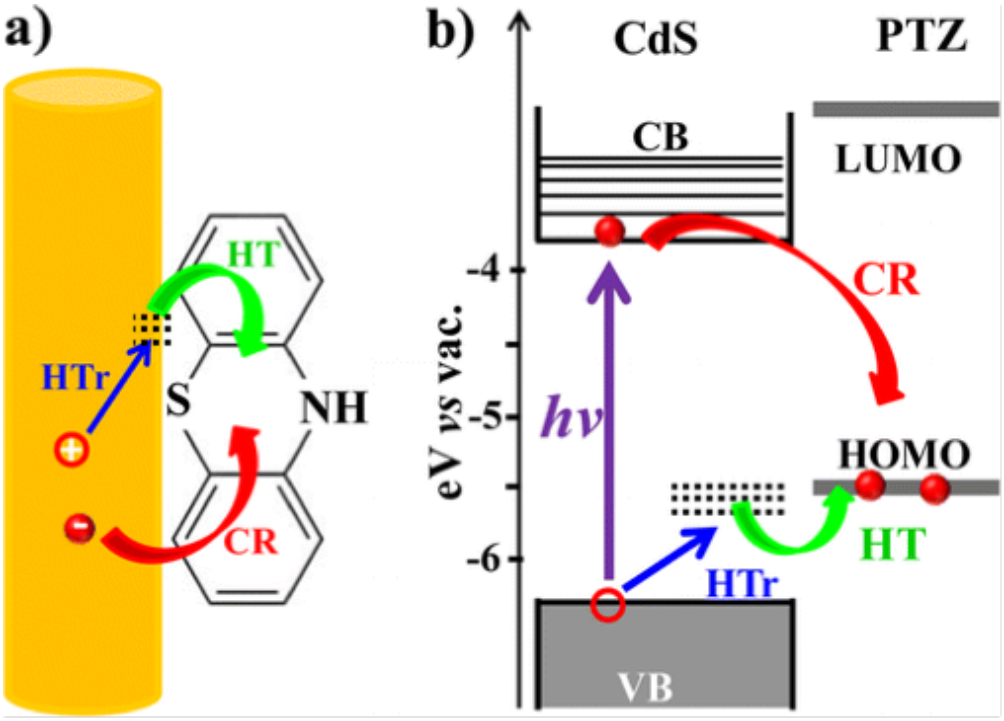

FIGURE 6.8: The trap mediated hole transfer process from CdS nanorods to PTZ (phenothiazine) molecules. The extraction of the trapped holes by PTZ molecules have 99% efficiency because of the long lifetime of the trapped holes. Reproduced with permission from Wu et al., J. Am. Chem. Soc. 137, 10224 (2015). Copyright 2015 American Chemical Society

6.4.6 The Influence of Ligands

Physical/Structural Effects of Ligands

The arrangement of ligands on the QD surface can be tuned to adjust the observed CT rate from QDs to reactants. For instance, in a QD-photocatalyzed photo-redox C-C coupling reaction between phenylpyrrolidine and vinyl-sulfone,[244] Zhang et al. found that substituting the native oleate ligand of CdS QDs with octylphosphonate increased the initial rate of the reaction by a factor of 2.3, due to disordering of the QD ligand shell. This disordering made the ligand shell more permeable to the phenylpyrrolidine substrate, accelerating the rate-limiting hole-transfer step. Ligands can also be used to introduce interactions between donor and acceptor that increase their electronic coupling. For instance, the catalytic activity of a combination of carboxylate-terminated CuInS2 QDs and positively charged Fe porphyrin co-catalysts for reduction of CO2 to CO is a factor of 11 higher than that of the same, uncharged sensitizer and co-catalyst.[245, 246] The authors modified the ionic strength of the catalytic reaction mixture (through addition of salt), and thereby correlated the catalytic activity to the size of the electrostatically bound QD-porphyrin aggregates.

Exciton Delocalization by Ligands

In contrast with our initial assumption that donor (QD) and acceptor (ligand) states can be neatly separated, exciton delocalizing ligands (EDLs) directly modify the energies and spatial distributions of excitonic states in QDs.[247–250] While some ligands modify exciton energies through electrostatic Stark Shifts, EDLs extend the carrier density of QDs beyond their quantum-confined cores to coupled ligand states. The band edge absorbance peak of QD shifts to lower energy with no change in the physical size of the core, as a

result of the hybridization between the frontier orbitals of EDLs and the valence or conduction band of QDs. Commonly used EDLs for QDs are conjugated S-containing ligands such as thiophenols and dithiocarbamates.

EDLs can greatly accelerate the process of charge extraction from the QD excitonic state via extended conjugation of the electron or hole wavefunctions beyond the core of the QD. In 2016, Lian et al. found that the rate of hole transfer from a QD to bound hole acceptor molecule covalently linked to the QD was faster through an EDL (τ_{CS} < 300 fs) than through a carboxylate ($\tau_{CS} \sim 1$ ps).[251] In 2017, Lee et al. observed that dithiocarbamate EDL capped-CdSe QDs participated in more efficient hole transfer to redox species in solution than MPA (mercaptopropionic acid)-capped QDs.[252] In 2018, Azzaro et al. reported that treating CdSe QDs with phenyldithiocarbamate enhanced the exciton hopping rate among the QDs in a solid film to (1/200) fs^1, 5 orders of magnitude larger than that in a film of oleic acid (OA)-capped QDs.[253]

One drawback for sulfur-based EDLs is that they quench the emission of many QDs as a result of their low oxidation potential and, therefore, limit QDs' application in optical devices. As an alternative, Westmoreland et al. discovered the exciton delocalizing ability of N-heterocyclic carbenes (NHCs; see Fig. 6.9).[254] They observed a bathochromic shift of >100 meV of the bandgap of CdSe QDs upon treatment with MeNHC and attributed the effect to a "back-bonding"-type interaction of the chalcogenide orbitals of the QDs and the π-type orbitals of the NHC. The treatment of QDs with only MeNHC decreased the photoluminescence quantum yield from 6% to ∼4%. Functionalization of the NHC could lead to new QD-molecule donor-acceptor pairs with exceptional yields of photoinduced CT.

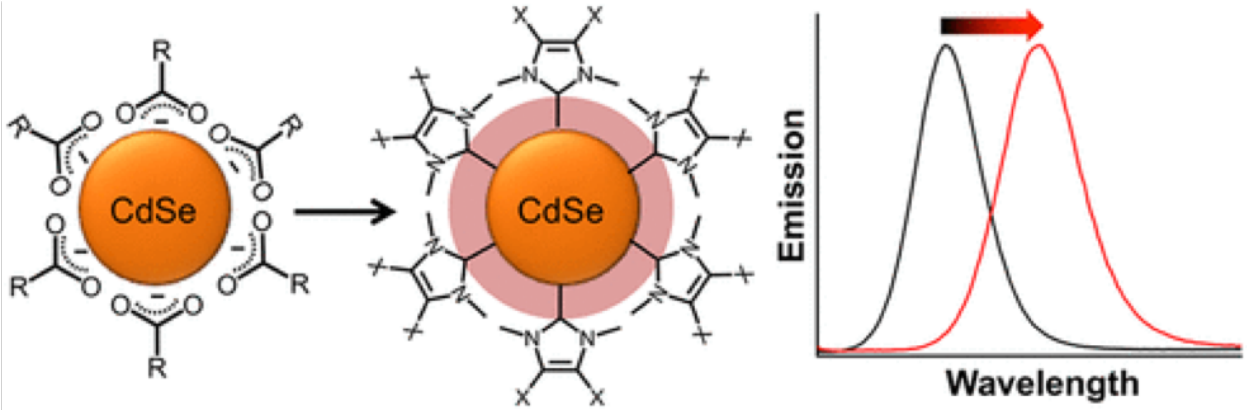

FIGURE 6.9: N-heterocyclic carbenes based exciton delocalizing ligands. 106 meV of bathochromic shift is observed due to the π-back bonding of the ligand. Reproduced with permission from Westmoreland et al., J. Am. Chem. Soc. 142, 2690 (2020). Copyright 2020 American Chemical Society

6.5 Synergistic Effects

Having covered how EnT/CT may generally be understood as mediated by direct coupling of exciton donor and ligand acceptor states in Sec. 6.3 and how individual features of CdSe nanocrystals complicate that simple picture in Sec. 6.4, we now highlight how these seemingly divergent and competing features can be simultaneously utilized. While it is often ideal to modify individual aspects of QDs, the tuning of one parameter often will have an effect on other QD properties. Here, we emphasize how a holistic understanding of the coupled parameter space may allow for QDs to perform functions far beyond what is possible in molecular systems, showcasing the full potential of QDs. Here we discuss three phenomena that are intended to illustrate the combination of some of the individual phenomena we have discussed in this chapter into more complex processes. These examples are only a peek at the possibly synergistic phenomena in QDs and are chosen because their general mechanisms have been investigated. There are certainly a

much larger set of synergies that are not understood at this level, and many more emergent phenomena that have not been identified.

6.5.1 Trap-Mediated TTEnT

Direct TTEnT from a QDs exciton to a molecule is typically suppressed by trap states, as they introduce additional non-radiative pathways for the excitons to return to the ground state. Previous studies that aim to optimize TTEnT through minimization of trap states or through passivation of surface traps indeed report enhanced TTEnT efficiencies.[255, 256] However, recently Jin et al. experimentally demonstrated that both band edge excitons and traps can be optimized to perform TTEnT in CdSe capped with 9-anthracene carboxylic acid (ACA), as shown in Fig. 6.10.[257] They found that a wide distribution of hole trap states are rapidly filled within 1 ps, outcompeting radiative decay. The decay of the traps' spectral features was correlated with the growth of the ACA triplet's features, so they proposed that the majority of TTEnT occurred from these trap states. Although TTEnT from the band edge excitons is a factor of 10 faster than from the trapped excitons, the long lifetime of trapped excitons resulted in a >95% yield of TTEnT. Although this paper does not reveal a mechanism by which the traps were coupled to the ACA triplet state, it is reasonable that the trapped hole must have some triplet character to participate in Dexter EnT.

6.5.2 Hot Exciton Processes Modulated by Dimensionality

The promise of extracting "hot" (above-bandgap) carriers, makes nanocrystals particularly appealing for applications in energy harvesting and photoredox catalysis. In Sec. 6.4, we discussed the conversion of hot excitons to multi-excitons that in turn served as

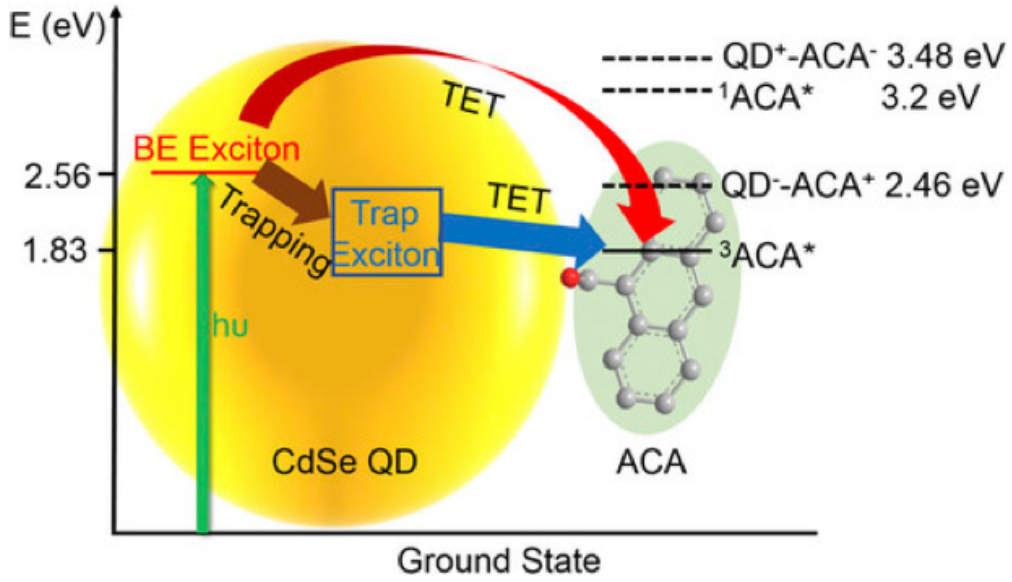

FIGURE 6.10: Trap-mediated triplet energy transfer process. The long lifetime of the trapped charge carriers can overcome the slow kinetics for the triplet energy transfer process. Reproduced with permission from T. Jin and T. Lian, J. Chem. Phys. 153, 074703 (2020). Copyright 2020 AIP Publishing

EnT/CT donors when transfer rates outpace the decay of the multi-exciton states.[230] Similarly, in order to extract "hot" excitons, all relaxation pathways that expedite the relaxation of the carrier to the band edge become parasitic. In QDs and nanorods, phonon mediated hot carrier relaxation occurs in hundreds of fs to a few ps. In NPLs, the higher density of states promotes electron-phonon coupling such that phonon-mediated hot carrier relaxation speeds up to 60–70 fs.[258] As a result, hot electrons have not been extracted from NPLs with molecular acceptors despite electron transfer on the hundreds of fs to a few ps timescale.[259] This fast cooling rate is not insurmountable. In fact, trapping of hot electrons on the QD surface has been implicated in their photoluminescence blinking.[260] There remains however the opportunity to optimize the dimensions and the nature of the facets to speed up the CT rate or slow the carrier cooling rate. Strategies include tuning exciton-phonon coupling through the lateral size of the NPL, shown

in Fig. 6.11, and controlling CT through spatial orientation of molecular electron acceptors relative to NPL confinement dimensionality.[261] Okuhata et al. showed that the same methyl viologen electron acceptor had drastically different CT rates depending on which edge of a rectangular NPL the ligand resided.[259] Another possibility is to replace molecular acceptors with other 2D materials; 2D-2D heterojunctions are known to exchange charge on the tens of fs timescale due to a large density of acceptor states.[262]

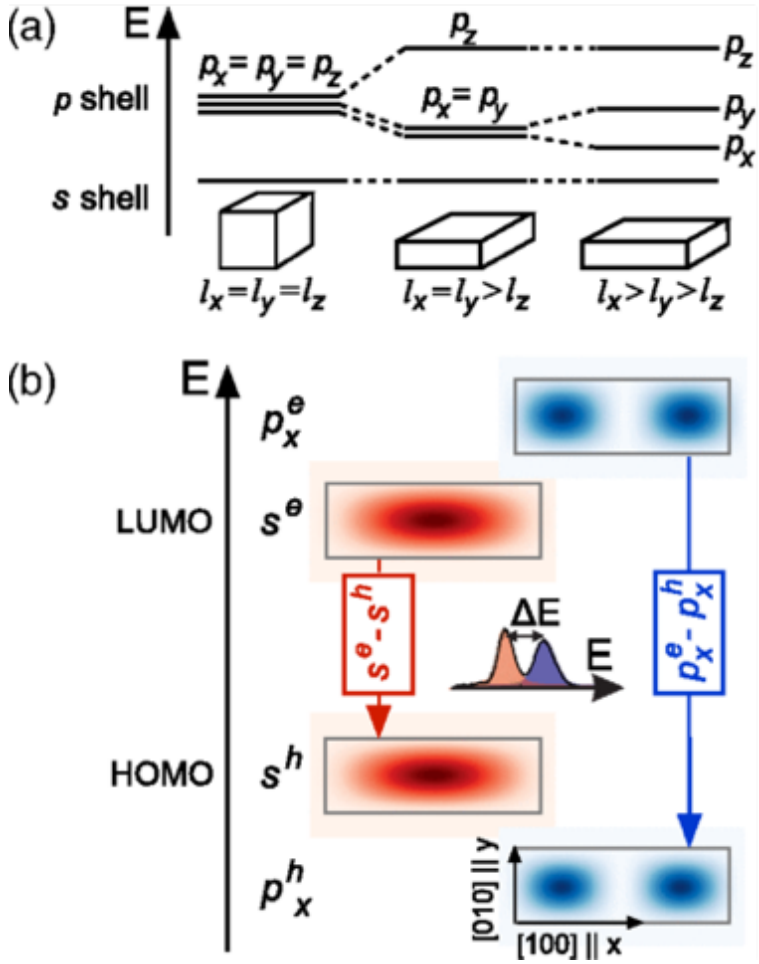

FIGURE 6.11: Modification of the excited state energy level driven by the unequal side length on the nanoplatelets. Tuning the s-p separation modifies coupling to longitudinal optical (LO) phonons. Reproduced with permission from Achtstein et al., Phys. Rev. Lett. 116, 116802 (2016). Copyright 2016 American Physical Society

6.5.3 Ligand Shells Templated by Nanocrystals

While the orientation of ligands on QD surfaces has a direct influence on EnT/CT coupling due to changes in transition dipole orientation or spatial overlap of wavefunctions, additional interactions may exist between ligands and anisotropic nanocrystals. One example is how an ensemble of ligands' dipoles may align to generate relatively large electrostatic fields, modifying the exciton energy. This behavior has been exploited to create energy level offsets in type II heterojunctions with the same size and type of QDs but different ligands [Fig. 6.12(a)].[263] With NPLs, this effect is even larger, and the band edges have been predicted to shift by up to 5 eV [Fig. 6.12(b)].[264] This effect was attributed to the NPLs behaving as a parallel plate capacitor, where the electrostatic effect from the surface ligands on the large facet is exacerbated due to the anisotropic shape compared to isotropic QDs. Given that the surface area can be synthetically controlled, the band edge shift may be tunable through a combination of the synthetic reaction time and post-synthetic ligand exchange. Ligands can also be used to tune the degree of quantum confinement imposed by the thickness of the NPL. By changing the ligands in NPL films from the native oleate to a variety of halide, thiolate, and phosphonate ligands, the bandgap (along with an inter-subband transition) undergoes a bathochromic shift due to delocalization from out-of-plane expansion of the potential well with some contributions from increases in biaxial strain.[265]

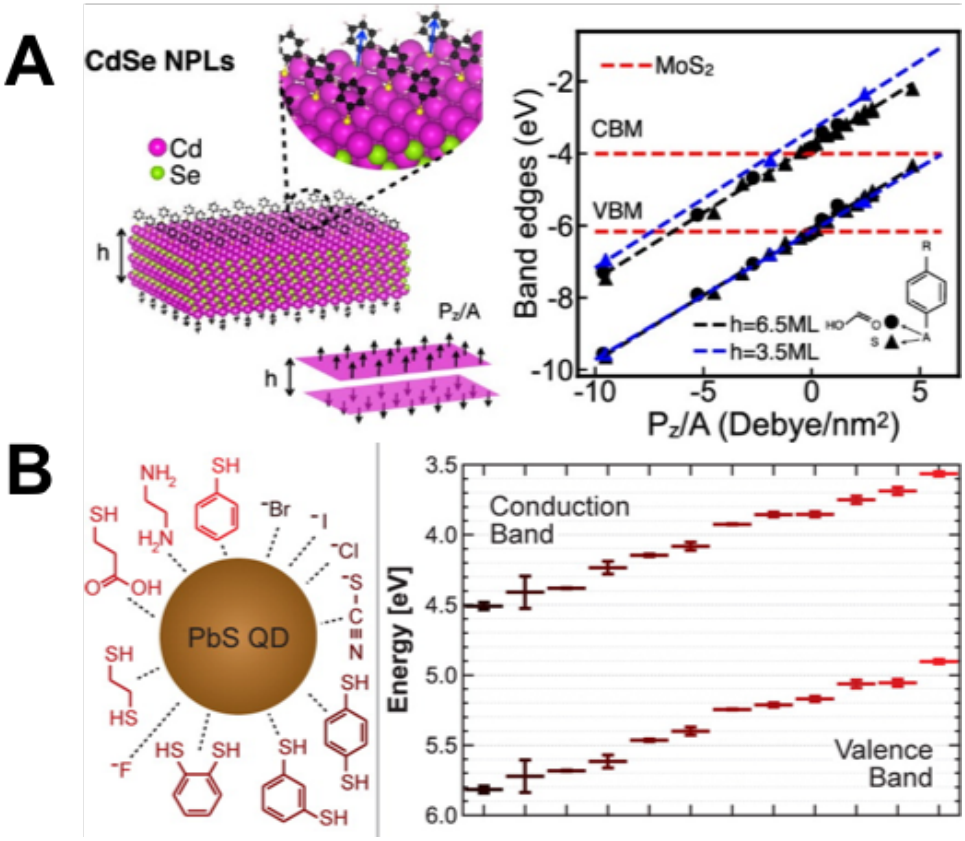

FIGURE 6.12: Band edge of (a) QDs and (b) NPLs depending on ligand molecules. NPLs predicted to be much more tunable with ligand exchange than QDs. Reproduced with permission from Brown et al., ACS Nano 8, 5863 (2014). Copyright 2014 American Chemical Society. Reproduced with permission from Zhou et al., Nano Lett. 19, 7124 (2019). Copyright 2019 American Chemical Society

A recent investigation by Jiang et al.[266] applied CdSe QDs as photocatalysts and structural scaffolds for [2 + 2] photocycloadditions occurring from the triplet excited state of the molecular reagent. The authors achieved up to 98% diastereoselectivity for the previously minor syn-cyclobutane products of homo- and hetero-intermolecular [2 + 2] photocycloadditions of 4-vinylbenzoic acid derivatives. Tethering of the substrates to the QD surface also resulted in up to 98% switchable regioselectivity for the products. This work is the ultimate demonstration of the simultaneous use of the QD as an optical coupling

element, an energy donor, and a physical template for molecular self-assembly. The result is high-yielding, selective chemistry not possibly with molecular photocatalysts.

6.6 Conclusion

The field of electronic processes in nanocrystal-molecule systems is well-established yet fast-evolving. This chapter aims to demonstrate how QD-molecule systems have the potential to move beyond what is possible in all-molecular systems for light-powered generation of charge and energy conversion schemes. Section 6.3 described energy and charge transfer in these inorganic-organic hybrid systems with the theory developed for molecular systems, including well-known results from Förster, Marcus, and Dexter. Section 6.4 showed how an understanding of EnT/CT in these systems requires additional considerations beyond the "direct coupling" of the initially prepared "donor" state and the final "acceptor" state. We explored topics such as how trap states act as kinetic intermediates and how ligands can affect exciton electronic structure in non-trivial ways. We also discussed how we might utilize, rather than minimize, unique features of QDs to access mechanisms of CT/EnT not available to molecules. Section 6.5 looked for ways to combine the features discussed in Sec. 6.4 synergistically to enable new functions, including photochemical transformations of the molecules that adsorb to the nanocrystal surface. We hope that by dissecting the QD-molecule system this way, we can inspire researchers to use quantitative models at all levels of theory to design the next generation of hybrid materials with intentional connections among components.

Coherence of Single Photons

Adapted from: **Irgen-Gioro, S.**; Wu, Y.; López-Arteaga, R.; Padgaonkar, S.; Olding, J.; Weiss, E.A. Evidence for Two Timescale-Specific Blinking Mechanisms in Room-Temperature Single Nanoplatelets *J. Phys. Chem. C*, **2021** DOI: 10.1021/acs.jpcc.1c03784

7.1 Single Photon "Blinking" From Room Temperature Single Nanoplatelets

Intermittent periods of low light emission ("blinking") and time-dependent emission spectra (spectral diffusion, SD) have proven major obstacles to the adoption of colloidal semiconductor nanocrystals as quantum emitters. One clue to the mechanisms behind these two phenomena is how they are related, which is difficult to determine at timescales faster than can be captured using a spectrometer ($\sim$100 ms). This work utilizes spectral correlations to access a range of timescales from 10 μs - 10 s, and determines that, for quasi-2D CdSe/CdS core/shell nanoplatelets (NPLs), blinking occurs on timescales from 100 μs to seconds but is only accompanied by SD on the $\sim$1 s timescale and slower. This result indicates that shorter-timescale blinking is due only to an equilibrium between dark and bright states with a shared, uncharged ground state, while longer-timescale blinking

receives contributions from an equilibrium between two distinct emissive states. The 10-15 meV energy range sampled by the NPL emission during SD implies that the two emissive states are an exciton and a trion.

7.2 Background

Under constant illumination and when observed as single particles, nearly all fluorophores emit intermittently.[267, 268] In organic molecules, this intermittency, colloquially known as "blinking", originates from competition among radiative and non-radiative pathways from a static set of excited states. The photoluminescence (PL) of semiconductor nanocrystals however often pauses for seconds at a time with no characteristic timescale for the "off" periods, defying this stochastic model.[269] Photodamage can be ruled out as the cause of the "on-to-off" transition since, after even the longest periods of reduced emission, QDs typically switch back to emitting light continuously as if the "off" period had never occurred. PL blinking is detrimental to certain applications of nanocrystals such as single photon emission, where a controllable, uninterrupted stream of light is desired.

Two general classes of models for blinking have been put forward (Figure 7.1); both involve trapping of excitonic carriers on undercoordinated ions on the nanocrystal surface, since chemical passivation of these states leads to more consistent light output.[270–275] In *mechanism 1* (Figure 7.1, left), one carrier (electron or hole) of the photogenerated exciton traps to a surface state while the other carrier remains delocalized in the core, and this trapped exciton recombines non-radiatively before the next photon is absorbed by the particle. In this case, the particle is non-emissive when the rate of trapping is larger

than the rate of radiative recombination of the band-edge exciton. In *mechanism 2* (Figure 7.1, right), the trapped exciton persists through many sequential photoexcitations of the nanocrystal. When the particle with a trapped exciton absorbs an additional photon, the result is a 3-body core state called a *trion*. A trion has an available non-radiative relaxation pathway called Auger recombination, in which the energy of the recombined exciton is transferred to the excess core charge. While the trapped exciton persists, Auger recombination competes with emission and increases the proportion of "off" time in the blinking trajectory. There is experimental evidence for both types of blinking mechanisms in semiconductor nanocrystals; in fact, they may operate simultaneously.[276–278]

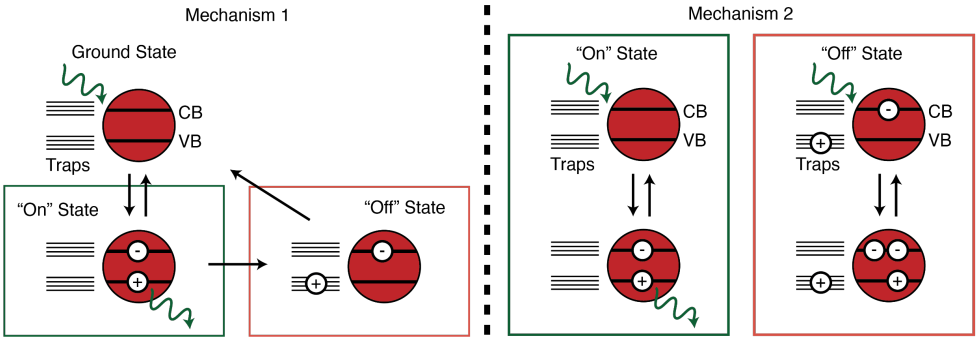

FIGURE 7.1: Two mechanisms for periods of low emission intensity, illustrated with a hypothetical spherical quantum dot. In *mechanism 1*, trapping kinetically competes with radiative recombination, so that periods of low emission (when trapping is faster than radiative recombination) have the same emission properties as the bright periods. In *mechanism 2*, the QDs absorbs a photon before the trapped carrier can recombine. The resulting 3-particle state is a *trion*, which can relax non-radiatively by Auger recombination. The trion usually has a different radiative rate and emission energy than the neutral exciton.

Since *mechanism 1* involves only one emitting species, while *mechanism 2* implies that multiple emitting species are present,[279] one important clue to which photophysical processes mediate blinking is how changes in PL intensity over time correlate with the spectral diffusion (SD) of the PL. Some of the earliest studies of blinking in nanocrystals

report that reduced emission periods - portions of the trajectory where a large fraction of the particles in the ensemble are "off" - had emission spectra that were shifted to lower energy from that of the exciton emission during "bright" periods. This result is consistent with a mechanism where surface-trapped excitons evolve to trions upon subsequent excitation, and that these trions have a lower probability of emission than uncharged excitons (*mechanism 2* in Figure 7.1). In the few instances where the radiative decay of the trion outcompetes Auger recombination, the emission is shifted to lower energy by 10-15 meV due to the presence of the extra charge.[280–282] Previous electrochemical studies have shown that changes to radiative rates and spectra concurrent with changes in emission intensity are attributable to switching between excitons and trions on the 100 ms timescale;[276, 280–287] however, the question remains of whether or not blinking that occurs faster than 100 ms is correlated with spectral diffusion. Investigations of the nature of PL intermittency on these faster timescales have been limited by available monitoring techniques: while blinking can be observed at timescales as fast as 10's of μs fairly easily using fast single photon detectors paired with fast electronics, monitoring SD traditionally requires the use of a spectrograph or monochromator to bin numerous photons over time to build up a spectrum.

Here, we use a combination of recently developed ratiometric and interferometric optical methods to investigate the correlation between blinking and SD in single colloidal CdSe/CdS core/shell nanoplatelets (NPLs) at timescales from 10 μs to 100's of s, including the 10 μs-100 ms timescale inaccessible with the traditional method of recording a time-ordered series of emission spectra. We study NPLs because their narrow, intense emission makes them exciting candidates as single photon emitters for quantum information networks, but such applications require a detailed understanding of processes

that limit their emission of spectrally pure photons on-demand.[288] Furthermore, NPLs are only strongly quantum-confined in one dimension, unlike the three dimensional confinement in their spherical analogs, colloidal quantum dots (QDs).[289] This reduction in confinement in two of three dimensions has been shown to reduce the Auger recombination rate and thereby increase the PL quantum yield (QY) of trions, so that the SD, if caused by trion emission, is more apparent in NPLs than in QDs.[290–294]

Our investigation finds a disconnect between the processes of blinking and SD for single NPLs. We observe that the intensity correlation of a NPL's PL trajectory starts to dip at 100 μs, indicating that blinking occurs on the $\sim$100 μs timescale. In contrast, SD is observed to only occur on the $\sim$1 s timescale, so blinking on the 100 μs-1 s timescale occurs without accompanying SD.

At slower (1 s) timescales, where SD and blinking are both occuring,[280, 282, 284–287] we conclude that blinking at least partially occurs due to transitions between the trion and exciton state (*mechanism 2*). Between 100 μs and 1 s, however, where blinking occurs with no change in the identity of the emitting species, we propose the sole operation of *mechanism 1*: "off states" caused by non-radiative recombination of short-lived trapped excitons. The operation of both mechanisms on a single particle implies that, while most trapped excitons can non-radiatively recombine before the NPL can absorb a new photon, other trap states persist for seconds.

7.3 Results

Figure 7.2(a) shows the ensemble absorption and emission spectra of the core/shell NPLs (and of the core-only NPLs, for comparison) dispersed in hexanes, and a transmission

electron micrograph of the core/shell NPLs. The CdS shell induces a strong bathochromic shift of the light-hole and heavy-hole transitions in the absorption spectra due to an increase in the total NPL thickness, while also broadening the emission spectrum of the 4ML NPL from 56 meV to 78 meV. The larger linewidth in core/shell NPLs has previously been attributed to coupling of the exciton to the phonon modes of the CdS shell.[295, 296]

We conducted all the measurements described below on single emitters. We diluted the NPLs to $\sim$1 nM, drop-cast them onto a clean coverslip, and studied them with a home-built confocal microscope. Details of sample preparation and images of the single emitters are in section 7.5. The CdS shell presumably reduces the density of surface traps; consequently, the core-shell NPLs have longer and more frequent periods of high-intensity emission (see Figure D.4 in Appendix D). Each potential target emitter is confirmed to be a single emitter with the standard Hanbury-Brown-Twiss experiment, see example traces in Appendix D. Verification of a single photon emitter requires a $g^{(2)}$ (τ=0)<0.5, with an ideal single photon emitter having a $g^{(2)}$ (0)=0.31 Here, the value of $g^{(2)}$ (τ=0)=0.2 suggests that the studied sample is a well-isolated single NPL and a good candidate for further monitoring of blinking and SD. The residual is due to a high probability of bi-exciton emission in NPLs.[293, 297] In selecting for particles with $g^{(2)}$ (τ=0)<0.5, we may also be selecting for NPLs with smaller lateral sizes, due to their more efficient biexciton Auger recombination.

One piece of evidence for the contribution of multiple emissive states to the emission of a single particle is variation in the PL lifetime of the particle during changes in particle intensity within the blinking trajectory. Figure 7.2(b) shows the intensity time trace of a single isolated core/shell NPL emitter binned with a bin size of 1 s. For each bin, we

generated a time correlated single photon counting (TCSPC) trace and fit it with a single exponential decay. Figure 7.2(c) is a plot of the resulting emission lifetimes vs. the total number of counts for each bin in the form of a heatmap. Blinking caused by *mechanism 1* results in changes in intensity, but not in lifetime and is sometimes called type-B blinking.[276] Blinking caused by *mechanism 2*, which involves the switching between two emissive species, is characterized by correlated changes in lifetime and intensity, since trions are known to have a faster emission rate than excitons.[298] In Figure 7.2(c), both mechanisms appear to be operational. Interpretation of Figure 7.2(c) needs to be approached with caution, because the lifetime and intensity data are collected in 1-s bins, so if a particular type of blinking is modulated, or if an NPL switches between blinking *mechanisms 1* and *2*, on a timescale on the order of 1 s or faster, the intensity and lifetime shown in the heat map in Figure 7.2(c) will be an average of that of "on" and "off" states in the blinking trajectory for one or both mechanisms. In this figure, the "purest" exciton emission appears with high intensity and long lifetimes: 800-1200 counts per second and lifetimes of 20 - 26 ns. The purest trion emission is lower-intensity and shorter-lifetime: 400-600 counts per second and lifetimes of 10 - 15 ns. For instance, the region defined by lifetimes of 15 - 25 ns and intensities of 300 - 400 counts per second likely includes time points in which multiple blinking mechanisms are active.

Without faster time resolution, we present the data in Figure 7.2(c) to show that there is, in fact, a range of exciton lifetimes associated with the range of emission intensities from a single NPL, a result that indicates the presence of both *mechanism 1* and *mechanism 2* -type blinking.

We first explicitly monitor the SD of a single particle using the conventional method of directing the emission to a spectrograph paired with a sensitive sCMOS camera. We record

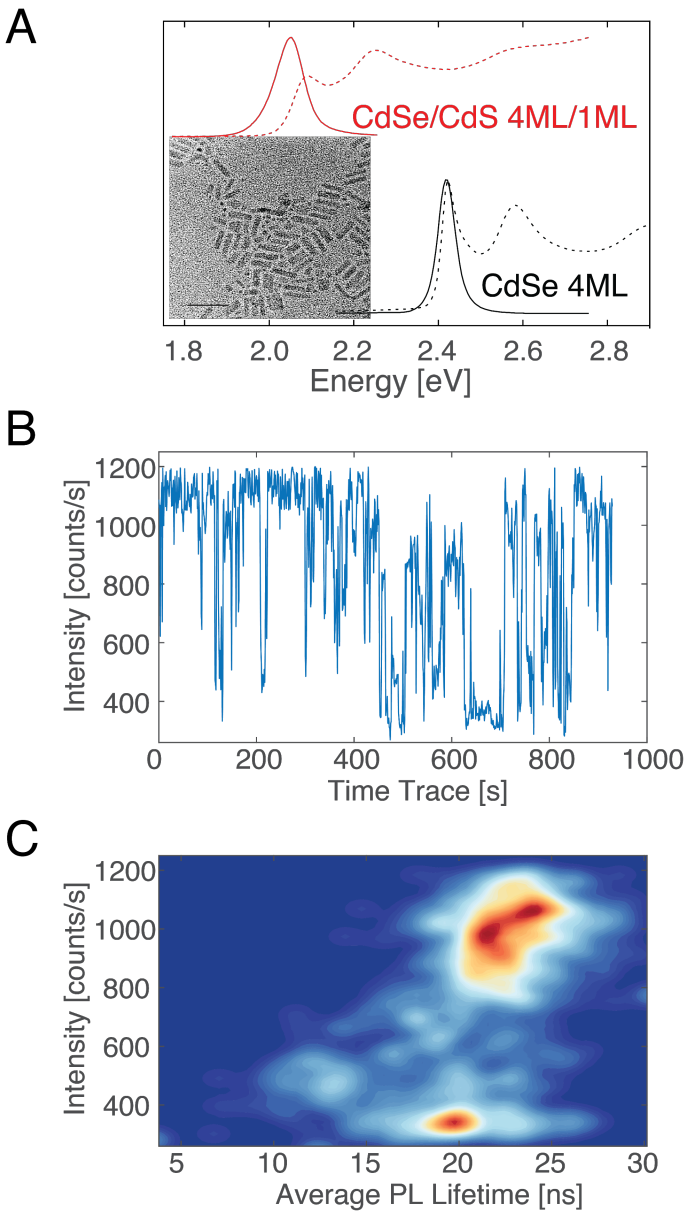

FIGURE 7.2: (a) Solution-phase absorption (dashed) and emission (solid) spectra of ensembles of CdSe 4ML and CdSe/CdS 4ML/1ML NPLs in hexanes, normalized to the band-edge peak. Inset: TEM of CdSe/CdS 4ML/1ML NPLs; the scalebar is 50 nm. (b) Emission intensity time traces for a single CdSe/CdS core/shell NPL. (c) Exciton lifetimes at each timepoint in B plotted vs. the emission intensity at that timepoint. These data points were acquired in 1-s bins; for each bin, we generated a TCSPC kinetic trace and fit it with a single exponential decay to determine the associated lifetime (see Figure D.7 of Appendix D).

the emission spectrum every 500 ms for 600 s, see Appendix D for details. Figure 7.3(a) plots the emission spectrum of a single core/shell NPL over time, with the integrated intensity at each timepoint plotted to the right of the heat map. On this timescale, the peak energy and intensity are correlated, Figure 7.3(b). The peak emission energy of the highest-intensity timepoints is ∼20 meV higher than the peak emission energy of the lowest-intensity timepoints. The large (10-20 meV) range of emission energies sampled during spectral diffusion of our NPLs is consistent with the difference in energy between excitons and trions ∼10 meV previously reported for NPLs at cryogenic temperatures, and inconsistent with the reported magnitude of the quantum-confined Stark Effect (QCSE), which results in energy fluctuations on the order of ∼1 meV.[299] Figure 7.3(c) shows the sums of emission spectra extracted from "high", "medium" and "low"-intensity timepoints from the spectrograph data in Figure 7.3(a). Comparison of these spectra shows that the Lorentzian emission linewidth decreases slightly from 0.070 eV at low intensity (E_{peak} = 2.055 eV) to 0.063 eV at medium intensity (E_{peak} = 2.061 eV) to 0.058 at high intensity (E_{peak} = 2.062 eV). This behavior is consistent with, but not necessarily proof of, the involvement of *mechanism 2* in the PL intermittency of the NPLs.

The findings shown in Figure 7.2(c) (the variation of radiative lifetime with emission intensity) and Figure 7.3(b) (the correlation of peak energy with emission intensity) are strong pieces of evidence that the scenario where multiple emissive species - presumably an exciton and a trion, given the magnitude of the energy shift during SD - within a single particle are responsible for the observed blinking and SD dynamics on this long timescale (*mechanism 2* of Figure 7.1).[280–282]

To more accurately specify the timescales on which SD is occurring, we use the data in Figure 7.3(a) to calculate the spectral correlation $p(\zeta, \tau) = \langle \int s(\omega, t)s(\omega + \zeta, t + \tau)d\omega \rangle$ of

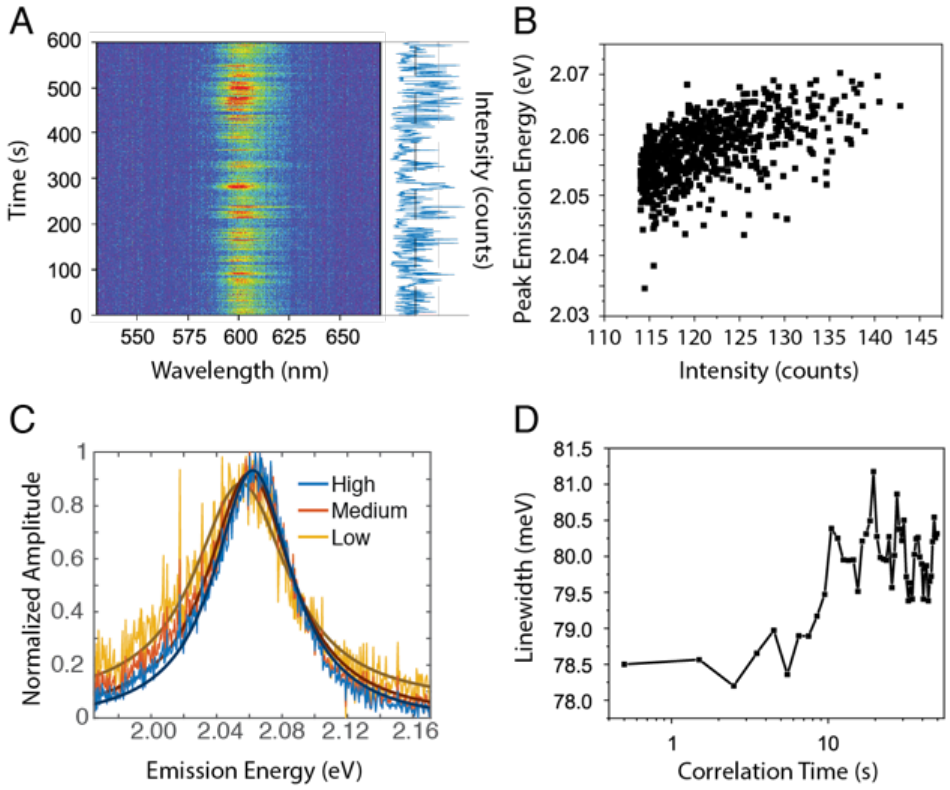

FIGURE 7.3: (a) Emission spectra of a single 4ML/1ML CdSe/CdS NPL acquired with a spectrograph every 500 ms, and corresponding PL intensity time trace (right). (b) Correlation between emission linewidth and peak emission energy extracted from the data in (a). Intense peaks are blue-shifted relative to less intense peaks. (c) Sums of emission spectra extracted from "high", "medium" and "low"-intensity timepoints in (a) and Lorentzian fits. The Lorenzian linewidth decreases from 0.070 eV at low intensity to 0.063 eV at medium intensity to 0.058 at high intensity. (d) The calculated effective emission linewidth σ_{eff} at different correlation times τ giving the timescale of SD.

this emission, where $\langle ... \rangle$ denotes time averaging, $s(\omega, t)$ is the single-particle spectrum at time t, and ζ is the energy displacement between two spectra. The spectral correlation reveals how similar two spectra separated by the correlation lag time τ are in energy, ζ. The calculation of correlation allows us to quantify SD by averaging over all recorded events separated by a time difference τ, and thereby increase the accuracy of the calculation by collecting signal for a longer time. From the spectral correlation, we extract an effective linewidth, $\sigma eff(\tau)$, which is how broad a static Gaussian function would need to be to generate the spectral correlation at a given τ (see Appendix D for details); a change $\sigma_{eff}(\tau)$ indicates SD. Figure 7.3(d) is a plot of σ_{eff} vs. lag time τ for a core/shell NPL. The effective linewidth is quite flat on the 1 s timescale but starts to rise as lag times approach 10 s. This result shows that, on average, emitted photons separated by 1 s are similar spectrally, but photons separated by 10s of seconds are likely to have different spectra. Although limited by the acquisition speed of the method, the spectral correlation plot shows that SD only begins to occur on a $\sim$1 s timescale.

To confirm that SD is not occurring on timescales faster than those plotted in Figure 7.3(d) (i.e., the μs-to-s timescale), we first convert spectral fluctuations into intensity fluctuations. In this experiment, we use two single photon detectors, where, through the use of spectral filters, one detector is sensitive to the low-energy side of the NPL's emission spectrum and other is sensitive to the high-energy side, Figure 7.4(a).[300, 301] The total emission spectra of a single core/shell NPL and the spectra after spectral filtering are shown in Figure 7.4(b). When there is no SD, the intensities on the detectors are correlated; the total counts on each of the two detectors increase and decrease together with the overall intensity fluctuations of the emitter, and the cross-correlation is identical to the autocorrelation. When SD shifts the center wavelength of emission to higher and

lower energies, the ratio of light hitting the two detectors changes in time, Figure 7.4(c). The timescale of SD can thus be extracted from when the cross-correlation between the two detectors begins to deviate from the autocorrelation. Figure 7.4(d) shows that these two plots are identical until $\sim$3 s, when the cross-correlation begins to decrease relative to the autocorrelation. The result that SD only becomes apparent on a >1 s timescale for core/shell NPLs is consistent with the spectral correlation obtained from the spectrograph (Figure 7.3), but additionally shows that SD does not occur between 1 ms and 3 s.

Our experiment spectrally biasing detectors, presented in Figure 7.4, shows that the core/shell NPL only experiences SD at >1 s timescale and the time resolution is limited only by the signal-to-noise ratio of the correlation traces and after-pulsing of the APDs. The technique is however restricted by the need for suitable spectral filters. An alternative, more flexible technique for measuring SD with even greater dynamic range is interferometry.[302] Specifically, we use a technique called Photon Correlation Fourier Spectroscopy (PCFS), which utilizes the cross-correlation between detectors at the output of a dithered Mach-Zender interferometer to extract the average linewidth of two photons separated by a time difference τ.[303, 304] Introduced over a decade ago, PCFS has been applied to study the evolution of PL linewidths of spherical QDs as a function of τ, in order to determine both the homogeneous linewidths hidden behind SD and the timescale of SD.[305–311] Figure 7.5(a) shows a schematic diagram of the interferometer we use in PCFS along with the form of the data extracted from this experiment. If the emitted photons are directed into the interferometer and the intensity of the output as a function of relative path length δ is recorded, a spectral interferogram is generated. The

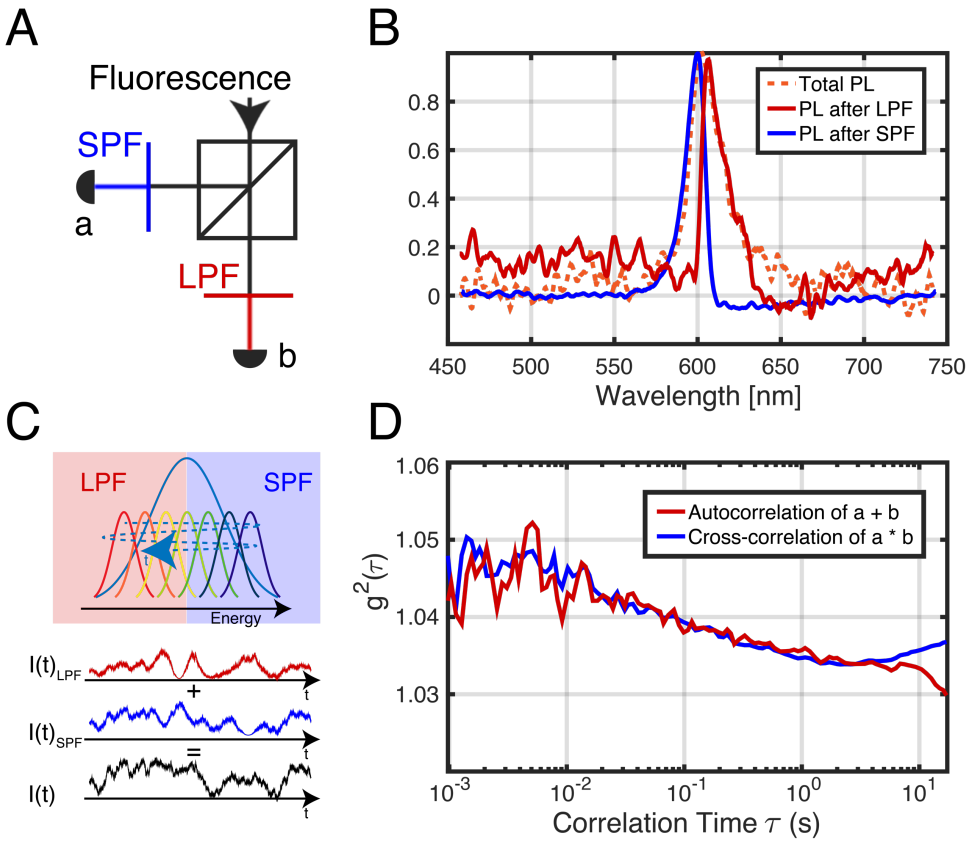

FIGURE 7.4: (a) Schematic for spectrally biased correlation measurements. Incoming PL is split by a 50/50 beam splitter; a long-pass filter (LPF) and a short pass filter (SPF) are placed in front of the respective detectors. (b) PL spectra of the core/shell NPL before and after introduction of the LPF and SPF. (c) Example time traces obtained using this ratiometric method in the presence of SD, which results in deviation of the signal from LPF and SPF detectors from each other and from the total intensity. (d) Spectrally biased correlation for a 4ML/1ML core/shell NPL. The cross-correlation (blue) and autocorrelation (red) traces overlay until ~3 s. Datasets for additional NPL particles are in Appendix D.

Fourier transform of that interferogram is the familiar emission spectrum. The PCFS experiment instead records the second order correlation $g^{(2)}(\tau, \delta)$ between the two detectors as a function of a very gradually changing relative pathlength, δ.

Figure 7.5(b) shows the autocorrelation function for the sum of the signals at detectors a and b and the cross-correlation between the signals at detectors for one core/shell NPL at $\delta = 0$. The autocorrelation reports the intensity fluctuation due to blinking. Here, the value of $g^{(2)}$ begins to drop at $\sim$100 μs; this loss of correlation with increasing τ indicates that blinking dynamics are occurring on that timescale.[312–315] This result, in conjunction with the spectrograph data in Figure 7.3, confirms that blinking occurs on numerous timescales, ranging from 100 μs to 10s of s.

The cross-correlation trace in Figure 7.5(b) reports on the degree of anti-correlation between the two detectors. When the interferometer has $\delta \approx 0$, the output of the interferometer at the two detectors is anti-correlated due to interference; this anti-correlation results in a lower cross-correlation value than an autocorrelation value. At timescales of $\sim$1 s, artifacts of the slowly moving stages can be seen, putting an upper limit on the timescale to which PCFS is sensitive. The degree of anti-correlation of the two detectors as a function of δ yields the envelope function of the spectral interferogram, which is related to the linewidth of the emitter by the coherence lifetime T_2. For a Lorentzian lineshape, the linewidth is $\Gamma = 2\hbar/T_2$. Figure 7.5(c) is a plot of T_2 vs. the correlation lag-time τ for a core/shell NPL (traces for additional NPLs are in Appendix D). For emitters that exhibit no SD, T_2 is independent of τ because the time separating two photons does not affect the degree of interference. If instead the photons entering the interferometer have different spectra, the interference decreases and T_2 decreases with τ. Figure 7.5(c) shows that the core/shell NPLs do not undergo SD on the 1 μs - 100 ms timescale, as indicated

by a constant value of T_2 (10 fs) over that set of correlation times. This value of T_2 corresponds to a Lorentzian linewidth of 131 meV, broader than measured in the spectrometer. Linewidths are inversely proportional to coherence lifetimes, so the error in the absolute value of broad linewidths is expected to be large. Such uncertainty in the absolute value of the linewidth does not however translate into uncertainty in the timescale of SD.

Using the three techniques described above, we determined that, between 1 μs and several hundred ms, blinking occurs in the absence of SD. Only at the $\sim$1 s timescale and longer is SD observed, and it is correlated with blinking. This result indicates that two types of blinking occur in these NPLs, and that they operate at different timescales. Low-intensity portions of the faster-timescale blinking trajectory - the blinking that is uncorrelated with SD - are likely due to non-radiative recombination of trapped excitons (*mechanism 1*, Figure 7.1). In this mechanism, each cycle of excitation and emission has similar emissive properties, even if there are lapses in emission intensity. The timescale over which this mechanism (μs - ms) is operative corresponds to the timescale on which these trap sites become available and unavailable, possibly by transient passivation due to reorganization of surface ligands. The correlation of slower blinking dynamics with SD indicates that blinking on this timescale ($\geq$ 3 s) is due to switching between different emissive states, particularly excitons and trions (*mechanism 2*, Figure 7.1). This result is consistent with previous work that concluded that switching between excitons and trions occurs slower than 100 ms.[316] Given that the trion states persist for seconds, the surface-trapped carriers that have escaped from the NPL to form the trion must require unlikely detrapping events to return to a neutral exciton or biexciton before returning to the ground state. This conclusion is consistent with the observation that low-temperature emission spectra of NPLs is dominated by trion emission.[298]

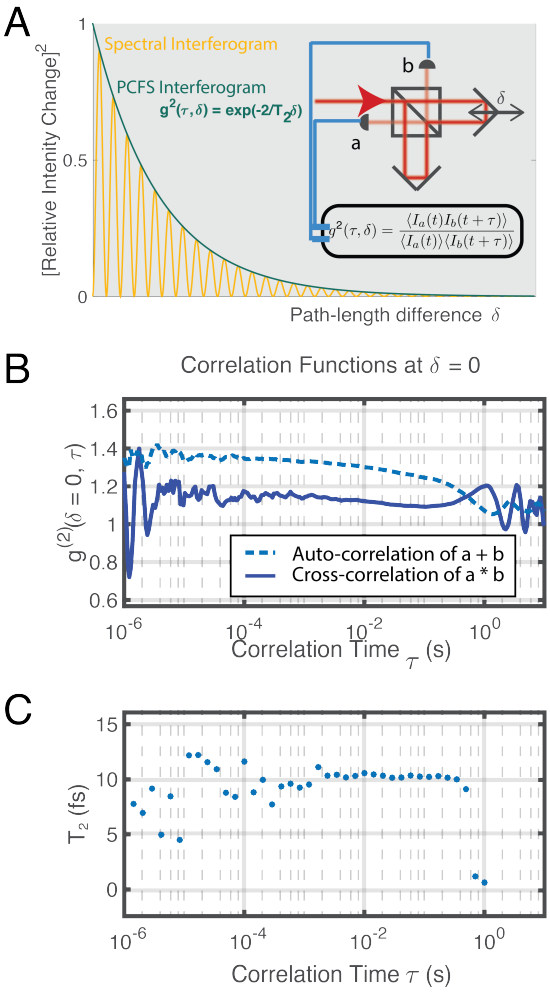

FIGURE 7.5: (a) Schematic diagram of PCFS. Spectral information is encoded using a Mach-Zender interferometer. PCFS retrieves the envelope function of spectral interferograms for photons separated by a time delay of τ. (b) Cross-correlation (solid line) and autocorrelation (dotted line) of detectors a and b at $\delta = 0$. The dither waveform that appears starting at roughly 10^{-1} s is an artifact. Appendix D shows the same traces for $\delta >> 0$, where there is no interference, so each detector experiences the same intensity fluctuations and the cross-correlation is identical to the autocorrelation. (c) The extracted coherence lifetime T_2 as a function of photon separation τ for 4 ML core/shell NPL. The decrease in T_2 starting between 10^{-1} s and 1 s is an artifact from the dithering. Appendix D contains these datasets for 20 different NPL particles.

7.4 Conclusions

We monitored SD with sequential spectrometer images (Figure 7.3), spectrally biased cross-correlation (Figure 7.4) and PCFS (Figure 7.5) and uncovered the timescales of two mechanisms of blinking. While all methods are able to extract SD information, only by combining the data obtained from all three were we able to show that (i) blinking occurs without accompanying SD on the $\sim$100 μs - 100 ms timescale, and (ii) on the 1 s timescale and slower, blinking is accompanied by, and correlated with, spectral diffusion. In regime (ii), the PL intermittency is modulated by switching between a brighter, higher-energy exciton state and a dimmer, lower-energy trion state. Sequential spectrometer images allowed for unambiguous confirmation of SD but is limited in the acquisition speed. Spectrally biased cross-correlation showed the transition from *mechanism 1*-type blinking to *mechanism 2*-type blinking but is limited by the use of spectral filters. PCFS allows for detection of SD on fast timescales (as fast as 10 μs), limited only by the APD afterpulsing and photon counts, but is not reliable at timescales longer than 100 ms due to artifacts inherent to the technique. When used in combination, PL intermittency mechanisms can be investigated over seven orders of magnitude in timescale. For core-shell NPLs, we find that the mechanism for intermittency changes at the $\sim$1 s timescale, a result that will guide the assignment of chemical mechanisms for both spectral diffusion and blinking, and allows us to rationally design synthetic and post-synthetic strategies to enable photon indistinguishability for NPL single photon emitters.

7.5 Methods

7.5.1 Materials

Cadmium nitrate tetrahydrate ($Cd(NO_3)_2 \cdot 4H_2O$, 98%), cadmium acetate dihydrate ($Cd(OAc)_2 \cdot 2H_2O$, 98%), myristic acid (98.0%), sodium hydroxide (NaOH, anhydrous), selenium powder (99.99% trace metals basis), 1-octadecene (ODE, 90%), oleic acid (OA, 90%), oleylamine (70%) and N-methylformamide (NMF, 99%) were purchased from Sigma Aldrich and used as received.

7.5.2 NPL Synthesis

We synthesized 4-monolayer CdSe core-only NPLs and shelled them with one layer of CdS using the colloidal atomic layer deposition method.[289]

7.5.3 4 ML CdSe NPLs

To prepare the precursor $Cd(myr)_2$, 120 mg (3 mmol) NaOH and 685.2 mg (3 mmol) myristic acid were sequentially dissolved in 20 mL methanol. After fully dissolved 10 mL 0.1 M cadmium nitrate (Cd(NO3)2) methanol solution was added dropwise under stirring. After 30 min the suspension was vacuum filtered, and the product was dried in vacuum oven overnight before use.

Freshly prepared 170 mg cadmium myristate ($Cd(myr)_2$), 12 mg selenium powder and 14 mL of 1 Octadecene (ODE) were added in a three-neck flask and degassed for 1 h at 100 C. The mixture was then heated to 190 C under nitrogen flow. When the temperature reached 190 C, 40 mg cadmium acetate was immediately added in the flask. The solution was further heated to and held at 240 C for 1 min to grow 4ML CdSe NPLs. After 1

min, the solution was cooled down. 2 mL oleic acid and 15 mL hexane were added at 70 C to stabilize the NPLs. The solution was centrifuged at 7000 rpm for 5 min and the pellets were dissolved in hexane. TEM image of the 4ML core-only NPL can be found in Appendix D.

7.5.4 4ML/1ML CdSe/CdS Core-Shell NPLs

Core-shell NPLs were synthesized with the colloidal atomic layer deposition (c-ALD) method. 1 mL of 4ML CdSe NPL solution (OD of ∼0.3 in a 2 mm cuvette) was mixed with 0.5 mL N-methylformamide (NMF). 10 μL of ∼40% ammonium sulfide (aq) was added, and the solution was shaken to induce the phase transfer of NPLs from hexane into NMF. The NMF phase containing the NPLs was rinsed with hexane twice, followed by precipitation with acetonitrile, redispersal in NMF, and addition of a 150 μL of a 0.15 M cadmium acetate solution in NMF. The shelled NPLs were precipitated with toluene and redispersed in NMF. The above constituted a full cycle of one-layer CdS shelling. To transfer shelled NPLs back in hexane, 1 mL hexane, 20 μL oleyamine and 20 μL oleic acid were added. The CdS-shelled NPLs were precipitated with ethanol and redispersed in hexane.

7.5.5 Preparation of Dilute Films of NPLs

NPL samples were serially diluted by factors of ten from a stock solution. Each dilution was examined in the microscope to find the correct dilution factor to reliably see individual particles. We found that the excitation power had a strong influence on the number of bi-excitons emitted; biexcitons negatively impact the $g^{(2)}$. We found that a pump fluence

of 15 W/cm^2 gave us the best balance of anti-bunching statistics without photodegradation, whilst still maintaining enough counts to perform PCFS. We did not find that encapsulation in a polymer matrix like PMMA reduced photodegradation.

7.5.6 Confocal Microscopy

A 70-ps pulsed laser running at 8 MHz and a central wavelength of 450 nm (LDH450-P-C-450B, PicoQuant) or a CW laser with a central wavelength of 475 nm (LDR-475, Laser-Glow Technologies) were focused through a pinhole to generate a transverse electromagnetic gaussian mode. After beam-waist expansion and collimation, the laser was directed to an immersion oil objective (100X, 1.3 NA, Zeiss) with a 475 nm long-pass dichroic mirror (Chroma, ZT473dcrbUF1). The laser was focused into the sample, which was mounted in a piezo scanning stage (PInano XYZ, P-545.3R8S). The PL collected by the objective was passed through a long-pass filter, which filtered out the excitation light, and sent either to a spectrograph (Shamrock SR-303i) equipped with a sCMOS camera (Zyla 4.2, Andor) or the Michaelson interferometer with 2 APDs (Micro-Photon-Devices PDM) at both outputs. One arm of the interferometer can be blocked to perform the Hong-Ou-Mandel anti-bunching experiment. For single particle localization, images of the samples were reconstructed with a commercial software (SymphoTime 64, PicoQuant).

7.6 Acknowledgements

This work was funded by the Department of Energy, Office of Science, Basic Energy Sciences, grant no. DE-SC0020168. This work made use of the EPIC facility of Northwestern University's NUANCE Center, which has received support from the SHyNE Resource (NSF ECCS-2025633), the IIN, and Northwestern's MRSEC program (NSF DMR-1720139).

Coherences at Larger Time and Spatial Scales

Adapted from : Riddle, J.; **Irgen-Gioro, S.**; Schooler, J. Nested Observer Windows (NOW): A Theory of Scale-Free Cognition *Under Review*, **2021**

Human cognition requires that information is integrated across multiple spatiotemporal scales of biology. Research into how information is integrated in cognition finds causal evidence for the role of brain nuclei, neurons, and proteins at different spatiotemporal scales. Despite progress in dedicated fields, investigations struggle to integrate across spatiotemporal scales. To address this gap, we introduce the Nested Observer Windows (NOW) model that phenomenologically describes how information is integrated hierarchically. Drawing from language used in modern cognative neuroscience, observer windows are formed via *synchrony* that accumulate and integrate information over stable temporal periods. Observer windows are refreshed in rhythmic cycles. Second, observer windows accumulate information laterally from other observer windows within the same spatiotemporal scale via *coherence*. Coherent observer windows form transient functional networks. Third, observer windows are nested such that each is composed of sub-windows. Bottom-up streams of information from sub-windows are bound into

abstract representations in the supervening observer window via *cross-frequency coupling*. By the same mechanism, top-down control signals are disseminated from a window to its sub-windows. The three principles of the NOW model - synchrony, coherence, and cross-frequency coupling - are found at multiple spatiotemporal scales in biology. Observer windows possess a capacity for phenomenal experience with implications for subjective experience. Altogether, the NOW model accounts for the speed of subjective experience, the richness of human perception, and how simple internal commands generate complex human behavior. The theoretical framework of the NOW model provides testable predictions for the interdisciplinary study of information integration in cognition.

8.1 Introduction

Understanding the biological basis of cognition is critical for advancing medicine and technology; however, each field of biology uses tools limited to a particular spatiotemporal scale. The cognitive neuroscientists analyzed the electrical activity and blood flow of nuclei and revealed functional connectivity patterns in distributed networks of brain regions that correspond to higher cognitive capacities.[317] The neurobiologists discovered that understanding the organization and firing sequence of neurons explained how perceptual information was calculated and how motor systems were engaged. The molecular biologists uncovered that signaling pathways of proteins amplified behaviorally meaningful information such as the detection of a photon and encoded memories by initiating structural changes in synapses. A limiting factor to understanding cognition is that biology spans many spatial and temporal scales - angstroms to centimeters and nanoseconds to seconds. The most appropriate level of analysis, or ideal experimental approach, for

consolidating theoretical understanding remains elusive. Furthermore, information integration in biology likely requires hierarchical organization with mechanisms by which activity is coordinated across scales. Thus, a model with general principles that enables information integration across multiple spatiotemporal scales is required to advance research.

Hierarchical organization is prominent in macroscopic neural phenomenon; information enters into early sensory regions and is processed sequentially through progressively regions associated with increasingly abstract cognition.[318] The more abstract processing systems are often more diffused and operate with a slower intrinsic timescale.[319] Thus, the cerebral cortex is organized hierarchically with a gradual change in spatiotemporal scale from faster to slower processing systems. Theoretical models based on this evidence, while compelling, are often relegated to a limited spatiotemporal range. However, biology is deeply interconnected such that each system is critically influenced by macroscopic and microscopic systems. For example, the activity of a neuron is influenced by both the electrical field of the brain nucleus within which it is embedded and by the dynamics of proteins embedded in its membrane. An accurate description of a neuron cannot afford to ignore the influence of neighboring spatiotemporal systems.

The Nested Observer Windows (NOW) model describes an information integration hierarchy, in which "windows" integrate information and are nested within each other such that information is integrated vertically across scales (Figure 8.1(a)). The NOW model describes the formation of a window that integrate information, how information is shared among windows at a spatiotemporal scale via functional networks, and between windows hierarchically organized across spatiotemporal scales. The principles of the NOW

model are universal such that they can be applied across multiple scales relevant to human cognition. Here, we explore three fundamentally distinct levels and present evidence for the NOW model at each level - the nucleus, the neuron, and the protein (Figure 8.1(b)). Each of these biological windows form a functional network with its spatiotemporal neighbors - a network of brain nuclei, a circuit of neurons, and a pathway of proteins. Furthermore, each nucleus comprises neurons that in turn comprise proteins.

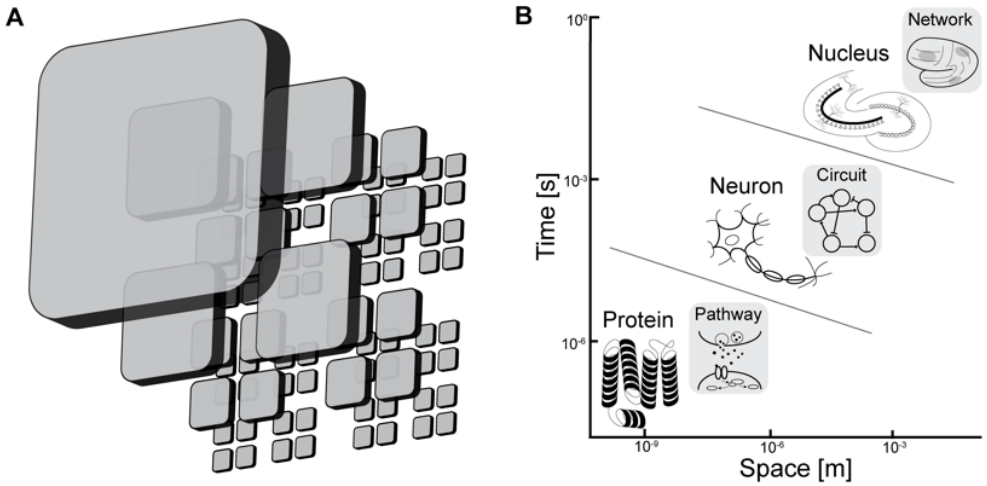

FIGURE 8.1: The Nested Observer Window (NOW) model describes how information is integrated hierarchically across spatiotemporal scales. (a) Depicted artistically, the NOW model describes how windows are formed that integrate information. These windows are nested within each other such that information can be integrated across spatiotemporal scales. Despite evidence that various spatiotemporal scales contribute to cognitive processes, a general model for how these scales interact is required. (b) Evidence for the NOW model is presented for biological windows from three distinct spatiotemporal scales –brain nuclei, neurons, and proteins. Each of these units form a functional network with its neighbors: a network of brain regions, a circuit of neurons, and a pathway of proteins (denoted by a grey box). Research often focuses exclusively on a single spatiotemporal scale (grey line dividing scales).

The NOW model provides a basic framework in which to investigate information integration within a window, among windows in a spatiotemporal scale, and between windows across spatiotemporal scales based on three basic principles: synchrony, coherence, and

cross-frequency coupling (Figure 8.2). The model was designed to include the fewest parameters and the greatest explanatory power. First, observer windows, defined by a high degree of internal synchrony such that component parts function as a single unit, are the basic units of information integration in biology. Observer windows require dedicated biological infrastructure and are defined by low internal entropy, near instantaneous internal information transfer, and a barrier to prevent environmental disruption. An observer window can be quantified by zero phase lag correlation for signals within the observer window. Once an observer window is formed, information is integrated over a brief period of time and then is refreshed.[319–321] The refresh rate of an observer windows is the frequency with peak power after spectral decomposition (e.g. Fourier Transform). Second, transient coherence of the refresh rate of two or more observer windows creates a functional network.[322–324] Functional networks transfer information laterally between observer windows within a spatiotemporal scale. Coherence is distinguishable from synchrony because observer windows that are coherent retain their independence and are only weakly coupled. While synchrony is defined as zero phase-lag, coherent observer windows have a non-zero phase-lag, as transmitted signals have physical limitations. Coherence is best quantified by metrics that exclude zero-lag coupling, such as weighted phase lag index ($wPLI$).[325] Third, observer windows are nested, meaning each window comprises sub-windows at a faster-smaller spatiotemporal scale. Similarly, each observer window can be a sub-window of an observer window at a slower-larger spatiotemporal scale. Nested observer windows orchestrate information integration by cross-frequency coupling.[326–328] For example, phase-amplitude coupling (PAC) is the strength of coupling between the phase of a low-frequency observer window at a larger-slower spatiotemporal scale and the amplitude of a high-frequency observer windows at a smaller-faster spatiotemporal scale. The NOW model is evident in nuclei, neurons, and

proteins with implications for understanding subjective experience.

8.1.1 Definitions in the Nested Observer Window Model

In neuroscience, oscillatory firing of of brain regions are common. To quantify synchrony, coherence, and cross-freqeuncy coupling of those signals, the following definitions are used. An *Observer Window* is the fundamental unit of information integration created by high synchrony. Information is integrated over a brief period of time, which sets a refresh rate for the observer window.

Synchrony is low entropy within a tightly coupled system often created by reducing environmental influence using a physical or electrical barrier. Synchrony can be quantified by a zero-phase lag relationship between two time domain signals, a positive correlation coefficient:

$$r = \frac{\sum_{t=1}^{N}(A_t - \mu_A)(B_t - \mu_B)}{\sqrt{\sum_{t=1}^{N}(A_t - \mu_A)^2 \sum_{t=1}^{N}(B_t - \mu_B)^2}}$$

where μ is the mean of the signal, N is number time points, t is time, A and B are signals

Coherence is weak coupling between observer windows that functions to transiently align their refresh rate such that information is shared laterally within a spatiotemporal scale. Coherence forms functional networks of observer windows. Coherence can be quantified as a non-zero phase-lag between coupled signals,

$$wPLI = |\sum_{t=1}^{N} imag(\mathcal{H}(C) \times \overline{\mathcal{H}(D)}|$$

where, $\mathcal{H}$ is the Hilbert transform, and *imag* takes the imaginary component

Cross-frequency Coupling is the coupling between spatiotemporal scales, e.g. the phase of a low-frequency observer window is coupled to the amplitude of a high-frequency observer window. As observer windows comprise observer windows, cross-frequency coupling allows information to be shared vertically between observer windows in neighboring spatiotemporal scales. One form of cross-frequency coupling is *Phase-Amplitude Coupling* and can be defined as:

$$PAC = |\frac{\sum_{t=1}^{N} M_C \times e^{i\theta A}}{N}|$$

where M is magnitude, θ is the phase angle of two complex exponential oscillations

8.2 Synchrony: Formation of an Obsever Window

Structure without process is inert. With LEDs attached to the limbs of a human walking through the night, the human form is easily recognizable from the coherent movement of the lights; but when the individual stands still, there is nothing recognizable as human. Biological function requires an anatomical foundation, but information processing necessitates dynamic activity. Just as the motion of a human is inferred from the synchronized movement of the lights, synchrony is proposed to be the foundation of information integration in biology. An observer window is defined as a biological system with high internal synchrony, often by formation of a barrier from the environment and synchrony is typically maintained with an electric field. In essence, synchrony establishes a single functional unit, an observer window, from a set of previously independent parts. When parts of an observer window are measured, the signals are highly correlated meaning that there the signals are of matched frequency and the phase lag approaches zero. In the

NOW model, observer windows dynamically integrate information. When an observer window is "opened" information is integrated and bound into a single gestalt representation. Then, the window is shut and the process is refreshed.

8.2.1 Synchrony in Nuclei, Neurons, and Proteins

Neurons are insulated from the environment by a phospholipid bilayer membrane that acts as an electrical capacitor. Protein batteries, e.g. sodium-potassium ATP pump, shuttle ions across the phospholipid bilayer membrane and create a strong electric gradient that builds capacitance. The resulting electric field within a neuron synchronizes electrical impulses that enter the cell membrane (near-zero phase-lag). Thus, neurons are observer windows by virtue of their strong internal synchrony. As other neurons generate electrical impulses that are transmitted to a neuron through chemical synapses, the post-synaptic electrical potentials accumulate and superpose in the synchronized electric field within the neuron. The integration time of an observer window of a neuron is determined by the duration of time that the generated voltage differential propagates within its intracellular space. If the integration of electric potentials breaches threshold to open voltage-gated sodium channels, then a neuron undergoes an action potential - the primary behavior of a neuron. The temporal window for electrical summation within a neuron, the refresh rate of the observer window, is at a timescale on the order of milliseconds. After producing an action potential, a neuron undergoes a period of hyperpolarization that reduces its sensitivity to new inputs. Thus, an observer window is opened for a brief period as a neuron integrate incoming electrical signals; then the observer window is closed for a period and, finally, refreshed. The rhythmic refresh rate of a neuron is in the kilohertz timescale and is defined by the time scale of electrical integration, not the firing rate per

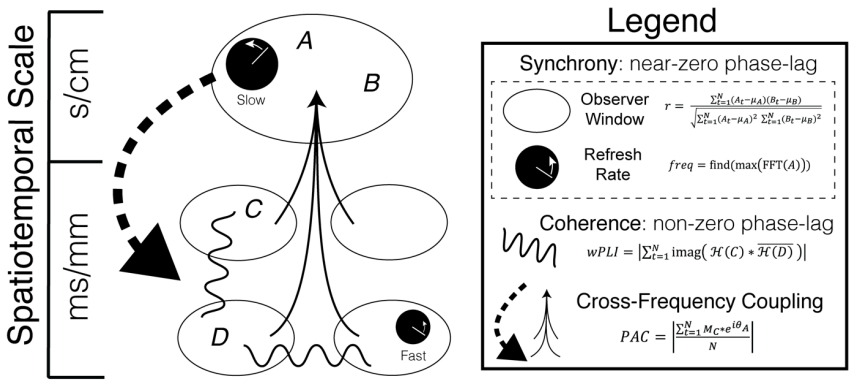

FIGURE 8.2: The three principles of the Nested Observer Window (NOW) model. The NOW model is based on three principles that describe a hierarchy of observer windows nested within each other that coordinate to integrate information. (1) Synchrony is a strong coupling between components with nearly zero phase-lag that forms an observer window. A positive correlation coefficient (r) quantifies two signals A and B that are in synchrony (see section 8.1.1). N is the number of time points. t is time. μ is mean of the signal. Each observer window has a refresh rate at which information is integrated. The refresh rate is the frequency (freq [Hz]) with the maximum power after Fourier transform. (2) Coherence is weak coupling between observer windows that functions to transiently align their refresh rate such that information is shared laterally within a spatiotemporal scale, i.e. functional networks. Coherence is quantified as a non-zero phase-lag between coupled signals such: weighted phase lag index ($wPLI$) is the magnitude of the sum of the imaginary component of the cross-spectral density of two signals. $\mathcal{H}$ is the Hilbert transform and assumes that C and D are band-limited signals with nearly the same refresh rate (see section 8.1.1). *imag* takes the imaginary component. (3) Cross-frequency Coupling is coupling between spatiotemporal scales. For example, phase-amplitude coupling (PAC) is when the phase of a low-frequency observer window (θ_A) is coupled to the amplitude of a high-frequency observer window (M_C) (see section 8.1.1). As observer windows comprise observer windows, cross-frequency coupling allows information to be shared vertically between observer windows in neighboring spatiotemporal scales.

se.

A nuance of observer windows observable in neurons, is that neurons can be electrically coupled to one another via gap junctions, or electrical synapses. Gap junctions are ion channels that are embedded into two different neurons that are directly linked such that the intracellular space of the two neurons is shared. The fused neurons share an electric potential such that their internal electric fields exhibit synchrony with each other. Electrically coupled neurons will generate action potentials in unison. Under these circumstances, the observer windows of each neuron connected by a gap junction are merged into a single observer window. This example illustrates how synchrony determines the boundary of an observer window.

Within a nucleus of 100s of thousands to millions of neurons, mesoscopic electric fields emerge from the synchronous activation of neurons.[329] For example, the architecture of the cerebral cortex is designed to facilitate the emergence of mesoscopic electric fields via ephaptic coupling. The axons of excitatory pyramidal neurons are arranged in parallel such that electric potential from one neuron will maximally impinge on its neighbors and produce electric current. With mass action of a sufficient number of neurons, a mesoscale electric field is generated with strong synchrony in the local region.[330] The electric field depolarizes and hyperpolarizes swaths of neurons in unison (near-zero phase-lag). The synchrony is strong enough that the electric fields are observable from the scalp using electroencephalography (EEG). Electric fields are the basis for the formation of observer windows in brain nuclei. While the electric field is generated by neural activity, the field itself then modulates neural activity in what is sometimes referred to as "circular causality".[331, 332] Once generated, the field is susceptible to mesoscale forces independent of any single neuron.

The hippocampus, a nucleus in the limbic system, exhibits synchronized electric fields, typically from 4 to 8 Hz in humans, that depolarize and hyperpolarize entire populations of neurons in synchrony.[333] As with most neural oscillations in nuclei, half of the cycle of a theta oscillation is characterized by excitatory activity, in which information is integrated, and half is associated with relative inactivity.[334] Features of neural oscillations in a brain nucleus can be used to decode task relevant information. For example, using only the amplitude and phase of theta oscillations across the hippocampus researchers decoded the location of a rat within a maze.[335] This decoding of position from hippocampal theta oscillations was more robust to noise than decoding approaches that used only neural spiking information. Although discovered in navigation, hippocampal theta oscillations play a critical role in a wider variety of cognitive processes such as memory formation.[336, 337]

Finally, synchrony is essential to the functional dynamics of a protein as it enables the millions of atoms within a protein to serve as a single functional unit. As experiments probing single protein structural fluctuations have demonstrated, each protein has a finite set of meta-stable molecular folding arrangements, called conformation states. In each of these conformation states, the vast majority of forces acting within the proteins are held in balance. However, a relatively small perturbation from the environment can trigger the collective conformational change such as loop or helix motion of the protein on the timescale of $\sim$10-100s of microseconds (near-zero phase-lag).[338, 339] Just as a neuron receives inputs in the form of chemical and electrical signals, proteins integrate information available in its local environment in the form of electron transfers and chemical bonds with neighbors. These environmental forces can push the protein to biological action, often in the form of a conformational change or phosphorylation of a neighboring

protein.

Some proteins may be sensitive to multiple information streams and their biological action integrates this information. For example, NMDA receptors are sensitive to changing voltage gradients and require ligands to bind to specific receptor sites. In this manner, NMDA receptors integrate information from two different sources (pre-synaptic chemical binding) and (post-synaptic intracellular voltage gradient) into a single biological action, the opening of its ion channel. Voltage-gated ion channels are often studied for their simplicity of having two primary conformation states (open and closed), and one state (the open state) is associated with a clear biological outcome. The rate of switching between the two conformational states has temporal limitations such that after biological action, proteins undergo a period of inactivity while the system is refreshed. Experiments with single voltage-gated ion channels that correlate current flow with conformational changes demonstrated that these proteins have characteristic timescales of opening and closing. While ion channels often display a wide distribution of timeframes for which they can remain closed, there is a distinct timescale at which they stay open.[340] When the ion channel is closed, it is primed to be opened and integrates information to trigger the event. After opening, it is inactivated for a brief period of time, e.g. by an ion that plugs the channel. Once the ion is stochastically dislodged, the receptor is refreshed and a new window is opened for information integration. These dynamics provide constraints on the rate at which proteins integrate information.

Just as neurons can be linked via gap junctions so that the synchronization boundary extends to encompass multiple neurons into a single observer window, complexes of proteins built from protein sub-units also highlight how synchronization binds disparate functional subunits into a single information integrating unit. Although sub-units

may perform functions individually, the formation of larger cooperative units allows for greater efficacy in their functionality. One representative example is globin, which is a protein sub-unit that can be utilized both individually and collectively. One major function of globin is to transport ligands, like oxygen, that bind probabilistically according to their concentration. Hemoglobin is a protein complex of four synchronized globin units. The binding of a ligand to one sub-unit triggers a structural shift of the entire protein complex so that the binding affinity of the other globin units is increased.[341] Although hemoglobin is constituted of multiple protein subunits, the hemoglobin is functionally synchronized such that all subunits adsorb and desorb ligands at once. When hemoglobin is in blood, the "all-or-nothing" response to oxygen concentration increases efficiency of oxygen transport. When moving from the oxygen-rich lungs to an oxygen-depleted region, either all of the oxygen is adsorbed or all released, as opposed to having individual subunits stochastically responding.[342]

Altogether, synchrony forms observer windows in nuclei, neurons, and proteins. Observer windows integrate information over brief periods of time determined by its spatiotemporal scale. After an observer window activates (e.g. action potential or conformation change), there is a subsequent inactivation period that gives rise to rhythmic cycles of activity - the refresh rate. The NOW model proposes that observer windows integrate information in rhythmic cycles. The implications to cognition and the instantiation of rhythmic cycles is explored in the next section.

8.2.2 Binding by Synchrony: Discrete Perception in Observer Windows

In psychology, the binding problem is the question of how a single perceptual gestalt is generated from information streams.[343] For example, the perception of a "chair" requires that many brain nuclei compute various aspects of the chair. The color visual system computes the hue and luminance of the chair. The ventral stream of the visual system computes the identity of the chair as an inanimate tool. The motor system computes the various ways the body could utilize the chair. The sensory cortex processes the predicted texture and feeling of the chair. All of these features for the chair are computed in dedicated observer windows in different brain nuclei, but how do these pieces of information become integrated and "bound" together into a single chair? One proposed mechanism for solving the binding problem is binding by synchrony.[344] In this framework, information that is sent to a brain nucleus is accumulated and bound together into a single integrated representation by synchrony. Synchrony defines an observer window and is the mechanism by which information is integrated in discrete time frames. With each refresh of the observer window, a gestalt representation is formed.

Each observer window has a refresh rate, or time constant, over which information can be integrated, such that information acquired in separate cycles is integrated into different gestalt representation. For example, the refresh rate of an observer window in the visual cortex is theorized to be determined by the peak frequency of the electric oscillations that synchronize the cortex, typically from 8-12 Hertz in the visual cortex, which is referred to as the alpha oscillation.[345] With each cycle of an alpha oscillations, visual information is integrated and then visual processing is suppressed as the mesoscopic electric field fluctuations determine a flickering sensitivity to incoming visual information.[346] When

a brief visual stimulus is presented to the retina, the phase of alpha oscillations in visual cortex is predictive of perceptual awareness.[347, 348] If visual information reaches visual cortex when the observer window is open, then the stimulus is more likely to reach awareness and be detected.

Since observer windows are proposed to exhibit discrete rhythmic dynamics, the presentation of dynamic stimuli to an observer window should result in perceptual illusions. While watching a film, a human perceives the actors to be moving continuously through space. In actuality, a television screen is refreshed at around 24 frames per second. The flickering images on the screen are quick enough that the transition between images is imperceptible to human perception. The consecutive images are bound together into a slower observer window via synchrony within the visual cortex. When multiple stimuli are presented consecutively, the refresh rate of the observer window relative to the rate of stimulus presentation determines how perception is shaped.

When a light is flashed twice in rapid succession, the perceiver will have the illusory experience of a single flash of light when the time between flashes is brief. The two flashes are considered to have fused. However, with enough time between each flash the observer sees a flicker of two distinct flashes. The precise inter-stimulus-interval at which the two flashes are said to shift from a flicker into a fusion is called the *flicker-fusion rate*. The flicker-fusion rate of visual perception is predicted from the peak oscillatory frequency of alpha oscillations in the visual cortex (Figure 8.3).[321] Participants with a faster alpha oscillation in visual cortex were able to perceive a flicker with a shorter inter-stimulus-interval relative to those with a slower alpha oscillation. If the two flashes fall within a single cycle of the alpha oscillation, then the information of each flash is integrated into a single observer window.[349] If the two flashes fall within separate cycles of an alpha

oscillation, then an observer window is refreshed and each flash will be integrated in different windows; and, thus, the two flashes are not integrated into a single flash. Similarly, when watching a film, the frame rate exceeds the refresh rate of the visual cortex and thus multiple frames are integrated into a single observer window. The integration of two or more frames of a film into a single observer window creates a gestalt representation of motion. With observer windows as the primary unit of information integration, perception is understood to flicker in dedicated frequency bands leading to the conclusion that perception is discrete and not continuous.[345] An additional illustrative example of frequency tuning of observer windows comes from the human language system.

Continuous human language is integrated as discrete phonemes in the theta frequency band (5-8Hz).[350] Speech is conveyed at a consistent rate across diverse cultures such that the speech envelope is consistently around 4-8 Hertz, the theta frequency band.[351] The theta frequency is a prominent frequency of human electrical brain activity, suggesting that language evolved with a carrier frequency optimized for integration into auditory and secondary association nuclei of the brain. A phoneme, typically a syllable, is the smallest unit of meaning conveyed via linguistic articulation. Phonemes within a sentence are parsed by the brain with an expectation for this temporal structure. A brain nucleus responsible for linguistic processing, such as primary auditory cortex, opens an observer window and the articulation is integrated into a gestalt representation of the phoneme. This gestalt is prepared for processing by other brain nuclei. Then, the observer window is refreshed and the next phoneme is integrated. Electrophysiology shows phase locking of theta frequency neural oscillations in auditory cortex to the speech envelope, and that this phase locking is greater when language is more intelligible to the listener.[352]

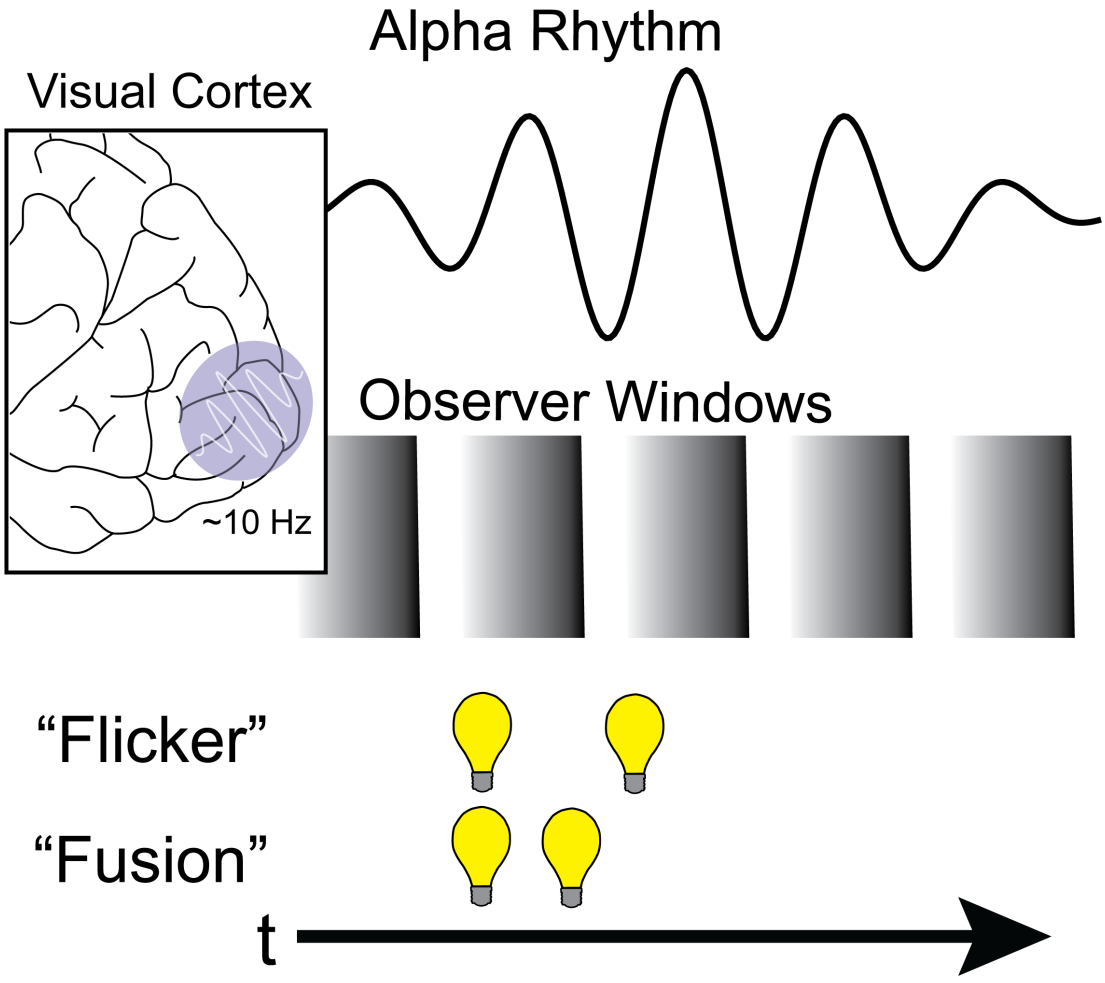

FIGURE 8.3: Flicker-fusion rate highlights observer window dynamics. Observer windows define a period of receptivity to integrate information. The visual cortex is a nucleus with a refresh rate determined by the frequency of alpha oscillations, typically around 10 Hertz. When two flashes of light (depicted as light bulbs) are presented within a single observer window, the stimuli are integrated into a single flash of light and appear to fuse. If the stimuli are received by different observer windows, then the two flashes are not integrated together and appear to flicker.

The strong correspondence between neural oscillations and cognition provides supporting evidence for the role of observer windows as described by the NOW model in information integration. Consistent with the definition of an observer window, experiments on neural oscillations find two different phases of neural oscillations. One phase is dedicated to the accumulation of information (typically the "up" state of the oscillation). In the second phase, on-going activity is suppressed (typically the "down" state of the oscillation) that creates a blank slate upon which new information can be integrated in the next up-state.[334] In the NOW model, synchrony is the fundamental principle by which biology is able to integrate information. In a chaotic environment, the creation of an observer window requires the evolution of dedicated biological infrastructure with the capacity for strong internal synchrony. In this section, three candidate observer windows were identified and evidence was provided for their role in integrating information at discrete time intervals. The following sections discuss the interactions between observer windows: laterally via coherence (Section 8.3) and vertically via cross-frequency coupling (Section 8.4).

8.2.3 Testable Predictions and Open Questions

The NOW model predicts that information integration occurs in rhythmic intervals at all scales of biology. Despite mounting evidence for the causal role of rhythmic activity in the function of neurons and brain nuclei, experiments on the temporal dynamics of proteins faces methodological limitations because the sampling rate of the measuring device must surpass the rate of the dynamic activity being investigated. Modern techniques that probe protein structure, such as NMR, Electron Microscopy, and X-ray crystallography, are biased towards rigid, inflexible proteins, while the amount of structural change

between free and bound proteins is thought to be a marker of strong influence in signaling.[353] However, there is evidence that an indicator for whether a protein is amenable to signaling is its intrinsic flexibility in its free state. The more flexible a protein, the larger the conformational difference observed upon binding.[354] Current techniques are good at capturing protein structures with long-lived assemblies, but many short-lived interactions involved in cell signaling are harder to characterize and thus less understood.[355, 356] Emerging technologies using either force spectroscopy tools (such as optical tweezers or atomic force microscopy) or fluorescence based methods to study proteins at a single molecule level are revealing additional mechanistic details about protein-protein interaction dynamics.[357] As measuring devices begin to allow for recording of trajectories of single protein conformations in time, the NOW model predicts that proteins have a rhythmic pattern of sensitivity and insensitivity with an oscillatory signature. The oscillation of a protein may have implications for between protein interaction (Section 8.3) or the protein-cellular interface (Section 8.4). Future research could run Fourier analysis on the time course of conformation changes and correlate this activity with generated product or cellular action.

At the scale of brain nuclei, regions of subcortex display clear delineation at the boundary between nuclei. For example, the hippocampus and nucleus accumbens display characteristic neural architecture with robust oscillatory electrical activity. However, the cerebral cortex often has much fuzzier boundaries between regions, or functional areas. The NOW model suggests that nuclei in the cerebral cortex form synchronized observer windows, but large-scale electrophysiology in cerebral cortex is required to validate whether electrical activity originates in demarcated functional regions of the cerebral cortex. Some

evidence for delineation comes from functional mapping of the cerebral cortex that discovered discrete retinotopic maps in primary and higher-order visual cortex. The NOW model predicts that these maps may display a stronger degree of internal electrical synchrony (near-zero phase lag) relative to any coherence between neighboring retinotopic maps (non-zero phase lag).

For simplicity, this chapter focuses on the role of neurons in information integration. However, other cells in the brain, e.g. glial cells, and cells throughout the body, might act as observer windows. The purpose of this chapter is to provide a general framework to inspire future investigation and is not intended to be an exhaustive survey of all biological activity that contributes to cognition. Furthermore, each experimental paradigm that attempts to relate a cognitive construct to a neural phenomenon is subject to a range of valid edge cases and exceptions, or may be subject to experimenter bias.

A critical, yet unknown, parameter of the NOW model is the time constants for which an observer window is open, and the time constant for which it is closed. With the two-flash experiment presented in this section, the two flashes presented in rapid succession might be fused due to integration of the information within a single observer window, or the information for one of the flashes might be loss during the inactivation period after the observer window is closed. The relative difference in time constants for opening and closing observer windows may differ significantly by system or possess a, yet unknown, standard ratio.

The NOW model suggests that the rhythmic activity in observer windows is the basis for discrete perception and action. Therefore, future work should continue to explore the discretization of cognition. Higher-order cognition that operates at a time scale that aligns

with measurable electrical activity is a prime candidate for cognitive neuroscience investigation. Furthermore, some domains of psychology have established spatial correlates such as the precuneus in mind-wandering [358], but currently lack a temporal signature.

8.3 Coherence: Lateral Information-Processing within Functional Networks

The second principle of the NOW model is that observer windows coordinate lateral information transfer via coherence. Coherence is a weaker form of coupling with a non-zero phase lag compared to the strong coupling with a near-zero phase lag in synchrony. An analogy useful to understand the distinction between coherence and synchrony is human conversation. As two humans carry out a conversation, each individual maintains strong internal synchrony. If the conversation is productive, then the exchange of information between the two individuals is facilitated and the two conversationalists communicate coherently. One speaker talks, while the other listens (i.e. a non-zero phase-lag); then, roles are reversed. The weak and phase-lagged coupling in conversation does not suggest that the two individuals merge into a single synchronized individual. The NOW model proposes that when two observer windows communicate, their observer windows become coherent and information is transferred between the two but with conduction delays determined by physical limitations, similar to human conversation. Each observer window accumulates information from the other and integrates that information with other inputs. However, the two observer windows are not considered to be a single observer window and the coherence is often transient. Consistent with this theoretical framework,

brain nuclei temporarily display coherent electric field oscillations during periods of increased information transfer.

8.3.1 Communication through Coherence

Two spatially separated brain nuclei occasionally align their electric field oscillations such that each neural population will be roughly depolarized and hyperpolarized with a consistent phase lag to transmit signals. The transient and lagged alignment of electric oscillations in brain nuclei is coherence. When neurons are connected via chemical synapse between two regions that are exhibiting coherent electric field oscillations, the action potential from a neuron in one nucleus is more likely to be received by a neuron in the second nucleus at a time when it is receptive to incoming inputs. Then, during the hyperpolarization phase of the oscillation, both nuclei are desensitized to incoming information. Pascal Fries proposed that brain nuclei utilize oscillating electric fields to establish functional network of interconnected nuclei of the brain to facilitate the exchange of information.[322, 359] Fries defined the formation of functional networks via alignment of electric fields as "neuronal communication through neuronal coherence." For example, a multimodal brain region may receive diverse inputs from a variety of nuclei.[360] At a given time, only a subset of pathways may be relevant to the current information processing demands.[361] If the multimodal association region needs to dedicate its resources to a subset of brain nuclei, then it aligns its electric field oscillations with the relevant brain nuclei so that inputs from these observer windows are preferentially received as opposed to a brain nucleus transmitting irrelevant information.[362] The temporal dynamics of electric fields are not strictly dependent on the synaptic strengths of connected region, and thus allows for increased flexibility as processing demands change (Figure 8.4).

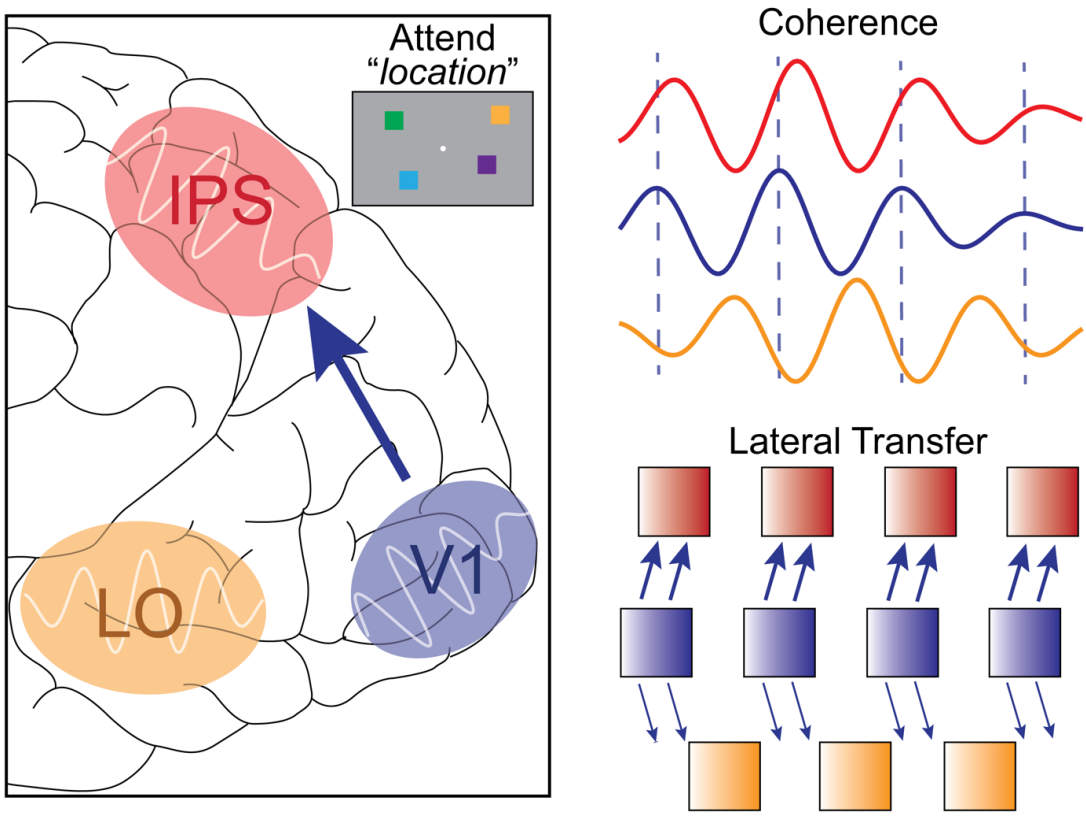

FIGURE 8.4: Coherence facilitates the lateral transfer of information between observer windows. In a cognitive control task, in which participants must attend to either location or color, visual information in the primary visual cortex (V1 in blue) will preferentially transfer information to a nucleus dedicated to spatial information integration (intraparietal sulcus (IPS) in red) and not to a nucleus dedicated to object-oriented stimulus properties (lateral occipital (LO) in yellow). Electric field activity will increase in coherence between V1 and IPS greater than between V1 and LO. Signals (blue arrows) from V1 (blue square) impinge on the window of the IPS (red square), but miss the window of the lateral occipital cortex (yellow square). The blue arrows depict the physical limitations for transferring a signal and illustrates the requirement of a non-zero phase-lag between coherent observer windows.

At the level of neurons, synaptic connections are organized in a manner such that rhythmic patterns of activity are generated. The principle of coherence plays a primary role. One common motif in neural circuits for generating coherence are central pattern generators.[363] A simple central pattern generator, the half-center oscillator, requires two neurons that are reciprocally connected with inhibitory synapses such that the activation of neuron A inhibits neuron B. With the release of inhibition, neuron B is more likely to fire and inhibit neuron A. The pattern repeats. The half-center oscillator creates a rhythmic oscillation. However, this emergent oscillation is unstable and easily modulated by other neural inputs. The neurons are coherent, but are not synchronized because coherence maintains the relative independence of each neuron. Instead, coherence allows for transient periods of coupled activity with a non-zero phase-lag for chemical transmission; coherence can also be transiently achieved by simultaneous driving inputs from a third neuron.

At the protein level, transient protein-protein interactions modulate protein activity, stability, and localization, which regulate the function of signal transduction, homeostasis, and organ formation.[364, 365] It is thought that proteins communicate through the movement of particles, such as electrons, charged ions [366], or molecules, that can cause conformation changes or chemical reactions such as phosphorylation. This paradigm is seen in metabolic pathways, which coordinate numerous types of proteins into an assembly chain of chemical reactions that generate products necessary for cellular function and organize complex cellular changes. In order to avoid overproducing intermediate products that may cause bottlenecks or underproducing essential molecules required for survival, metabolic pathways require communication between proteins to ensure a smooth and consistent output of final product. One way that these particles affect the activity of a

protein is through allosteric regulation. Proteins are generally conceived to have a functional "active" site, where binding of ligands is directly related to the functionality of the protein, and an allosteric "regulatory" site, where effector molecules can alter the activity of the protein.[367] For example, if a negative feedback loop is desired to regulate the total amount of product generated, a protein early in the assembly chain might have an allosteric site that is sensitive to the final product. Thus, when high concentrations of the product diffuse to the upstream protein, the product molecule binds to the allosteric site, changing the conformation of the upstream protein, lowering the rate of reaction for that protein, and thus slowing production.[368] While there is ample evidence for the importance of protein-protein signaling, the inherent temporal nature of these interactions is lacking. In the NOW model, we suggest that these temporal interactions are inherently oscillatory and different feedback loops may exhibit coherence similar to the examples in the neuron and functional brain regions. Within the context of the NOW model, each protein is an observer window awaiting conditions to undergo a conformation change (the synchronous movement of millions of atoms that constitute the protein) and signaling between proteins typically happens via messenger molecules (ligands, physical limitations giving rise to a non-zero phase-lag), which trigger conformation changes. The NOW model suggests that the final product of a protein pathway is not only sensitive to the existence of a feedback loop but to the relative phase alignment between competing oscillatory feedback loops. The NOW model emphasizes that proteins pathways do not exist in isolation but are dependent on a functional network of protein interactions.[369]

Coherence is critical to orchestrating information transfer between observer windows within the same spatiotemporal level. When the refresh rates of observer windows are transiently aligned with a non-zero phase lag, information from one observer window

may be transferred to another observer window. Coherence is flexibly engaged or disengaged depending on the processing demands of the organism resulting in dynamic functional networks. In cognitive neuroscience, functional connectivity (or coherence) between brain nuclei has offered novel biological signals that uniquely relate to aspects of cognition and behavior.[370]

8.3.2 Functional Networks for Cognition

While synchronization forms observer windows for accumulating information, coherence provides a means by which independent observer windows share information with other observer windows to build complex representations. In the previous example in which the gestalt representation of a chair is generated, many brain nuclei are required to process various aspect of the chair and this information must be transferred to a higher order region of inferior temporal cortex where the identity of a chair is integrated. In order for that information to be effectively transferred to the appropriate destination, brain nuclei transiently align their electric field oscillations to establish coherent pathways of information transfer. Within this coherent functional network, information is transferred to the nucleus in inferior temporal cortex that accumulates the variety of information streams.

A rhythm essential to the transfer of perceptual features is the theta rhythm (4-8 Hz).[371] In the previous section, we explored how the theta frequency neural oscillation in the hippocampus plays a critical role in navigation and memory. The hippocampus is a critical node within an interconnected hippocampal memory network, also classified as the default mode network. Many nuclei exhibit coherence with the hippocampus during the formation of memories.[372, 373] Given the privileged role of the hippocampus in memory formation, many perceptual and behavioral systems regularly exhibit coherence with

the hippocampus in order to laterally share their information so that it can be bound into an integrated episodic memory. For example, the auditory cortex and language processing nuclei readily establish coherence with the hippocampus as language is perceived in the theta frequency band.[350, 374] In addition, the oculomotor network initiates saccadic eye movement in the theta range which results in a phase reset within the hippocampus during active visual exploration.[375] Thus, visual and auditory systems in the human were evolutionarily tuned to resonate in theta frequency to enhance trans-modal integration via coherence.

If auditory and visual information are presented in visual flashes and auditory snippets coherently at the theta frequency, these separate percepts are more readily integrated and more efficiently encoded into memory.[371] This boost in memory encoding with coherent presentation was specific to the theta frequency, and was not witnessed if auditory and visual information was presented coherently outside of the theta frequency, either slower or faster, nor was there a boost in memory when the information was presented anti-phase in the theta frequency. Clouter et al. further performed source localization of theta frequency neural activity (magnetoencephalography) and found distinct nuclei for processing visual (primary visual cortex) and auditory (primary auditory cortex) information which resonated at theta frequency. When this information was integrated, the visual and auditory nuclei increased in phase alignment. This experiment provides direct evidence in support of the framework of the NOW model in which separate observer windows for distinct cognitive modalities become coherent to integrate information across observer windows. However, coherence does not explain how different spatiotemporal scales meaningfully interact to guide behavior and cognition. In the next section, the third principle, cross-frequency coupling, is provided as a mechanistic bridge for integrating

information across spatiotemporal scales.

8.3.3 Testable prediction and open questions

Investigation into coherence at the scale of neurons and nuclei has yielded emerging fields of study with a promising link to human cognition. However, investigation into coherence at the protein scale is difficult due to the fast temporal dynamics and limitations in temporal and spatial resolution of protein structural information. Here, we predict that the transient synchronization of oscillatory observer windows in neurons and nuclei can similarly be observed in protein-protein interactions. Analogous to how coherence is observed at larger spatial and slower temporal timescales, the oscillatory behavior of the conformations of two protein may also be transiently coherent. While it is known that proteins may dynamically interact to change their quaternary structure when triggered by, for example, ligand binding, the practical limitations to observing protein coherence are that the setting under which proteins meaningfully interact often requires naturalistic conditions (in vivo) that preclude high resolution spatial and temporal imaging. Beyond the time-frequency analysis of conformational states needed to substantiate protein observer windows discussed in section 8.2.3, the observation of protein conformational state coherence requires the tracking of protein structure of multiple populations of proteins performing biological action. The most direct evidence for protein coherence envisioned in the NOW model would involve comparing protein conformational changes under two conditions. In one condition, the proteins are functionally interacting, and the measured conformation changes may be coherent in time with a non-zero phase-lag. In another condition, the proteins are not functionally interacting and thus their conformation changes are uncorrelated in time.

At the scale of brain nuclei, certain cognitive manipulations facilitate coherence between regions. Given that higher order task instructions are often required to guide the coherence of multiple regions, research could be done to better understand how two regions come to be coherent. For example, a higher-order brain nucleus could drive functional coherence between two lower-order nuclei by phase aligning both regions into a functional network. Furthermore, certain brain nuclei have been proposed to play a privileged role in creating coherence between nuclei of functional brain networks such as the pulvinar nucleus of the thalamus [376] or the claustrum [377, 378]. Alternatively, simultaneous engagement with environment stimuli via behavior, e.g. theta frequency saccadic eye movements, may result in emergent coherence between brain regions. Future research could differentiate the mechanisms by which coherence is orchestrated by higher-order goals or is emergent from environmental influence.

Finally, an emerging field in cognitive neuroscience is the study of network properties in imaging of the whole brain.[370] These analyses have found that the brain maintains a critical balance between sparse connections and hyperconnectivity. Thus, neural states with an over expression of coherence may be detrimental to information processing, e.g. a seizure, because the balance of autonomy (synchrony) and cooperation (coherence) between regions is vital to effective information integration.

It should be noted that given the slow temporal resolution of functional MRI, the use of a correlation analysis for functional connectivity does not suggest a near-zero phase-lag between regions, but is instead a limitation of the method. For analogy, the ability to run a Fourier transform does not in principle mean that there is oscillatory activity - instead an oscillatory peak must be confirmed.[379] Similarly, for fMRI the regions in the brain assumed to be in coherence as evidenced by MEG data with sufficient temporal

resolution.[371] Furthermore, researchers often conflate correlation with coherence. If two signals are coherent, then the signals will also be correlated. However, two signals that are correlated will not necessarily by coherent with a non-zero phase-lag. Future research should explicitly differentiate these two forms of connectivity.

8.4 Cross-frequency Coupling: Bottom-up Integration and Top-down Control

Hierarchical organization provides an optimal solution to complex processing demands. Observer windows at multiple scales can specialize in information processing at different levels of abstraction and the outcome of this processing can then inform processing at other scales.[380] The NOW model posits that cross-frequency coupling is the neural mechanism by which information is integrated between spatiotemporal scales. Cross-frequency coupling is a critical biological mechanism that harnesses the nested nature of observer windows: a brain nucleus is composed of neurons that are composed of proteins. In the NOW model, bottom-up information from faster-smaller observer windows is integrated into slower-larger observer windows; and top-down control signals from slower-larger observer windows are impressed upon the activity of faster-smaller observer windows. The integration of these bottom-up information signals builds abstraction. Top-down control signals guide behavior and provide feedback for perception. Altogether, cross-frequency coupling gives rise to scale-free brain dynamics.

8.4.1 Cross-frequency Coupling between Spatiotemporal Scales

Cross-frequency coupling was first defined within the context of coupling between the scale of individual neurons and the electrical activity of brain nuclei. The first experimental demonstration of cross-frequency coupling was between high frequency activity of neurons (gamma oscillations from 30-150 Hz and spiking activity with signals up to the kilohertz range) and theta frequency oscillations (5-6 Hz) of the hippocampus (see [381] for review). Neurons are observer windows at a smaller and faster spatiotemporal scale relative to the larger and slower observer window of a hippocampus, within which neurons are nested. In a landmark study, a rat traveled through a maze with simultaneous recording of neural activity (spiking) and hippocampal electrical field activity (local field potential).[382] Neurons in the hippocampus called "place cells" fired when the rat was in a particular location.[383] As the rodent traveled through the maze, a sequence of place cells activated. The sequence of place cells that activated represented the immediate past, then present, then future in chronological order.[384] In addition, the sequence of place cell activation was locked to the electric field of the hippocampus, at a slower-larger spatiotemporal scale in theta frequency (4-8 Hz). Within the up-phase of the theta cycle, the place-cells [385] were activated in sequence; then, in the down-phase of the theta cycle, the place-cells were silenced. This pattern of activity is referred to as phase-amplitude coupling: the amplitude of high frequency gamma oscillations was locked to the phase of a theta oscillation. Hippocampal observer windows with a refresh rate in the theta range accumulate information about the location of an organism in space from a sequence of gamma observer windows. A theta observer window integrates information from gamma observer windows into a trajectory of motion. When this theta-gamma coding scheme was engaged, a trajectory of motion could be decoded from characteristics of

the theta oscillations alone.[335]

Motion is a sequencing of places, not the binding of places into a more detailed place. In the NOW model, cross-frequency coupling is a means by which perceptual information is abstracted into higher order representations by organizing or sequencing lower order information. Abstraction requires multiple spatiotemporal scales, such that a larger-slower observer window can accumulate information from smaller-faster observer windows. Since its discovery, the theta-gamma neural code was found to play an important role in a wide variety of contexts in which perceptual information must be encoded into higher order representations as is required in working memory [386, 387] and episodic memory [388]. This evidence suggests that information content originating in lower order observer windows that is integrated into a higher order observer window creates an abstracted higher order representation and this process may be a domain-general principle of information processing in biology. While the exact method of abstraction is unknown, one suggestion is a form of information compression.[389]

Cross-frequency coupling is also evident between a neuron and its proteins. Macroscopic quantities such as voltage have a direct influence on the activity of individual proteins, and the collective behavior of proteins drives neural activity. For example, one well studied intra-protein messenger is the calcium ion (Ca2+) whose concentration has also been observed to oscillate rhythmically at the cellular level.[390] Although the overall concentration of Ca2+ is a macroscopic property, it is regulated by individual proteins on a microscopic scale. Some proteins are designed for positive feedback. When one protein releases Ca2+, it diffuses to neighboring proteins triggering additional Ca2+ release. Collectively, a so called a Ca2+ wave, or Ca2+ transient, is generated. Alternatively, when a neuron produces an action potential, a Ca2+ wave is generated in its intracellular space

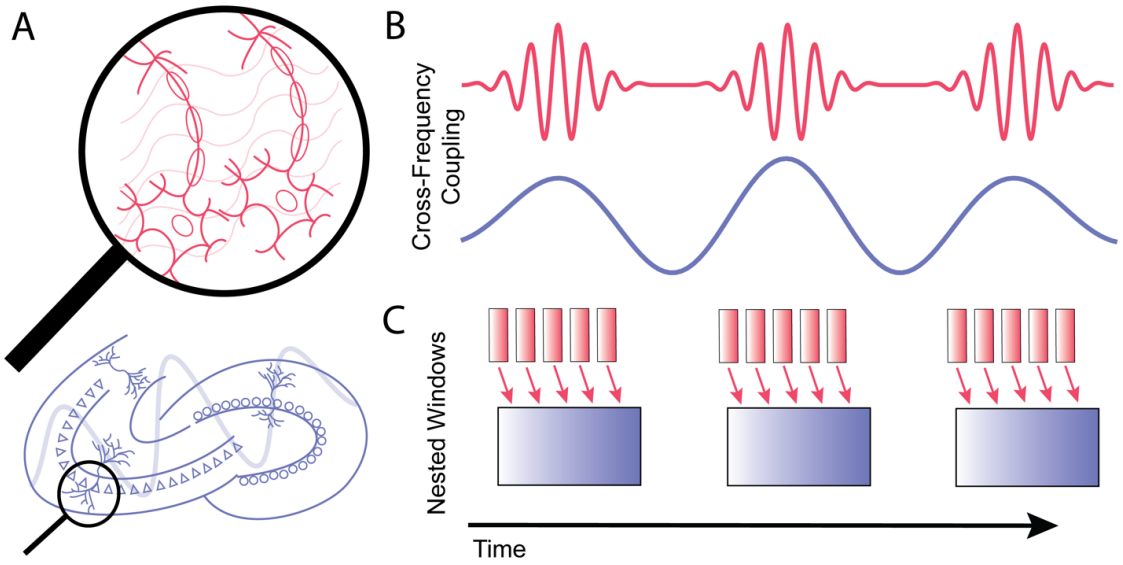

FIGURE 8.5: Cross-frequency coupling enables perceptual and motor abstraction. For example, place cells are neurons in the hippocampus that activate when the organism is in a particular location. Place cells are observer windows that activate in the gamma range (35-150 Hz). Their activity is nested within the electrical activity (4-8 Hz) of the hippocampus. Place cells are sequentially activated every cycle of the theta oscillations. The sequential activation of place cells corresponds to a series of locations in the external environment. Sequences of place cell activation are integrated in the slower-larger observer window of the hippocampus. Once integrated, the electric fields in the hippocampus encode a trajectory of motion, an abstract representation emergent from a sequencing of places.

[391] enabling the functional imaging of individual neurons from recordings at the population level.[392] Since the presence of Ca2+ triggers a wide variety proteins and protein pathways [393, 394], activity within a slower-larger observer window, a neuron, directly influences the activity of proteins at faster-smaller spatiotemporal scale via Ca2+ waves, and vice versa.

8.4.2 Abstraction by Bottom-up Integration

Cross-frequency coupling via nested observer windows may serve to build higher order abstract representations from simpler lower order representations. Here, a distinction is drawn between binding implemented via synchronization (see Section 8.2.2) and abstracting implemented via cross-frequency coupling. Binding is the integration of features into a more detailed representation that encompasses all of the individual features, whereas abstraction is an emergent property where the level of description is transformed into a higher order representation from a lower order representation through sequencing or ordering (see a theoretical model of information compression [389]).

Evidence from neuroimaging suggests an abstraction gradient along the rostral-caudal axis of the frontal cortex.[395] Information relating to the context of a situation in encoded by more rostral nuclei of the prefrontal cortex. These regions are more abstract, but not necessarily more complex or detailed than caudal regions that encode concrete actions plans. In the NOW model, a salient stimulus enters the faster-smaller perceptual observer windows. First, this concrete information becomes integrated within a smaller-faster observer window via synchrony (e.g. contrast properties in a visual scene). Then, those features emerge into a higher level of abstraction within a larger-slower observer window (e.g. an object in the foreground). The term emergence is used here because

of the bulk direction of information integration from faster-smaller observer windows into slower-larger observer windows. This causal flow leads to a temporal lag where the faster-smaller observer windows will typically activate before the slower-larger observer windows.[396] Therefore, the activation of more abstract representations will lag behind the activation of less abstract representations and will be processed in observer windows with a relatively slower refresh rate. Thus, more abstract representations are expected to be found in brain nuclei with a slower intrinsic rate of processing. Indeed regions that process more abstract information operate with a slower intrinsic processing rate.[319]

8.4.3 Top-down Cognitive Control

Cross-frequency coupling also enables top-down control signals from higher-order observer windows to constrain the activity of lower order observer windows. In the previous section, cross-frequency coupling was demonstrated to arise when lower-order information about location in neurons was abstracted into an emergent higher-order representation of a trajectory of motion. However, slow frequency oscillations in prefrontal cortex have also been found to modulate faster activity patterns in lower order regions of cortex to guide perception and behavior.[397–399] In these experiments, the research participant has information that is predictive about the timing or information content of an upcoming stimulus. This information guides the allocation of attention and thus can be utilized to modulate the processing of lower order regions according to higher order task demands. In some instances, the slower frequency oscillations in higher-order observer windows will alter the timing of the lower-order observer windows to increase its sensitivity to new information when the timing of an upcoming stimulus is known.[321, 398]

Prefrontal cortex also engages cross-frequency coupling during goal-directed behavior in a top-down manner. During a decision-making task, slow frequency oscillations in prefrontal cortex modulated the relative decision threshold for a bimanual visual discrimination task.[400] At rhythmic intervals, delta oscillations (2-4 Hertz) in prefrontal cortex preceded a change in activity in the motor cortices that updated their relative distribution of beta oscillations (15-30 Hertz). Certain cross-frequency coupling pairs such as delta-beta coupling may be particularly relevant for guiding top-down goal-directed behavior, whereas theta-gamma coupling may be particularly relevant for bottom-up perceptual processing.[401] Taken together, cross-frequency coupling provides a mechanism for bottom-up abstraction building and top-down control signaling within a nested hierarchy of observer windows.

8.4.4 Scale-free Dynamics

Cross-frequency coupling provides a generalized means of integrating information across spatiotemporal levels in the NOW model: either through abstraction into higher order perceptual information (emergence) or by guiding goal-directed behavior via the allocation of top-down control signals (submergence). If cross-frequency coupling is a general principle that guides the interaction of many spatiotemporal scales within a biological hierarchy, then recordings of the brain should find evidence of scale-free dynamics in the brain. Indeed, when recording the electrical activity of the whole brain, nuclei, neurons, and proteins, there is a prominent power law ($1/f$) in the distribution of spectral amplitude.[402, 403] This pink noise, or aperiodic signal, permeates the background spectra of almost all biological recordings: brain recordings [404], heart beats [405], neuron spiking [406], and protein surfaces [407]. An important feature of fractal mathematics is the Hurst

exponent, which describes the ratio at which a function is invariant after a transformation [408]. Essentially, any fractal equation will display a specific pattern when viewed from some perspective. Upon zooming in or zooming out, there will be novel patterns. After a determined amount of zooming, the initial pattern that was observed from the first perspective is repeated. The amount of zooming required before a fractal pattern repeats is defined by the Hurst exponent. In the NOW model, the Hurst exponent provides a mathematical description for the spatiotemporal separation between observer windows in biology (Figure 8.6). Inspired by the Hurst exponent, a novel hypothesis proposed in the NOW model is that there may not be an arbitrary, nor infinite, number of spatiotemporal scales at which observer windows are found in biology; but instead, cross-frequency coupling might be witnessed between specific spatiotemporal scales and there may be mathematical determinants for the spatiotemporal separation between observer windows across levels.

Similarly, the principles of harmonic resonance dictate that for a given standing wave there are a finite number of resonant frequencies with a numeric relationship to the original wave. Similar to the Hurst exponent, the principles of harmonic resonance suggest that there will not be an infinite, nor arbitrary, number of valid spatiotemporal scales in the brain, but instead we speculate that observer windows might occur only at distinct levels. For example, a novel approach to cross-frequency coupling proposed that coupled frequency pairs are harmonic ratios.[409]

8.4.5 Testable predictions and open questions

Cross-frequency coupling within the context of the NOW model produces novel hypotheses for future inquiry. First, the proposal that action plans may originate in higher order

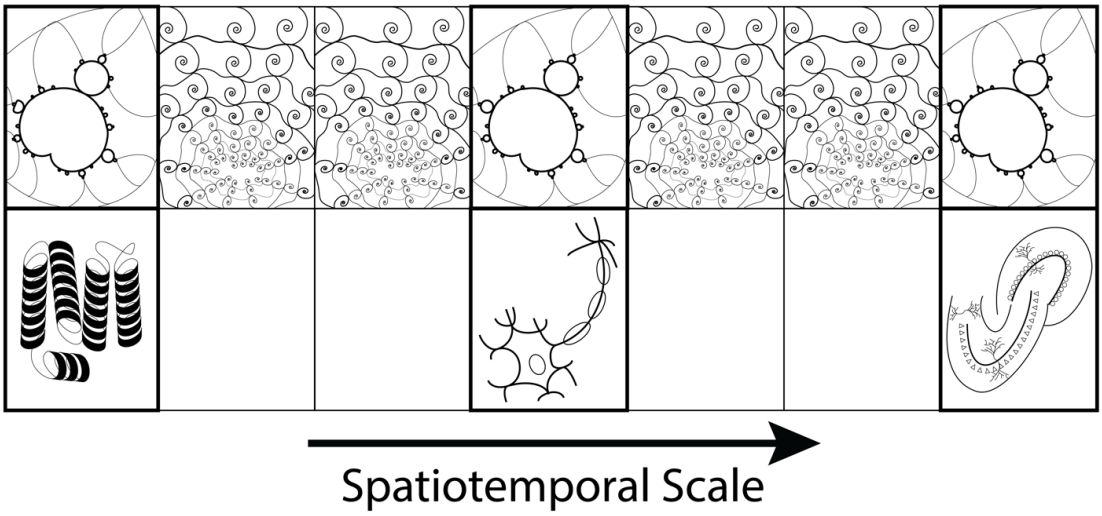

FIGURE 8.6: Depiction of the Hurst exponent in fractal mathematics. Observer windows might be found only at distinct spatiotemporal levels with a fixed interval between levels, and not found continuously, infinitely, nor arbitrarily throughout spatiotemporal scales. The Mandelbrot set is artistically depicted.

cortex in the form of low frequency oscillations has not been explicitly tested. To validate this hypothesis, two competing models must be pitted against each other: (*1*) the null model that the intent to act originates from purely bottom-up processes that emerge into higher order brain regions, and (*2*) the NOW model in which the intent to act can originate in higher order cortex, then submerge into motor cortex. In addition, cognitive states may originate in higher order cortex and submerge into lower order. For example, in mind-wandering spontaneous thoughts could originate in higher order cortex and submerge into more local activity. Another direct consequence of the NOW model is that abstract thought should correlate with increased strength of cross-frequency coupling. There is already some evidence for this in that abstract decision-making recruits greater levels of phase-amplitude coupling in prefrontal cortex.[397, 401]

Cross-frequency coupling is proposed to facilitate the sharing of information across spatiotemporal scales. While there is abundant evidence between the neural and nuclei scales, there is no direct experimental evidence for cross-frequency coupling between the protein and neural scale. Spike-triggered Ca2+ waves are proposed as a potential mechanism by which a low-frequency signal generated by neurons directly modulates the activity of proteins. To validate cross-frequency coupling between proteins and neurons, experiments would have to be run that simultaneously recorded the activity of spike-triggered Ca2+ waves in the neuron and relate that time course to the transient activation of feedback loops in protein pathways. The example of Ca2+ waves is used given the breadth of previous research, but other functionally relevant signaling molecules could be shown to exhibit cross-frequency coupling. One critical element of the NOW model with respect to cross-frequency coupling is that each spatiotemporal scale maintains functional independence within its level, but also meaningfully interacts with neighboring levels. In other words, the higher order and lower order levels cannot be one-to-one reduced to each other.

The Hurst exponent suggests that observer windows are found at specific spatiotemporal scales, but are absent at arbitrary points between those scales. An experiment to validate this prediction would investigate the occurrence of behaviorally relevant activity at scales between known observer windows, e.g. between a protein and neuron. The NOW model proposes three relevant spatiotemporal scales, proteins, neurons, and nuclei, due to the strong evidence for these biological systems. However, there may exist intermediary spatiotemporal scales, e.g. microtubules.[410] Furthermore, observer windows may exist at spatiotemporal scales relevant to cognition at more foundational level, e.g. the molecular or quantum scale, or at supervening levels, e.g. the electric field of the body [409, 411]

or between individuals in social settings [412, 413]. Computational modeling is required to establish the exact spatiotemporal separation at which observer windows occur in a human brain.

8.5 Conclusion

The Nested Observer Window (NOW) model expands language from modern cognative neuroscience to provide a framework for information integration hierarchy at new spaciotemporal scales. Biological function is deeply interdependent across spatiotemporal scales with neural function dependent simultaneously on the brain nucleus in which it is embedded and on the expression of proteins within it. Hierarchical organization is an optimal solution for processing information at multiple scales of abstraction. In order to integrate information across these spatiotemporal scales, the NOW model explains how observer windows are formed that integrate information via *synchrony*, how these observer windows share information laterally within a spatiotemporal scale via *coherence*, and vertically across spatiotemporal scales via *cross-frequency coupling*.

Supplementary Information For: Chapter 2

A.1 Assignment of Coherences to Excited State

In order to assign these modes to either the ground or excited state, we compare 2DES signal from the non-resonant solvent-only scan and PCDTBT in solvent. The solvent-only scan can be definitively assigned to the ground state owing to the fact no electronic states are accessible by pulse energy, while the PCDTBT in solvent likely contains both excited state and ground state pathways. Although nDES gains pathway selectivity through the fact the signal is radiated in a well-defined direction related to the addition of the input pulse k vectors, finite pulse lengths create issues in terms of exactly which signal is being observed.[414] Represented diagrammatically in figure A.1a, the ambiguity arises because the non-rephasing and rephasing pathways appear in the same direction depending on which pulse is considered pulse 1 and 2. The result is that if the first time delay (τ) is near 0, there exist contributions from both rephasing and non-rephasing signals as shown in figure A.1b. This means that researchers have to be careful when assigning signals to specific pathways. Based off these pathways, it' s often claimed that seeing roughly symmetric coherences along ω_T is indicative of excited state processes.[415, 416]

A thorough examination of this argument and the pathways involved can be found in ref [415]. However, as seen in figure A.1c, when the signal around $\tau = 0$ is included, signal explicitly known to be from the ground state can have symmetric features. However, when the time points around 0 are not considered, asymmetry arises in accordance with the rephasing pathway. The same procedure applied to the PCDTBT data is shown in figure A.1d. Even as a window along tau is applied, the signal symmetry does not change significantly. This allows a more definitive assignment of the coherences observed in our experiment to be originating from the excited state. To further confirm that the coherences we are observing in PCDTBT are from the excited state, non-resonant Raman was taken with an excitation wavelength of 785 nm, far from the resonant absorption. The peaks that differ between the two scans are attributed to solvent peaks, and match literature values. The peaks that do not shift between the two scans are attributed to ground state modes and also correspond to previous measurements.[417] However, these modes are not seen with appreciable intensity in the coherences detected using 2DES.

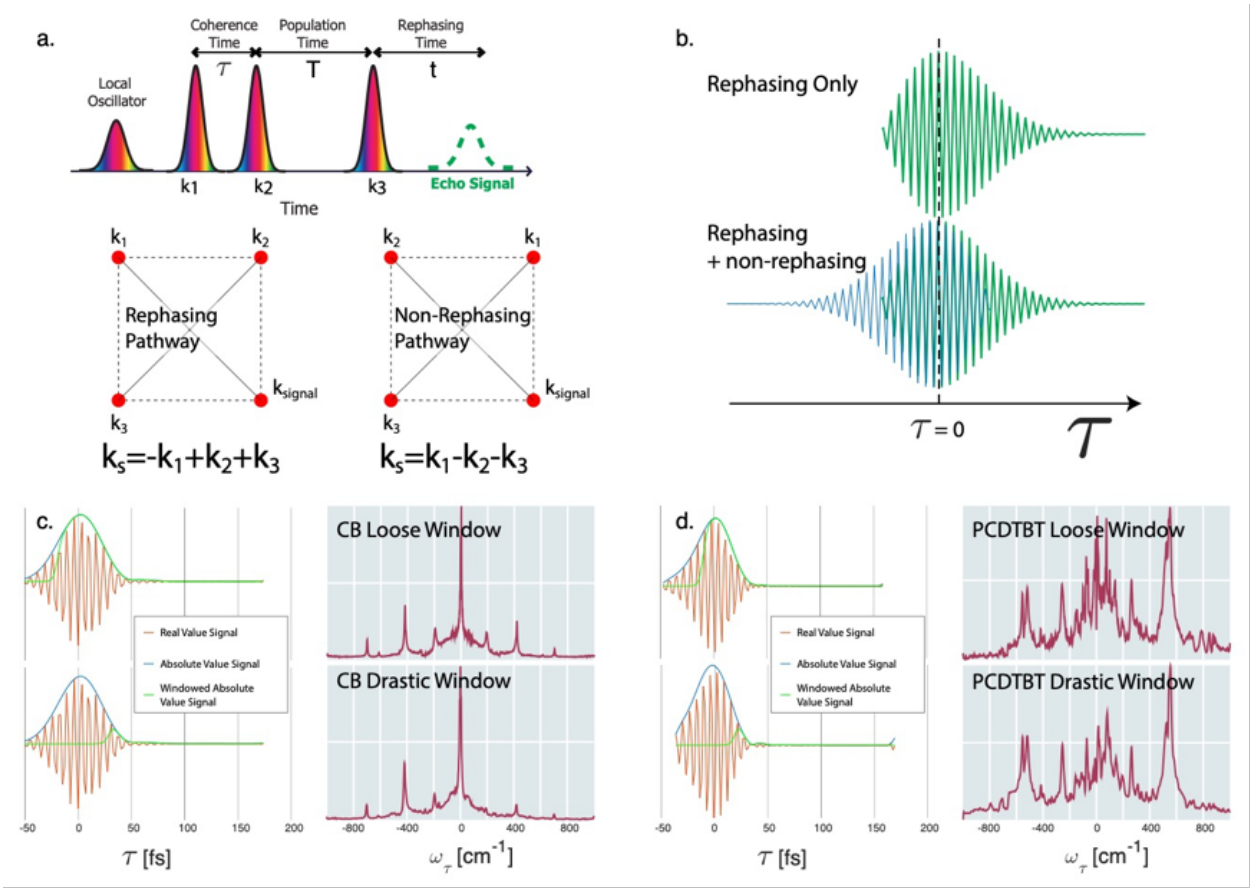

FIGURE A.1: While assignment of excited state vs ground state pathways is well established and detailed in ref [415] through the relative amplitude of positive and negative coherences along ω_T, uncertainty persists due to overlapping rephrasing and non-rephasing signals. (a) Rephasing and non-rephasing signals appear overlapped depending on which beams are considered to be beams "1" and "2" . (b) Finite pulse width causes the signal that is generated around $\tau = 0$ to be a combination of both rephasing and non-rephasing signals. (c) If points around $\tau = 0$ are not removed in analysis, signals that are known to be generated from the ground state can have symmetry indicative of excited state processes. However, when the signal is drastically windowed to not include early τ, the expected asymmetry appears. (d) This analysis applied to PCDTBT shows that the coherence symmetry does not change appreciably when τ is windowed. This along with the relative symmetry of positive and negative coherences allow for assignment of the observed vibrational modes to the excited state.

A.2 Additional Figures

A.2.1 Beatmaps for PCDTBT in Chlorobenzene

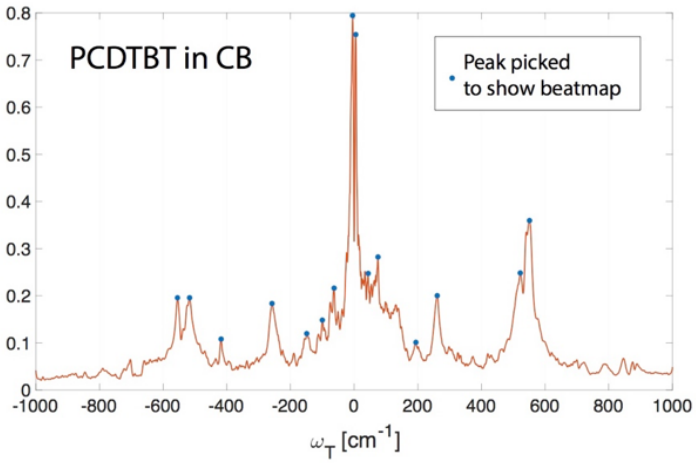

FIGURE A.2: Vibrational coherences found in PCDTBT in chlorobenzene. The blue dots serve as a guide for where the beatmaps in figure A.3 are picked from.

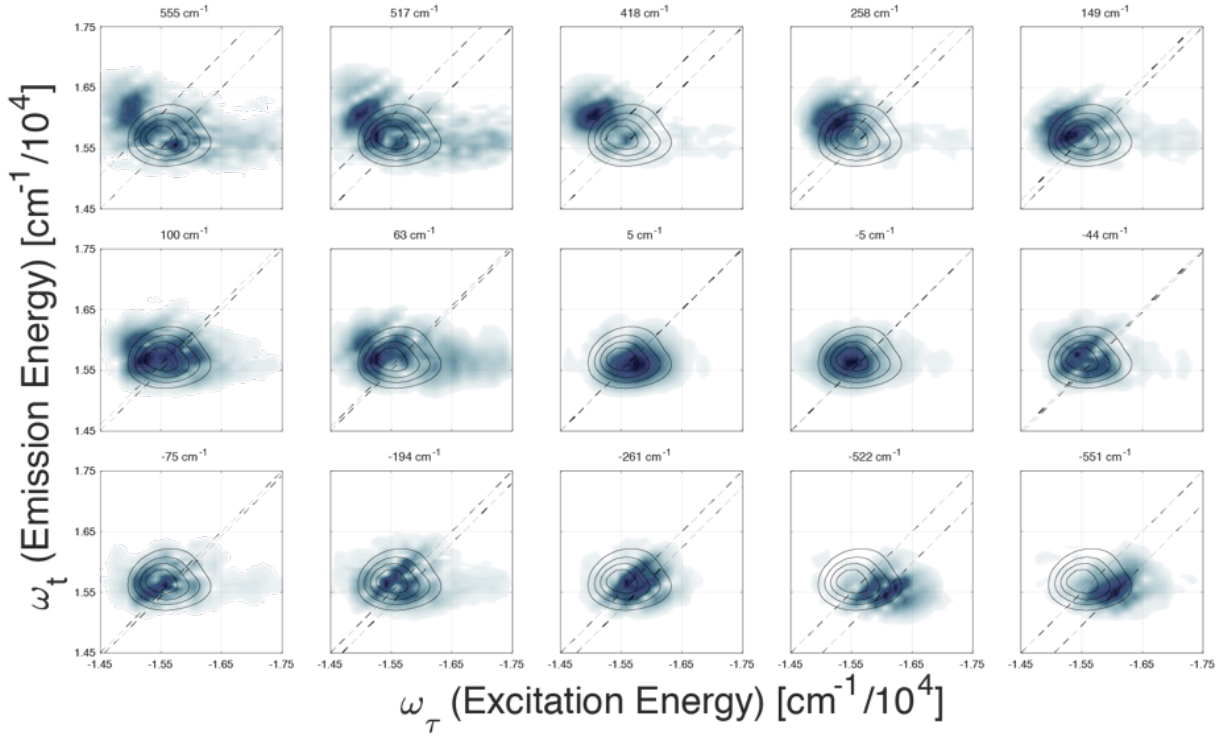

FIGURE A.3: Beatmaps of PCDTBT in chlorobenzene. Contour lines represent where the absolute value of the 2DES signal is found. The vibrational coherences are broad, making assigning modes to any particular exciton/polaron state challenging

A.2.2 Pulse Characterization

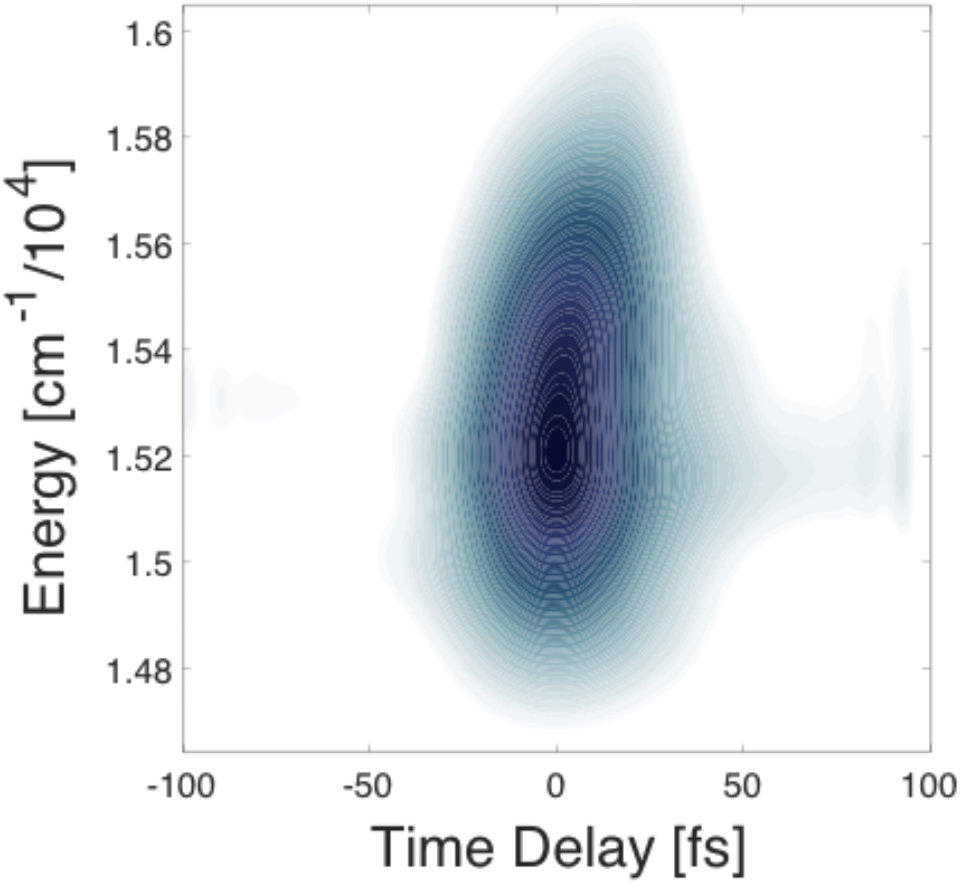

FIGURE A.4: TG-FROG signal taken from Chlorobenzene only solvent scan at the sample position. Instead of Fourier transforming along τ, a single τ point is considered and the slice of the 3D data cube is displayed as a function of time delay between pulses 2 and 3. The rise and fall of the non-resonant response shows that our pulses arrives for different colors at the same time

A.2.3 All TA DAS Components

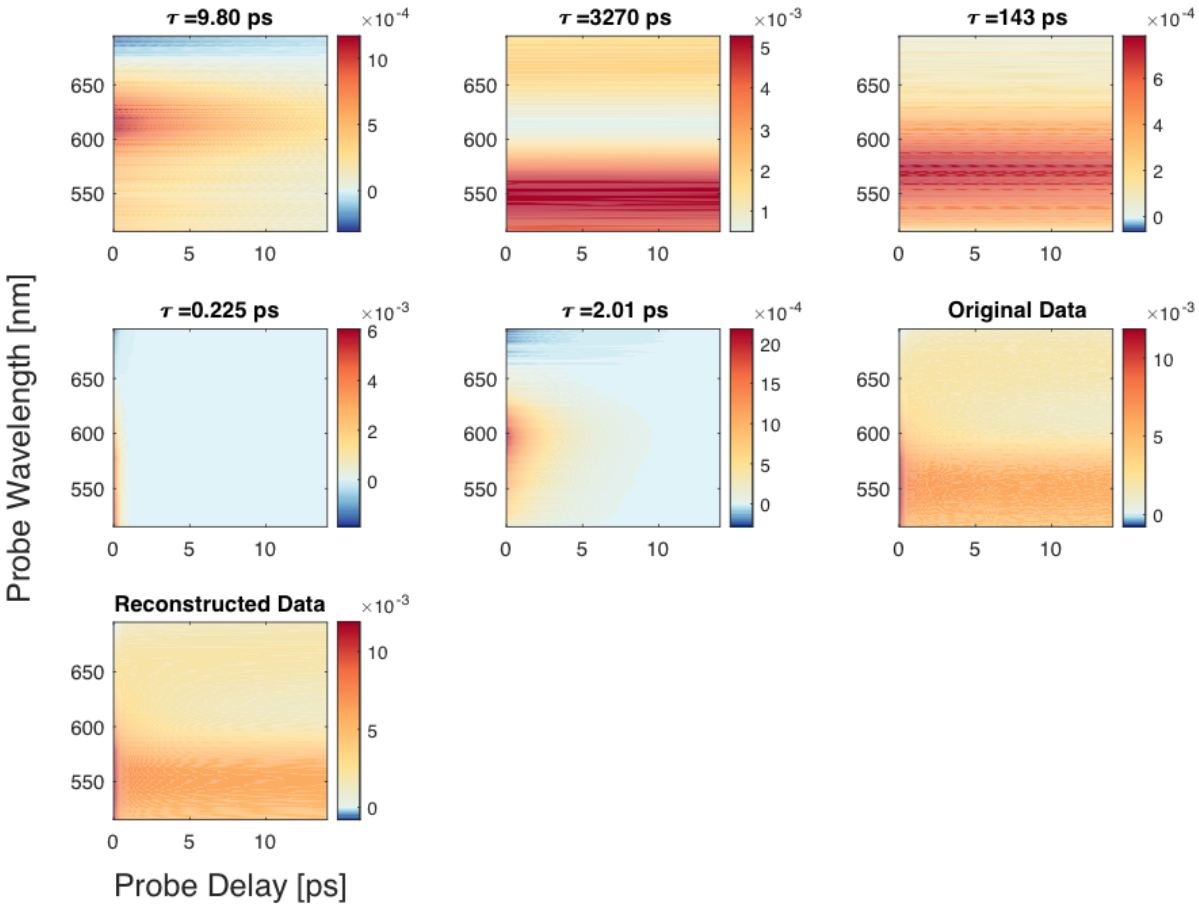

FIGURE A.5: All DAS components extracted from the transient absorption scan of PCDTBT in chlorobenzene. Scans were taken out to 3 ns, but only the first 12 ps are shown.

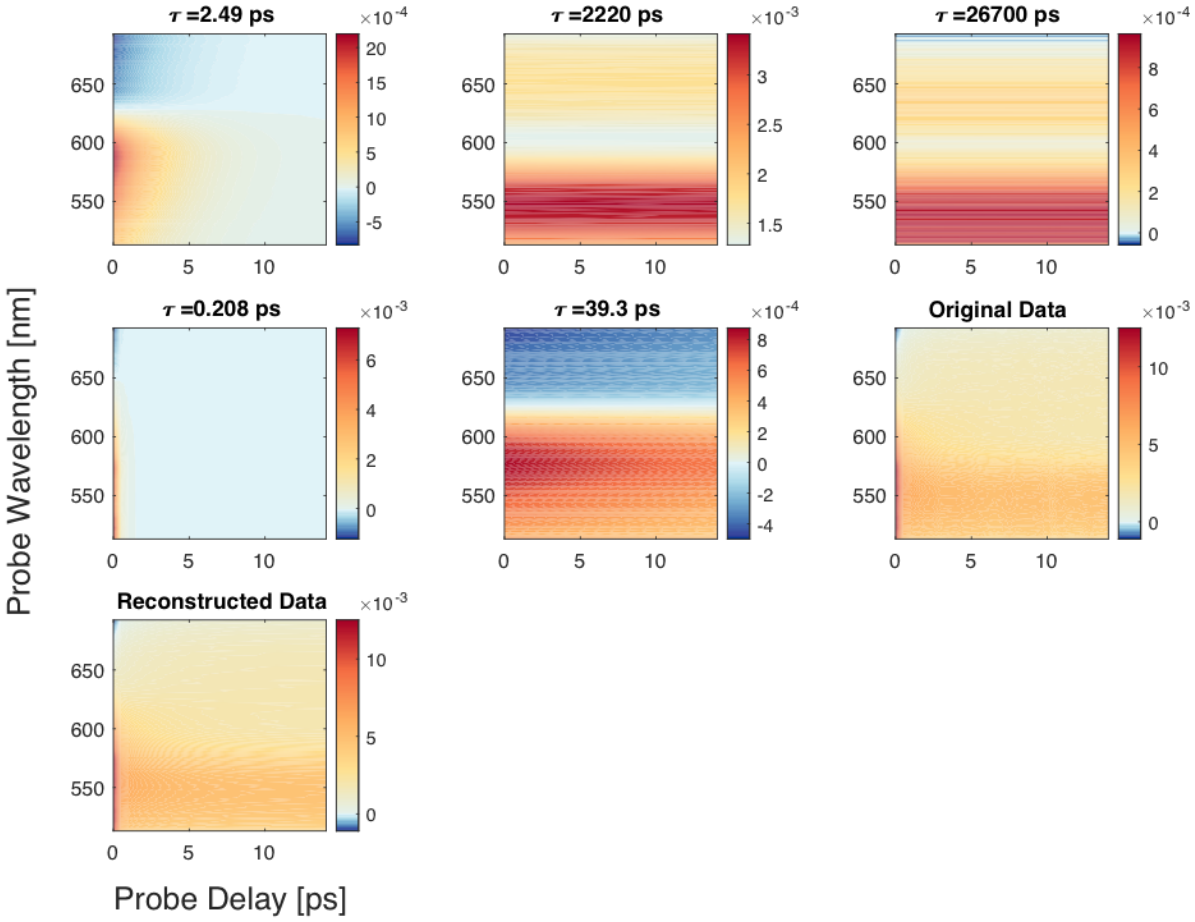

FIGURE A.6: All DAS components extracted from the TA scan of PCDTBT in toluene

Supplementary Information For: Chapter 4

B.1 Experimental Methods

B.1.1 Sample Growth and Isolation

Rhodobacter *sphaeroides* 2.4.1 (ATCC 17023) is grown semi-anaerobically under lamps at 30C in a shaker in ATCC Medium 550: R 8 A H medium. Cells were pelleted with a Sorvall RC6+ ultracentrifuge and resuspended in a 20 mM Tris buffer (pH 8) in preparation to be lysed. The concentrated cell solution is first disrupted with a sonicator for 5 mins at a 30% duty cycle and then run through a French press five times to ensure complete breakage of the cellular membrane. The resulting suspension is then centrifuged again to collect the large membrane fragments into a pellet. The pellet is again diluted with the same Tris buffer now containing 1% lauryldimethylamine oxide (LDAO) by weight to the desired OD for our measurement and shaken for an hour at room temperature. The LDAO helps solubilize the protein and reduces the amount of dynamic scatter. The solution is once again centrifuged to reduce remaining large membrane fragments and run through an AKTAxpress FPLC to ensure purity. The resulting proteins are concentrated

using Amicon centrifugal filters so the optical density of is 0.3 OD passing through a 200 um flow cell from Starna. The purified protein is passed through a 100 nm syringe filter to allow for smooth passage in the 220 nm filter used in the closed loop peristaltic pump system.

BChl*a* is extracted from the same cell pellet the LH2 is extracted from. The BChl*a* is solubilized in methanol (plus .005 M sodium ascorbate) and stirred in the dark and cold for about half an hour. This mixture is then sedimented by centrifugation and repeated until the sedimentation is colorless. The resulting supernatant contains both BChl*a* and carotenoids, which is separated through AKTAxpress FPLC to ensure purity. The concentration is increased by rotovaping to remove excess methanol to achieve a suitable optical density for spectroscopic measurements.

The FMO complex was isolated from Chlorobaculum tepidum cells cultured in CL medium [418] according to the procedure in Saer et al. [419] with some modifications. Briefly, cells were harvested by centrifugation at 7000 $\times$ g, and resuspended in 20 mM Tris HCl, 2 mM MgCl2, pH 8.0. The cell suspension was sonicate to lyse the cells. This lysate was centrifuged at 12,000 $\times$ g for 10 minutes to remove cell debris, and subsequently ultracentifuged at 100,000 $\times$ g for 1 hour to pellet the cell membranes. Membranes were resuspended in 20 mM Tris HCl, pH 8.0, and sodium carbonate was added to a final concentration of 0.4 M. The mixture was left to stir overnight at 4 C . The alkalinity of this mixture was neutralized by adding sodium bicarbonate to a concentration of 0.4 M, and the mixture was then ultracentrifuged for 2 hours at 235,000 $\times$ g. The supernatant was dialyzed overnight against 20 mM CAPS, pH 10.5 and subsequently purified with a strong anion exchanger. FMO eluted from the column at 250 mM NaCL. The eluate was concentrated with a 50,000 kDa ultrafilter and further purified by gel filtration chromatography.

Pure FMO protein exhibited a 260:371 nm absorption ratio of under 0.6.

The concentrations of all the samples were adjusted so that when flowed through a .2 mm cell, an OD of .3 was achieved for the absorption maximum. All experiments were conducted at room temperature.

B.1.2 Data Collection

The broadband coverage of the B800 and B850 was achieved using a home-built second harmonic non-collinear optical parametric amplifier (2H-NOPA) pumped with a PHAROS fundamental pulse running at 200 kHz and compressed with chirped mirrors (Layertech 109347). The signal is collected in the GRAPES geometry and the phase of the signal is retrieved using the phase of a non-resonant solvent scan, which is purely dispersive. The resulting phased spectra is then checked with a degenerate pump-probe experiment taken with the same sample and setup with one of the beams blocked. This transient-absorption measurement is equivalent to our 3DES signal summed along the excitation dimension and has the added benefit of already being properly phased relative to the probe pulse. The same phase mask is applied to our entire signal. The ability to not have to phase the data for every time delay is due to passively phase stabilizing the interferometer as well as collecting the entire 3DES dataset in under 2 seconds, getting rid of most of the $1/f$ phase noise. The ability to collect the data quickly also gets rid of much of the $1/f$ amplitude noise that hinder measurement sensitivity. Typical "point-by-point" measurements of 3DES require two time delays to be sampled. Our experiment focuses the beams to a line instead of a point, which allow us a spatial dimension in which we can encode a time delay. Pulses 1 and 2 are tilted relative to each other so that each row has a slightly different time delay between them. Pulse 3 is parallel to 2, so that time delay

is scanned with a stage. The Newport XPS stage system we use can output triggers at preset locations without stopping. We use this feature to "rapid-scan" the delay between 2 and 3, using the stage to trigger the camera to take a picture at a given time delay. Not stopping the stage and running an Andor Xyla 5.5 high speed CMOS camera at 650 hz allows us to complete at $128 \times 916 \times 2560$ pixel scan in under 2 seconds.

B.2 Simulation of 3D Electronic Spectra

Simulated 3DES were created to both test the accuracy of the zero-quantum coherence subtraction procedure and identify factors that cause asymmetry in the 4WM beating spectra. The simulation calculates the optical response of a system of N chromophores and M vibrational modes described by the following Hamiltonian (neglecting anharmonicity):

$$\begin{aligned} \hat{H} &= \hat{H}_{el} + \hat{H}_{vib} + \hat{H}_{el-el} \\ &= \sum_{n=1}^{N} \epsilon_n |n\rangle\langle n| + \sum_{m=1}^{M} \hbar\omega_m \hat{b}_m^\dagger \hat{b}_m + \sum_{n=1}^{N} |n\rangle\langle n| \sum_{m=1}^{M} S_{nm}(\hat{b}_m^\dagger + \hat{b}_m) + ... \\ &\qquad \sum_{n,n'=1}^{N} J_{nn'}(|n\rangle\langle n'| + |n'\rangle\langle n|) \end{aligned} \tag{B.1}$$

where $|n\rangle$ and $\hat{b}_m$ denote the electronic site basis and vibrational annihilation operator. S_{nm} is the Huang-Rhys factor coupling the mth vibrational mode to the nth chromophore (related to the dimensionless displacement γ_{nm} via $S_{nm} = (\frac{\gamma_{nm}^2}{2})$ and $J_{nn'}$ is the inter-chromophore Coulomb coupling. The Hamiltonian was diagonalized and the eigenvalues were obtained to calculate the 3rd-order optical response functions in the impulsive

limit (pulse duration goes to 0) and under the rotating wave approximation using a sum-over-states procedure for the photon echo pathway ($k_{sig} = -k_1 + k_2 - k_3$). A pulse bandwidth of 1500 cm^{-1} is used to window the observable signals. Using the Condon approximation to separate electronic and nuclear contributions to the dipole transition moment, the response functions can be calculated in the Fourier domain using the following expressions:

$$\begin{cases} R^{\mathrm{ESE}}(\omega_1,\omega_2,\omega_3) = |\mathbf{d}|^4 \sum_{\alpha a \beta b} \langle a|\alpha\rangle \langle b|\alpha\rangle \langle \beta|a\rangle \langle \beta|b\rangle I_{a\alpha}(\omega_1) I_{ab}(\omega_2) I_{\beta b}(\omega_3) \rho_{\alpha\alpha}(0) \\ R^{\mathrm{GSB}}(\omega_1,\omega_2,\omega_3) = |\mathbf{d}|^4 \sum_{\alpha a \beta b} \langle a|\alpha\rangle \langle b|\alpha\rangle \langle \beta|a\rangle \langle \beta|b\rangle I_{a\alpha}(\omega_1) I_{\alpha\beta}(\omega_2) I_{\beta b}(\omega_3) \rho_{\alpha\alpha}(0) \\ R^{\mathrm{ESA}}(\omega_1,\omega_2,\omega_3) = |\mathbf{d}|^4 \sum_{\alpha a b f} \langle a|\alpha\rangle \langle b|\alpha\rangle \langle f|a\rangle \langle b|f\rangle I_{a\alpha}(\omega_1) I_{ab}(\omega_2) I_{fb}(\omega_3) \rho_{\alpha\alpha}(0) \end{cases}$$

In these expressions, Greek letters denote states in the ground-state manifold while Roman letters are states in the excited state manifolds (including doubly excited f-states). The nuclear overlaps are denoted by expressions of the form $\langle a|\alpha\rangle$ while the electronic dipole moment $|\mathbf{d}|$ is assumed to be the same for all interactions. The lineshape $I_{ab}(\omega_i)$ represents either a Gaussian, Lorentzian, or Voigt function centered at frequency $\omega_{ab} = \omega_a = \omega_b$ with FWHM broadening of Γ_{ab} along frequency dimension ω_i. Note that the Voigt functions used in this work had equal homogeneous and inhomogeneous broadenings of Γ_{ab}. The total signal was calculated as the sum of the signals from the three different pathways. The laser pulse shape was not incorporated into these simulations.

B.3 Vibrational Coherence Subtraction Procedure

To test the vibrational coherence subtraction procedure's ability to isolate the electronic coherences in the system, a simple three-level system (two excited state sharing a common

ground state) was simulated with electronic dephasing lifetime of 100 fs and vibrational dephasing lifetime of 3.3 ps, as shown in Figure B.1(a). All three signals were simulated but notice that for such a system, only the GSB and ESE will produce signals within the observable bandwidth; the doubly excited f-states are well out of reach. One vibration at 215 cm^{-1} is present in the system with a Huang-Rhys factor of 0.14 for both excited state manifolds. For this model, Lorentzian lineshapes were used to parameterize the spectrum along all 3 coherent dimensions. The spectrum for $T > 1.33$ ps was fit using global analysis to extract the long-lived vibrational coherences whose beat maps and coherent components are shown in Figure B.1(c)-(d). The dynamic components were extrapolated back to $T = 0$, recombined with their beat maps and subtracted from the total 3D spectrum using the same procedure described in the main text. Figure B.1(e) shows the population time dynamics of the spectrum for each step of this procedure; the blue curve is the original time evolution and the purple shows the late-time fit. This procedure fits the late times and propagates to 0 with good accuracy. Their residual is shown in red, isolating the features of the electronic coherences. The Fourier transform of the residual in Figure B.1(f) shows broad peaks centered at near 800 cm^{-1}. The black lines are placed at exactly $\pm$800 cm^{-1}; it is evident that some error is introduced in identifying the excitonic coherence frequencies using this procedure, but the offset is minimal.

B.4 ESA-induced Beating Spectrum Asymmetry

Upon examining the equations for the response functions, one finds that the waiting time coherences for the ESE and ESA must be symmetric over positive and negative values since the frequencies ω_{ab} and ω_{ba} will be sampled evenly. The GSB will be symmetric for all energies up the highest thermally-occupied state (indicated by the α-states) for the

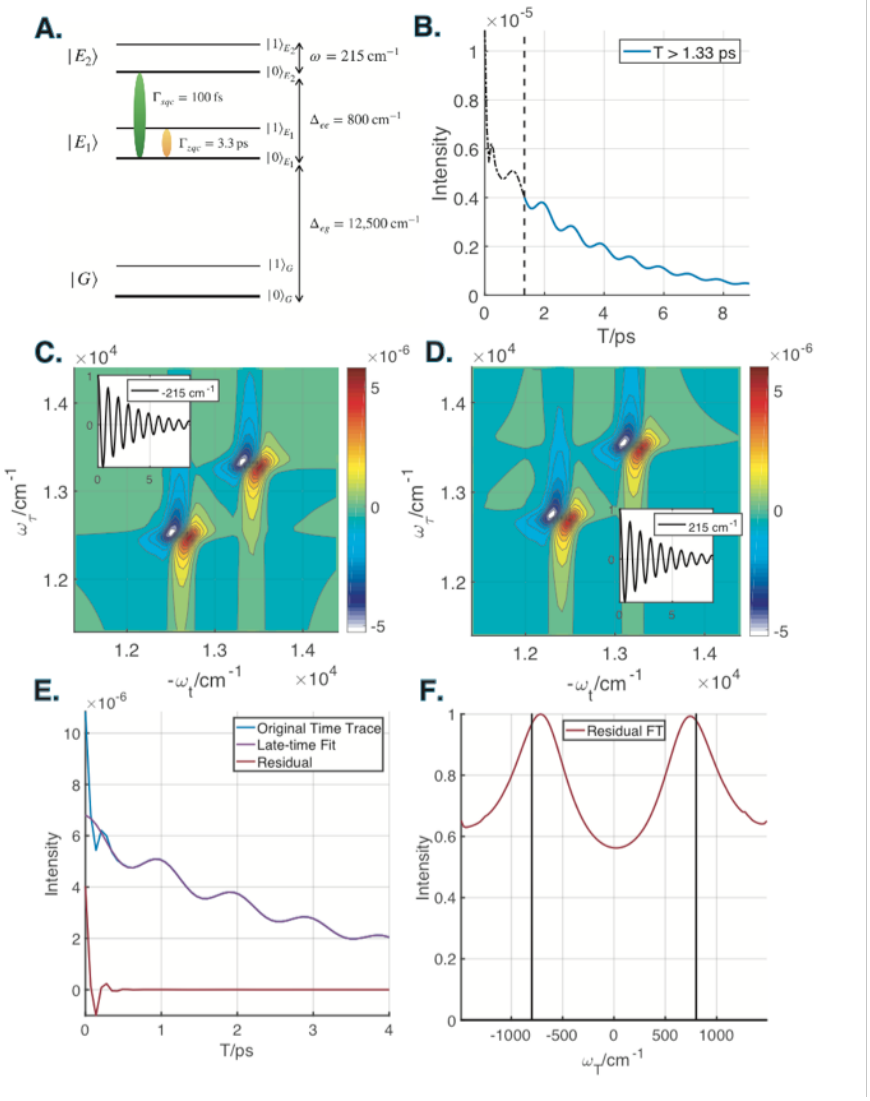

FIGURE B.1: (a) Energy level diagram of the three-level system used to illustrate the vibrational coherence subtraction procedure. Single-quantum (electronic) coherences dephase with a lifetime of 100 fs while zero-quantum (vibrational) coherences dephase with a lifetime of 3.3 ps. (b) Waiting time dynamics of simulated spectrum with 1.33 ps marked so show where the spectrum was fit for the late-time regime. (c)-(d) Zero-quantum coherence beat maps corresponding to the vibrational coherence at 215 cm^{-1} (shown in the inset). (e) Time traces of each step of the subtraction procedure. (f) Fourier transform of the residual demonstrating that the procedure can find the position and broadening of the electronic coherence.

same reason, but all of its other frequencies will only appear on the negative side. Since the total signal is the sum of these three pathways, asymmetry can be introduced in myriad ways. Since the GSB and ESA always nearly overlap, the asymmetry caused by the GSB simply manifests as negative coherence frequencies having larger amplitude than the corresponding positive ones. This is a somewhat trivial source of asymmetry. The ESA on the other hand can appear at any point on the spectrum based on the location of the doubly excited f-states which tend to densely span a large range of energy in multichromophoric systems. Furthermore, since the ESA is a negative signal, it can produce highly asymmetric features based on partial cancellation due to its position relative to the GSB and ESE. To investigate the ESA-induced asymmetry, the spectrum of a 4-level system with 1 ground state, 2 singly-excited states, and 1 f-state was simulated and the relative amplitude of positive and negative peaks in the beating spectrum was plotted as a function of f-state position, as defined in Figure B.2(a). Only the ESE and ESA were simulated to investigate the effect of ESA-induced asymmetry. For a "balanced" configuration in which the energy gap ω_{f1} equals the 5500 cm^{-1} (the sum of the Δ_{eg} = 5000 cm-1 and Δ_{ee} = 500 cm^{-1}), the ESA feature appears exactly on the off-diagonal positions coinciding with the ESE signal. Since these signals have the same dipole moments, they completely cancel. On the other end, if we shift the f-state down by 500 cm^{-1} to 5000 cm^{-1}, the positive peak cancels as in Figure B.2(c), and if it is shifted up to 6000 cm^{-1}, the negative peak cancels as shown in Figure B.2(d). Figure B.2(e) shows the continuous trend of partial cancellation with f-state position.

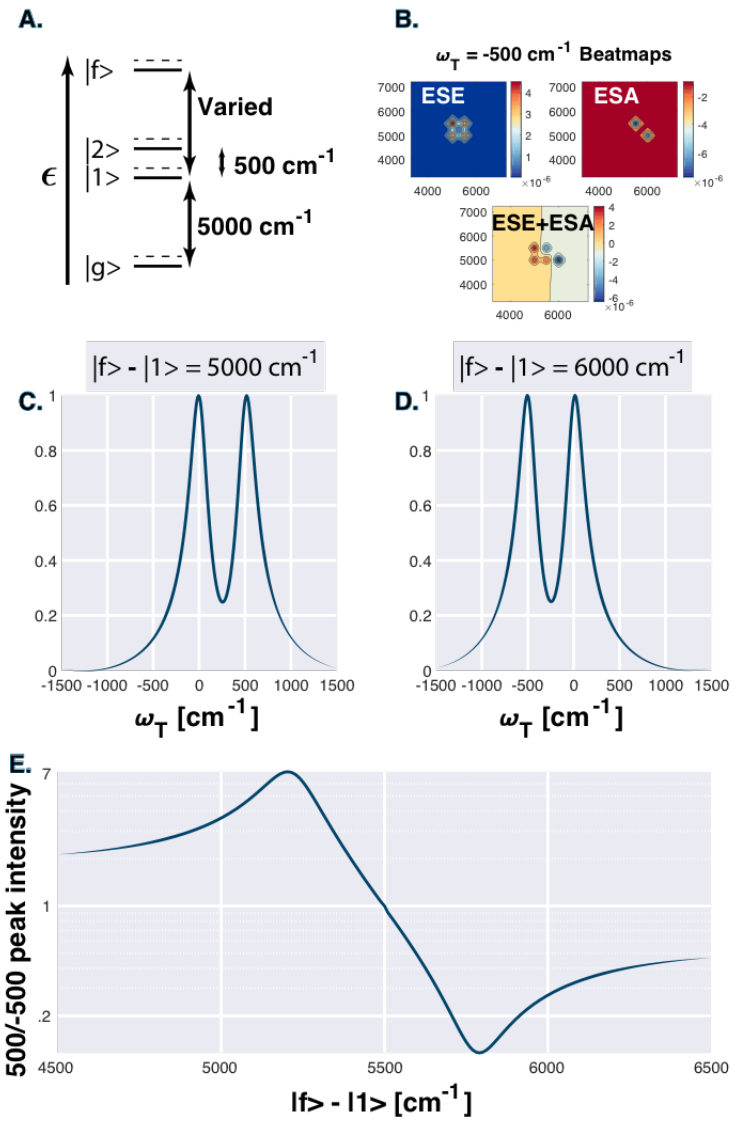

FIGURE B.2: (a) Energy level diagram for the 4-level system used to explore ESA-induced asymmetry. (b) Images of the spectrum along the electronic dimensions showing the canonical structure of the ESE signal and the ESA signal at off-diagonal positions. The ESA can be shifted left to right by tuning the f-state gap. (c) Beating spectrum of the total signal for an f-state at 5000 cm^{-1}, cancelling out the negative peak. (d) Beating spectrum of the total signal for an f-state at 5500 cm^{-1}, cancelling out the positive peak. (e) Relative amplitude of positive and negative SQC peak as a function of f-state position.

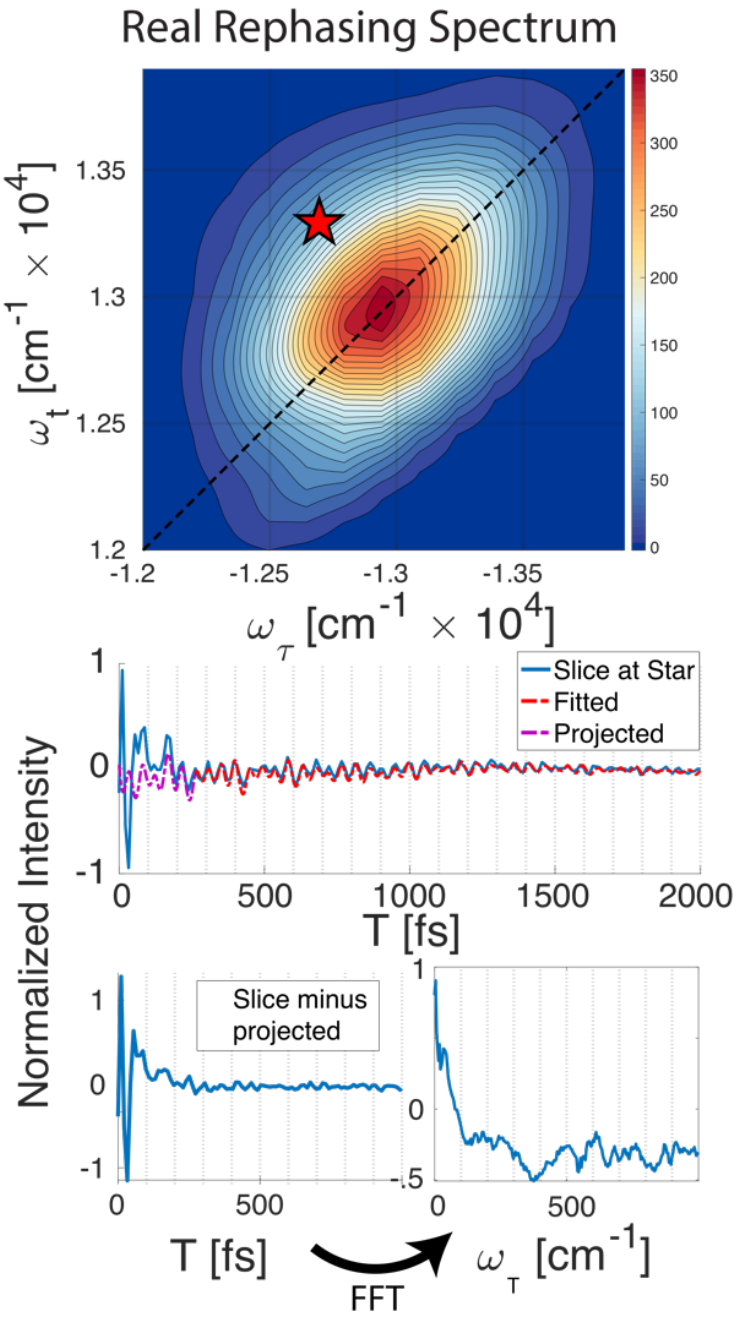

FIGURE B.3: The 2D-SQC plot of BChl*a* is all positive with no ESA. The back propagation method leaves no peaks in the frequency domain.

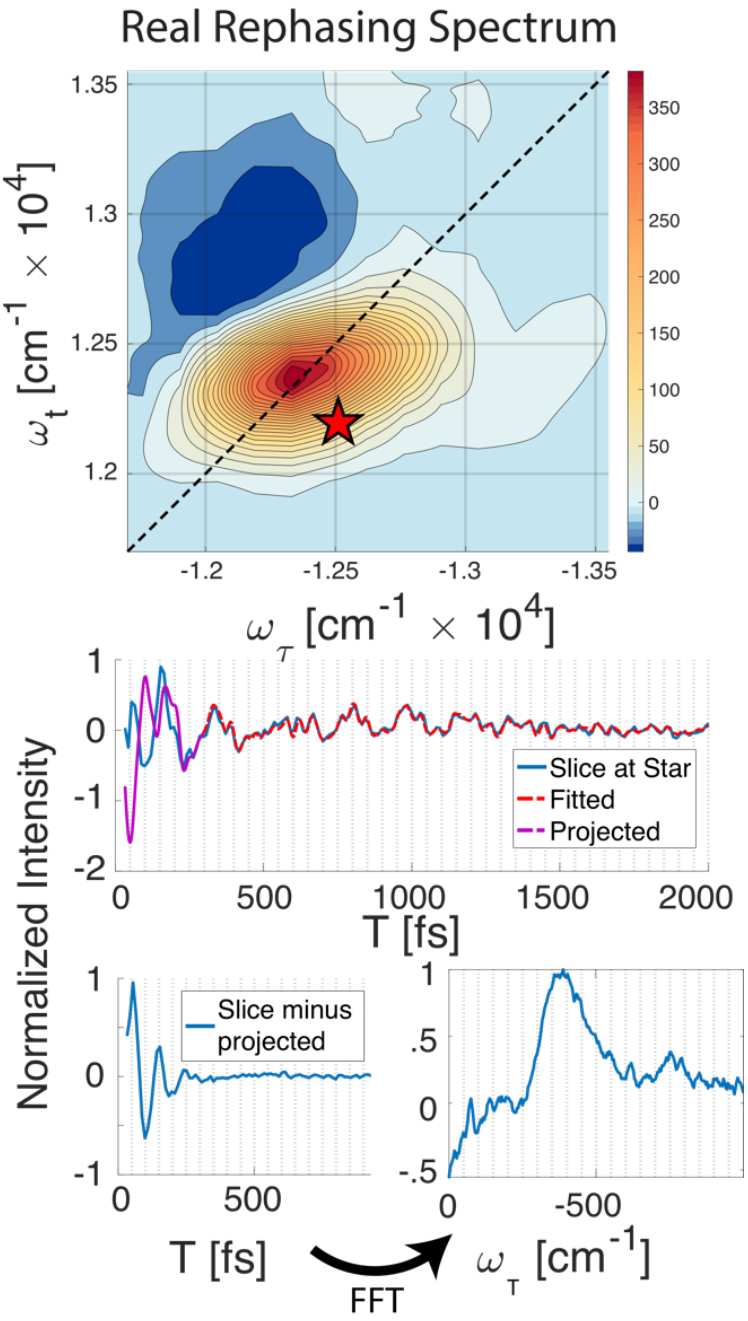

FIGURE B.4: FMO 2D-SQC plot at T = 250 fs and example subtraction slice. Estimating the dephasing from the FWHM of the FT of a single slice gives a dephasing time of $\sim$ 60 fs using $\tau = [\pi c \Delta]^{-1}$

B.5 Vibrational Coherence Subtraction Procedure Applied to BChl*a* and FMO

B.6 DAS Interpretation

Although it is tempting to associate growth and decay of signal from different parts of the DAS as transfer between the respective states, the real picture is more nuanced. When as DAS regression is performed, the time evolution of the 3D signal along population time is fit to a linear combination of exponentials

$$I^{DAS}(\omega_\tau, \omega_t, T) = \sum_k c_k(\omega_\tau, \omega_t) e^{-|\lambda_k| T}$$

If we assume population transfer is described by a kinetic rate model, the real dynamic evolution is parameterized by a rate matrix $\mathbf{K}$ where element K_{ij} controls the rate of excitation transfer from state $|i\rangle \rightarrow |j\rangle$. The dynamic evolution is governed by:

$$I(\omega_\tau, \omega_t, T) = \sum_{ij} \tilde{c}_{ij}(\omega_\tau, \omega_t) e^{K_{ij} T}$$

where $\tilde{c}_{ij}(\omega_\tau, \omega_t)$ is a beat map that characterizes the dynamic process transffering excitation from $|i\rangle \rightarrow |j\rangle$. In transient absorption spectroscopy, these are often called species associated spectra (SAS). These two representations are related by diagonalizing $\mathbf{K} = \mathbf{V}\Lambda\mathbf{V}^{-1}$:

$$I(\omega_\tau, \omega_t, T) = \sum_{ij} \tilde{c}_{ij}(\omega_\tau, \omega_t) e^{K_{ij} T} = \sum_{ijk} \tilde{c}_{ij}(\omega_\tau, \omega_t) V_{ik} V^{-1}_{kj} e^{\lambda_k T}$$

Therefore, the DAS fit recovers the eigenvalues of the population rate matrix **K**; the corresponding DAS beat maps are linear combinations of the SAS beat maps. This is illustrated in for the kinetic scheme shown in figure B.5(a). The DAS components and beat maps indeed recover the eigenvalues, as shown in figure B.5(b). Furthermore, it is clear that while there are only 4 beat maps, there are 16 individual transfer processes (elements in K), meaning that each DAS map contains mixed information from multiple transfer processes. This is the inherent difficulty in interpreting the DAS; however, when the peaks are well-separated, the DAS is very useful for determining which states are related by kinetic processes. These considerations do throw ambiguity into interpreting DAS, but the time scales in which processes occur still offer a clue to the dynamics happening in each DAS. Though the rate of transfer is not definitive, the fact that cross peaks do show up between different states (as in the 74 fs DAS of LH2) indicate they are not independent states in the <100 fs regime. Lastly, it is worthwhile to point out that the eigenvalues of triangular matrixes are the entries on the main diagonal. This means in the limit of low uphill energy transfer, the **K** matrix becomes a lower triangular matrix and the extracted rates are the main diagonal entries.

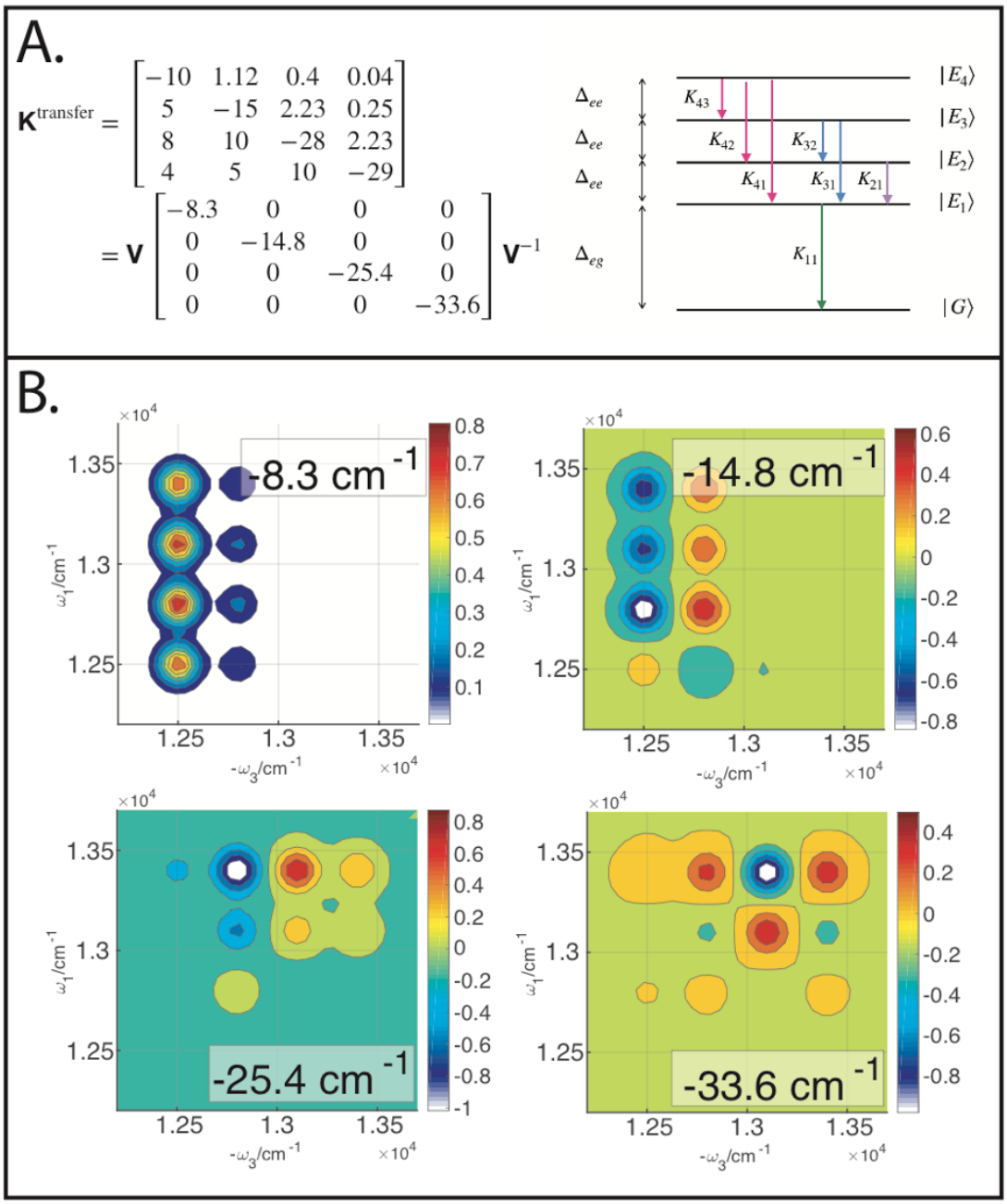

FIGURE B.5: Simulation of DAS which highlight the difficulty in assigning a rate constant between two states. (a) The kinetic scheme used in the simulation. A four level system with transfer rates between states described in the full kinetic matrix **K**. (b) DAS extracted from **K** matrix, showing that the DAS extracts only the eigenvalues of the full **K** matrix.

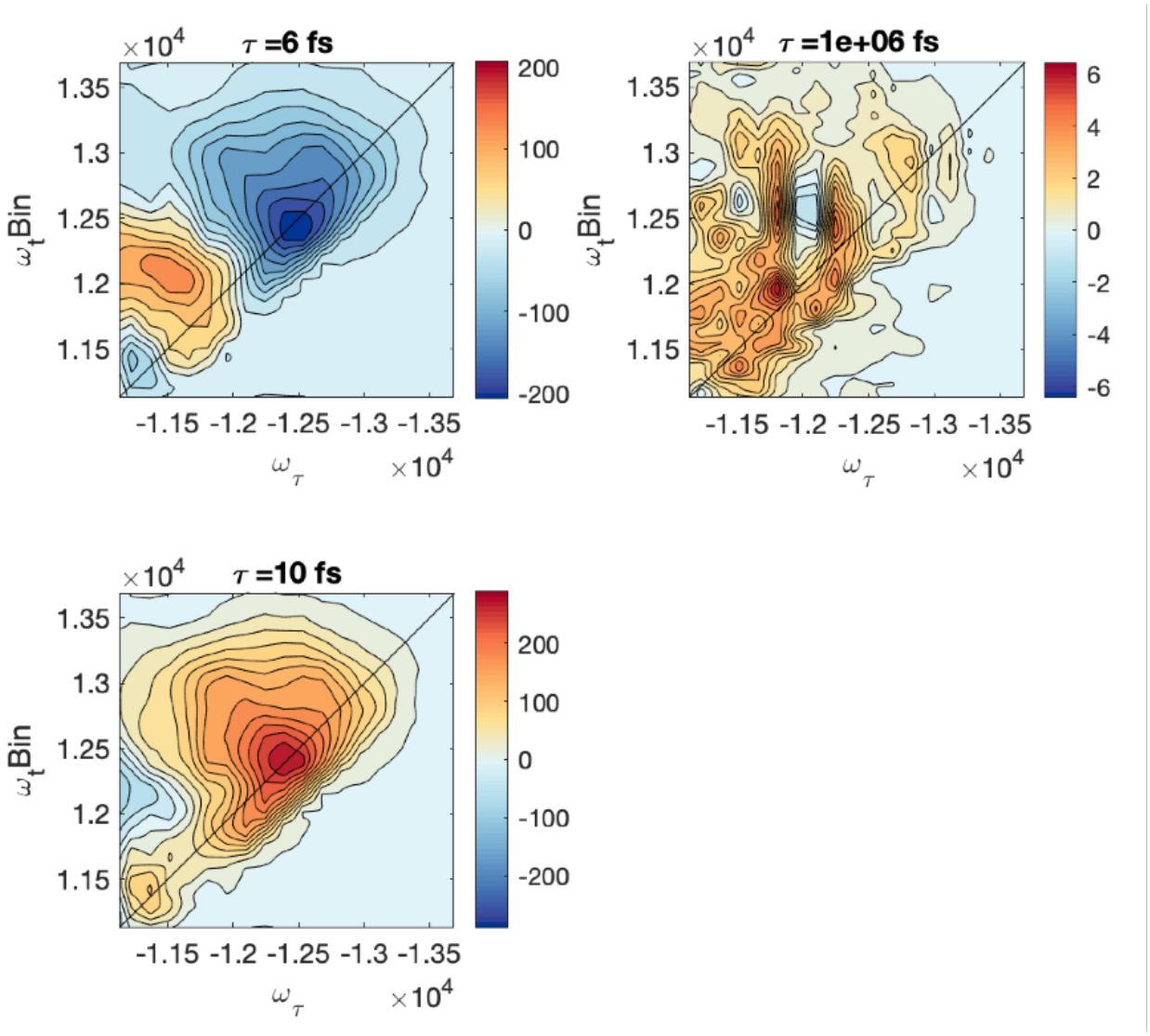

FIGURE B.6: DAS of non-resonant scan of buffer.

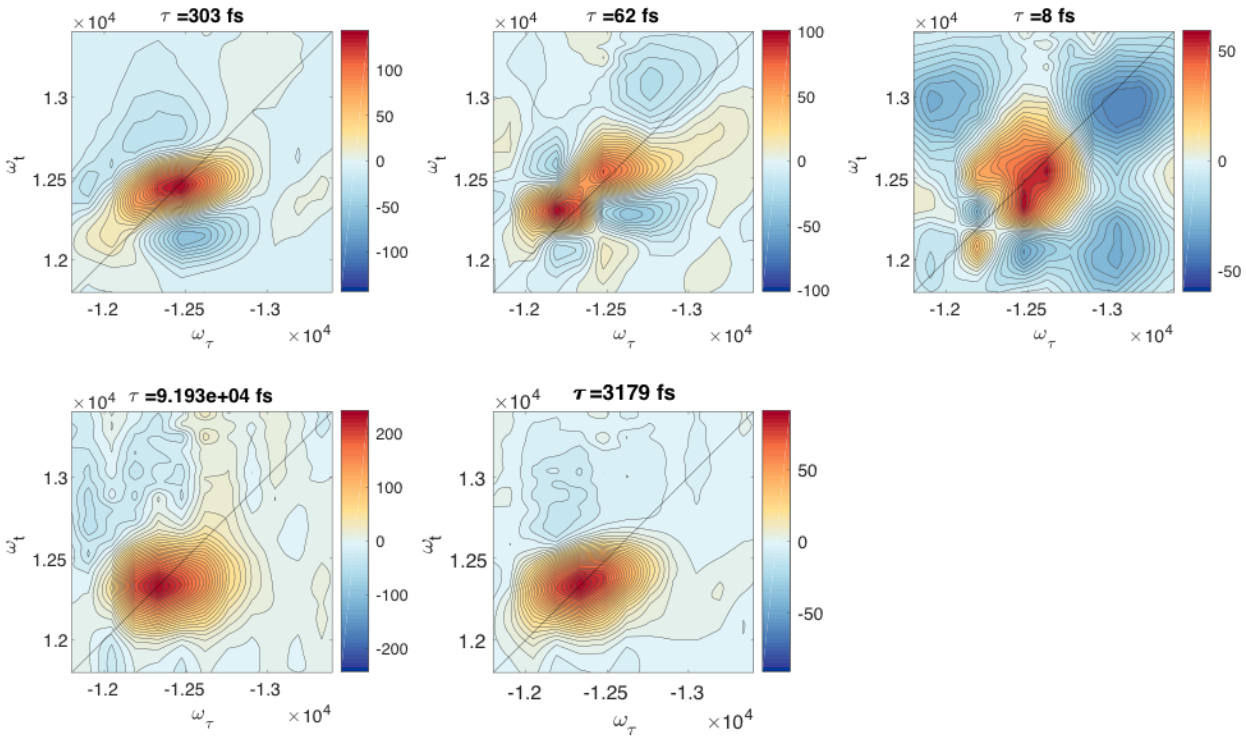

FIGURE B.7: DAS of the FMO complex.

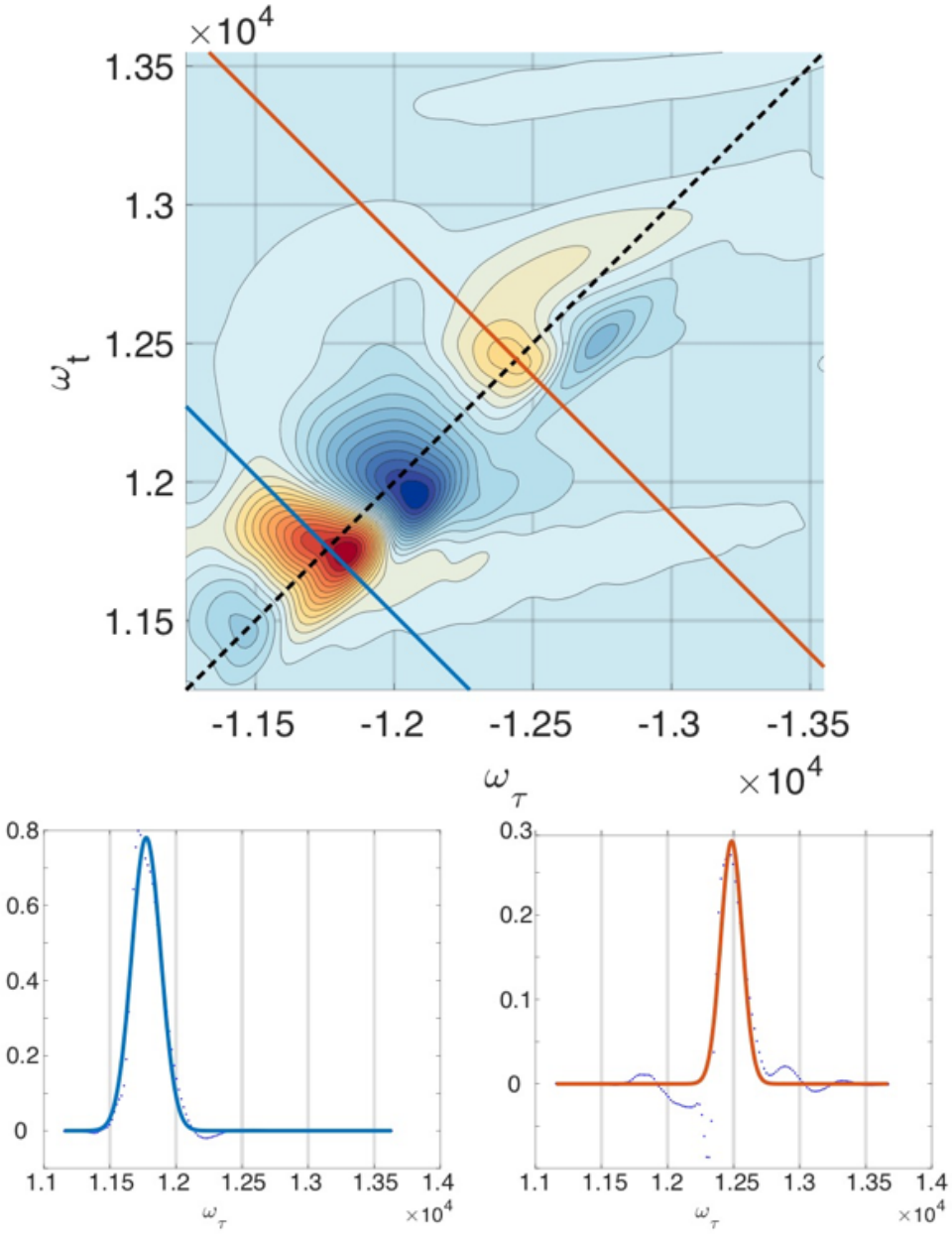

FIGURE B.8: The dephasing lifetimes of the B800 and B850 bands are estimated from the anti-diagonal slices of the 2D-SQC at 30 fs. The dephasing lifetime is calculated using $\tau = [\pi c \Delta]^{-1}$ is found to have a shorter lifetime than the electronic dephasing of the system.

Supplementary Information For: Chapter 5

C.1 Simulation Details

To investigate the effects of vibronic coupling on population transfer rates, a dimer system with a one harmonic mode was modeled using a Holstein Hamiltonian described by the following equations in the site basis

$$H_g = \frac{p^2}{2m} + \frac{1}{2}m\omega_0^2 q^2 = \hbar\omega_0\left(b^+ b + \frac{1}{2}\right)$$

$$H_{e_1} = \frac{p^2}{2m} + \frac{1}{2}m\omega_0^2(q - D_1)^2 + \Delta_{ge_1} = \hbar\omega_0\left(b^+ b + \frac{1}{2}\right) + \hbar\omega_0 d_1(b + b^+) + ... \quad (\Delta_{ge_1} + \hbar\omega_0 d_1^2) \tag{C.1}$$

$$H_{e_2} = \frac{p^2}{2m} + \frac{1}{2}m\omega_0^2(q - D_2)^2 + \Delta_{ge_2} = \hbar\omega_0\left(b^+ b + \frac{1}{2}\right) + \hbar\omega_0 d_2(b + b^+) + ... \quad (\Delta_{ge_2} + \hbar\omega_0 d_2^2) \tag{C.2}$$

$$H_{tot} = \begin{bmatrix} H_g & 0 & 0 \\ 0 & H_{e_1} & J \\ 0 & J & H_{e_2} \end{bmatrix}$$

The operators b^+/b are bosonic creation/annihilation operators for the mode ω_0 defined by $b = \sqrt{\frac{m\omega_0}{2\hbar}}\left(q + \frac{i}{m\omega_0}p\right)$ and $= \sqrt{\frac{m\omega_0}{2\hbar}}\left(q - \frac{i}{m\omega_0}p\right)$. Each mode defines a single-particle Hilbert space of dimensionality equal to the number of vibrational quanta n_q allowed per manifold. For the present simulation, $n_q = 2$. We model excited states using the displaced harmonic oscillator Hamiltonian parameterized by D_n, the physical displacement of the potential energy manifold $|e_n\rangle$ relative to the ground state which induces linear electron-phonon coupling via the dimensionless coupling constant $d_n = D_n\left(\frac{m\omega_0}{2\hbar}\right)^{1/2}$ which we will generally refer to as the displacement of the mode in excited state n. The quantities $\Delta_{ge_{1(2)}}$ are the 0-0 electronic energy gaps between the ground state and each excited states. The site basis of the single-exciton manifold is spanned by product states $|e, \nu\rangle$ where $e = 1, 2$ and $\nu = 0, 1$ describe the first and second excited states with their included harmonic vibrational rungs. In the site basis, the total Hamiltonian matrix is a block-matrix enumerated by the states. The diagonal blocks describe the individual electronic state with its associated vibrations and is of size $n_q \times n_q$. The off-diagonal blocks describe interchromophore coupling, assumed to originate from local Coulombic interactions, and are diagonal in the site basis: $\langle e_2\nu_2|e_1|\nu_1\rangle = \langle e_2|e_1\rangle\langle\nu_2|\nu_1\rangle = JI_{n_q\times n_q}$. From the site basis, one can rotate to two other bases. Upon diagonalizing H_{e_1} and H_{e_2}, one obtains the vibronic basis where the diagonal blocks of H_{tot} are diagonal matrices themselves but the interchromophore coupling is non-diagonal and expressed as $J\langle\nu|\nu'\rangle$ where $\langle\nu|\nu'\rangle$ is

the Franck-Condon matrix describing nuclear overlap between harmonic and displaced-harmonic oscillator eigenstates. Complete diagonalization of H_{tot} results in the delocalized excitonic basis. For a physical picture of excitation dynamics, it is often useful to use states in the site basis.

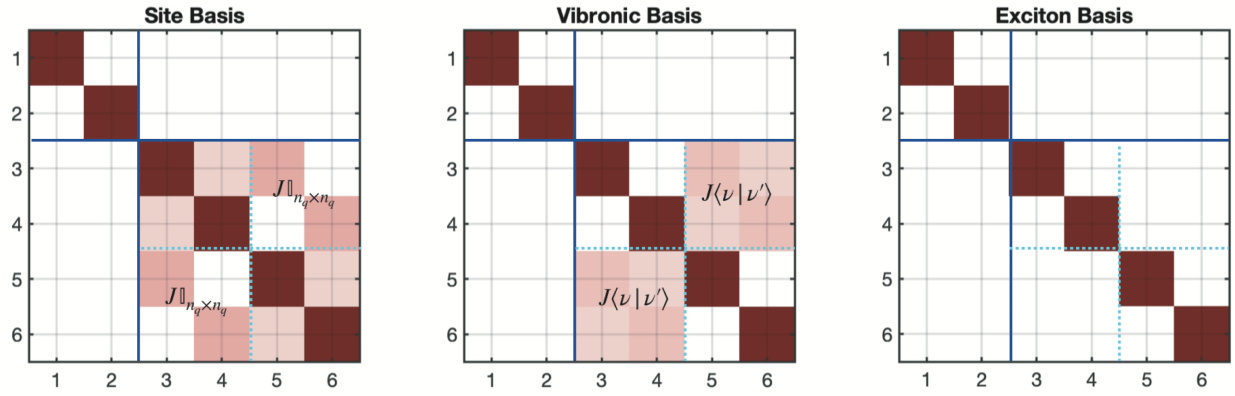

FIGURE C.1: Block representation of how Hamiltonian is constructed. State 1, 3, and 5 are the electronic states and 2, 4, and 6 are vibrational states. States 3/4 constitute $|e_1\rangle$ and 5/6 constitute $|e_2\rangle$. The coupling strength between 3/4 is determined by the displacement of the harmonic potential and is what we refer to as intra-pigment electronic-vibrational coupling. Coupling between the electronic states 3 and 5 is J-coupling. When written in the vibronic basis, the off-diagonal elements within a harmonic potential disappear, but now coupling between states 3/6 and 4/5 appear. This is how J-coupling might couple the electronic state of one pigment to the vibrations of another. Finally, in the exciton basis there exist no off-diagonal elements. This is the system that is experimentally accessible. The eventual set of states can roughly be described as having contributions from primarily electronic or vibrational contributions.

C.2 Franck-Condon Effect on Exciton Energy Transport

To calculate the Franck-Condon overlaps as function of excited state displacement, as shown in Figure 5.3(b), the analytical formula provided by Palma et al. was used.[420]

For an individual mode of the nth excited state with curvature β_n and displacement γ_n, the following formula computes the elements of the Franck-Condon matrix

$$\langle e_n \nu_I | g \nu_j \rangle \equiv X_{IJ}^{(n)}$$

$$= \left(\frac{2\beta_n}{1+\beta_n^2} \right)^{1/2} exp\left(-\frac{\beta_n^2 \gamma_n^2}{2(1+\beta_n^2)} \right) \times \left(\frac{1-\beta_n^2}{2(1+\beta_n^2)} \right)^{\frac{I+J}{2}} (I!J!)^{1/2}$$

$$\times \sum_{k=0}^{min(I,J)} \left(\frac{4\beta_n}{1-\beta_n^2} \right)^k \frac{(-i)^{I-k}}{k!(I-k)!(J-k)!} H_{I-k}\left(\frac{i\beta_n^2 \gamma_n}{(1-\beta_n^4)^{1/2}} \right) H_{J-k}\left(-\frac{\beta_n \gamma_n}{(1-\beta_n^4)^{1/2}} \right)$$

where $H_p(\xi)$ is the p^{th} Hermite polynomial. There are two such Franck-Condon matrices $X_{IJ}^{(1)}$ and $X_{IJ}^{(2)}$. In order to calculate an effective measure of vibronic enhancement to excitation energy transfer (EET), we consider the thermal rate constant describing the transfer of energy from all states $|e_k \nu_J\rangle$ $(k > 1)$ to a sink state $|e_1 \nu_1\rangle$ obtained using Fermi's Golden Rule

$$k_{EET} = \frac{2\pi}{\hbar} \sum_{J,k \geq 1} p_{J1}^k |\langle e_k \nu_j | \hat{\mu} | e_1 \nu_1 \rangle|^2 \delta(\Delta_k^0 + J_{\omega_k})$$

where $p_{k1} = Z^{-1} e^{-(E_k - E_1)/k_B T}$ is the thermal driving force and Δ_k^0 is the 0-0 energy gap to the k^{th} state. If the nuclear and electronic degrees of freedom are uncoupled, $|e_k \nu_J\rangle = |k\rangle \otimes |\nu_{KJ}\rangle$, and under the Condon approximation,

$$k_{EET} = \frac{2\pi}{\hbar} \sum_{J,k>1} p_{k1} |\langle k | \hat{\mu} | 1 \rangle|^2 |\langle \nu_{kJ} | \nu_{11} \rangle|^2 \delta(\Delta_k^0 + J\omega_k)$$

$$= \frac{2\pi}{\hbar} \sum_{J,k>1} p_{k1} |\langle k | \hat{\mu} | 1 \rangle|^2 |\langle \nu_{2j} | \nu_{11} \rangle|^2 \delta(\Delta_k^0 + J\omega_k)$$

For the dimer model used in Chapter 5:

$$k_{EET} = \frac{2\pi}{\hbar} \sum_J |\langle 2|\hat{\mu}|1\rangle|^2 f(\Delta E) |\langle \nu_{2J}|\nu_{11}\rangle|^2$$

Where $\Delta E = \Delta^0 + J\omega_0$ and $f(\Delta E) = p_{k1}\delta(\Delta E)$ jointly accounts for effects due to the energy gap and overlap of density of states of the different chromophores. The above expression shows that the EET rate constant has the form of a thermally-weighted density of states multiplying a Franck-Condon weighting factor which is a function of displacement and curvature. In Figure 5.3(b), we plot solely the Franck-Condon weight as a function of chromophore displacements (d_1, d_2)

$$FC(d_1, d_2) = \sum_{I,J} |\langle \nu_{2J}|\nu_{gI}\rangle\langle \nu_{gI}|\nu_{11}\rangle|^2 = \sum_{I,J} |X^{(2)}_{IJ}(d_1) X^{(1)}_{J1}(d_1)|^2$$

to capture the bare effect of vibronic coupling, namely the increased efficiency of vibrational transfer channels, on the energy transfer rate. To enable the use of the above formula for Franck-Condon transition elements, we have resolved identity using the vibrational basis of the ground state manifold.

To analyze the effect of an increasing number of vibrational states, we calculated the above Franck-Condon weight (using the same parameters as in the Chapter 5) for 10 vibrational quanta in each excited state manifold to produce the following plot in Figure C.2. We see that the overall trend of the weight remains the same compared to Figure 5.3(b). However, the increased number of vibrational pathways flattens the sensitivity of Franck-Condon weight to the precise balance of d_A and d_B.

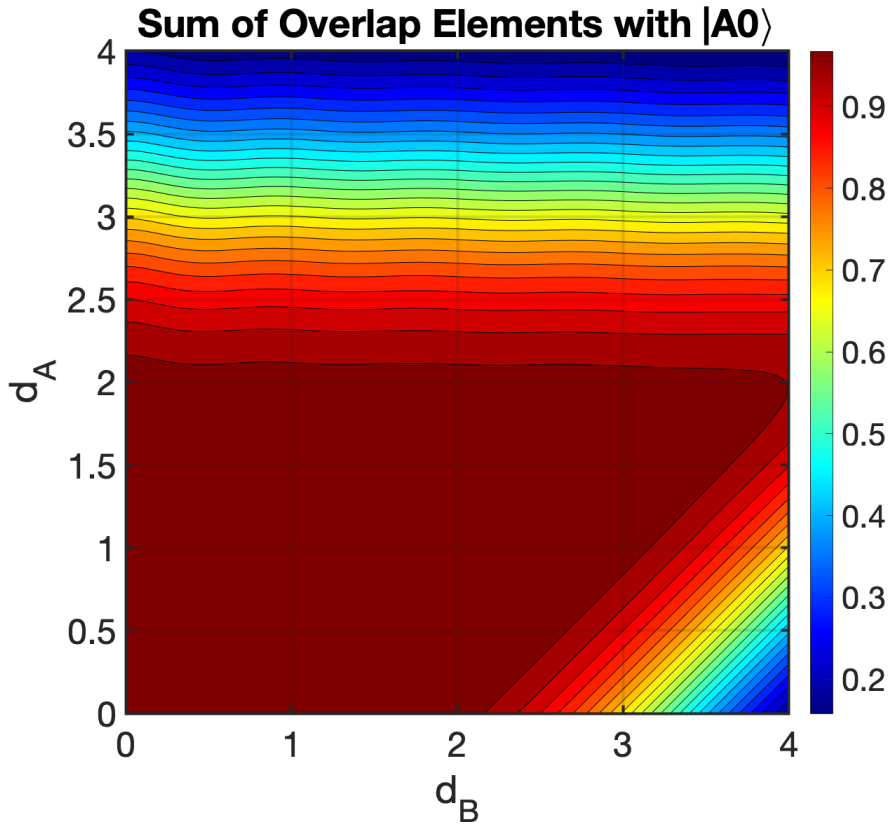

FIGURE C.2: Sum of Franck-Condon overlap factors described by the above equation for $FC(d_1, d_2)$ for a 2-level system as a function of chromophore displacements from the shared ground state.

C.3 Coherent Modified Redfield Theory

We will briefly outline the contents of Coherent Modified Redfield Theory (CMRT) used to model the population transfer kinetics in the dimer system. A full explanation of CMRT can be found in Ref [145]. Under the assumptions of a Markovian phonon bath, the time evolution of the system reduced density matrix can be expressed as

$$\frac{d\sigma_{\alpha\beta}}{dt} = R_{\alpha\beta\gamma\delta}\sigma_{\gamma\delta}$$

where $\alpha, \beta, \gamma, \delta$ enumerate indices of sites in a suitable complete basis. The object $R_{\alpha\beta\gamma\delta}$ is known as the Redfield tensor and describes both coherent time evolution and kinetic relaxation of elements of the system density matrix as introduced in Chapter 1. Under the secular approximation, $R_{\alpha\beta\gamma\delta}$ is independent of time. If we consider the site basis labelled by Roman letters $|n\rangle$,$|m\rangle$, etc. and the exciton basis labelled by Greek letters $|\alpha\rangle$,$|\beta\rangle$, etc., where we have generically included vibrational states in these single indices, we have the mapping between the site and exciton basis expressed as

$$|\alpha\rangle = \sum_n \langle\alpha|n\rangle\langle n| = \sum_n c_{n,\alpha}|n\rangle$$

As shown in section C.1, c_n^α includes information about vibronic coupling (via Huang-Rhys factor) and inter-pigment coupling (J-coupling) within the system Hamiltonian. The system and environment interact via a harmonic heat bath consisting of an infinite number of modes $\{\omega_k\}_{k=1}^{k=\infty}$ that couple to each site in the system with Huang-Rhys factor $S_{n,k}$. We remark that the Huang-Rhys factors varied in this study are not these bath coupling strengths, but the coupling strength of the single mode retained in the system description. The system-bath interaction can be written as

$$V = \sum_{n,k} S_{n,k}\omega_k(b_k^+ + b_k)|n\rangle\langle n| = \sum_{k,n,\alpha\neq\beta} S_{n,k}\omega_k c_{n,\alpha}c_{n,\beta}^*(b_k^+ + b_k)|\alpha\rangle\langle\beta|.$$

Applying a second-order perturbative expansion of the Liouville-von-Neumann equation, one obtains the resulting analytical expression for the Redfield tensor:

$$\frac{d\sigma(t)}{dt} = -Tr_B\left\{\int_0^\infty [V,[V,\sigma(t)\otimes\rho_{eq}]]\right\} = R\sigma(t)$$

$$R_{\alpha\beta\gamma\delta} = R^{(1)}_{\alpha\beta\gamma\delta} - R^{(2)}_{\alpha\beta\gamma\delta} - R^{(3)}_{\alpha\beta\gamma\delta} - R^{(4)}_{\alpha\beta\gamma\delta}$$

where the individual terms are related to bath-averaged correlation functions of the system-bath coupling:

$$R^{(1)}_{\alpha\beta\gamma\delta} = \delta_{\beta\delta} \sum_{\eta} \int_0^{\infty} d\tau e^{-i(E_\eta - E_\delta)\tau} Tr_B(V_{\alpha\eta}(0) V_{\eta\delta}(\tau))$$

$$R^{(2)}_{\alpha\beta\gamma\delta} = \int_0^{\infty} d\tau e^{-i(E_\delta - E_\beta)\tau} Tr_B(V_{\alpha\gamma}(0) V_{\delta\beta}(\tau)$$

$$R^{(3)}_{\alpha\beta\gamma\delta} = \int_0^{\infty} d\tau e^{-i(E_\alpha - E_\gamma)\tau} Tr_B(V_{\alpha\gamma}(\tau) V_{\delta\beta}(0)$$

$$R^{(4)}_{\alpha\beta\gamma\delta} = \delta_{\gamma\alpha} \sum_{\eta} \int_0^{\infty} d\tau e^{-i(E_\delta - E_\eta)\tau} Tr_B(V_{\delta\eta}(\tau) V_{\eta\beta}(0)).$$

The bath-averaged correlation function is given by

$$Tr_B(V_{\alpha\beta}(0) V_{\gamma\delta}(\tau)) = \sum_{n,m} c_{n,\alpha} c^*_{n,\beta} c_{m,\gamma} c^*_{m,\delta} \int_0^{\infty} d\omega I(\omega) (cos(\omega\tau) coth(\frac{\omega}{2k_B T}) + ... \; isin(\omega\tau)) \tag{C.3}$$

where $I(\omega)$ is the spectral density. Note that $Tr_B(V_{\alpha\beta}(0) V_{\gamma\delta}(\tau)) = -Tr_B(V_{\alpha\beta}(\tau) V_{\gamma\delta}(0)$. For the work in Chapter 5, a super-Ohmic form parameterized by an exciton-phonon bath coupling strength γ and a cutoff frequency ω_c was used.

$$I_\omega = \frac{\gamma \omega^3 e^{-\omega/\omega_c}}{\pi \omega_c^2}.$$

These parameters were fixed at $\gamma = 0.05$ and $\omega_c = 200$ cm^{-1}. Critically, all relevant physics with respect to variation of the Huang-Rhys factors in the system Hamiltonian

occurs in the string of eigenvector elements $c_{n,\alpha}c^*_{n,\beta}c_{m,\gamma}c^*_{m,\delta}$. When J=0, this string of elements is δ_{nm}. Therefore non-zero inter-pigment coupling is needed for any population transfer relaxation. For $J \neq 0$ and $S = 0$, relaxation can only occur between corresponding rungs within excited states, e.g. between site basis states $|10\rangle$ and $|20\rangle$ and $|11\rangle$ and $|21\rangle$. For $J \neq$0,$S \neq 0$, population transfer can occur between states of unequal vibrational quanta, e.g. between $|10\rangle$ and $|21\rangle$ and $|11\rangle$ and $|20\rangle$. To assess nominal population transfer rate, the state $|10\rangle$ was assigned to be the terminal state, consistent with the mechanism of exciton flow in light-harvesting bacteria.[421] An initial site-basis population of 0.50 in each of the states $|20\rangle$ and $|21\rangle$ was chosen for $\sigma(0)$. This initial state was rotated to the exciton basis and the Redfield equation was integrated to solve for $\sigma(t)$. The time evolution of the lowest energy state was fit to a growing exponential model $c_1(1 - e^{-kt}) + c_0$ to extract the effective rate constant k in cm^{-1}.

C.3.1 Structured vs Unstructured Spectral Densities

Given that spectral densities are generally regarded as the driving force of a Redfield calculation, however it is worth discussing that there exist multiple decompositions of a spectral density, and therefore different methods of performing density matrix propagations.[422, 423] In particular, the spectral density can be decomposed into a structured and unstructured (or "continuous") spectral density

$$I(\omega) = I_{struct}(\omega) + I_{cont}(\omega)$$

$$I_{struc}(\omega) = \sum_n I^{(n)}_{struct}(\omega)$$

$$I^{(n)}_{struct}(\omega) = \sum_k S_{n,k}\omega_{n,k}\frac{\omega\gamma_{n,k}}{(\omega - \omega_{n,k})^2 + \Gamma^2_d}$$

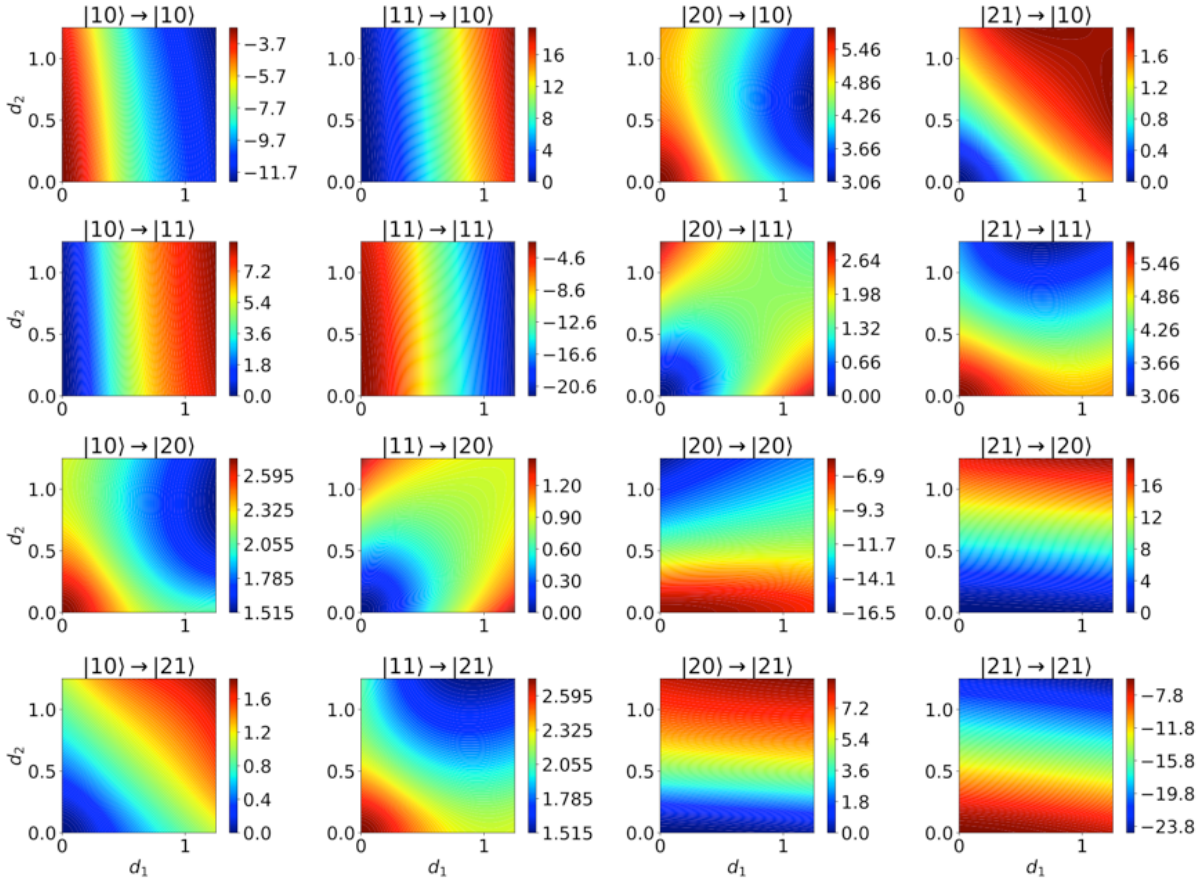

FIGURE C.3: Kinetic rates calculated from CMRT for all sets of states in our model as a function of displacements of the two harmonic potentials. The nomenclature is same as Figure 5.3

where n runs over all electronic states and k runs over all modes with $S_{n,k}$, $\omega_{n,k}$, and $\gamma_{n,k}$ denote the Huang-Rhys factor, frequency, and Brownian damping factor for the kth mode coupled to the nth electronic state. The factor Γ_d is simply the vibrational dephasing which is typically on the order of a few cm^{-1}. Structured spectral densities typically correspond to prominent vibrational peaks belonging to intrachrompohore vibrations and environmental (e.g. solvent or protein backbone) vibrational modes while the continuous density is well-described by coarse-grained Brownian oscillator models, such as the

super-Ohmic density used above. There are instances when it is advantageous to consider only the continuous portion of the spectral density.[424] Such a situation occurs when pigment modes are suspected to not play a role in kinetics and therefore one wishes to isolate the effects of the environment. However, we note that any degree of freedom relegated to the spectral density necessarily results in a loss of information. Thus, if one wishes to study the limit in which pigment vibrations are taken to be the driving force for excitation transfer kinetics, such as in this work, one should include those vibrations explicitly in the system Hamiltonian. In fact, this separation of the structured portion of the spectral density into the system is easily accommodated in the multilevel Coherent Modified Redfield Formalism and gives us more information about the population dynamics specific to each state, as shown in Figure C.3. This justifies our use of the super-Ohmic spectral density as we are only modeling the effects of the environmental modes in a coarse-grained manner. All pigment modes are explicitly correlated to one another.

C.4 Discussion of Signal Pathways

A number of differing mechanisms may cause inhomogeneous vibrational landscapes as a function of ω_τ in observed in Figure 5.2, but all appear with slightly different signatures. The possible effects include: finite pulse bandwidth, differing ground state enhancements for Franck-Condon pathways, and differing J-coupling in different excitonic manifolds. While only the J-coupling mechanism directly affects the energy of the vibrational states, it is possible that different energy modes appear and disappear into the noise floor giving the appearance of energy levels changing. We will examine each of these possibilities in the context of whether they are plausible explanations for the result shown in figure 5.2 of Chapter 5.

Because coherences are generated using compressed pulses, the bandwidth of the pulse dictate what coherences are possibly generated for a given set of energy levels. In order to generate a coherence between two energy levels, the pulses need to have the bandwidth to simultaneously excite both energies. Furthermore, the particular phase matching condition used in our experiment ($-k_1 + k_2 + k_3$) generates either positive or negative frequency coherences depending on if the first interaction excites the higher lying vibration or lower lying state of a given coherence. However in 2DES, the pulse bandwidth is often of similar magnitude as the electronic transition linewidth being studied. Thus, the pulse bandwidth and the center frequency of the pulses serve to select for certain pathways with more or less amplitude, with certain pathways being completely disallowed. Many works have detailed the effects of pulse spectrum, and demonstrated that it can change both peak positions and shape along ω_τ and ω_t.[425–427] Along ω_T, work by Camargo et al. is especially relevant, which demonstrates that the pulse spectrum filters certain coherence pathways to change the amplitude of peaks, but not to change the frequency.[428] If the pulse is centered on the red or blue side of the electronic transition, either the negative or positive frequency vibrations will be observed with less amplitude. The reason the frequency does not change is because the bandwidth of the pulse is still generally much broader the linewidth of a vibrational state. Figure C.4 diagrammatically describes the situation for the excited state emission pathway. The solid and dotted arrows each denote actions of the dipole operator on the bra or ket side of the density matrix. The end result is that depending on if the pulse is centered on the red or blue side of the electronic transition, either the negative or positive frequency vibrations will be observed with less amplitude. This effect highlights the necessity for smooth pulse spectra, as structured spectra effectively scramble the relative peak heights even for peaks close

in energy to each other. Additional effects are possible for pulses with non-flat phase profiles, but these challenges are circumvented experimentally by using pulses that exhibit both a smooth spectral profile and flat spectral phase. The pulses used in this experiment exhibit both these properties and the TG-FROG trace measured at our sample location can be found in figure C.7.

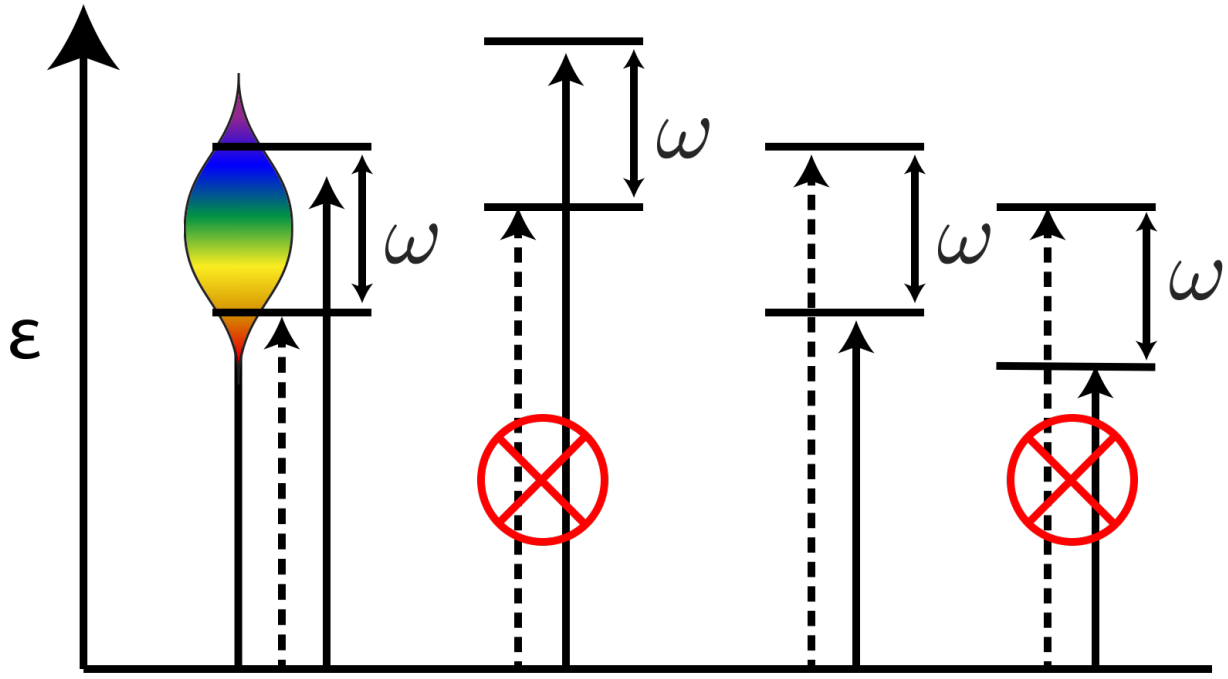

FIGURE C.4: Effect of pulse bandwidth on ω_T coherences.

The next possibility is that the differences of vibrational energies as a function of ω_T arise from either a difference in ground state vibrations or from different Franck-Condon pathways modulating ground state vibrational amplitudes. In order to explain the observed peak splitting phenomenon from different Franck-Condon enhancements of ground state modes, all three energies of vibrations would need to exist in the ground state, and when

excited at B800, the Franck-Condon factors would need to enhance only the middle energy peak while simultaneously suppressing the two other peaks below the noise floor. When excited at B850, the middle energy peak would need to be suppressed below the noise floor, while simultaneously enhancing the two peaks around it. The most direct way to address this question would be to compare our results to Resonance Raman results from excitation at B800 or B850 to slices of our data at those same excitation energies. However, isolated LH2 is highly fluorescent in the Qy state and that specific experiment that would allow for direct comparison to our study has not been successfully performed due to this technical challenge.[429] For our particular question of whether or not differences in vibrational landscapes can be explained through ground state processes, there are other experiments that serve as useful comparisons. Mattioli et al. collected a Fourier Transform Raman spectrum with 1064 nm excitation of LH2 from r. sphaeroides and found ground state vibrations in the low frequency region with energies of 574, 735, 895, and 950 cm^{-1}.[430] Our experiment summing all the coherences finds these vibrations at 570, 731, 895, and 955 cm^{-1}. In addition, our experiment finds many additional modes, evidence that at least these additional modes are from the excited state. However, this does not answer the question of whether or not B800 and B850 have different ground state modes. Robert et al. performed Resonance Raman spectroscopy on the soret bands of both native LH2 r. *sphaeroides* as well as the LH2 complex depleted of the B800 ring and found that only one mode under <1000 cm^{-1} changed after the B800 depletion, which was the band located at 792 cm^{-1} for the native species shifting to 795 cm^{-1} for the depleted species.[431] With evidence that the B800 and B850 share the same ground state modes, the only remaining question is regarding if certain modes are enhanced relative to others differently after excitation at 800 nm or 850 nm. Chumanov et al. performed pre-resonant surface-enhanced Raman with an excitation at 752 nm, which quenched the

fluorescence with Ag nanoparticles.[432] This experiment found no modes of LH2 from r. sphaeroides under 565 cm^{-1} in agreement with Mattioli et al.'s non-resonant experiment. Experiments examining B850's enhanced Franck-Condon pathways have been performed working with the strong fluorescence rather than getting around it with delta fluorescence linewidth narrowing (FLN) to observe low frequency vibrational modes. Freiberg et al. previously has used this technique to obtain high quality FLN spectra of FMO with many vibrational modes, but only observed a broad phonon-side band in the <200 cm^{-1} region with excitation at 871 nm.[433, 434] In summary, B800 and B850 share the same ground state vibrational modes, and the observation of modes in 2DES not seen in previous ground state experiments make it likely that the modes observed in our study are from the excited state.

If the vibrational modes are coupled to the excited electronic states, then the differences in *J*-coupling between the B800 and B850 band would inherently change the energies and coupling strength of the vibrations as described in detail in section C.1. Previous work in our group and work by both the Collini and Ogilvie groups have established that coherences of BChla report on excited state vibrations.[99, 138, 139] Figure 5.1 demonstrates that the coherences observed in LH2 and FMO primarily have contribution from the pigment coherences. It is known that the B850 band of LH2 has stronger *J*-coupling relative to the B800 band, which has the effect of modulating the coupling of different pigments vibronic states resulting in different excited excitonic landscapes.[435, 436] In this case, not only would energies of states shift, but they would naturally split. However, due to the large number of states in the system and the unknowns of which states are actually being coupled, the *J*-coupling cannot be estimated from the splitting of vibrational states. Thus, the relative simplicity in which the *J*-coupled vibronic model is able to encapsulate

the features of our spectra qualitatively prompts us to assign the inhomogeneous vibrational differences between B800 and B850 to differences in the excited state landscape.

Examination of the pathways that generate the 2DES signal also offer a methodology to determine whether vibrational coherences originate from an excited state or ground state pathway. Broad congested overlapping electronic features makes this sort of analysis uncertain, but it is still worthwhile to discuss what it may reveal. Figure C.5(a) shows a slice of the LH2 nDES dataset at a short time delay (T = 43 fs). The negative features result from excited state absorption (ESA), while positive features represent either ground state bleach (GSB) or excited state emission (ESE), or a combination of both. Features I and III can be assigned to be GSB from the B850 ring and B800 ring respectively from the ground state absorption spectrum. The feature denoted II has the same rate of growth and decay as the GSB of I shown in figure C.6. From this characteristic lifetime, the ESA in region II has previously been assigned to be from the excited B850 ring.[437] Figure C.5(b) diagrammatically shows the three possible pathways, illustrating which pathways would report on ground vs excited state vibrational coherences and which pathways result in positive and negative coherence frequencies.[438] ESE signal may have both positive and negative frequencies, while GSB features can only have negative frequencies unless the initial state of the system is an excited vibrational state. Ground state vibrations above 207 cm^{-1} (298K $\times$ k_B) have little initial thermal population. Therefore, positive frequency coherences are not expected from the GSB above that energy with great amplitude. Fourier transforming the time domain coherences along the pump-probe delay dimension reveals the coherences associated with features I-III in figure C.5(c). Because ESA only contains coherences from the excited state, features in II are assigned to vibrations of the excited

B850 band. While both GSB and ESE features may overlap in section I, the high amplitude of high frequency positive coherences indicates these are excited state vibrations on the B850 manifold. Since the ESE and ESA pathways report on the same coherences, the similarity of the plots for sections I and II adds more evidence that the observed coherences can be assigned to the excited state. Due to the large transition dipole of the B850 band compared to B800, a separate scan with the bandwidth of the laser pulse centered around B800 was performed to investigate that band in more detail. Figures C.7 and C.8 show the coherences found in all regions of both scans. Shown in figure C.5(c) in region III, a similar symmetric density of positive and negative coherences are observed. A visual guide for what the asymmetric ground state bleach signal might look like is included for regions I and III. Since positive GSB coherences only arise from thermally populated ground state vibrations, the negative frequency coherences are multiplied by the Boltzmann distribution with T = 298K and overlaid on top of the positive coherences. Another way to visualize this idea is shown in figure C.5(d), where the ratio of the amplitude of all coherences above and below 200 and -200 cm^{-1} is displayed. Along the diagonal, the ratio is roughly equal, while above and below the diagonal there are more negative and positive coherences respectively, as is expected for vibronic coherences.[439]

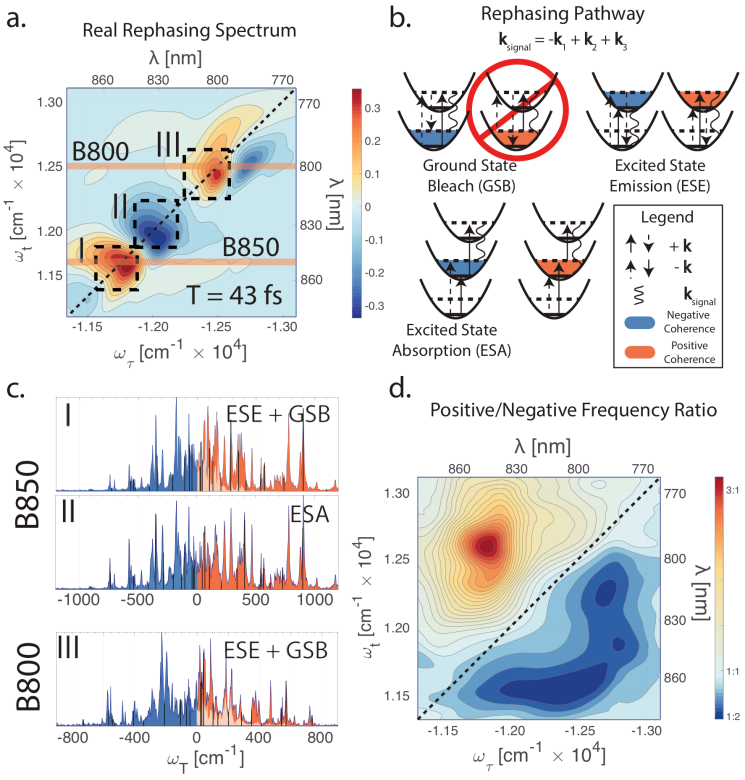

FIGURE C.5: (a) Real rephasing portion of the nDES spectra at T = 43 fs. The x axis corresponds to the first time dimension and can be thought of as the electronic states being pumped. The y axis corresponds to the detection or "probe" axis. The diagonal line represents pumping and probing at the same energy. (b) Pathways can be distinguished based on the sign of the coherence frequency. Ground state bleach cannot have a positive frequency unless there is initial population in an excited vibrational state ($\sim k_B T$ = 207 cm^{-1}). Thus seeing symmetric coherences gives information about vibrations on the excited state manifold. (c) Coherence frequencies from the boxed regions in (a). The broadband scan was used for the B850 coherences while the scan centered around 800 nm was used for the B800. The negative frequencies in I and III are reflected and multiplied by the Boltzmann distribution with T=298K to visualize what the signal might look like if only GSB contributed. Coherences for all regions for both scans can be found in figures C.7 and C.8. (d) The ratio of positive and negative frequencies above 200 cm^{-1} and below -200 cm^{-1} respectively. This shows roughly equal intensity of positive and negative frequencies on diagonal and positive and negative frequencies above and below diagonal as would be expected vibronic coherences on the rephasing pathway.

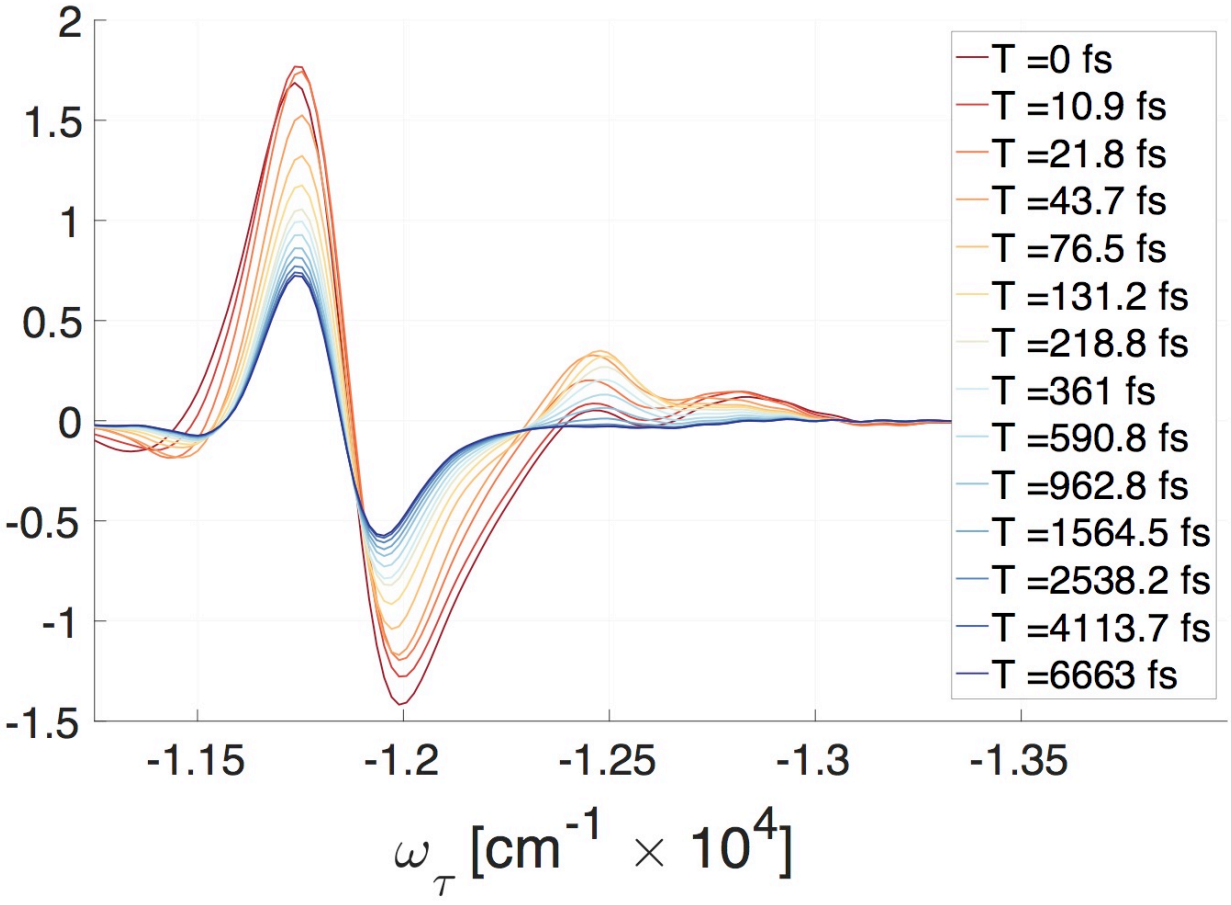

FIGURE C.6: Diagonal slice as a function of time. The GSB and ESA features around 11700 and 12000 cm^{-1} decay at the same rate and thus the ESA is assigned to absorption from the B850 band. The sections drawn in Figure C.5 are based off this plot.

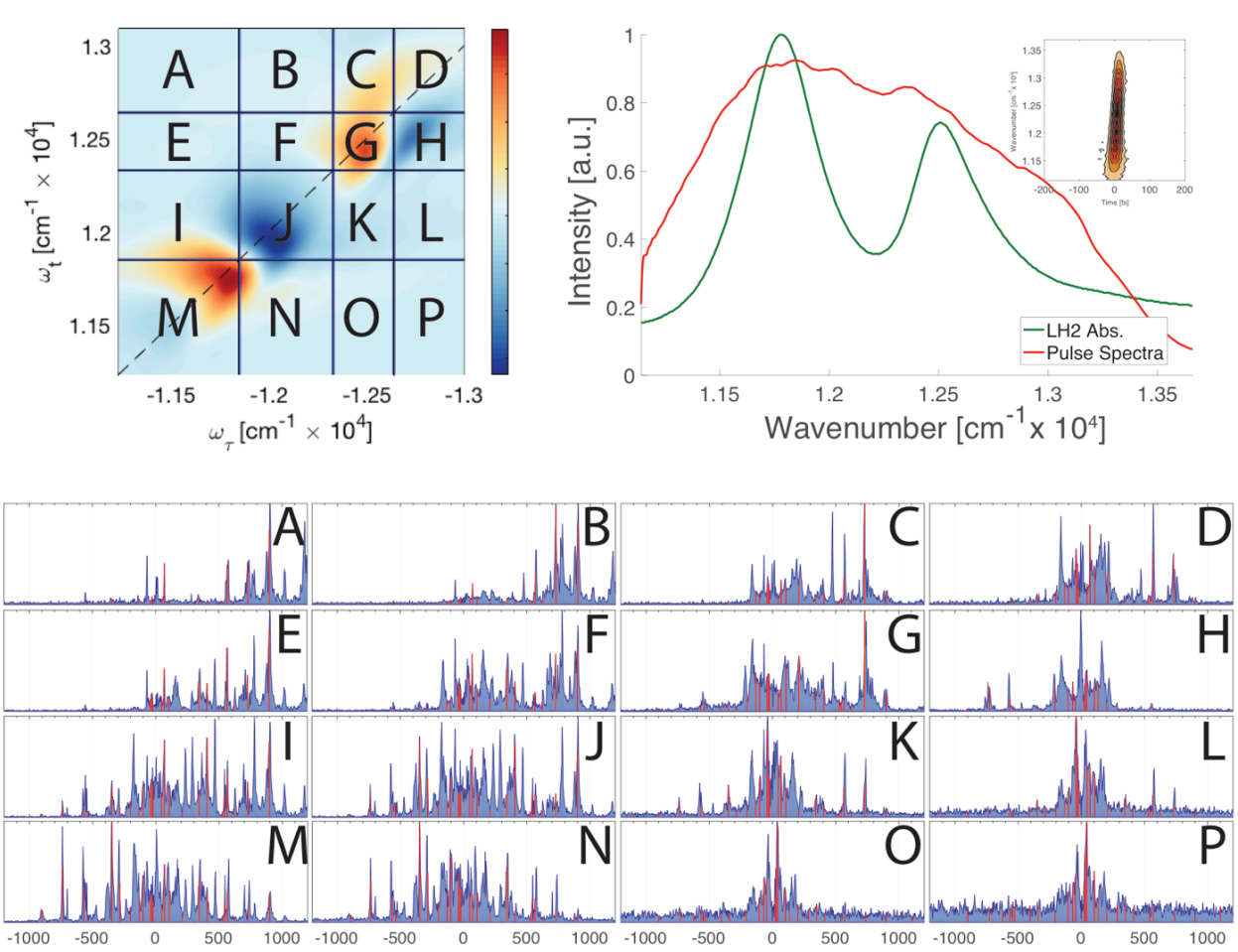

FIGURE C.7: Summed coherences of each section of the 2D spectra displayed in the top left. The pulse spectra used is displayed on the top right with the TG-FROG trace as an insert. This scan had a very strong ESA feature because of the large population created in B850 leading to an asymmetry in coherences above and below the diagonal.

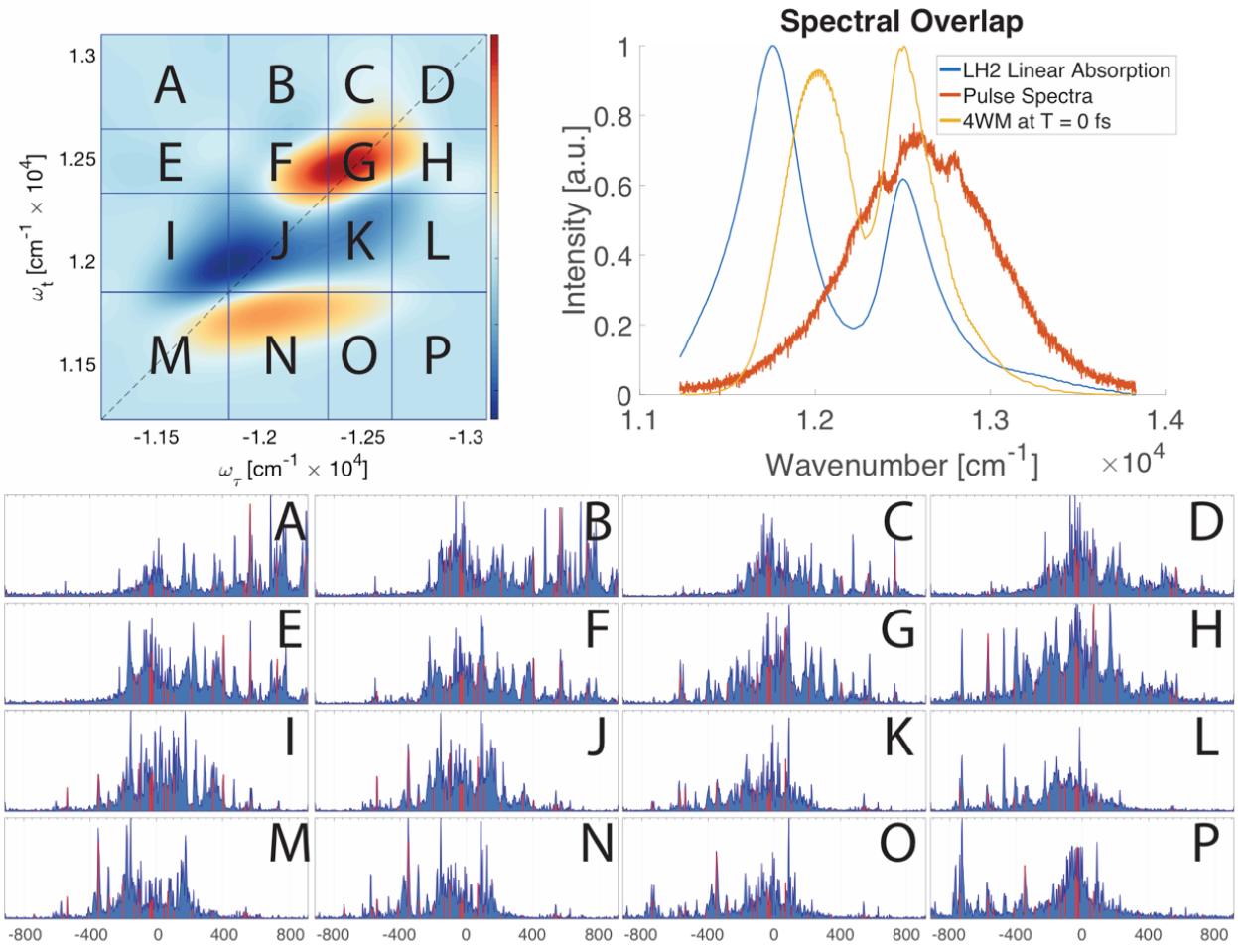

FIGURE C.8: Summed coherences of each section of the 2D spectra displayed in the top left for the scan with the pulse bandwidth centered on the B800 transition.

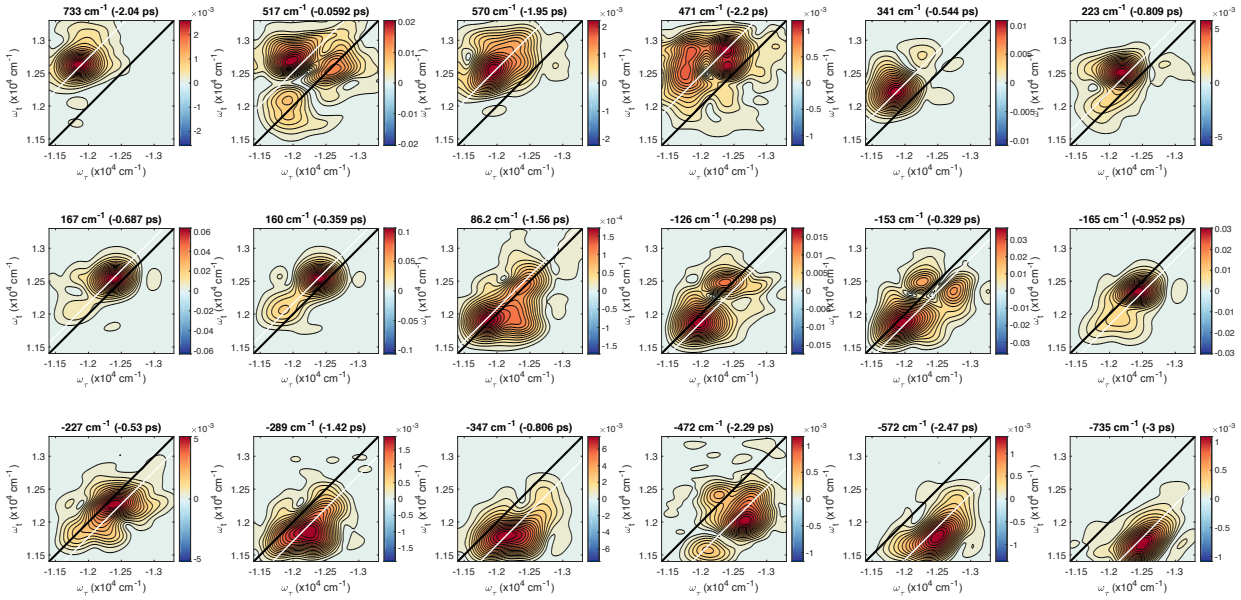

FIGURE C.9: Amplitudes of oscillations resolved over the pump and probe dimensions. The title of each plot contains the oscillation frequency as well as the decay lifetime in parentheses extracted using global analysis.

Supplementary Information For: Chapter 7

D.1 Electron Microscopy of Nanoplatelets

The CdSe NPLs and CdSe/CdS core/shell NPLs were synthesized following published procedures with minor modifications.[440–442] Transmission electron microscope (TEM) images for the 4ML core-only NPLs (Figure D.1) and 4ML core-shell NPLs (Figure D.2) and corresponding size distributions are shown below.

D.2 Representative Single-Particle Spectra and Blinking Trajectories

An exemplary spatial image of emitters is shown in Figure D.3. The dilution of the film is such that emitters are separated by at least a few microns, on average. The resulting emission can be directed into a spectrograph to examine the time-averaged emission spectra, as shown in Figure D.3, or, emission spectra can be taken sequentially to obtain successive spectra used to observe spectral diffusion on a $>\sim$100 ms timescale. The emission

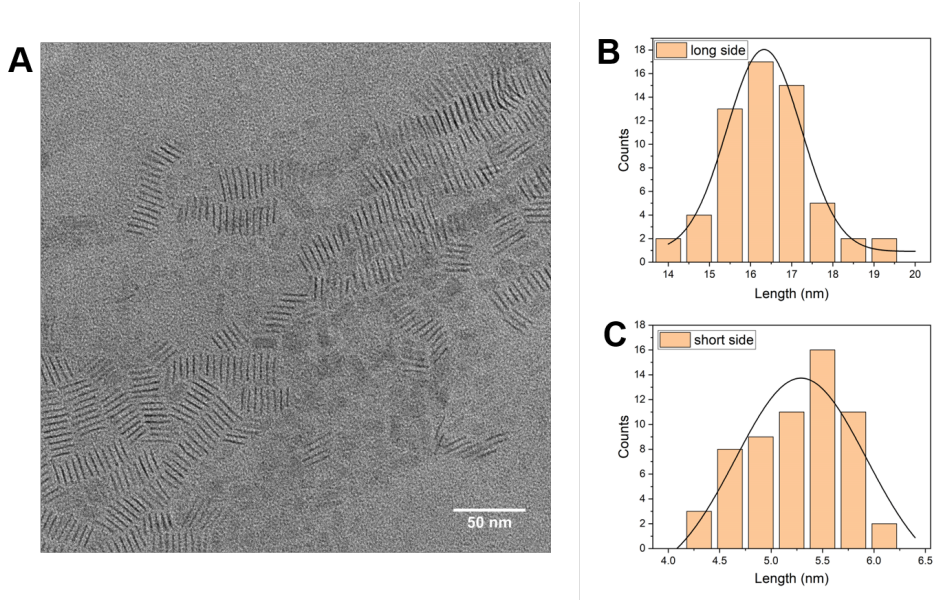

FIGURE D.1: (a) TEM image of 4ML CdSe core-only NPLs. (b,c) Histograms of the lengths of the long side and short side of core-shell NPLs yield an average size of $(16.3 \pm 0.9) \times (5.3 \pm 0.6)$ nm.

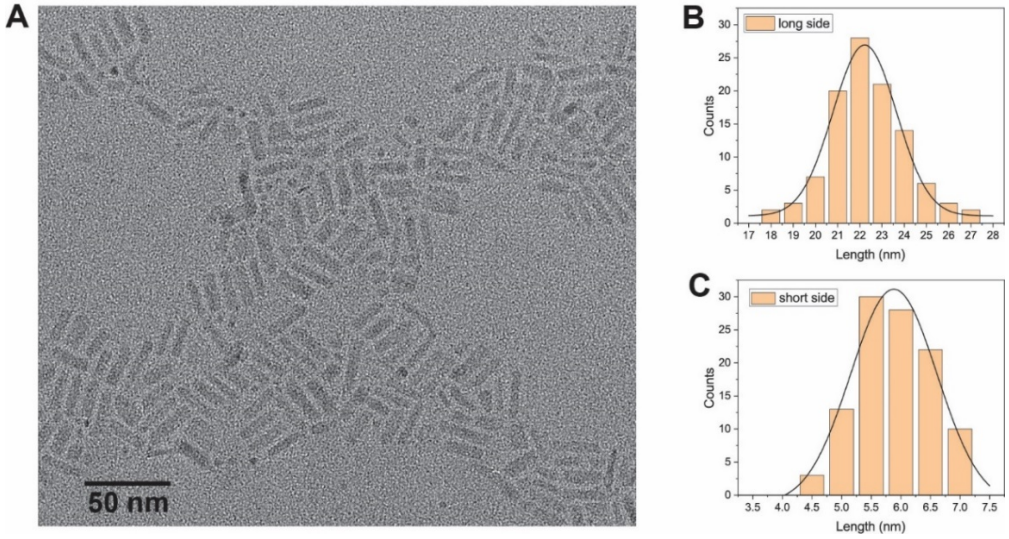

FIGURE D.2: (a) TEM image of 4ML/1ML CdSe/CdS core/shell NPLs. (b,c) Histograms of the lengths of the long side and short side of core-shell NPLs yield an average size of $(22.2 \pm 1.7) \times (5.9 \pm 0.8)$ nm.

of spatially separated emitters can also be sent to APDs resulting in a stream of photons that can be converted into a time trace like Figure D.4, and this data can be compiled into count rate histograms as in Figure D.5. For the representative data shown in this figure, the core-only sample spends 35% of the time in the "on" state while the core-shell is 98% "on".

Taking the photon streams from the two APDs, we cross-correlated the counts detected to generate an anti-bunching plot (Figure D.6). Once we have determined we are indeed looking at a single photon emitter through a confirmation of $g^{(2)}$ ($\tau = 0$)<0.5, we proceed to monitoring spectral diffusion.

D.3 Fitting of the Time-Correlated Single Photon Counting Time Traces

Intensity time traces, like that in Figure 7.2(b) of the Chapter 7, also contain the timing of photon arrival relative to the excitation pulse, allowing us to create a Time-Correlated Single Photon Counting (TCSPC) trace for each time point. The traces are fit with single exponential functions to extract the lifetimes of the states emitting each photon. The lifetime is then plotted against the emission intensity to generate the plot seen in Figure 7.2(c) of Chapter 7.

Figure D.7 is a reproduction of Figure 7.2(b) of Chapter 7, where three regions are highlighted: x = 18-27 ns, y = 750 - 1250 counts for Region I, x = 15 - 25 ns, y = 280 - 400 counts for region II, and x = 9 - 16 ns, y = 350 - 650 counts for region III. From each region, three TCSPC traces are chosen at random and plotted below along with the single exponential fits.

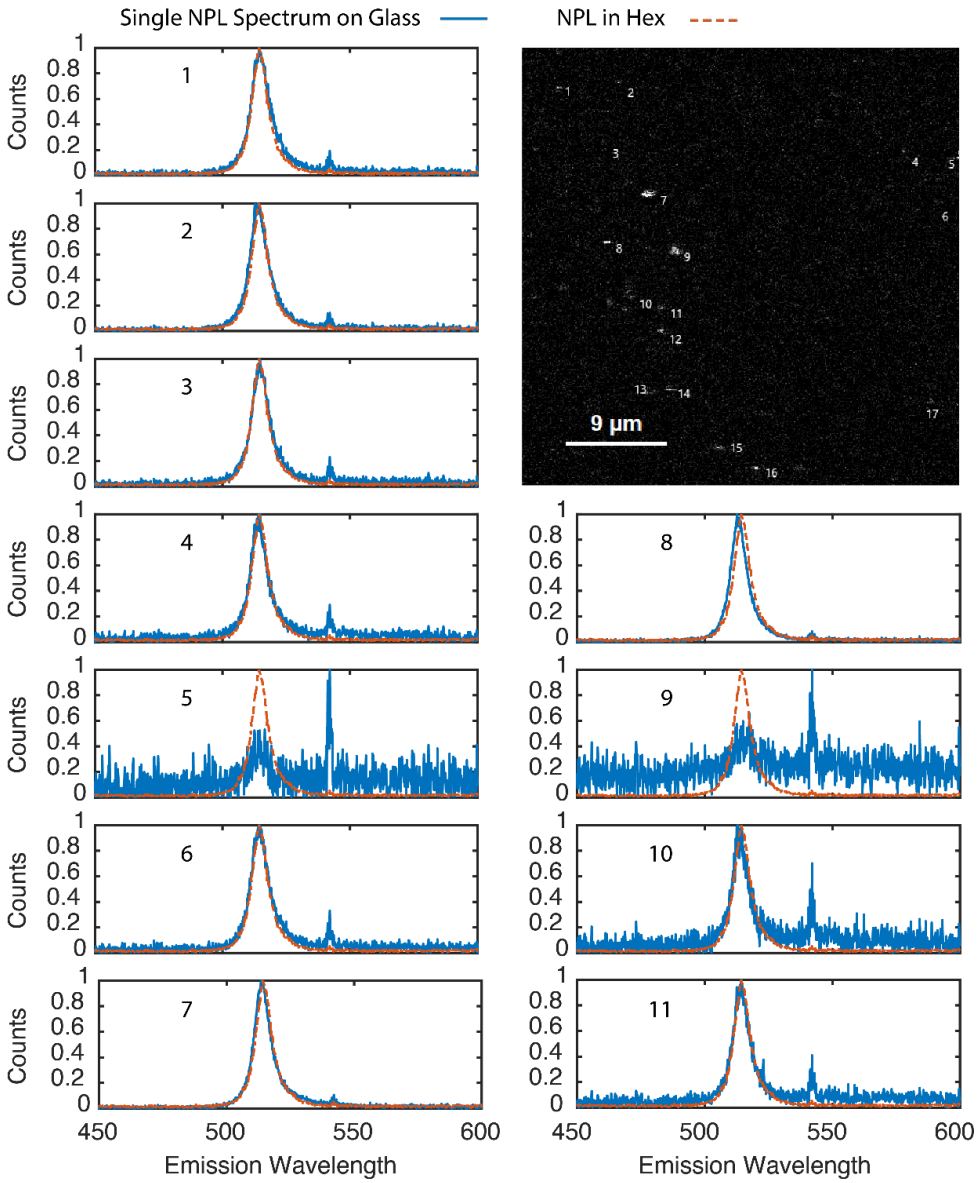

FIGURE D.3: A spatial image of individual 4ML CdSe NPL emitters. The spectrum from each numbered location is displayed, along with the emission spectra of the ensemble of NPLs dispersed in hexane (for comparison). The small peak at 540 nm in the emission spectra is background light.

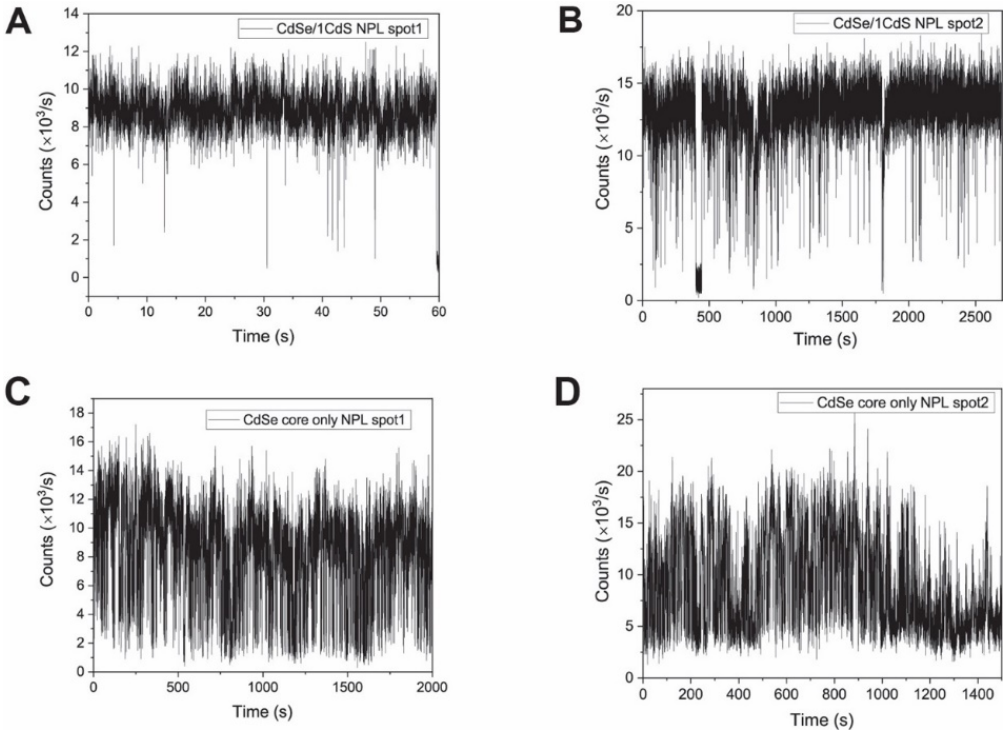

FIGURE D.4: Time traces obtained from two separate 4ML/1ML CdSe/CdS core/shell NPLs (a/b), and two separate 4ML CdSe NPLs (c/d).

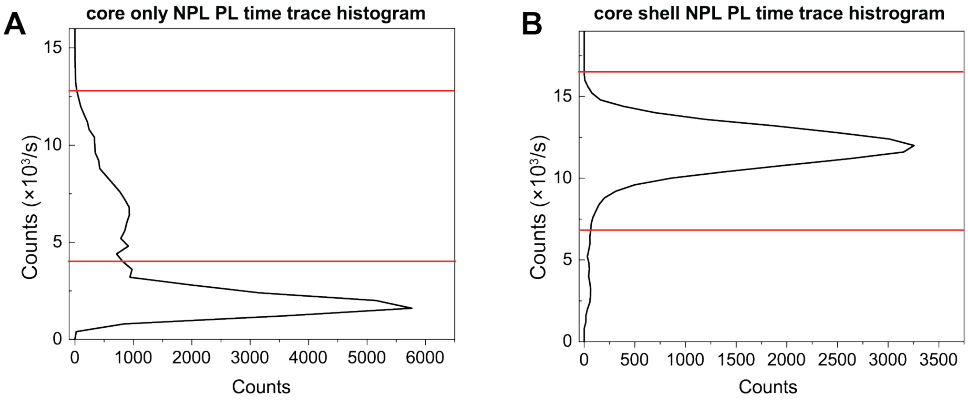

FIGURE D.5: Histograms of the emission count rate for a 4ML core-only CdSe NPL (a), constructed from the data in Figure D.4(b); and a 4ML/1ML CdSe/CdS core/shell NPL (b), constructed from the data in Figure S4C. The bin size is 400 counts per second. The "on" time percentages (35% for the core-only NPLs and 98% for the core/shell NPLs) are determined by integrating the region between red lines divided by the total number time bins.

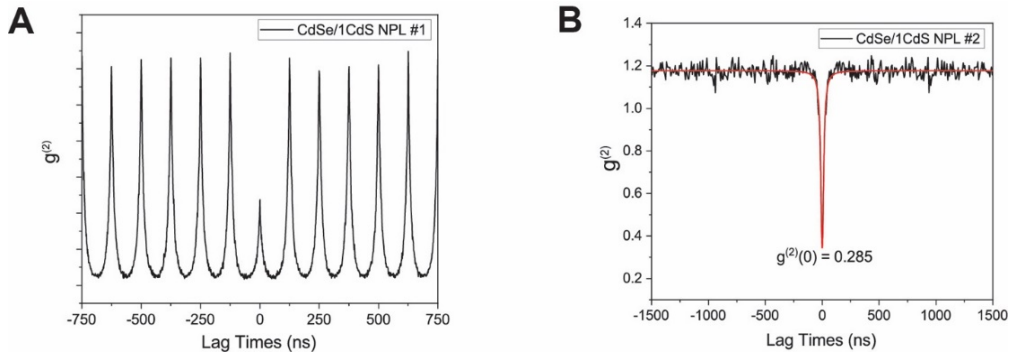

FIGURE D.6: Examples of antibunching plots for single 4ML/1ML CdSe/CdS NPLs using pulsed laser excitation (a), and CW laser excitation (b).

D.4 Correlation Analysis of Sequential Emission Spectra

Observation of spectral diffusion in the spectrometer is most simply done by taking sequential spectra of emitters. Sequential spectra like the one shown in Figure 7.3(a) of Chapter 7 can be analyzed to obtain a characteristic timescale of spectral diffusion. This is done through the use of spectral correlations.

If we assume the spectrum of the emitter $s_{eff}(\omega)$ is a Gaussian peak with linewidth $_{eff}(\tau)$ evolving with correlation time τ,

$$s_{eff}(\omega) = \frac{1}{\sigma_{eff}\sqrt{2\pi}} e^{-\frac{(\omega-\omega_0)^2}{2\sigma_{eff}^2}}$$

then the spectral correlation function $p(\zeta, \tau)$ can be written as:

$$p(\zeta,\tau) = \int_{-\infty}^{\infty} s(\omega)s(\omega+\zeta)d\omega$$

$$= \int_{-\infty}^{\infty} \frac{1}{\sigma_{eff}\sqrt{2\pi}} e^{-\frac{(\omega-\omega_0)^2}{2\sigma_{eff}^2}} \frac{1}{\sigma_{eff}\sqrt{2\pi}} e^{-\frac{(\omega+\zeta-\omega_0)^2}{2\sigma_{eff}^2}} d\omega$$

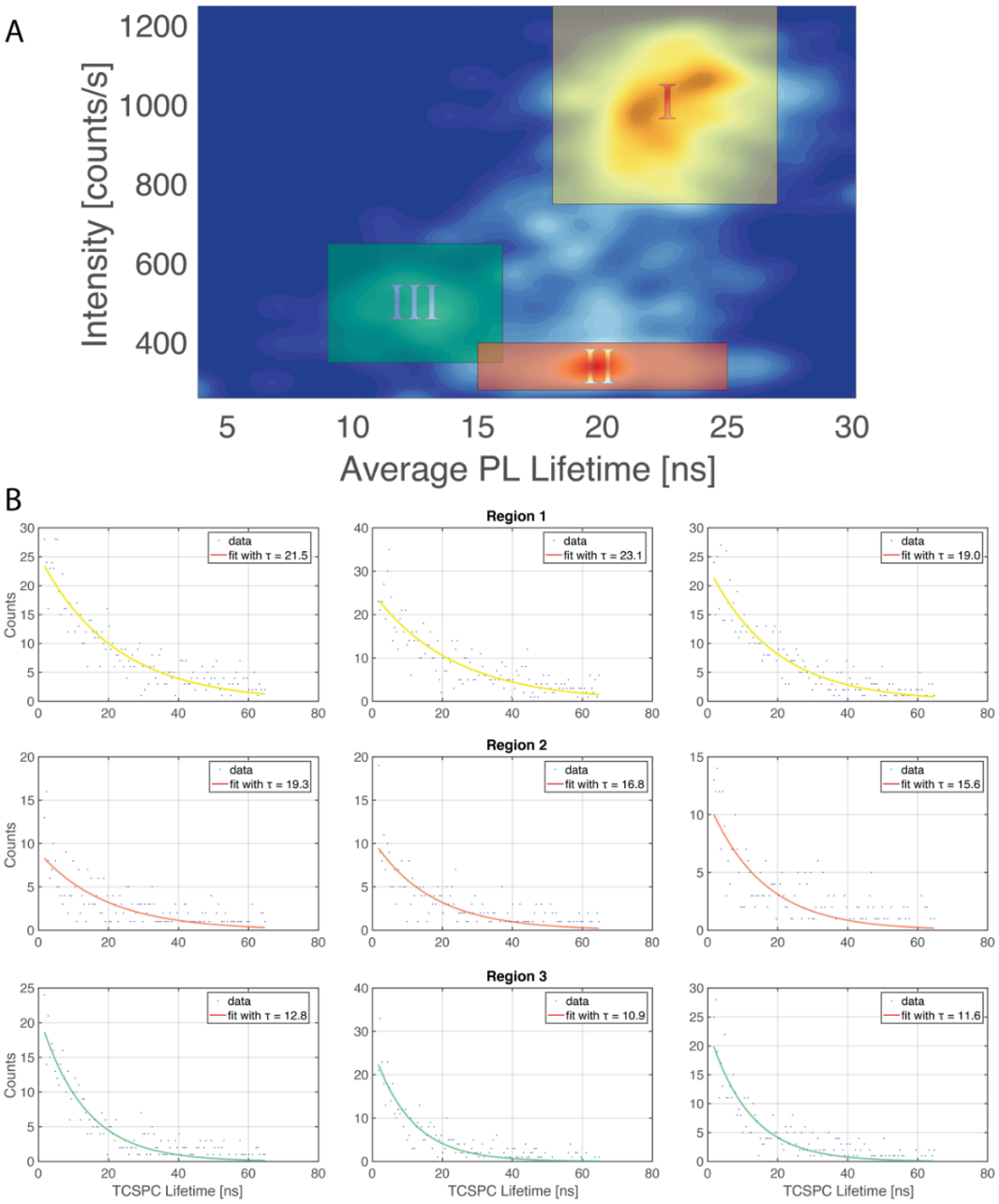

FIGURE D.7: (a) Recreation of Figure 7.2(b) of Chapter 7 with 3 regions highlighted. (b) Representative traces from each region with the single exponential fit functions used to extract the PL lifetimes.

$$= \frac{1}{2\sigma_{eff}^2\pi}\int_{-\infty}^{\infty} e^{-\frac{(2\omega^2+2\omega_0^2-4\omega_0\omega+2\zeta\omega-2\zeta\omega_0+\zeta^2)}{2\sigma_{eff}^2}} d\omega$$

$$= \frac{1}{2\sigma_{eff}^2\pi}\int_{-\infty}^{\infty} e^{-\frac{(2(\omega-\omega_0+\zeta/2)^2+\zeta^2/2)}{2\sigma_{eff}^2}} d\omega$$

$$= \frac{1}{2\sigma_{eff}^2\pi} e^{-\frac{\zeta^2}{2(\sqrt{2}\sigma_{eff})^2}} \int_{-\infty}^{\infty} e^{-\frac{(2(\omega-\omega_0+\zeta/2)^2)}{2\sigma_{eff}^2}} d\omega$$

$$= \frac{1}{2\sigma_{eff}^2\sqrt{\pi}} e^{-\frac{\zeta^2}{2(\sqrt{2}\sigma_{eff})^2}}$$

The spectral correlation function of a Gaussian spectrum is also a Gaussian, but centered at ζ=0 and with a linewidth of $\sqrt{2}\sigma_{eff}$. We first calculated the spectral correlation function from the data of Figure 7.3(a). By fitting the spectral correlation function with Gaussian peak function and using the relationship of $\sqrt{2}\sigma_{eff}$ with σ_{eff}, we plot the effective linewidth σ_{eff} vs correlation time τ in Figure 7.3(c).

D.5 Averaging Spectrally Biased Cross-correlation Traces

We used multiple spectrally biased cross-correlation traces similar to Figure 7.4(d) in order to identify the transition between SD-free blinking at <1 s timescales and SD-correlated blinking at >1 s. We did not simply average these traces from separate experiments, since each blinking trajectory results in a different correlation trace. Instead, we averaged the ratio between the cross-correlation and the autocorrelation at each time point. With no SD, the cross-correlation is identical to the autocorrelation and the ratio of the two is 1. SD introduces anti-correlation in the cross-correlation, so,

with SD present, the ratio dips below 1. Figure D.8 shows the average of seven cross-correlation:autocorrelation ratios from separate experiments plus the standard deviation from the average as an area plot. The raw individual traces are shown as smaller plots below the main plot. As shown in Figure 7.4(d) in Chapter 7, the ratio is within one standard deviation of 1 until ∼3 s, when it dips below 1.

D.6 Photon-Correlated Fourier Spectroscopy (PCFS)

The details of the PCFS technique have been extensively documented by the Bawendi group.[443–447] After photoluminescence is collected from our homebuilt confocal microscope, it is directed to a Michaelson interferometer, which consists of a 2" non-polarizing beam splitter (Newport 20BC17MB.1) and two corner cube retroreflectors (PLX OW-25-1D) mounted on two computer-controlled stages. The corner cube used to dither around a setpoint was a closed-loop piezo stage (Thorlabs NFLDP20S controlled by BPC301). The closed loop functionality allowed us to introduce a sawtooth waveform with a function generator to guarantee a consistent dither movement over two interference fringes at 0.5 Hz. The coarse stage controlling δ was a Newport SMC100. The output of the interferometer was coupled into two APDs (Micro-Photon Devices PDM) using achromatic lenses (Thorlabs AL1225M-B) mounted in a XYZ translation mount (Thorlabs CXYZ05). The outputs of the APDs were connected to timing electronics that recorded every photon arrival time (Picoquant Picoharp 300). All hardware control was written using Labview with supplied DLLs and data processing was done in Matlab. The log-spaced correlation was calculated using an open source function available online.[448] The spectrally biased cross-correlation measurements were conducted inside the same interferometer, with the SMC100 stage moved to δ=5 ps so that there was no contribution from interference. Color

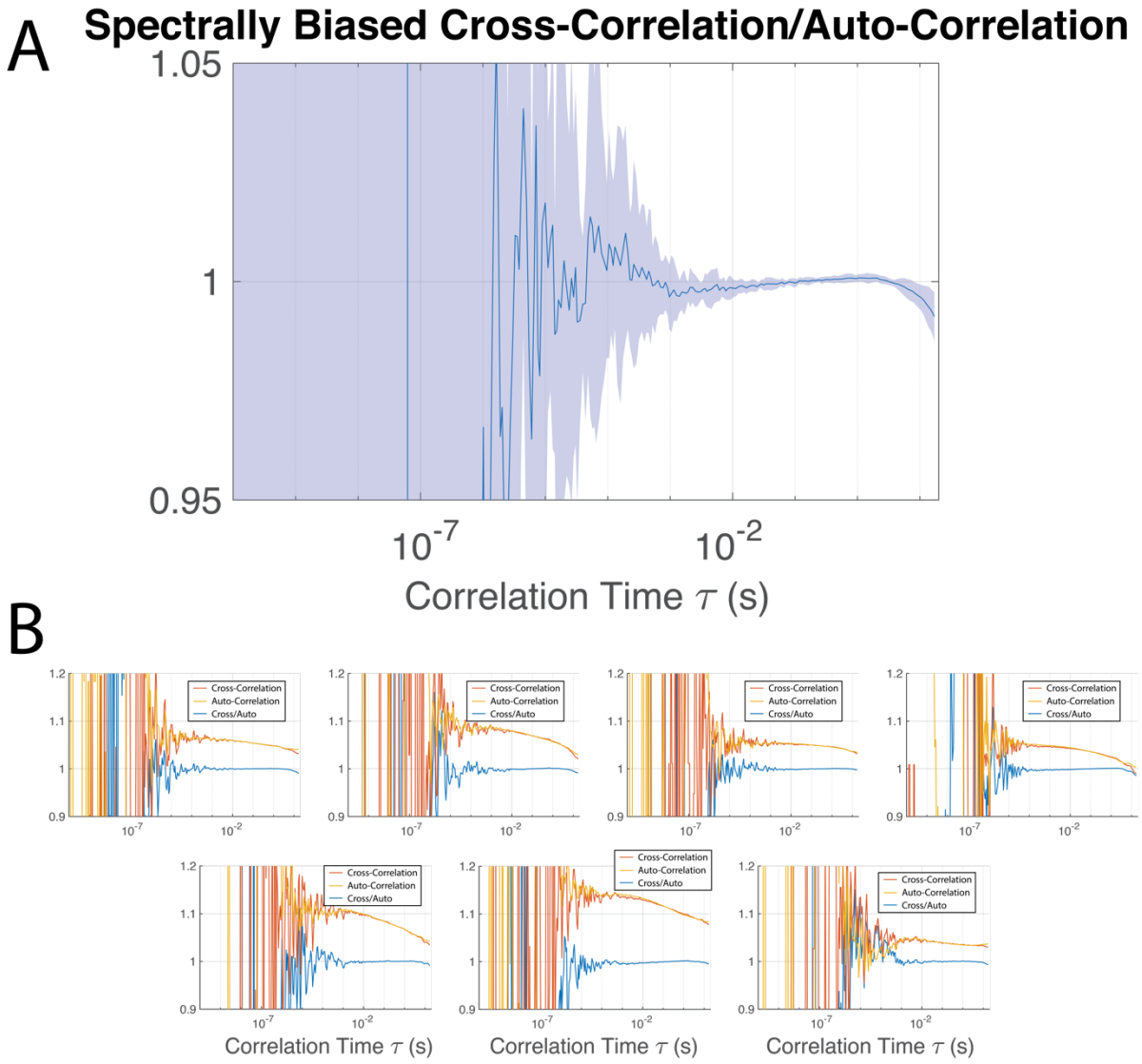

FIGURE D.8: Additional Spectrally Biased Cross Correlation Traces. The average and standard deviation of 7 different spectrally biased cross-correlation/auto-correlation ratios (a). Individual traces of spectrally biased cross-correlations and auto-correlations (b). The ratio of cross/auto correlation is used to average the different traces and not the correlations directly, which vary depending on blinking behavior.

glass long-pass and short-pass filters were placed in front of the two detectors. All subsequent optics, electronics, and processing was performed similar to the PCFS measurement.

Representative data from the PCFS are shown in Figure D.9. Figures D.9(a,b) are the intensity time traces for the two detectors (detector 1 in orange and detector 2 in blue) with a bin size of 100 ms. The traces in Figures D.9(a,c) result from photon streams exhibiting interference, and the traces in Figures D.9(b,d) result from photon streams with no interference. When interference is present, the intensity time trace shows oscillatory behavior as introduced by the stage dither (a), and the cross-correlation falls below the auto-correlation (c). When no interference is present, the intensity on the two detectors look the same, as the stage dither has no detectable effect (b). The lack of interference results in overlapped auto-correlation and cross-correlation traces (d). The use of correlations allows for an extraction of the amplitude of interference for photons separated by a certain lag time τ.

The sensitivity of PCFS is limited at slow timescales due to the timescale on which the optical interference is generated by a stage dither. The stage dither causes the cross-correlation at long timescales to oscillate so that a comparison of cross-correlation and auto-correlation is no longer valid. Slowing down the dither can improve this sensitivity, but it introduces additional issues such as microscope drift and sample degradation, because the experiment takes longer to complete. At fast timescales, PCFS is limited due to artifacts of afterpulsing of the APDs. APDs have a finite probability of registering another event after a photon arrives at the APD, so that in the auto-correlation there is a higher probability of seeing another "photon" $\sim$1 ns after the actual photon arrives. This is not an issue for the cross-correlation, since on the 1 ns timescale, a photon arrival on detector

1 does not change the probability of a photon arriving on detector 2. In Figure D.9(c,d), the timescales at which PCFS are limited are shaded orange. We do not interpret data in these regions.

D.7 Statistical Analysis of PCFS Traces

Figure D.10 shows 20 additional plots of coherence lifetime (T_2) vs. correlation time for single CdSe/CdS core/shell NPLs. The blue line is the average of these parameters for the 20 samples and the blue shaded region represents one standard deviation from the mean; the raw traces are shown below the average plot. On the timescales at which PCFS is sufficiently sensitive (1 ns - 100 ms), no change in T_2 is observed with correlation time, indicating a lack of SD on those timescales.

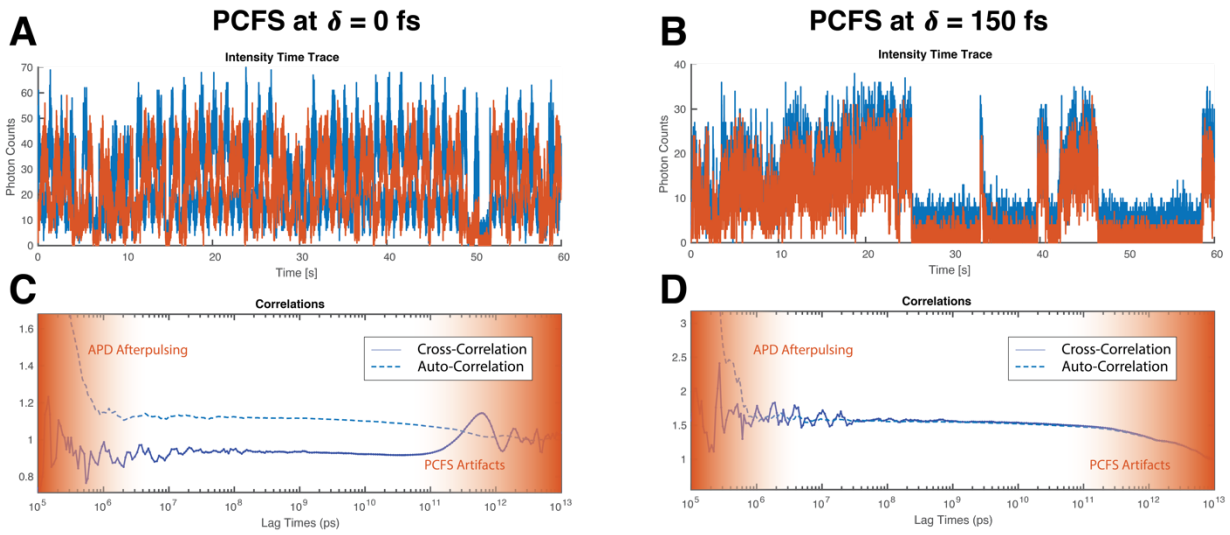

FIGURE D.9: Example of photons exhibiting interference (a,c) and no interference (b,d). The intensity time traces are shown for the two detectors with a bin size of 100 ms, for detector 1 in orange and detector 2 in blue. When interference is present, the intensity time trace shows oscillatory behavior as introduced by the stage dither (a), and the cross-correlation falls below the auto-correlation (c). When no interference is present, the intensity on the two detectors look the same, as the stage dither has no detectable effect (b). The lack of interference results in overlapped auto-correlation and cross-correlations traces (d). The orange shaded regions indicate timescales at which PCFS is not sensitive due to either APD afterpulsing or artifacts.

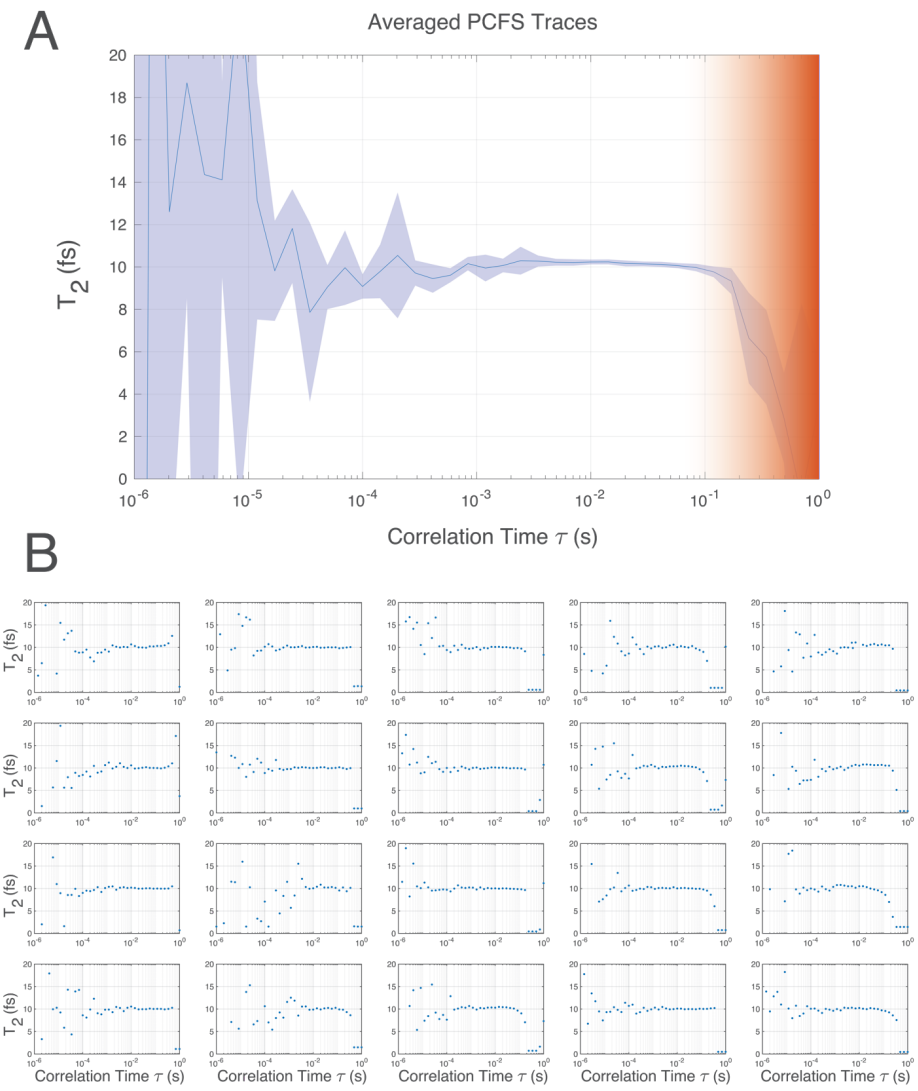

FIGURE D.10: (a) Average of the coherence lifetimes (T_2) of 20 different particles (with individual traces collected in (b)) extracted from PCFS data. The orange region is the timescale at which the stage dither limits the sensitivity of PCFS, so we cannot interpret data in this region. Otherwise, T_2 is constant within one standard deviation of the mean as a function correlation time, which indicates no SD occurs on that timescale. The noise between correlation times of 10^{-6} and 10^{-4} s is present in some, but not all, individual traces and is caused by low count rates. Inspection of the individual traces in (b) with lower noise in that region show that T_2 is indeed constant down to a correlation time of at least 10^{-5} s.

Bibliography

[1] Donald Ervin Knuth. *The art of computer programming*. Vol. 3. Pearson Education, 1997.

[2] Brian Hayes. "Clock of Ages". In: *The Sciences* 39.6 (1999), pp. 9–13.

[3] Alessandro Attanasi et al. "Information transfer and behavioural inertia in starling flocks". In: *Nature Physics* 10.9 (Sept. 2014), pp. 691–696.

[4] Bakul Gohel et al. "Evaluation of Phase-Amplitude Coupling in Resting State Magnetoencephalographic Signals: Effect of Surrogates and Evaluation Approach". In: *Frontiers in Computational Neuroscience* 10 (2016), p. 120.

[5] Sylvain Meunier and Isabelle Vernos. "Microtubule assembly during mitosis – from distinct origins to distinct functions?" In: *Journal of Cell Science* 125.12 (June 2012), pp. 2805–2814.

[6] "Generalized Huang-Rhys factors for molecular aggregates". In: *Chemical Physics* 528 (2020), p. 110495.

[7] Robert W Boyd. *Nonlinear optics*. Academic press, 2020.

[8] Rick Trebino. "Frog". In: *Frequency-resolved optical gating: the measurement of ultrashort laser pulses*. Springer, 2003, pp. 101–115.

[9] Gilbert Grynberg, Alain Aspect, and Claude Fabre. *Introduction to quantum optics: from the semi-classical approach to quantized light*. Cambridge university press, 2010.

[10] Avshalom C Elitzur and Lev Vaidman. “Quantum mechanical interaction-free measurements”. In: *Foundations of Physics* 23.7 (1993), pp. 987–997.

[11] Nathan S. Lewis. “Toward Cost-Effective Solar Energy Use”. In: *Science* 315.5813 (2007), p. 798.

[12] Fabian Etzold et al. “Ultrafast Exciton Dissociation Followed by Nongeminate Charge Recombination in PCDTBT:PCBM Photovoltaic Blends”. In: *Journal of the American Chemical Society* 133.24 (2011), pp. 9469–9479.

[13] Sung Heum Park et al. “Bulk heterojunction solar cells with internal quantum efficiency approaching 100%”. In: *Nature Photonics* 3 (2009), p. 297.

[14] Simon Gélinas et al. “Ultrafast Long-Range Charge Separation in Organic Semiconductor Photovoltaic Diodes”. In: *Science* 343.6170 (2014), p. 512.

[15] Jean-Luc Brédas, Edward H. Sargent, and Gregory D. Scholes. “Photovoltaic concepts inspired by coherence effects in photosynthetic systems”. In: *Nature Materials* 16 (2016), p. 35.

[16] Natalie Banerji et al. “Exciton Formation, Relaxation, and Decay in PCDTBT”. In: *Journal of the American Chemical Society* 132.49 (2010), pp. 17459–17470.

[17] P. Prins et al. “High Intrachain Hole Mobility on Molecular Wires of Ladder-Type Poly(*p*-Phenylenes)”. In: *Physical Review Letters* 96.14 (2006), p. 146601.

[18] Andreas C. Jakowetz et al. “Visualizing excitations at buried heterojunctions in organic semiconductor blends”. In: *Nature Materials* 16 (2017), p. 551.

[19] Inchan Hwang et al. “Ultrafast relaxation of charge-transfer excitons in low-bandgap conjugated copolymers”. In: *Chemical Science* 3.7 (2012), pp. 2270–2277.

[20] Jiamo Guo et al. “Near-IR Femtosecond Transient Absorption Spectroscopy of Ultrafast Polaron and Triplet Exciton Formation in Polythiophene Films with Different Regioregularities”. In: *Journal of the American Chemical Society* 131.46 (2009), pp. 16869–16880.

[21] Raphael Tautz et al. “Structural correlations in the generation of polaron pairs in low-bandgap polymers for photovoltaics”. In: *Nature Communications* 3 (2012), p. 970.

[22] Gregory D. Scholes. “Long-Range Resonance Energy Transfer in Molecular Systems”. In: *Annual Review of Physical Chemistry* 54.1 (2003), pp. 57–87.

[23] Veaceslav Coropceanu et al. “Charge Transport in Organic Semiconductors”. In: *Chemical Reviews* 107.4 (2007), pp. 926–952.

[24] Paulo B. Miranda, Daniel Moses, and Alan J. Heeger. “Ultrafast photogeneration of charged polarons in conjugated polymers”. In: *Physical Review B* 64.8 (2001), p. 081201.

[25] Palas Roy et al. “Ultrafast bridge planarization in donor--acceptor copolymers drives intramolecular charge transfer”. In: *Nature Communications* 8.1 (2017), p. 1716.

[26] Françoise Provencher et al. “Direct observation of ultrafast long-range charge separation at polymer–fullerene heterojunctions”. In: *Nature Communications* 5 (2014), p. 4288.

[27] Timothy J. Magnanelli and Arthur E. Bragg. “Time-Resolved Raman Spectroscopy of Polaron Pair Formation in Poly(3-hexylthiophene) Aggregates”. In: *The Journal of Physical Chemistry Letters* 6.3 (2015), pp. 438–445.

[28] Antonietta De Sio et al. “Tracking the coherent generation of polaron pairs in conjugated polymers”. In: *Nature Communications* 7 (2016), p. 13742.

[29] Sarah Maria Falke et al. “Coherent ultrafast charge transfer in an organic photovoltaic blend”. In: *Science* 344.6187 (2014), p. 1001.

[30] Hiroyuki Tamura, Irene Burghardt, and Masaru Tsukada. “Exciton Dissociation at Thiophene/Fullerene Interfaces: The Electronic Structures and Quantum Dynamics”. In: *The Journal of Physical Chemistry C* 115.20 (2011), pp. 10205–10210.

[31] Hiroyuki Tamura et al. “Quantum dynamics of ultrafast charge transfer at an oligothiophene-fullerene heterojunction”. In: *The Journal of Chemical Physics* 137.22 (2012), 22A540.

[32] Gregory D. Scholes. “Insights into Excitons Confined to Nanoscale Systems: Electron–Hole Interaction, Binding Energy, and Photodissociation”. In: *ACS Nano* 2.3 (2008), pp. 523–537.

[33] Christopher M. Pochas and Frank C. Spano. “New insights on the nature of two-dimensional polarons in semiconducting polymers: Infrared absorption in poly(3-hexylthiophene)”. In: *The Journal of Chemical Physics* 140.24 (2014), p. 244902.

[34] Nicholas E. Jackson et al. “The Next Breakthrough for Organic Photovoltaics?” In: *The Journal of Physical Chemistry Letters* 6.1 (2015), pp. 77–84.

[35] Shu-Hao Yeh et al. “Elucidation of near-resonance vibronic coherence lifetimes by nonadiabatic electronic-vibrational state character mixing”. In: *Proceedings of the National Academy of Sciences* (2018), p. 201701390.

[36] Vivek Tiwari, William K. Peters, and David M. Jonas. “Electronic resonance with anticorrelated pigment vibrations drives photosynthetic energy transfer outside the adiabatic framework”. In: *Proceedings of the National Academy of Sciences* 110.4 (2013), p. 1203.

[37] Shahnawaz Rafiq and Gregory D. Scholes. “Is back-electron transfer process in Betaine-30 coherent?” In: *Chemical Physics Letters* 683 (2017), pp. 500–506.

[38] Steven G. Boxer. “Stark Realities”. In: *The Journal of Physical Chemistry B* 113.10 (2009), pp. 2972–2983.

[39] Stephen D. Fried and Steven G. Boxer. “Measuring electric fields and noncovalent interactions using the vibrational stark effect”. In: *Accounts of chemical research* 48.4 (2015), pp. 998–1006.

[40] N. Blouin, A. Michaud, and M. Leclerc. “A Low-Bandgap Poly(2,7-Carbazole) Derivative for Use in High-Performance Solar Cells”. In: *Advanced Materials* 19.17 (2007), pp. 2295–2300.

[41] Serge Beaupré and Mario Leclerc. “PCDTBT: en route for low cost plastic solar cells”. In: *Journal of Materials Chemistry A* 1.37 (2013), pp. 11097–11105.

[42] Craig H. Peters et al. “High Efficiency Polymer Solar Cells with Long Operating Lifetimes”. In: *Advanced Energy Materials* 1.4 (2011), pp. 491–494.

[43] Natalie Banerji et al. “Breaking Down the Problem: Optical Transitions, Electronic Structure, and Photoconductivity in Conjugated Polymer PCDTBT and in Its Separate Building Blocks”. In: *The Journal of Physical Chemistry C* 116.21 (2012), pp. 11456–11469.

[44] Loren G. Kaake et al. “Photoinduced Charge Generation in a Molecular Bulk Heterojunction Material”. In: *Journal of the American Chemical Society* 134.48 (2012), pp. 19828–19838.

[45] Jens Niklas et al. “Highly-efficient charge separation and polaron delocalization in polymer–fullerene bulk-heterojunctions: a comparative multi-frequency EPR and DFT study”. In: *Physical Chemistry Chemical Physics* 15.24 (2013), pp. 9562–9574.

[46] Shawn Irgen-Gioro et al. “Coherences of Bacteriochlorophyll a Uncovered Using 3D-Electronic Spectroscopy”. In: *The Journal of Physical Chemistry Letters* 9.20 (2018), pp. 6077–6081.

[47] Elad Harel, Andrew F. Fidler, and Gregory S. Engel. “Real-time mapping of electronic structure with single-shot two-dimensional electronic spectroscopy”. In: *Proceedings of the National Academy of Sciences* 107.38 (2010), p. 16444.

[48] Elad Harel. “Zooming in on vibronic structure by lowest-value projection reconstructed 4D coherent spectroscopy”. In: *The Journal of Chemical Physics* 148.19 (2018), p. 194201.

[49] Minghong Tong et al. “Charge carrier photogeneration and decay dynamics in the poly(2,7-carbazole) copolymer PCDTBT and in bulk heterojunction composites with $PC_{70}BM$”. In: *Physical Review B* 81.12 (2010), p. 125210.

[50] Yin Song et al. “Vibrational coherence probes the mechanism of ultrafast electron transfer in polymer–fullerene blends”. In: *Nature Communications* 5 (2014), p. 4933.

[51] Suyog Padgaonkar et al. “Molecular-Orientation-Dependent Interfacial Charge Transfer in Phthalocyanine/MoS2 Mixed-Dimensional Heterojunctions”. In: *The Journal of Physical Chemistry C* 123.21 (2019), pp. 13337–13343.

[52] John M. Olson and Beverly K. Pierson. “Evolution of Reaction Centers in Photosynthetic Prokaryotes”. In: *International Review of Cytology*. Ed. by G. H. Bourne, K. W. Jeon, and M. Friedlander. Vol. 108. Academic Press, 1987, pp. 209–248.

[53] Melih Sener et al. “Overall energy conversion efficiency of a photosynthetic vesicle”. In: *eLife* 5 (2016), e09541.

[54] H. Scheer. *Chlorophylls*. CRC-Press, 1991.

[55] Bruno Robert and Marc Lutz. “Structures of antenna complexes of several Rhodospirillales from their resonance Raman spectra”. In: *Biochimica et Biophysica Acta (BBA) - Bioenergetics* 807.1 (1985), pp. 10–23.

[56] Sergei Savikhin, Daniel R. Buck, and Walter S. Struve. “Oscillating anisotropies in a bacteriochlorophyll protein: Evidence for quantum beating between exciton levels”. In: *Chemical Physics* 223.2 (1997), pp. 303–312.

[57] Gregory S. Engel et al. “Evidence for wavelike energy transfer through quantum coherence in photosynthetic systems”. In: *Nature* 446 (2007), p. 782.

[58] Gitt Panitchayangkoon et al. “Long-lived quantum coherence in photosynthetic complexes at physiological temperature”. In: *Proceedings of the National Academy of Sciences* 107.29 (2010), p. 12766.

[59] Elisabetta Collini et al. “Coherently wired light-harvesting in photosynthetic marine algae at ambient temperature”. In: *Nature* 463 (2010), p. 644.

[60] Elisabet Romero et al. “Quantum coherence in photosynthesis for efficient solar-energy conversion”. In: *Nature Physics* 10 (2014), p. 676.

[61] Tessa R. Calhoun et al. “Quantum Coherence Enabled Determination of the Energy Landscape in Light-Harvesting Complex II”. In: *The Journal of Physical Chemistry B* 113.51 (2009), pp. 16291–16295.

[62] Marco Ferretti et al. “The nature of coherences in the B820 bacteriochlorophyll dimer revealed by two-dimensional electronic spectroscopy”. In: *Physical Chemistry Chemical Physics* 16.21 (2014), pp. 9930–9939.

[63] Elad Harel and Gregory S. Engel. “Quantum coherence spectroscopy reveals complex dynamics in bacterial light-harvesting complex 2 (LH2)”. In: *Proceedings of the National Academy of Sciences* 109.3 (2012), p. 706.

[64] Francesca Fassioli et al. “Photosynthetic light harvesting: excitons and coherence”. In: *Journal of The Royal Society Interface* 11.92 (2014).

[65] Kelly A. Fransted et al. “Two-dimensional electronic spectroscopy of bacteriochlorophyll a in solution: Elucidating the coherence dynamics of the Fenna-Matthews-Olson complex using its chromophore as a control”. In: *The Journal of Chemical Physics* 137.12 (2012), p. 125101.

[66] Shuai Yue et al. “Coupling of multi-vibrational modes in bacteriochlorophyll a in solution observed with 2D electronic spectroscopy”. In: *Chemical Physics Letters* 683 (2017), pp. 591–597.

[67] Nerine J. Cherepy et al. “Near-Infrared Resonance Raman Spectroscopy of the Special Pair and the Accessory Bacteriochlorophylls in Photosynthetic Reaction Centers”. In: *The Journal of Physical Chemistry* 98.23 (1994), pp. 6023–6029.

[68] Yuan Feng, Ilya Vinogradov, and Nien-Hui Ge. “General noise suppression scheme with reference detection in heterodyne nonlinear spectroscopy”. In: *Optics Express* 25.21 (2017), pp. 26262–26279.

[69] Andrea Volpato et al. “Global analysis of coherence and population dynamics in 2D electronic spectroscopy”. In: *Optics Express* 24.21 (2016), pp. 24773–24785.

[70] D.C. Amett, T.S. Yang, and N.F. Scherer. “Optical and Vibrational Coherence in Bacteriochlorophyll a”. In: (1997).

[71] S. Mukamel. *Principles of nonlinear optical spectroscopy*. Oxford University Press, 1995.

[72] Margherita Maiuri et al. “Coherent wavepackets in the Fenna–Matthews–Olson complex are robust to excitonic-structure perturbations caused by mutagenesis”. In: *Nature Chemistry* 10 (2018), p. 177.

[73] Jordan M. Womick and Andrew M. Moran. “Vibronic Enhancement of Exciton Sizes and Energy Transport in Photosynthetic Complexes”. In: *The Journal of Physical Chemistry B* 115.6 (2011), pp. 1347–1356.

[74] Matteo Ceccarelli, Marc Lutz, and Massimo Marchi. "A Density Functional Normal Mode Calculation of a Bacteriochlorophyll a Derivative". In: *Journal of the American Chemical Society* 122.14 (2000), pp. 3532–3533.

[75] Kazimierz Czarnecki et al. "Characterization of the Strongly Coupled, Low-Frequency Vibrational Modes of the Special Pair of Photosynthetic Reaction Centers via Isotopic Labeling of the Cofactors". In: *Journal of the American Chemical Society* 119.2 (1997), pp. 415–426. ISSN: 0002-7863.

[76] H. van der Laan et al. "Permanent hole burning with a diode laser: excited-state dynamics of bacteriochlorophyll in glasses and micelles". In: *Journal of the Optical Society of America B* 9.6 (1992), pp. 931–940.

[77] V. P. Singh et al. "Towards quantification of vibronic coupling in photosynthetic antenna complexes". In: *The Journal of Chemical Physics* 142.21 (2015), p. 212446.

[78] Felipe Caycedo-Soler et al. "Theory of Excitonic Delocalization for Robust Vibronic Dynamics in LH2". In: *The Journal of Physical Chemistry Letters* 9.12 (2018), pp. 3446–3453.

[79] Erling Thyrhaug et al. "Identification and characterization of diverse coherences in the Fenna–Matthews–Olson complex". In: *Nature Chemistry* 10.7 (2018), pp. 780–786.

[80] Elad Harel, Andrew F. Fidler, and Gregory S. Engel. "Single-Shot Gradient-Assisted Photon Echo Electronic Spectroscopy". In: *The Journal of Physical Chemistry A* 115.16 (2011), pp. 3787–3796.

[81] Austin P. Spencer et al. "Exciton–Phonon Spectroscopy of Quantum Dots Below the Single-Particle Homogeneous Line Width". In: *The Journal of Physical Chemistry Letters* 9.7 (2018), pp. 1503–1508.

[82] V. P. Singh et al. “Independent phasing of rephasing and non-rephasing 2D electronic spectra”. In: *The Journal of Chemical Physics* 139.8 (2013), p. 084201.

[83] Peter D. Dahlberg et al. “Energy Transfer Observed in Live Cells Using Two-Dimensional Electronic Spectroscopy”. In: *The Journal of Physical Chemistry Letters* 4.21 (2013), pp. 3636–3640.

[84] Julien Nillon et al. “2 MHz tunable non collinear optical parametric amplifiers with pulse durations down to 6 fs”. In: *19th International Conference on Ultrafast Phenomena*. OSA Technical Digest (online). Optical Society of America, 09.Wed.P3.57.

[85] J. Oelze. “9 Analysis of Bacteriochlorophylls**Dedicated to Prof. Dr. N. Pfennig on the occasion of his 60th birthday in recognition of his numerous contributions on the ecology and taxonomy of phototrophic bacteria”. In: *Methods in Microbiology*. Ed. by T. Bergan. Vol. 18. Academic Press, 1985, pp. 257–284.

[86] Ivo H. M. van Stokkum, Delmar S. Larsen, and Rienk van Grondelle. “Global and target analysis of time-resolved spectra”. In: *Biochimica et Biophysica Acta (BBA) - Bioenergetics* 1657.2 (2004), pp. 82–104.

[87] H.D. Zeh. “On the interpretation of measurement in quantum theory”. In: *Foundations of Physics* 1.1 (1970), pp. 69–76.

[88] G.S. Engel et al. “Evidence for wavelike energy transfer through quantum coherence in photosynthetic systems”. In: *Nature* 446.7137 (2007), pp. 782–786.

[89] E. Harel and G.S. Engel. “Quantum coherence spectroscopy reveals complex dynamics in bacterial light-harvesting complex 2 (LH2)”. In: *Proceedings of the National Academy of Sciences of the United States of America* 109.3 (2012), pp. 706–711.

[90] E. Collini et al. “Coherently wired light-harvesting in photosynthetic marine algae at ambient temperature”. In: *Nature* 463.7281 (2010), pp. 644–647.

[91] M.B. Plenio and S.F. Huelga. “Dephasing-assisted transport: Quantum networks and biomolecules”. In: *New Journal of Physics* 10 (2008).

[92] M. Mohseni et al. “Environment-assisted quantum walks in photosynthetic energy transfer”. In: *Journal of Chemical Physics* 129.17 (2008).

[93] A. Ishizaki and G.R. Fleming. “Theoretical examination of quantum coherence in a photosynthetic system at physiological temperature”. In: *Proceedings of the National Academy of Sciences of the United States of America* 106.41 (2009), pp. 17255–17260.

[94] S. Lloyd. “Quantum coherence in biological systems”. In: vol. 302. 1. 2011.

[95] H.-M. Wu et al. “Femtosecond and hole-burning studies of B800’s excitation energy relaxation dynamics in the LH2 antenna complex of Rhodopseudomonas acidophila (strain 10050)”. In: *Journal of Physical Chemistry* 100.29 (1996), pp. 12022–12033.

[96] G.D. Scholes and G.R. Fleming. “On the Mechanism of Light Harvesting in Photosynthetic Purple Bacteria: B800 to B850 Energy Transfer”. In: *Journal of Physical Chemistry B* 104.8 (2000), pp. 1854–1868.

[97] N. Christensson et al. “Origin of long-lived coherences in light-harvesting complexes”. In: *Journal of Physical Chemistry B* 116.25 (2012), pp. 7449–7454.

[98] M.B. Plenio, J. Almeida, and S.F. Huelga. “Origin of long-lived oscillations in 2D-spectra of a quantum vibronic model: Electronic versus vibrational coherence”. In: *Journal of Chemical Physics* 139.23 (2013).

[99] S. Irgen-Gioro et al. “Coherences of Bacteriochlorophyll a Uncovered Using 3D-Electronic Spectroscopy”. In: *Journal of Physical Chemistry Letters* 9.20 (2018), pp. 6077–6081.

[100] M. Maiuri et al. “Coherent wavepackets in the Fenna-Matthews-Olson complex are robust to excitonic-structure perturbations caused by mutagenesis”. In: *Nature Chemistry* 10.2 (2018), pp. 177–183.

[101] H.-G. Duan et al. “Nature does not rely on long-lived electronic quantum coherence for photosynthetic energy transfer”. In: *Proceedings of the National Academy of Sciences of the United States of America* 114.32 (2017), pp. 8493–8498.

[102] M.F. Gelin, R. Borrelli, and W. Domcke. “Origin of Unexpectedly Simple Oscillatory Responses in the Excited-State Dynamics of Disordered Molecular Aggregates”. In: *Journal of Physical Chemistry Letters* 10.11 (2019), pp. 2806–2810.

[103] V.P. Singh et al. “Towards quantification of vibronic coupling in photosynthetic antenna complexes”. In: *Journal of Chemical Physics* 142.21 (2015).

[104] H.-G. Duan et al. “Two-Dimensional Electronic Spectroscopy of Light-Harvesting Complex II at Ambient Temperature: A Joint Experimental and Theoretical Study”. In: *Journal of Physical Chemistry B* 119.36 (2015), pp. 12017–12027.

[105] E. Thyrhaug et al. “Identification and characterization of diverse coherences in the Fenna-Matthews-Olson complex”. In: *Nature Chemistry* 10.7 (2018), pp. 780–786.

[106] Y. Feng, I. Vinogradov, and N.-H. Ge. “General noise suppression scheme with reference detection in heterodyne nonlinear spectroscopy”. In: *Optics Express* 25.21 (2017), pp. 26262–26279.

[107] A. Volpato et al. “Global analysis of coherence and population dynamics in 2D electronic spectroscopy”. In: *Optics Express* 24.21 (2016), pp. 24773–24785.

[108] E. Thyrhaug et al. “Exciton Structure and Energy Transfer in the Fenna-Matthews-Olson Complex”. In: *Journal of Physical Chemistry Letters* 7.9 (2016), pp. 1653–1660.

[109] R.E. Fenna and B.W. Matthews. “Chlorophyll arrangement in a bacteriochlorophyll protein from chlorobium limicola”. In: *Nature* 258.5536 (1975), pp. 573–577.

[110] J. Adolphs and T. Renger. "How proteins trigger excitation energy transfer in the FMO complex of green sulfur bacteria". In: *Biophysical Journal* 91.8 (2006), pp. 2778–2797.

[111] A.M. Van Oijen et al. "Unraveling the electronic structure of individual photosynthetic pigment-protein complexes". In: *Science* 285.5426 (1999), pp. 400–402.

[112] A. Halpin et al. "Two-dimensional spectroscopy of a molecular dimer unveils the effects of vibronic coupling on exciton coherences". In: *Nature Chemistry* 6.3 (2014), pp. 196–201.

[113] S. Tretiak et al. "Exciton Hamiltonian for the Bacteriochlorophyll System in the LH2 Antenna Complex of Purple Bacteria". In: *Journal of Physical Chemistry B* 104.18 (2000), pp. 4519–4528.

[114] M. Ferretti et al. "Dark States in the Light-Harvesting complex 2 Revealed by Two-dimensional Electronic Spectroscopy". In: *Scientific Reports* 6 (2016).

[115] C.P. Van Der Vegte et al. "Atomistic modeling of two-dimensional electronic spectra and excited-state dynamics for a light harvesting 2 complex". In: *Journal of Physical Chemistry B* 119.4 (2015), pp. 1302–1313.

[116] J. Strümpfer and K. Schulten. "Light harvesting complex II B850 excitation dynamics". In: *Journal of Chemical Physics* 131.22 (2009).

[117] L. Guo et al. "The observation of excited-state dynamical evolution in light-harvesting complex LH2 from Rhodobacter sphaeroides". In: *FEBS Letters* 511.1-3 (2002), pp. 69–72.

[118] G.R. Fleming and R.V. Grondelle. "Femtosecond spectroscopy of photosynthetic light-harvesting systems". In: *Current Opinion in Structural Biology* 7.5 (1997), pp. 738–748.

[119] R.G. Saer and R.E. Blankenship. “Light harvesting in phototrophic bacteria: Structure and function”. In: *Biochemical Journal* 474.13 (2017), pp. 2107–2131.

[120] N.C.M. Magdaong et al. “Excitation energy transfer kinetics and efficiency in photosynthetic green sulfur bacteria”. In: *Biochimica et Biophysica Acta - Bioenergetics* 1859.10 (2018), pp. 1180–1190.

[121] J.M. Olson. “The FMO protein”. In: *Photosynthesis Research* 80.1-3 (2004), pp. 181–187.

[122] R.Y.-C. Huang et al. “Hydrogen-deuterium exchange mass spectrometry reveals the interaction of Fenna-Matthews-Olson protein and chlorosome CsmA protein”. In: *Biochemistry* 51.1 (2012), pp. 187–193.

[123] M. Mohseni et al. “Geometrical effects on energy transfer in disordered open quantum systems”. In: *Journal of Chemical Physics* 138.20 (2013).

[124] S. Jesenko and M. nidari. “Optimal number of pigments in photosynthetic complexes”. In: *New Journal of Physics* 14 (2012).

[125] F. Cardoso Ramos et al. “The molecular mechanisms of light adaption in light-harvesting complexes of purple bacteria revealed by a multiscale modeling”. In: *Chemical Science* 10.42 (2019), pp. 9650–9662.

[126] R.J. Cogdell et al. “How photosynthetic bacteria harvest solar energy”. In: *Journal of Bacteriology* 181.13 (1999), pp. 3869–3879.

[127] C.A. Wraight and R.K. Clayton. “The absolute quantum efficiency of bacteriochlorophyll photooxidation in reaction centres of Rhodopseudomonas spheroides”. In: *BBA - Bioenergetics* 333.2 (1974), pp. 246–260.

[128] S. Hess et al. “Direct Energy Transfer from the Peripheral LH2 Antenna to the Reaction Center in a Mutant of Rhodobacter sphaeroides That Lacks the Core LH1 Antenna”. In: *Biochemistry* 32.39 (1993), pp. 10314–10322.

[129] S.C. Massey et al. “Orientational Dynamics of Transition Dipoles and Exciton Relaxation in LH2 from Ultrafast Two-Dimensional Anisotropy”. In: *Journal of Physical Chemistry Letters* 10.2 (2019), pp. 270–277.

[130] E. Harel. “Long range excitonic transport in a biomimetic system inspired by the bacterial light-harvesting apparatus”. In: *Journal of Chemical Physics* 136.17 (2012).

[131] F. Caycedo-Soler et al. “Theory of Excitonic Delocalization for Robust Vibronic Dynamics in LH2”. In: *Journal of Physical Chemistry Letters* 9.12 (2018), pp. 3446–3453.

[132] V. Butkus et al. “Vibrational vs. electronic coherences in 2D spectrum of molecular systems”. In: *Chemical Physics Letters* 545 (2012), pp. 40–43.

[133] V. Tiwari, W.K. Peters, and D.M. Jonas. “Electronic resonance with anticorrelated pigment vibrations drives photosynthetic energy transfer outside the adiabatic framework”. In: *Proceedings of the National Academy of Sciences of the United States of America* 110.4 (2013), pp. 1203–1208.

[134] A. Chenu et al. “Enhancement of vibronic and ground-state vibrational coherences in 2D spectra of photosynthetic complexes”. In: *Scientific Reports* 3 (2013).

[135] A. Chenu and G.D. Scholes. “Coherence in energy transfer and photosynthesis”. In: *Annual Review of Physical Chemistry* 66 (2015), pp. 69–96.

[136] D.M. Jonas. “Two-Dimensional Femtosecond Spectroscopy”. In: *Annual Review of Physical Chemistry* 54 (2003), pp. 425–463.

[137] N. Christensson et al. “High frequency vibrational modulations in two-dimensional electronic spectra and their resemblance to electronic coherence signatures”. In: *Journal of Physical Chemistry B* 115.18 (2011), pp. 5383–5391.

[138] E. Meneghin, D. Pedron, and E. Collini. "Characterization of the coherent dynamics of bacteriochlorophyll a in solution". In: *Chemical Physics* 519 (2019), pp. 85–91.

[139] V.R. Policht, A. Niedringhaus, and J.P. Ogilvie. "Characterization of Vibrational Coherence in Monomeric Bacteriochlorophyll a by Two-Dimensional Electronic Spectroscopy". In: *Journal of Physical Chemistry Letters* 9.22 (2018), pp. 6631–6637.

[140] S. Irgen-Gioro et al. "Electronic coherence lifetimes of the Fenna-Matthews-Olson complex and light harvesting complex II". In: *Chemical Science* 10.45 (2019), pp. 10503–10509.

[141] S.-H. Yeh et al. "Elucidation of near-resonance vibronic coherence lifetimes by nonadiabatic electronic-vibrational state character mixing". In: *Proceedings of the National Academy of Sciences of the United States of America* 116.37 (2019), pp. 18263–18268.

[142] J.M. Womick and A.M. Moran. "Vibronic enhancement of exciton sizes and energy transport in photosynthetic complexes". In: *Journal of Physical Chemistry B* 115.6 (2011), pp. 1347–1356.

[143] T.M. Cotton and R.P. Van Duyne. "Characterization of Bacteriochlorophyll Interactions in Vitro by Resonance Raman Spectroscopy". In: *Journal of the American Chemical Society* 103.20 (1981), pp. 6020–6026.

[144] T. Mirkovic et al. "Light absorption and energy transfer in the antenna complexes of photosynthetic organisms". In: *Chemical Reviews* 117.2 (2017), pp. 249–293.

[145] Y.-H. Hwang-Fu, W. Chen, and Y.-C. Cheng. "A coherent modified Redfield theory for excitation energy transfer in molecular aggregates". In: *Chemical Physics* 447 (2015), pp. 46–53.

[146] H.-G. Duan et al. “Intramolecular vibrations enhance theăquantum efficiency of excitonic energy transfer”. In: *Photosynthesis Research* 144.2 (2020), pp. 137–145.

[147] V.I. Novoderezhkin, D. Rutkauskas, and R. Van Grondelle. “Dynamics of the emission spectrum of a single LH2 complex: Interplay of slow and fast nuclear motions”. In: *Biophysical Journal* 90.8 (2006), pp. 2890–2902.

[148] V. May and O. Kühn. *Charge and Energy Transfer Dynamics in Molecular Systems: Third Edition*. 2011.

[149] J. Nillon et al. “Two MHz tunable non collinear optical parametric amplifiers with pulse durations down to 6 fs”. In: *Optics Express* 22.12 (2014), pp. 14964–14974.

[150] E. Harel, A.F. Fidler, and G.S. Engel. “Real-time mapping of electronic structure with single-shot two-dimensional electronic spectroscopy”. In: *Proceedings of the National Academy of Sciences of the United States of America* 107.38 (2010), pp. 16444–16447.

[151] George C. Schatz and Mark A. Ratner. *Quantum mechanics in chemistry*. Mineola, N.Y.: Dover Publications, 2002, xix, 361 p.

[152] Gregory D. Scholes. “Long-Range Resonance Energy Transfer in Molecular Systems”. In: *Annual Review of Physical Chemistry* 54.1 (2003), pp. 57–87.

[153] Neil A. Anderson and Tianquan Lian. “Ultrafast Electron Transfer at the Molecule-Semiconductor Nanoparticle Interface”. In: *Annual Review of Physical Chemistry* 56.1 (2004), pp. 491–519.

[154] Volkhard May and Oliver Kuhn. *Charge and energy transfer dynamics in molecular systems*. 3rd, rev. and enl. Weinheim: Wiley-VCH, 2011.

[155] Al L. Efros and M. Rosen. “The Electronic Structure of Semiconductor Nanocrystals”. In: *Annual Review of Materials Science* 30.1 (2000), pp. 475–521.

[156] Andrew M. Smith and Shuming Nie. "Semiconductor Nanocrystals: Structure, Properties, and Band Gap Engineering". In: *Accounts of Chemical Research* 43.2 (2010), pp. 190–200. ISSN: 0001-4842.

[157] Todd D. Krauss and Jeffrey J. Peterson. "Electronic structure and optical transitions in colloidal semiconductor nanocrystals". In: *Colloidal Quantum Dot Optoelectronics and Photovoltaics*. Ed. by Edward H. Sargent and Gerasimos Konstantatos. Cambridge: Cambridge University Press, 2013, pp. 59–86.

[158] Peter C. Sercel and Alexander L. Efros. "Band-Edge Exciton in CdSe and Other II–VI and III–V Compound Semiconductor Nanocrystals Revisited". In: *Nano Letters* 18.7 (2018), pp. 4061–4068.

[159] Emily A. Weiss. "Organic Molecules as Tools To Control the Growth, Surface Structure, and Redox Activity of Colloidal Quantum Dots". In: *Accounts of Chemical Research* 46.11 (2013), pp. 2607–2615.

[160] Adam J. Morris-Cohen et al. "Chemical, Structural, and Quantitative Analysis of the Ligand Shells of Colloidal Quantum Dots". In: *Chemistry of Materials* 25.8 (2013), pp. 1155–1165.

[161] Rachel D. Harris et al. "Electronic Processes within Quantum Dot-Molecule Complexes". In: *Chemical Reviews* 116.21 (2016), pp. 12865–12919.

[162] Niko Hildebrandt et al. "Energy Transfer with Semiconductor Quantum Dot Bioconjugates: A Versatile Platform for Biosensing, Energy Harvesting, and Other Developing Applications". In: *Chemical Reviews* 117.2 (2017), pp. 536–711.

[163] Mohamad S. Kodaimati et al. "Viewpoint: Challenges in Colloidal Photocatalysis and Some Strategies for Addressing Them". In: *Inorganic Chemistry* 57.7 (2018), pp. 3659–3670.

[164] A. J. Nozik et al. “Semiconductor Quantum Dots and Quantum Dot Arrays and Applications of Multiple Exciton Generation to Third-Generation Photovoltaic Solar Cells”. In: *Chemical Reviews* 110.11 (2010), pp. 6873–6890.

[165] Christopher J. Bardeen. “The Structure and Dynamics of Molecular Excitons”. In: *Annual Review of Physical Chemistry* 65.1 (2014), pp. 127–148.

[166] Nicholas J. Hestand and Frank C. Spano. “Expanded Theory of H- and J-Molecular Aggregates: The Effects of Vibronic Coupling and Intermolecular Charge Transfer”. In: *Chemical Reviews* 118.15 (2018), pp. 7069–7163.

[167] Naomi S. Ginsberg and William A. Tisdale. “Spatially Resolved Photogenerated Exciton and Charge Transport in Emerging Semiconductors”. In: *Annual Review of Physical Chemistry* 71.1 (2020), pp. 1–30.

[168] R. A. Marcus. “On the Theory of OxidationReduction Reactions Involving Electron Transfer. I”. In: *The Journal of Chemical Physics* 24.5 (1956), pp. 966–978.

[169] H. Zhu et al. “Charge Transfer Dynamics from Photoexcited Semiconductor Quantum Dots”. In: *Annual Review of Physical Chemistry* 67 (2016), pp. 259–81.

[170] D. L. Dexter. “A Theory of Sensitized Luminescence in Solids”. In: *The Journal of Chemical Physics* 21.5 (1953), pp. 836–850.

[171] Th Förster. “Zwischenmolekulare Energiewanderung und Fluoreszenz”. In: *Annalen der Physik* 437.1-2 (2006), pp. 55–75.

[172] Marcus Jones, Shun S. Lo, and Gregory D. Scholes. “Quantitative modeling of the role of surface traps in CdSe/CdS/ZnS nanocrystal photoluminescence decay dynamics”. In: *Proceedings of the National Academy of Sciences* (2009), pnas.0809316106.

[173] Marcus Jones, Shun S. Lo, and Gregory D. Scholes. “Signatures of Exciton Dynamics and Carrier Trapping in the Time-Resolved Photoluminescence of Colloidal

CdSe Nanocrystals". In: *The Journal of Physical Chemistry C* 113.43 (2009), pp. 18632–18642.

[174] Richard D. Harcourt, Gregory D. Scholes, and Kenneth P. Ghiggino. "Rate expressions for excitation transfer. II. Electronic considerations of direct and through–configuration exciton resonance interactions". In: *The Journal of Chemical Physics* 101.12 (1994), pp. 10521–10525.

[175] Alexandra Olaya-Castro and Gregory D. Scholes. "Energy transfer from Förster–Dexter theory to quantum coherent light-harvesting". In: *International Reviews in Physical Chemistry* 30.1 (2011), pp. 49–77.

[176] Zhi-Qiang You, Chao-Ping Hsu, and Graham R. Fleming. "Triplet-triplet energy-transfer coupling: Theory and calculation". In: *The Journal of Chemical Physics* 124.4 (2006), p. 044506.

[177] Cédric Mongin et al. "Direct observation of triplet energy transfer from semiconductor nanocrystals". In: *Science* 351.6271 (2016), pp. 369–372.

[178] Sofia Garakyaraghi et al. "Delayed Molecular Triplet Generation from Energized Lead Sulfide Quantum Dots". In: *The Journal of Physical Chemistry Letters* 8.7 (2017), pp. 1458–1463.

[179] Emily A. Weiss, Michael R. Wasielewski, and Mark A. Ratner. "Molecules as Wires: Molecule-Assisted Movement of Charge and Energy". In: *Molecular Wires and Electronics*. Berlin, Heidelberg: Springer Berlin Heidelberg, 2005, pp. 103–133.

[180] Spiros S. Skourtis et al. "Dexter energy transfer pathways". In: *Proceedings of the National Academy of Sciences* 113.29 (2016), p. 8115.

[181] Timothy C. Berkelbach, Mark S. Hybertsen, and David R. Reichman. "Microscopic theory of singlet exciton fission. I. General formulation". In: *The Journal of Chemical Physics* 138.11 (2013), p. 114102.

[182] K. Leung, S. Pokrant, and K. B. Whaley. "Exciton fine structure in CdSe nanoclusters". In: *Physical Review B* 57.19 (1998), pp. 12291–12301.

[183] C. Delerue, G. Allan, and Y. M. Niquet. "Collective excitations in charged nanocrystals and in close-packed arrays of charged nanocrystals". In: *Physical Review B* 72.19 (2005), p. 195316.

[184] Marek Korkusinski, Oleksandr Voznyy, and Pawel Hawrylak. "Fine structure and size dependence of exciton and biexciton optical spectra in CdSe nanocrystals". In: *Physical Review B* 82.24 (2010), p. 245304.

[185] S. Steiger et al. "NEMO5: A Parallel Multiscale Nanoelectronics Modeling Tool". In: *IEEE Transactions on Nanotechnology* 10.6 (2011), pp. 1464–1474. ISSN: 1941-0085.

[186] Gabriel Bester. "Electronic excitations in nanostructures: an empirical pseudopotential based approach". In: *Journal of Physics: Condensed Matter* 21.2 (2008), p. 023202.

[187] Wang and Alex Zunger. "High-Energy Excitonic Transitions in CdSe Quantum Dots". In: *The Journal of Physical Chemistry B* 102.34 (1998), pp. 6449–6454.

[188] A. Franceschetti et al. "Many-body pseudopotential theory of excitons in InP and CdSe quantum dots". In: *Physical Review B* 60.3 (1999), pp. 1819–1829.

[189] Gabriel Bester, Selvakumar Nair, and Alex Zunger. "Pseudopotential calculation of the excitonic fine structure of million-atom self-assembled $In_{1-x}Ga_xAs/GaAs$ quantum dots". In: *Physical Review B* 67.16 (2003), p. 161306.

[190] Marco Califano, Alberto Franceschetti, and Alex Zunger. "Lifetime and polarization of the radiative decay of excitons, biexcitons, and trions in CdSe nanocrystal quantum dots". In: *Physical Review B* 75.11 (2007), p. 115401.

[191] P. C. Sercel and A. L. Efros. “Band-Edge Exciton in CdSe and Other II-VI and III-V Compound Semiconductor Nanocrystals - Revisited”. In: *Nano Lett* 18.7 (2018), pp. 4061–4068.

[192] J. M. Pietryga et al. “Spectroscopic and Device Aspects of Nanocrystal Quantum Dots”. In: *Chem Rev* 116.18 (2016), pp. 10513–622.

[193] L Efros AI and AL Efros. “Interband Absorption of Light in a Semiconductor Sphere”. In: *Sov. Phys. Semicond* 16 (1982), pp. 772–775.

[194] Cathy Y. Wong et al. “Relaxation in the Exciton Fine Structure of Semiconductor Nanocrystals”. In: *The Journal of Physical Chemistry C* 113.3 (2008), pp. 795–811.

[195] D. Jena and A. Konar. “Enhancement of carrier mobility in semiconductor nanostructures by dielectric engineering”. In: *Phys Rev Lett* 98.13 (2007), p. 136805.

[196] S. Schulz and G. Czycholl. “Tight-binding model for semiconductor nanostructures”. In: *Physical Review B* 72.16 (2005).

[197] O. Lehtonen, D. Sundholm, and T. Vanska. “Computational studies of semiconductor quantum dots”. In: *Phys Chem Chem Phys* 10.31 (2008), pp. 4535–50.

[198] Mohamad S. Kodaimati et al. “Distance-Dependence of Interparticle Energy Transfer in the Near-Infrared within Electrostatic Assemblies of PbS Quantum Dots”. In: *ACS Nano* 11.5 (2017), pp. 5041–5050.

[199] M. Nirmal et al. “Observation of the "Dark Exciton" in CdSe Quantum Dots”. In: *Physical Review Letters* 75.20 (1995), pp. 3728–3731.

[200] Olivier Labeau, Philippe Tamarat, and Brahim Lounis. “Temperature Dependence of the Luminescence Lifetime of Single CdSe/ZnS Quantum Dots”. In: *Physical Review Letters* 90.25 (2003), p. 257404.

[201] L. Biadala et al. “Direct Observation of the Two Lowest Exciton Zero-Phonon Lines in Single CdSe/ZnS Nanocrystals”. In: *Physical Review Letters* 103.3 (2009), p. 037404.

[202] Al L. Efros et al. “Band-edge exciton in quantum dots of semiconductors with a degenerate valence band: Dark and bright exciton states”. In: *Physical Review B* 54.7 (1996), pp. 4843–4856.

[203] Jeongho Kim, Cathy Y. Wong, and Gregory D. Scholes. “Exciton Fine Structure and Spin Relaxation in Semiconductor Colloidal Quantum Dots”. In: *Accounts of Chemical Research* 42.8 (2009), pp. 1037–1046.

[204] Junhui Wang et al. “Spin-Controlled Charge-Recombination Pathways across the Inorganic/Organic Interface”. In: *Journal of the American Chemical Society* 142.10 (2020), pp. 4723–4731.

[205] David J. Weinberg et al. “Spin-Selective Charge Recombination in Complexes of CdS Quantum Dots and Organic Hole Acceptors”. In: *Journal of the American Chemical Society* 136.41 (2014), pp. 14513–14518.

[206] H. C. Brenner, J. C. Brock, and C. B. Harris. “Energy exchange in a coherently coupled ensemble”. In: *Chemical Physics* 31.1 (1978), pp. 137–164.

[207] Victor Gray et al. “Direct vs Delayed Triplet Energy Transfer from Organic Semiconductors to Quantum Dots and Implications for Luminescent Harvesting of Triplet Excitons”. In: *ACS Nano* 14.4 (2020), pp. 4224–4234.

[208] Mengfei Wu et al. “Solid-state infrared-to-visible upconversion sensitized by colloidal nanocrystals”. In: *Nature Photonics* 10.1 (2016), pp. 31–34.

[209] Stijn Flamee et al. “Fast, High Yield, and High Solid Loading Synthesis of Metal Selenide Nanocrystals”. In: *Chemistry of Materials* 25.12 (2013), pp. 2476–2483.

[210] Cédric Mongin et al. “Thermally activated delayed photoluminescence from pyrenyl-functionalized CdSe quantum dots”. In: *Nature Chemistry* 10.2 (2018), pp. 225–230.

[211] Tao Jin et al. “Competition of Dexter, Förster, and charge transfer pathways for quantum dot sensitized triplet generation”. In: *The Journal of Chemical Physics* 152.21 (2020), p. 214702.

[212] François Federspiel et al. “Distance Dependence of the Energy Transfer Rate from a Single Semiconductor Nanostructure to Graphene”. In: *Nano Letters* 15.2 (2015), pp. 1252–1258.

[213] R. S. Swathi and K. L. Sebastian. “Long range resonance energy transfer from a dye molecule to graphene has (distance)4 dependence”. In: *The Journal of Chemical Physics* 130.8 (2009), p. 086101. ISSN: 0021-9606.

[214] R. S. Swathi and K. L. Sebastian. “Distance dependence of fluorescence resonance energy transfer”. In: *Journal of Chemical Sciences* 121.5 (2009), p. 777. ISSN: 0973-7103.

[215] Zheyuan Chen et al. “Energy Transfer from Individual Semiconductor Nanocrystals to Graphene”. In: *ACS Nano* 4.5 (2010), pp. 2964–2968.

[216] Nima Taghipour et al. “Near-Unity Efficiency Energy Transfer from Colloidal Semiconductor Quantum Wells of CdSe/CdS Nanoplatelets to a Monolayer of MoS2”. In: *ACS Nano* 12.8 (2018), pp. 8547–8554.

[217] A. Szemjonov et al. “Ligand-stabilized CdSe nanoplatelet hybrid structures with tailored geometric and electronic properties. New insights from theory”. In: *RSC Advances* 4.99 (2014), pp. 55980–55989.

[218] Alexandra Brumberg et al. “Material Dimensionality Effects on Electron Transfer Rates Between CsPbBr3 and CdSe Nanoparticles”. In: *Nano Letters* 18.8 (2018), pp. 4771–4776.

[219] Benjamin T. Diroll et al. “Surface-Area-Dependent Electron Transfer Between Isoenergetic 2D Quantum Wells and a Molecular Acceptor”. In: *Journal of the American Chemical Society* 138.35 (2016), pp. 11109–11112.

[220] Yunan Gao, Mark C. Weidman, and William A. Tisdale. “CdSe Nanoplatelet Films with Controlled Orientation of their Transition Dipole Moment”. In: *Nano Letters* 17.6 (2017), pp. 3837–3843.

[221] Onur Erdem et al. “Orientation-Controlled Nonradiative Energy Transfer to Colloidal Nanoplatelets: Engineering Dipole Orientation Factor”. In: *Nano Letters* 19.7 (2019), pp. 4297–4305.

[222] Thomas Simon et al. “Electron Transfer Rate vs Recombination Losses in Photocatalytic H2 Generation on Pt-Decorated CdS Nanorods”. In: *ACS Energy Letters* 1.6 (2016), pp. 1137–1142.

[223] Suyog Padgaonkar et al. “Emergent Optoelectronic Properties of Mixed-Dimensional Heterojunctions”. In: *Accounts of Chemical Research* 53.4 (2020), pp. 763–772.

[224] H. Benisty, C. M. Sotomayor-Torrès, and C. Weisbuch. “Intrinsic mechanism for the poor luminescence properties of quantum-box systems”. In: *Physical Review B* 44.19 (1991), pp. 10945–10948.

[225] V. A. Kharchenko and M. Rosen. “Auger relaxation processes in semiconductor nanocrystals and quantum wells”. In: *Journal of Luminescence* 70.1 (1996), pp. 158–169.

[226] Arthur J. Nozik. “SPECTROSCOPY AND HOT ELECTRON RELAXATION DYNAMICS IN SEMICONDUCTOR QUANTUM WELLS AND QUANTUM DOTS”. In: *Annual Review of Physical Chemistry* 52.1 (2001), pp. 193–231.

[227] R. D. Schaller and V. I. Klimov. “High Efficiency Carrier Multiplication in PbSe Nanocrystals: Implications for Solar Energy Conversion”. In: *Physical Review Letters* 92.18 (2004), p. 186601.

[228] Randy J. Ellingson et al. “Highly Efficient Multiple Exciton Generation in Colloidal PbSe and PbS Quantum Dots”. In: *Nano Letters* 5.5 (2005), pp. 865–871.

[229] A. Franceschetti, J. M. An, and A. Zunger. “Impact Ionization Can Explain Carrier Multiplication in PbSe Quantum Dots”. In: *Nano Letters* 6.10 (2006), pp. 2191–2195.

[230] Clare E. Rowland et al. “Picosecond energy transfer and multiexciton transfer outpaces Auger recombination in binary CdSe nanoplatelet solids”. In: *Nature Materials* 14.5 (2015), pp. 484–489.

[231] Pallavi Singhal and Hirendra N. Ghosh. “Hot Charge Carrier Extraction from Semiconductor Quantum Dots”. In: *The Journal of Physical Chemistry C* 122.31 (2018), pp. 17586–17600.

[232] Yaohong Zhang et al. “Photoexcited carrier dynamics in colloidal quantum dot solar cells: insights into individual quantum dots, quantum dot solid films and devices”. In: *Chemical Society Reviews* 49.1 (2020), pp. 49–84.

[233] Haipeng Lu et al. “Transforming energy using quantum dots”. In: *Energy & Environmental Science* 13.5 (2020), pp. 1347–1376.

[234] Haiming Zhu et al. “Auger-Assisted Electron Transfer from Photoexcited Semiconductor Quantum Dots”. In: *Nano Letters* 14.3 (2014), pp. 1263–1269.

[235] Kim Hyeon-Deuk, Joonghan Kim, and Oleg V. Prezhdo. "Ab Initio Analysis of Auger-Assisted Electron Transfer". In: *The Journal of Physical Chemistry Letters* 6.2 (2015), pp. 244–249.

[236] Jacob H. Olshansky et al. "Hole Transfer from Photoexcited Quantum Dots: The Relationship between Driving Force and Rate". In: *Journal of the American Chemical Society* 137.49 (2015), pp. 15567–15575.

[237] Jacob H. Olshansky et al. "Temperature-Dependent Hole Transfer from Photoexcited Quantum Dots to Molecular Species: Evidence for Trap-Mediated Transfer". In: *ACS Nano* 11.8 (2017), pp. 8346–8355.

[238] Gustavo M. Dalpian and James R. Chelikowsky. "Self-Purification in Semiconductor Nanocrystals". In: *Physical Review Letters* 96.22 (2006), p. 226802.

[239] Carlo Giansante and Ivan Infante. "Surface Traps in Colloidal Quantum Dots: A Combined Experimental and Theoretical Perspective". In: *The Journal of Physical Chemistry Letters* 8.20 (2017), pp. 5209–5215.

[240] Kaifeng Wu et al. "Efficient Extraction of Trapped Holes from Colloidal CdS Nanorods". In: *Journal of the American Chemical Society* 137.32 (2015), pp. 10224–10230.

[241] Gouranga H. Debnath, Prasun Mukherjee, and David H. Waldeck. "Optimizing the Key Variables to Generate Host Sensitized Lanthanide Doped Semiconductor Nanoparticle Luminophores". In: *The Journal of Physical Chemistry C* (2020).

[242] Demetra A. Chengelis et al. "Incorporating Lanthanide Cations with Cadmium Selenide Nanocrystals: A Strategy to Sensitize and Protect Tb(III)". In: *Journal of the American Chemical Society* 127.48 (2005), pp. 16752–16753.

[243] Yun Ye et al. “Charge-Transfer Dynamics Promoted by Hole Trap States in CdSe Quantum Dots–Ni2+ Photocatalytic System”. In: *The Journal of Physical Chemistry C* 121.32 (2017), pp. 17112–17120.

[244] Zhengyi Zhang et al. “Enhancing the rate of quantum-dot-photocatalyzed carbon–carbon coupling by tuning the composition of the dot’s ligand shell”. In: *Journal of the American Chemical Society* 139.12 (2017), pp. 4246–4249.

[245] Shichen Lian, Mohamad S Kodaimati, and Emily A Weiss. “Photocatalytically active superstructures of quantum dots and iron porphyrins for reduction of CO2 to CO in water”. In: *ACS nano* 12.1 (2018), pp. 568–575.

[246] Shichen Lian et al. “Powering a CO2 reduction catalyst with visible light through multiple sub-picosecond electron transfers from a quantum dot”. In: *Journal of the American Chemical Society* 139.26 (2017), pp. 8931–8938.

[247] Matthew T Frederick and Emily A Weiss. “Relaxation of exciton confinement in CdSe quantum dots by modification with a conjugated dithiocarbamate ligand”. In: *ACS nano* 4.6 (2010), pp. 3195–3200.

[248] Matthew T Frederick et al. “Control of exciton confinement in quantum dot–organic complexes through energetic alignment of interfacial orbitals”. In: *Nano letters* 13.1 (2013), pp. 287–292.

[249] Meghan B Teunis et al. “Elucidating the role of surface passivating ligand structural parameters in hole wave function delocalization in semiconductor cluster molecules”. In: *Nanoscale* 9.37 (2017), pp. 14127–14138.

[250] Barbara Vercelli et al. “Multilayers of Carbodithioate and Sulfide-Linked CdSe Nanocrystals: Progressive Increase of Exciton Delocalization”. In: *The Journal of Physical Chemistry C* 123.37 (2019), pp. 23159–23166.

[251] Shichen Lian et al. “Subpicosecond photoinduced hole transfer from a CdS quantum dot to a molecular acceptor bound through an exciton-delocalizing ligand”. In: *ACS nano* 10.6 (2016), pp. 6372–6382.

[252] Jonathan R Lee et al. “Hydrophilic, hole-delocalizing ligand shell to promote charge transfer from colloidal CdSe quantum dots in water”. In: *The Journal of Physical Chemistry C* 121.28 (2017), pp. 15160–15168.

[253] Michael S Azzaro et al. “Exciton-delocalizing ligands can speed up energy migration in nanocrystal solids”. In: *Nano letters* 18.5 (2018), pp. 3259–3270.

[254] Dana E Westmoreland, Rafael López-Arteaga, and Emily A Weiss. “N-Heterocyclic Carbenes as Reversible Exciton-Delocalizing Ligands for Photoluminescent Quantum Dots”. In: *Journal of the American Chemical Society* 142.5 (2020), pp. 2690–2696.

[255] Victor Gray et al. “CdS/ZnS core–shell nanocrystal photosensitizers for visible to UV upconversion”. In: *Chemical Science* 8.8 (2017), pp. 5488–5496.

[256] Melika Mahboub, Zhiyuan Huang, and Ming Lee Tang. “Efficient Infrared-to-Visible Upconversion with Subsolar Irradiance”. In: *Nano Letters* 16.11 (2016), pp. 7169–7175.

[257] Tao Jin and Tianquan Lian. “Trap state mediated triplet energy transfer from CdSe quantum dots to molecular acceptors”. In: *The Journal of Chemical Physics* 153.7 (2020), p. 074703.

[258] Philipp Sippel et al. “Femtosecond Cooling of Hot Electrons in CdSe Quantum-Well Platelets”. In: *Nano Letters* 15.4 (2015), pp. 2409–2416.

[259] Tomoki Okuhata and Naoto Tamai. “Face-Dependent Electron Transfer in CdSe Nanoplatelet–Methyl Viologen Complexes”. In: *The Journal of Physical Chemistry C* 120.30 (2016), pp. 17052–17059.

[260] Christophe Galland et al. “Two types of luminescence blinking revealed by spectroelectrochemistry of single quantum dots”. In: *Nature* 479.7372 (2011), pp. 203–207.

[261] Alexander W. Achtstein et al. “p -State Luminescence in CdSe Nanoplatelets: Role of Lateral Confinement and a Longitudinal Optical Phonon Bottleneck”. In: *Physical Review Letters* 116.11 (2016), p. 116802.

[262] Xiang-Yang Liu et al. “Nonadiabatic Dynamics Simulations Reveal Distinct Effects of the Thickness of PTB7 on Interfacial Electron and Hole Transfer Dynamics in PTB7@MoS2 Heterostructures”. In: *The Journal of Physical Chemistry Letters* 10.11 (2019), pp. 2949–2956.

[263] Patrick R. Brown et al. “Energy Level Modification in Lead Sulfide Quantum Dot Thin Films through Ligand Exchange”. In: *ACS Nano* 8.6 (2014), pp. 5863–5872.

[264] Qunfei Zhou et al. “Large Band Edge Tunability in Colloidal Nanoplatelets”. In: *Nano Letters* 19.10 (2019), pp. 7124–7129.

[265] Benjamin T. Diroll. “Ligand-Dependent Tuning of Interband and Intersubband Transitions of Colloidal CdSe Nanoplatelets”. In: *Chemistry of Materials* 32.13 (2020), pp. 5916–5923.

[266] Yishu Jiang et al. “Regio-and diastereoselective intermolecular [2+ 2] cycloadditions photocatalysed by quantum dots”. In: *Nature chemistry* 11.11 (2019), pp. 1034–1040.

[267] Robert M. Dickson et al. “On/off blinking and switching behaviour of single molecules of green fluorescent protein”. In: *Nature* 388.6640 (1997), pp. 355–358.

[268] Kristin L. Wustholz et al. “Dispersive Kinetics from Single Molecules Oriented in Single Crystals of Potassium Acid Phthalate”. In: *The Journal of Physical Chemistry C* 111.26 (2007), pp. 9146–9156.

[269] Alexander L. Efros and David J. Nesbitt. “Origin and control of blinking in quantum dots”. In: *Nature Nanotechnology* 11.8 (2016), pp. 661–671.

[270] Yongfen Chen et al. “ “Giant” Multishell CdSe Nanocrystal Quantum Dots with Suppressed Blinking”. In: *Journal of the American Chemical Society* 130.15 (2008), pp. 5026–5027.

[271] Benoit Mahler et al. “Towards non-blinking colloidal quantumădots”. In: *Nature Materials* 7.8 (2008), pp. 659–664.

[272] Amy A. Cordones and Stephen R. Leone. “Mechanisms for charge trapping in single semiconductor nanocrystals probed by fluorescence blinking”. In: *Chemical Society Reviews* 42.8 (2013), pp. 3209–3221.

[273] Ou Chen et al. “Compact high-quality CdSe–CdS core–shell nanocrystals with narrow emission linewidthsăandăsuppressed blinking”. In: *Nature Materials* 12.5 (2013), pp. 445–451.

[274] Haiyan Qin et al. “Single-Dot Spectroscopy of Zinc-Blende CdSe/CdS Core/Shell Nanocrystals: Nonblinking and Correlation with Ensemble Measurements”. In: *Journal of the American Chemical Society* 136.1 (2014), pp. 179–187.

[275] Benard Omogo et al. “Reducing Blinking in Small Core–Multishell Quantum Dots by Carefully Balancing Confinement Potential and Induced Lattice Strain: The “Goldilocks” Effect”. In: *ACS Nano* 10.4 (2016), pp. 4072–4082.

[276] Christophe Galland et al. “Two types of luminescence blinking revealed by spectroelectrochemistry of single quantum dots”. In: *Nature* 479.7372 (2011), pp. 203–207.

[277] Gangcheng Yuan et al. “Two Mechanisms Determine Quantum Dot Blinking”. In: *ACS Nano* 12.4 (2018), pp. 3397–3405.

[278] Minhal Hasham and Mark W. B. Wilson. “Sub-Bandgap Optical Modulation of Quantum Dot Blinking Statistics”. In: *The Journal of Physical Chemistry Letters* 11.15 (2020), pp. 6404–6412.

[279] Vl K. Busov and P. A. Frantsuzov. “Models of Semiconductor Quantum Dots Blinking based on Spectral Diffusion”. In: *Optics and Spectroscopy* 126.1 (2019), pp. 70–82.

[280] S. A. Empedocles, D. J. Norris, and M. G. Bawendi. “Photoluminescence Spectroscopy of Single CdSe Nanocrystallite Quantum Dots”. In: *Physical Review Letters* 77.18 (1996), pp. 3873–3876.

[281] R. G. Neuhauser et al. “Correlation between Fluorescence Intermittency and Spectral Diffusion in Single Semiconductor Quantum Dots”. In: *Physical Review Letters* 85.15 (2000), pp. 3301–3304.

[282] Mark J. Fernée, Philippe Tamarat, and Brahim Lounis. “Spectroscopy of single nanocrystals”. In: *Chemical Society Reviews* 43.4 (2014), pp. 1311–1337.

[283] Praket P. Jha and Philippe Guyot-Sionnest. “Trion Decay in Colloidal Quantum Dots”. In: *ACS Nano* 3.4 (2009), pp. 1011–1015.

[284] S. A. Empedocles and M. G. Bawendi. “Influence of Spectral Diffusion on the Line Shapes of Single CdSe Nanocrystallite Quantum Dots”. In: *The Journal of Physical Chemistry B* 103.11 (1999), pp. 1826–1830.

[285] M. Kuno et al. “Nonexponential “blinking” kinetics of single CdSe quantum dots: A universal power law behavior”. In: *The Journal of Chemical Physics* 112.7 (2000), pp. 3117–3120.

[286] A. Lyasota et al. “Limiting the Spectral Diffusion of Nano-Scale Light Emitters using the Purcell effect in a Photonic-Confined Environment”. In: *Scientific Reports* 9.1 (2019), p. 1195.

[287] Felipe V. Antolinez et al. “Observation of Electron Shakeup in CdSe/CdS Core/Shell Nanoplatelets”. In: *Nano Letters* 19.12 (2019), pp. 8495–8502.

[288] H. J. Kimble. “The quantum internet”. In: *Nature* 453.7198 (2008), pp. 1023–1030.

[289] Sandrine Ithurria and Dmitri V. Talapin. “Colloidal Atomic Layer Deposition (c-ALD) using Self-Limiting Reactions at Nanocrystal Surface Coupled to Phase Transfer between Polar and Nonpolar Media”. In: *Journal of the American Chemical Society* 134.45 (2012), pp. 18585–18590.

[290] George E Cragg and Alexander L Efros. “Suppression of Auger processes in confined structures”. In: *Nano letters* 10.1 (2010), pp. 313–317.

[291] Victor I. Klimov. “Multicarrier Interactions in Semiconductor Nanocrystals in Relation to the Phenomena of Auger Recombination and Carrier Multiplication”. In: *Annual Review of Condensed Matter Physics* 5.1 (2014), pp. 285–316.

[292] Qiuyang Li and Tianquan Lian. “Area- and Thickness-Dependent Biexciton Auger Recombination in Colloidal CdSe Nanoplatelets: Breaking the “Universal Volume Scaling Law” ”. In: *Nano Letters* 17.5 (2017), pp. 3152–3158.

[293] Xuedan Ma et al. “Size-Dependent Biexciton Quantum Yields and Carrier Dynamics of Quasi-Two-Dimensional Core/Shell Nanoplatelets”. In: *ACS Nano* 11.9 (2017), pp. 9119–9127.

[294] Elena V. Shornikova et al. “Addressing the exciton fine structure in colloidal nanocrystals: the case of CdSe nanoplatelets”. In: *Nanoscale* 10.2 (2018), pp. 646–656.

[295] M. D. Tessier et al. “Spectroscopy of Colloidal Semiconductor Core/Shell Nanoplatelets with High Quantum Yield”. In: *Nano Letters* 13.7 (2013), pp. 3321–3328.

[296] Mickaël D. Tessier et al. “Efficient Exciton Concentrators Built from Colloidal Core/Crown CdSe/CdS Semiconductor Nanoplatelets”. In: *Nano Letters* 14.1 (2014), pp. 207–213.

[297] Daniel Amgar et al. “Higher-Order Photon Correlation as a Tool To Study Exciton Dynamics in Quasi-2D Nanoplatelets”. In: *Nano Letters* 19.12 (2019), pp. 8741–8748.

[298] Elena V. Shornikova et al. “Negatively Charged Excitons in CdSe Nanoplatelets”. In: *Nano Letters* 20.2 (2020), pp. 1370–1377.

[299] Lintao Peng et al. “Bright trion emission from semiconductor nanoplatelets”. In: *Physical Review Materials* 4.5 (2020).

[300] G. Sallen et al. “Subnanosecond spectral diffusion measurement using photon correlation”. In: *Nature Photonics* 4.10 (2010), pp. 696–699.

[301] S. Bounouar et al. “Extraction of the homogeneous linewidth of the spectrally diffusing line of a CdSe/ZnSe quantum dot embedded in a nanowire”. In: *Physical Review B* 86.8 (2012), p. 085325.

[302] Janik Wolters et al. “Measurement of the Ultrafast Spectral Diffusion of the Optical Transition of Nitrogen Vacancy Centers in Nano-Size Diamond Using Correlation Interferometry”. In: *Physical Review Letters* 110.2 (2013), p. 027401.

[303] X. Brokmann et al. “Photon-correlation Fourier spectroscopy”. In: *Opt Express* 14.13 (2006), pp. 6333–41.

[304] L. Coolen et al. “Emission characterization of a single CdSe-ZnS nanocrystal with high temporal and spectral resolution by photon-correlation Fourier spectroscopy”. In: *Phys Rev Lett* 100.2 (2008), p. 027403.

[305] Lisa Faye Marshall. “Spectral dynamics of single quantum dots: A study using photon-correlation Fourier spectroscopy for submillisecond time resolution at low temperature and in solution”. Thesis. 2011.

[306] Andrew P. Beyler et al. “Direct Observation of Rapid Discrete Spectral Dynamics in Single Colloidal CdSe-CdS Core-Shell Quantum Dots”. In: *Physical Review Letters* 111.17 (2013), p. 177401.

[307] Andrew Paul Beyler. “Single-nanocrystal photon correlation: a versatile tool for elucidating basic physics and characterizing applications-relevant properties”. Thesis. 2015.

[308] Justin R. Caram et al. “PbS Nanocrystal Emission Is Governed by Multiple Emissive States”. In: *Nano Letters* 16.10 (2016), pp. 6070–6077.

[309] Sophie N. Bertram et al. “Single Nanocrystal Spectroscopy of Shortwave Infrared Emitters”. In: *ACS Nano* 13.2 (2019), pp. 1042–1049. ISSN: 1936-0851.

[310] Hendrik Utzat et al. “Coherent single-photon emission from colloidal lead halide perovskite quantum dots”. In: *Science* (2019), eaau7392.

[311] Boris Spokoyny et al. “Effect of Spectral Diffusion on the Coherence Properties of a Single Quantum Emitter in Hexagonal Boron Nitride”. In: *The Journal of Physical Chemistry Letters* 11.4 (2020).

[312] G. Messin et al. “Bunching and antibunching in the fluorescence of semiconductor nanocrystals”. In: *Optics Letters* 26.23 (2001), pp. 1891–1893.

[313] Freddy T. Rabouw et al. “Microsecond Blinking Events in the Fluorescence of Colloidal Quantum Dots Revealed by Correlation Analysis on Preselected Photons”. In: *The journal of physical chemistry letters* 10.13 (2019), pp. 3732–3738.

[314] Rogier Verberk, Antoine M. van Oijen, and Michel Orrit. “Simple model for the power-law blinking of single semiconductor nanocrystals”. In: *Physical Review B* 66.23 (2002), p. 233202.

[315] Matthew Pelton et al. “Evidence for a diffusion-controlled mechanism for fluorescence blinking of colloidal quantum dots”. In: *Proceedings of the National Academy of Sciences* 104.36 (2007), p. 14249.

[316] Stijn O. M. Hinterding et al. “Single Trap States in Single CdSe Nanoplatelets”. In: *ACS Nano* (2021).

[317] Astrid Von Stein and Johannes Sarnthein. “Different frequencies for different scales of cortical integration: from local gamma to long range alpha/theta synchronization”. In: *International journal of psychophysiology* 38.3 (2000), pp. 301–313.

[318] Martin Vinck et al. “An improved index of phase-synchronization for electrophysiological data in the presence of volume-conduction, noise and sample-size bias”. In: *Neuroimage* 55.4 (2011), pp. 1548–1565.

[319] Ole Jensen and Laura L Colgin. “Cross-frequency coupling between neuronal oscillations”. In: *Trends in cognitive sciences* 11.7 (2007), pp. 267–269.

[320] Ryan T Canolty and Robert T Knight. “The functional role of cross-frequency coupling”. In: *Trends in cognitive sciences* 14.11 (2010), pp. 506–515.

[321] J Matias Palva and Satu Palva. “Functional integration across oscillation frequencies by crossfrequency phase synchronization”. In: *European Journal of Neuroscience* 48.7 (2018), pp. 2399–2406.

[322] György Buzsáki, Costas A Anastassiou, and Christof Koch. “The origin of extracellular fields and currents—EEG, ECoG, LFP and spikes”. In: *Nature reviews neuroscience* 13.6 (2012), p. 407.

[323] Michael X Cohen. “Where does EEG come from and what does it mean?” In: *Trends in neurosciences* 40.4 (2017), pp. 208–218.

[324] Gyorgy Buzsaki. *Rhythms of the Brain*. Oxford University Press, 2006.

[325] Flavio Fröhlich and David A McCormick. “Endogenous electric fields may guide neocortical network activity”. In: *Neuron* 67.1 (2010), pp. 129–143.

[326] György Buzsáki. “Theta oscillations in the hippocampus”. In: *Neuron* 33.3 (2002), pp. 325–340.

[327] Misha V Tsodyks et al. “Population dynamics and theta rhythm phase precession of hippocampal place cell firing: a spiking neuron model”. In: *Hippocampus* 6.3 (1996), pp. 271–280.

[328] Gautam Agarwal et al. “Spatially distributed local fields in the hippocampus encode rat position”. In: *Science* 344.6184 (2014), pp. 626–630.

[329] BT Thomas Yeo et al. “Functional specialization and flexibility in human association cortex”. In: *Cerebral cortex* 25.10 (2014), pp. 3654–3672.

[330] György Buzsáki and Edvard I Moser. “Memory, navigation and theta rhythm in the hippocampal-entorhinal system”. In: *Nature neuroscience* 16.2 (2013), p. 130.

[331] Bradley C Lega, Joshua Jacobs, and Michael Kahana. “Human hippocampal theta oscillations and the formation of episodic memories”. In: *Hippocampus* 22.4 (2012), pp. 748–761.

[332] Hoi Sung Chung et al. “Single-molecule fluorescence experiments determine protein folding transition path times”. In: *Science* 335.6071 (2012), pp. 981–984.

[333] Gregory R Bowman and Vijay S Pande. “Protein folded states are kinetic hubs”. In: *Proceedings of the National Academy of Sciences* 107.24 (2010), pp. 10890–10895.

[334] Dibyendu Kumar Sasmal, Rajeev Yadav, and H Peter Lu. “Single-molecule patch-clamp FRET anisotropy microscopy studies of NMDA receptor ion channel activation and deactivation under agonist ligand binding in living cells”. In: *Journal of the American Chemical Society* 138.28 (2016), pp. 8789–8801.

[335] William A Eaton et al. “Is cooperative oxygen binding by hemoglobin really understood?” In: *Nature structural biology* 6.4 (1999), pp. 351–358.

[336] JM Berg, JL Tymoczko, and L Stryer. “Section 10.2: Hemoglobin Transports Oxygen Efficiently by Binding Oxygen Cooperatively”. In: *Biochemistry* (2002).

[337] Anne Treisman. “The binding problem”. In: *Current opinion in neurobiology* 6.2 (1996), pp. 171–178.

[338] Wolf Singer and Charles M Gray. “Visual feature integration and the temporal correlation hypothesis”. In: *Annual review of neuroscience* 18.1 (1995), pp. 555–586.

[339] Andreas K Engel and Wolf Singer. “Temporal binding and the neural correlates of sensory awareness”. In: *Trends in cognitive sciences* 5.1 (2001), pp. 16–25.

[340] Rufin VanRullen and Christof Koch. “Is perception discrete or continuous?” In: *Trends in cognitive sciences* 7.5 (2003), pp. 207–213.

[341] Rufin VanRullen. “Perceptual cycles”. In: *Trends in cognitive sciences* 20.10 (2016), pp. 723–735.

[342] Enoch Callaway and Charles L Yeager. “Relationship between reaction time and electroencephalographic alpha phase”. In: *Science* 132.3441 (1960), pp. 1765–1766.

[343] Simon Hanslmayr et al. “The role of alpha oscillations in temporal attention”. In: *Brain research reviews* 67.1-2 (2011), pp. 331–343.

[344] Francisco J Valera et al. “Perceptual framing and cortical alpha rhythm”. In: *Neuropsychologia* 19.5 (1981), pp. 675–686.

[345] David Poeppel and M Florencia Assaneo. “Speech rhythms and their neural foundations”. In: *Nature Reviews Neuroscience* (2020), pp. 1–13.

[346] Jonathan E Peelle, Joachim Gross, and Matthew H Davis. “Phase-locked responses to speech in human auditory cortex are enhanced during comprehension”. In: *Cerebral cortex* 23.6 (2013), pp. 1378–1387.

[347] Joseph A Marsh and Sarah A Teichmann. “Structure, dynamics, assembly, and evolution of protein complexes”. In: *Annual review of biochemistry* 84 (2015), pp. 551–575.

[348] Joseph A Marsh, Sarah A Teichmann, and Julie D Forman-Kay. “Probing the diverse landscape of protein flexibility and binding”. In: *Current opinion in structural biology* 22.5 (2012), pp. 643–650.

[349] James R Perkins et al. “Transient protein-protein interactions: structural, functional, and network properties”. In: *Structure* 18.10 (2010), pp. 1233–1243.

[350] Peter Tompa et al. “A million peptide motifs for the molecular biologist”. In: *Molecular cell* 55.2 (2014), pp. 161–169.

[351] Hisham Mazal and Gilad Haran. “Single-molecule FRET methods to study the dynamics of proteins at work”. In: *Current opinion in biomedical engineering* 12 (2019), pp. 8–17.

[352] Manuela Ruzzoli et al. “The relevance of alpha phase in human perception”. In: *Cortex* 120 (2019), pp. 249–268.

[353] Christopher SY Benwell et al. “Prestimulus EEG power predicts conscious awareness but not objective visual performance”. In: *Eneuro* 4.6 (2017).

[354] Kalina Christoff et al. “Experience sampling during fMRI reveals default network and executive system contributions to mind wandering”. In: *Proceedings of the National Academy of Sciences* 106.21 (2009), pp. 8719–8724.

[355] Pascal Fries. “A mechanism for cognitive dynamics: neuronal communication through neuronal coherence”. In: *Trends in cognitive sciences* 9.10 (2005), pp. 474–480.

[356] Thomas Akam and Dimitri M Kullmann. “Oscillatory multiplexing of population codes for selective communication in the mammalian brain”. In: *Nature Reviews Neuroscience* 15.2 (2014), p. 111.

[357] John T Serences and Steven Yantis. “Selective visual attention and perceptual coherence”. In: *Trends in cognitive sciences* 10.1 (2006), pp. 38–45.

[358] Yixiang Zhang, Peng Gao, and Joshua S Yuan. “Plant protein-protein interaction network and interactome”. In: *Current genomics* 11.1 (2010), pp. 40–46.

[359] Montse Morell et al. “Detection of transient protein–protein interactions by bimolecular fluorescence complementation: The AblSH3 case”. In: *Proteomics* 7.7 (2007), pp. 1023–1036.

[360] Bintian Zhang et al. “Electronic Conductance Resonance in Non-Redox-Active Proteins”. In: *Journal of the American Chemical Society* 142.13 (2020), pp. 6432–6438.

[361] Qiang Cui and Martin Karplus. “Allostery and cooperativity revisited”. In: *Protein science* 17.8 (2008), pp. 1295–1307.

[362] Robert A Copeland. *Enzymes: a practical introduction to structure, mechanism, and data analysis*. John Wiley & Sons, 2004.

[363] Guanghong Wei et al. “Protein ensembles: how does nature harness thermodynamic fluctuations for life? The diverse functional roles of conformational ensembles in the cell”. In: *Chemical reviews* 116.11 (2016), pp. 6516–6551.

[364] Danielle S Bassett and Olaf Sporns. “Network neuroscience”. In: *Nature neuroscience* 20.3 (2017), pp. 353–364.

[365] Andrew Clouter, Kimron L Shapiro, and Simon Hanslmayr. “Theta phase synchronization is the glue that binds human associative memory”. In: *Current Biology* 27.20 (2017), 3143–3148. e6.

[366] Björn H Schott et al. “The relationship between level of processing and hippocampal–cortical functional connectivity during episodic memory formation in humans”. In: *Human brain mapping* 34.2 (2013), pp. 407–424.

[367] Alexander R Backus et al. “Hippocampal-prefrontal theta oscillations support memory integration”. In: *Current Biology* 26.4 (2016), pp. 450–457.

[368] Hyojin Park et al. “Frontal top-down signals increase coupling of auditory low-frequency oscillations to continuous speech in human listeners”. In: *Current Biology* 25.12 (2015), pp. 1649–1653.

[369] Kari L Hoffman et al. “Saccades during visual exploration align hippocampal 3–8 Hz rhythms in human and non-human primates”. In: *Frontiers in systems neuroscience* 7 (2013), p. 43.

[370] Yuri B Saalmann et al. “The pulvinar regulates information transmission between cortical areas based on attention demands”. In: *Science* 337.6095 (2012), pp. 753–756.

[371] Quanxin Wang et al. “Organization of the connections between claustrum and cortex in the mouse”. In: *Journal of Comparative Neurology* 525.6 (2017), pp. 1317–1346.

[372] Trichur R Vidyasagar and Ekaterina Levichkina. “An integrated neuronal model of claustral function in timing the synchrony between cortical areas”. In: *Frontiers in neural circuits* 13 (2019), p. 3.

[373] Thomas Donoghue et al. “Parameterizing neural power spectra into periodic and aperiodic components”. In: *Nature neuroscience* 23.12 (2020), pp. 1655–1665.

[374] Catherine Wacongne et al. “Evidence for a hierarchy of predictions and prediction errors in human cortex”. In: *Proceedings of the National Academy of Sciences* 108.51 (2011), pp. 20754–20759.

[375] John E Lisman and Ole Jensen. "The theta-gamma neural code". In: *Neuron* 77.6 (2013), pp. 1002–1016.

[376] John O'Keefe and Michael L Recce. "Phase relationship between hippocampal place units and the EEG theta rhythm". In: *Hippocampus* 3.3 (1993), pp. 317–330.

[377] Vegard H Brun et al. "Place cells and place recognition maintained by direct entorhinal-hippocampal circuitry". In: *Science* 296.5576 (2002), pp. 2243–2246.

[378] John Lisman and György Buzsáki. "A neural coding scheme formed by the combined function of gamma and theta oscillations". In: *Schizophrenia bulletin* 34.5 (2008), pp. 974–980.

[379] Laura Lee Colgin et al. "Frequency of gamma oscillations routes flow of information in the hippocampus". In: *Nature* 462.7271 (2009), p. 353.

[380] Paul Sauseng et al. "Brain oscillatory substrates of visual short-term memory capacity". In: *Current biology* 19.21 (2009), pp. 1846–1852.

[381] Ali Bahramisharif et al. "Serial representation of items during working memory maintenance at letter-selective cortical sites". In: *PLoS biology* 16.8 (2018), e2003805.

[382] Andrew C Heusser et al. "Episodic sequence memory is supported by a theta–gamma phase code". In: *Nature neuroscience* 19.10 (2016), p. 1374.

[383] Daniele Fanelli. "A theory and methodology to quantify knowledge". In: *Royal Society Open Science* 6.4 (2019), p. 181055.

[384] Niall M Woods, KS Roy Cuthbertson, and Peter H Cobbold. "Repetitive transient rises in cytoplasmic free calcium in hormone-stimulated hepatocytes". In: *Nature* 319.6054 (1986), pp. 600–602.

[385] Nelson Spruston et al. "Activity-dependent action potential invasion and calcium influx into hippocampal CA1 dendrites". In: *Science* 268.5208 (1995), pp. 297–300.

[386] Diana Smetters, Ania Majewska, and Rafael Yuste. “Detecting action potentials in neuronal populations with calcium imaging”. In: *Methods* 18.2 (1999), pp. 215–221.

[387] Anirvan Ghosh and Michael E Greenberg. “Calcium signaling in neurons: molecular mechanisms and cellular consequences”. In: *Science* 268.5208 (1995), pp. 239–247.

[388] Michael J Berridge. “Neuronal calcium signaling”. In: *Neuron* 21.1 (1998), pp. 13–26.

[389] David Badre and Derek Evan Nee. “Frontal cortex and the hierarchical control of behavior”. In: *Trends in cognitive sciences* 22.2 (2018), pp. 170–188.

[390] Semir Zeki. “The disunity of consciousness”. In: *Trends in cognitive sciences* 7.5 (2003), pp. 214–218.

[391] Bradley Voytek et al. “Oscillatory dynamics coordinating human frontal networks in support of goal maintenance”. In: *Nature neuroscience* 18.9 (2015), p. 1318.

[392] Randolph F Helfrich et al. “Prefrontal cortex modulates posterior alpha oscillations during top-down guided visual perception”. In: *Proceedings of the National Academy of Sciences* 114.35 (2017), pp. 9457–9462.

[393] Ian C Fiebelkorn, Mark A Pinsk, and Sabine Kastner. “A dynamic interplay within the frontoparietal network underlies rhythmic spatial attention”. In: *Neuron* 99.4 (2018), 842–853. e8.

[394] Valentin Wyart et al. “Rhythmic fluctuations in evidence accumulation during decision making in the human brain”. In: *Neuron* 76.4 (2012), pp. 847–858.

[395] Justin Riddle et al. “Distinct oscillatory dynamics underlie different components of hierarchical cognitive control”. In: *Journal of Neuroscience* (2020).

[396] Bradley Voytek et al. “Age-related changes in 1/f neural electrophysiological noise”. In: *Journal of Neuroscience* 35.38 (2015), pp. 13257–13265.

[397] Biyu J He. "Scale-free brain activity: past, present, and future". In: *Trends in cognitive sciences* 18.9 (2014), pp. 480–487.

[398] Claude Bedard, Helmut Kroeger, and Alain Destexhe. "Does the 1/f frequency scaling of brain signals reflect self-organized critical states?" In: *Physical review letters* 97.11 (2006), p. 118102.

[399] Plamen Ch Ivanov et al. "Multifractality in human heartbeat dynamics". In: *Nature* 399.6735 (1999), p. 461.

[400] Malvin C Teich. "Fractal character of the auditory neural spike train". In: *IEEE Transactions on Biomedical Engineering* 36.1 (1989), pp. 150–160.

[401] Thomas Goetze and Jürgen Brickmann. "Self similarity of protein surfaces". In: *Biophysical journal* 61.1 (1992), pp. 109–118.

[402] Armin Bunde and Shlomo Havlin. "A brief introduction to fractal geometry". In: *Fractals in science*. Springer, 1994, pp. 1–26.

[403] Wolfgang Klimesch. "The frequency architecture of brain and brain body oscillations: an analysis". In: *European Journal of Neuroscience* 48.7 (2018), pp. 2431–2453.

[404] Stuart R Hameroff and Richard C Watt. "Information processing in microtubules". In: *Journal of Theoretical Biology* 98.4 (1982), pp. 549–561.

[405] Wolfgang Klimesch. "An algorithm for the EEG frequency architecture of consciousness and brain body coupling". In: *Frontiers in human neuroscience* 7 (2013), p. 766.

[406] Suzanne Dikker et al. "Brain-to-brain synchrony tracks real-world dynamic group interactions in the classroom". In: *Current Biology* 27.9 (2017), pp. 1375–1380.

[407] Carolyn Parkinson, Adam M Kleinbaum, and Thalia Wheatley. "Similar neural responses predict friendship". In: *Nature communications* 9.1 (2018), pp. 1–14.

[408] SA Kotz, A Ravignani, and WT Fitch. "The evolution of rhythm processing". In: *Trends in cognitive sciences* 22.10 (2018), pp. 896–910.

[409] Bernard J Baars. "Global workspace theory of consciousness: toward a cognitive neuroscience of human experience". In: *Progress in brain research* 150 (2005), pp. 45–53.

[410] Bernard J Baars and Stan Franklin. "An architectural model of conscious and unconscious brain functions: Global Workspace Theory and IDA". In: *Neural networks* 20.9 (2007), pp. 955–961.

[411] Stanislas Dehaene, Michel Kerszberg, and Jean-Pierre Changeux. "A neuronal model of a global workspace in effortful cognitive tasks". In: *Proceedings of the national Academy of Sciences* 95.24 (1998), pp. 14529–14534.

[412] Bernard J Baars. "In the theatre of consciousness. Global workspace theory, a rigorous scientific theory of consciousness". In: *Journal of Consciousness Studies* 4.4 (1997), pp. 292–309.

[413] David Chalmers. "Panpsychism and panprotopsychism". In: *Consciousness in the physical world: Perspectives on Russellian monism* (2015), pp. 246–276.

[414] David M. Jonas. "Two-Dimensional Femtosecond Spectroscopy". In: *Annual Review of Physical Chemistry* 54.1 (2003), pp. 425–463.

[415] Yin Song et al. "The separation of vibrational coherence from ground- and excited-electronic states in P3HT film". In: *The Journal of Chemical Physics* 142.21 (2015), p. 212410.

[416] Joachim Seibt and Tõnu Pullerits. "Beating Signals in 2D Spectroscopy: Electronic or Nuclear Coherences? Application to a Quantum Dot Model System". In: *The Journal of Physical Chemistry C* 117.36 (2013), pp. 18728–18737.

[417] Nor Asmaliza Bakar, Azzuliani Supangat, and Khaulah Sulaiman. "Elaboration of PCDTBT nanorods and nanoflowers for augmented morphological and optical properties". In: *Materials Letters* 131 (2014), pp. 27–30.

[418] Niels-Ulrik Frigaard and Donald A Bryant. "Chromosomal gene inactivation in the green sulfur bacterium Chlorobium tepidum by natural transformation". In: *Applied and environmental microbiology* 67.6 (2001), p. 2538.

[419] Rafael Saer et al. "Perturbation of bacteriochlorophyll molecules in Fenna–Matthews–Olson protein complexes through mutagenesis of cysteine residues". In: *Biochimica et Biophysica Acta (BBA)-Bioenergetics* 1857.9 (2016), pp. 1455–1463.

[420] A. Palma and J. Morales. "Franck–condon factors and ladder operators. I. harmonic oscillator". In: *International Journal of Quantum Chemistry* 24.S17 (1983), pp. 393–400. ISSN: 0020-7608.

[421] Elad Harel. "Long range excitonic transport in a biomimetic system inspired by the bacterial light-harvesting apparatus". In: *The Journal of Chemical Physics* 136.17 (2012), p. 174104.

[422] Mi Kyung Lee, Pengfei Huo, and David F. Coker. "Semiclassical Path Integral Dynamics: Photosynthetic Energy Transfer with Realistic Environment Interactions". In: *Annual Review of Physical Chemistry* 67.1 (2016), pp. 639–668.

[423] Francesco Segatta et al. "A Quantum Chemical Interpretation of Two-Dimensional Electronic Spectroscopy of Light-Harvesting Complexes". In: *Journal of the American Chemical Society* 139.22 (2017), pp. 7558–7567.

[424] Kirsten Claridge, Daniele Padula, and Alessandro Troisi. "How fine-tuned for energy transfer is the environmental noise produced by proteins around biological chromophores?" In: *Physical Chemistry Chemical Physics* 20.25 (2018), pp. 17279–17288.

[425] Pawe J. Nowakowski, M. Faisal Khyasudeen, and Howe-Siang Tan. “The effect of laser pulse bandwidth on the measurement of the frequency fluctuation correlation functions in 2D electronic spectroscopy”. In: *Chemical Physics* 515 (2018), pp. 214–220.

[426] Thanh Nhut Do, Maxim F. Gelin, and Howe-Siang Tan. “Simplified expressions that incorporate finite pulse effects into coherent two-dimensional optical spectra”. In: *The Journal of Chemical Physics* 147.14 (2017), p. 144103.

[427] Xuan Leng et al. “Effects of finite laser pulse width on two-dimensional electronic spectroscopy”. In: *Chemical Physics Letters* 667 (2017), pp. 79–86.

[428] Franco V. de A. Camargo et al. “Resolving Vibrational from Electronic Coherences in Two-Dimensional Electronic Spectroscopy: The Role of the Laser Spectrum”. In: *Physical Review Letters* 118.3 (2017), p. 033001.

[429] Marc Lutz. “Red-band resonance raman spectroscopy of chlorophyll cofactors in photosynthetic proteins”. In: *Biospectroscopy* 1.5 (1995), pp. 313–327.

[430] Tony A. Mattioli et al. “Application of near-IR Fourier transform resonance Raman spectroscopy to the study of photosynthetic proteins”. In: *Spectrochimica Acta Part A: Molecular Spectroscopy* 49.5 (1993), pp. 785–799.

[431] Bruno Robert and Marc Lutz. “Structures of antenna complexes of several Rhodospirillales from their resonance Raman spectra”. In: *Biochimica et Biophysica Acta (BBA) - Bioenergetics* 807.1 (1985), pp. 10–23.

[432] George Chumanov et al. “Resonance Raman and Surface-Enhanced Resonance Raman Spectra of LH2 Antenna Complex from Rhodobacter sphaeroides and Ectothiorhodospira sp. Excited in the Qx and Qy Transitions ”. In: *Photochemistry and Photobiology* 71.5 (2000), pp. 589–595.

[433] Margus Rätsep and Arvi Freiberg. "Electron–phonon and vibronic couplings in the FMO bacteriochlorophyll a antenna complex studied by difference fluorescence line narrowing". In: *Journal of Luminescence* 127.1 (2007), pp. 251–259.

[434] Arvi Freiberg et al. "Excitonic polarons in quasi-one-dimensional LH1 and LH2 bacteriochlorophyll a antenna aggregates from photosynthetic bacteria: A wavelength-dependent selective spectroscopy study". In: *Chemical Physics* 357.1 (2009), pp. 102–112.

[435] Ralph Jimenez et al. "Electronic Excitation Transfer in the LH2 Complex of Rhodobacter sphaeroides". In: *The Journal of Physical Chemistry* 100.16 (1996), pp. 6825–6834.

[436] Robert E. Blankenship. "Antenna Complexes and Energy Transfer Processes". In: *Molecular Mechanisms of Photosynthesis*. 2nd ed. Blackwell Science, 2008. Chap. 5, pp. 61–94.

[437] Lijun Guo et al. "The observation of excited-state dynamical evolution in light-harvesting complex LH2 from Rhodobacter sphaeroides 601". In: *FEBS Letters* 511.1 (2002), pp. 69–72.

[438] Yin Song et al. "The separation of vibrational coherence from ground- and excited-electronic states in P3HT film". In: *The Journal of Chemical Physics* 142.21 (2015), p. 212410.

[439] David M. Jonas. "Vibrational and Nonadiabatic Coherence in 2D Electronic Spectroscopy, the Jahn–Teller Effect, and Energy Transfer". In: *Annual Review of Physical Chemistry* 69.1 (2018), pp. 327–352.

[440] S. Ithurria et al. "Colloidal nanoplatelets with two-dimensional electronic structure". In: *Nature Materials* 10.12 (2011), pp. 936–941.

[441] Sandrine Ithurria and Dmitri V. Talapin. "Colloidal Atomic Layer Deposition (c-ALD) using Self-Limiting Reactions at Nanocrystal Surface Coupled to Phase Transfer between Polar and Nonpolar Media". In: *Journal of the American Chemical Society* 134.45 (2012), pp. 18585–18590.

[442] Zachary A. VanOrman et al. "Green-to-Blue Triplet Fusion Upconversion Sensitized by Anisotropic CdSe Nanoplatelets". In: *Chemistry of Materials* 32.11 (2020), pp. 4734–4742.

[443] Andrew Paul Beyler. "Single-nanocrystal photon correlation: a versatile tool for elucidating basic physics and characterizing applications-relevant properties". Thesis. 2015.

[444] X. Brokmann et al. "Photon-correlation Fourier spectroscopy". In: *Opt Express* 14.13 (2006), pp. 6333–41.

[445] L. Coolen et al. "Emission characterization of a single CdSe-ZnS nanocrystal with high temporal and spectral resolution by photon-correlation Fourier spectroscopy". In: *Phys Rev Lett* 100.2 (2008), p. 027403.

[446] Zhongjian Hu et al. "Influence of morphology on the blinking mechanisms and the excitonic fine structure of single colloidal nanoplatelets". In: *Nanoscale* 10.48 (2018), pp. 22861–22870.

[447] Lisa Faye Marshall. "Spectral dynamics of single quantum dots: A study using photon-correlation Fourier spectroscopy for submillisecond time resolution at low temperature and in solution". Thesis. 2011.

[448] Boris Spokoyny. *Photon Arrival Time Correlation*. Computer Program. 2017. URL: https://www.mathworks.com/matlabcentral/fileexchange/64605-photon-arrival-time-correlation.